

Magnetism in layered Nickelates and Cobaltates

Dissertation

zur Erlangung des Akademischen Grades
Doctor rerum naturalium (Dr. rer. nat.)
der Fakultät Mathematik und Naturwissenschaften
der Technischen Universität Dresden

vorgelegt von
Jan Yvo Drees
geboren am 18.10.1981 in Braunschweig

Dresden 2014

Gutachter:

Prof. Dr. Liu Hao Tjeng

Prof. Dr. Michael Loewenhaupt

Prof. Dr. Vladimir Hinkov

Eingereicht am: 17.12.2014

Verteidigung am: 04.11.2015

Die Dissertation wurde in der Zeit von April 2011
bis November 2014 am Max-Planck-Institut
für Chemische Physik fester Stoffe angefertigt.

Contents

1	Introduction	1
1.1	Fascinating World of Transition Metal Oxides	1
1.2	Crystal Structure of 214 Compounds	5
1.3	Mutual Octahedra Tilting	8
1.4	Structural Phase Transitions	9
1.5	Oxygen Stoichiometry	11
1.6	Mott-Hubbard	14
1.7	Zaanen-Sawatzky-Allen Model	16
1.8	Intersite Exchange Interactions	18
1.9	Spin blockade Mechanism	22
1.10	Magnetic Order	24
1.10.1	$\text{La}_{2-x}\text{Sr}_x\text{CuO}_4$	24
1.10.2	$\text{La}_{2-x}\text{Sr}_x\text{NiO}_4$	25
1.10.3	$\text{La}_{2-x}\text{Sr}_x\text{CoO}_4$	27
1.11	Scope of this Thesis	28
2	Experimental Methods	31
2.1	Sample Preparation	32
2.1.1	Polycrystalline Samples	33
2.1.2	Floating Zone Technique	35
2.1.3	Growth of Incongruent Melting Crystals	38
2.2	Powder X-ray Diffraction Technique	43
2.3	Energy-dispersive and Wavelength-dispersive X-ray Spectroscopy	46
2.4	ICP-OES and CGHE	48
2.5	Triple Axis Spectrometer	48
2.5.1	Sample Orientation and Mounting	51
3	Sample Characterization: Results	53
3.1	$\text{La}_{2-x}\text{Sr}_x\text{NiO}_4$	53
3.1.1	Powder X-ray Diffraction	53

3.1.2	EDX and WDX	57
3.1.3	ICP-OES	60
3.2	$\text{La}_{2-x}\text{Sr}_x\text{CoO}_4$	61
3.2.1	Powder X-ray Diffraction	61
3.2.2	EDX and WDX	65
3.2.3	ICP-OES and CGHE	69
3.2.4	Oxygen Content Determination	70
3.2.5	Thermogravimetric	71
3.3	$\text{La}_{1-x}\text{Sr}_{1+x}\text{FeO}_4$	75
3.3.1	Powder X-ray Diffraction	75
3.3.2	Titration of $\text{La}_{2-x}\text{Sr}_x\text{FeO}_4$	77
4	$\text{La}_{2-x}\text{Sr}_x\text{NiO}_4$	81
4.1	Temperature Dependence of the Lattice Parameter in Low Doped Nickelates	83
4.2	Incommensurate Magnetic Order	89
4.3	Magnetic Excitations	95
4.4	Reciprocal Space Maps with FlatCone	102
4.5	Polarized Neutrons	110
4.6	Conclusions	119
5	$\text{La}_{2-x}\text{Sr}_x\text{CoO}_4$	123
5.1	Sample and TAS Instrument Setup	125
5.2	HTT-LTO Phase Transition	126
5.2.1	High Resolution Powder X-ray Diffraction	126
5.2.2	Neutron Diffraction	128
5.3	Spin and Charge Order	129
5.3.1	Low Energy Synchrotron Diffraction	129
5.3.2	Elastic Neutron TAS Measurements	130
5.3.3	Hard X-ray Single Crystal Measurements	133
5.4	Electron-Phonon Coupling	136
5.5	Magnetic Excitations	138
5.6	Discussion	149
6	Appendix	155
6.1	List of Grown Single Crystals	156
6.2	List of Measured Crystals	157
6.3	List of TG Results in the Cobaltates	160
6.4	Additional Neutron Data in the Nickelates	161
6.5	Temperature Dependence of the Magnetic Order in $\text{La}_{4/3}\text{Sr}_{1/3}\text{CoO}_4$	164
	Bibliography	165

Abstract	191
List of Abbreviations	191
Acknowledgements	195
Versicherung	199
Publications	198

Chapter 1

Introduction

1.1 Fascinating World of Transition Metal Oxides

“Transition metal oxides constitute one of the most fascinating classes of inorganic solids, exhibiting a very wide variety of structures, properties and phenomena.” [1] Due to the unique nature of the outer d electrons the metal-oxygen bonding ranges from nearly ionic to metallic, leading to the unusual properties of transition metal oxides. The relatively low reactivity of unpaired d-electrons allows a stabilization of different oxidation states with partially filled d-shells. Serious attempts to characterize and understand the electronic and magnetic properties of transition metal oxides began in the late 1930s as X-ray sources became better and cheaper. Materials in this class range from oxides with metallic properties (e.g. RuO_2 , ReO_3 , LaNiO_3 [2–4]) to oxides with insulating behavior (e.g. BaTiO_3) and oxides that cross the boundary between both regimes with change in temperature, pressure or composition (e.g. V_2O_3 [5], $\text{La}_{1-x}\text{Sr}_x\text{VO}_3$ [6]). Ordering phenomena like charge-density waves (e.g. $\text{K}_{0.3}\text{MoO}_3$ [7]), charge ordering (e.g. Fe_3O_4 [8]) and defect ordering (e.g. $\text{Ca}_2\text{Mn}_2\text{O}_5$ and $\text{Ca}_2\text{Fe}_2\text{O}_5$ [9]) give rise to interesting electronic properties while the magnetic properties vary from ferromagnetic (e.g. CrO_2 , $\text{La}_{0.5}\text{Sr}_{0.5}\text{MnO}_3$) over ferrimagnetic (e.g. Fe_3O_4 , $\text{Ca}_2\text{Fe}_2\text{O}_5$) to antiferromagnetic (e.g. NiO , LaCrO_3). Not to forget, there are oxides with switchable orientation states as in ferroelectric (e.g. BaTiO_3 [10] and KNbO_3 [11]) and ferroelastic (e.g. $\text{Gd}_2(\text{MoO}_4)_3$ [12]) materials and oxides with the formula $\text{Ln}_{1-x}\text{A}_x\text{MnO}_3$ (Ln = rare earth, A = alkaline earth) exhibiting giant magnetoresistance [13, 14]. Finally, high temperature superconductivity in the cuprates that was discovered by Bednorz and Müller [15] in 1986 has attracted enormous attention.

Unusual properties that distinguish the transition metal oxides from metal-

lic elements, covalent semiconductors and ionic insulators originate from several factors. The overlap between metal d and oxygen p orbitals is small and the resulting electronic bands are narrow (typical of the order of 1-2 eV rather than 5-15 eV as in most metals) causing electron correlation effects to play an important role. Furthermore, the polarizability of the oxygen is of importance. While the O^{2-} ion does not describe the state of oxygen accurately, configurations such as O^- have to be accounted for. (cf. [1, 16])

Among the large number of transition metal oxides the single layer perovskite oxides with the K_2NiF_4 [17] structure form a small subgroup with the formula A_2TO_4 (214-perovskite), where A = alkaline earth or lanthanide metal and T = transition metal. The remarkable variety of phenomena that can be observed in this class of materials makes them interesting for fundamental research as well as technological applications.

Single layer perovskite oxides are composed of alternating planes of transition metal oxide and alkaline earth metal oxide or lanthanide oxide. Such compounds exist for the whole range of 3d metals from Sr_2TiO_4 [18] to Sr_2CuO_4 [19–24] (except for nickel so far) and from $LaSrVO_4$ [25] to $LaSrCuO_{4+\delta}$ [26–31]. The large structural differences between the in plane directions and the stacking direction are responsible for a pronounced anisotropy of the physical properties. Such anisotropies can lead to low dimensional features like in La_2CuO_4 and La_2NiO_4 [32] which are quasi two dimensional compared with the related three dimensional perovskites $LaCuO_3$ and $LaNiO_3$.

A variation of the properties by doping generally induces changes in more than one way e.g. doping lanthanum for strontium induces chemical pressure due to size differences and at the same time changes the electronic configuration of the transition metal due to hole doping. It is possible to influence the properties of the transition metal oxygen layer with electron/hole doping by the interchange of lanthanum(III) and strontium(II) in the other layer. Thus, due to the low dimensionality of the 214-perovskites the effect of chemical pressure does not interfere as much with the tuned properties. This makes low dimensional structures to ideal systems on which the influence of variation of a single parameter can be tested.

The most prominent property within the transition metal oxides is the high-temperature superconductivity (HTSC) in the cuprates for which the 214-perovskite $La_{2-x}Sr_xCuO_4$ can be considered as the prototypical system. The extensive research in this field is reflected by the vast number of publications in the past 28 years. Among the peculiarities of the HTSC cuprates are also the phenomenon of charge stripe order (CSO) and a distinct shape of the magnon dispersion which resembles an hourglass.

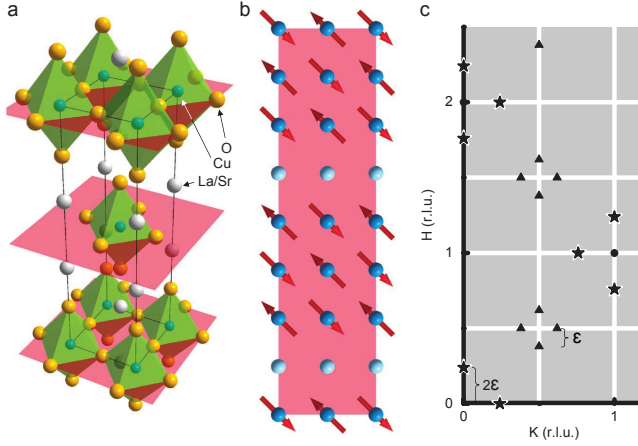


Figure 1.1: Charge stripe order in cuprates. (a) Crystal structure of the layered perovskite $\text{La}_{2-x}\text{Sr}_x\text{CuO}_4$. Cu-O planes marked in red. (b) Model of site-centered charge stripe order for $x = 1/8$ within the Cu-O planes. Only the Cu sites are shown while light blue denotes hole-rich sites and arrows indicate the spin direction. (c) Reciprocal space map with fundamental Bragg peaks (filled circles), spin order (triangles) and charge-order (stars) superstructure reflections related to the stripe phase. Revised from Wu et al. [33].

- **Charge Stripe Order:** This particular charge ordering was initially predicted by theoretical studies which dealt with the introduction of charges into the Hubbard model. It was found that charged domain walls are stable solutions [34–37]. The later discovery of static charge and magnetic stripe ordering in $\text{La}_{1.6-x}\text{Nd}_{0.4}\text{Sr}_x\text{CuO}_4$ [38] and $\text{La}_{2-x}\text{Ba}_x\text{CuO}_4$ [39, 40] lead to an intensive search throughout the cuprate family (see Figure 1.1).
- **Magnon Dispersion:** Hourglass shaped spin excitations were established for most HTSC and experiments indicate that spin fluctuations evolve continuously from the antiferromagnetic (AF) insulating state of the parent compounds [41] (see Figure 1.2). Many theorists believe that AF fluctuations are involved in the superconducting pairing mechanism [42–44]. However, alternative models have also been proposed for the pairing among which those based on electron-phonon interaction form a second fundamental direction of thought [45, 46].

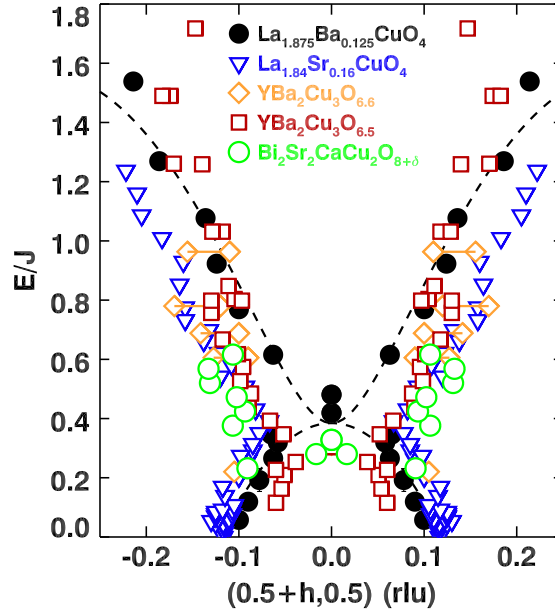


Figure 1.2: "Hourglass" magnetic dispersion relation parallel to the Cu-O bonds in various cuprate HTSC. Data published for $\text{La}_{1.875}\text{Ba}_{0.125}\text{CuO}_4$ [47], $\text{La}_{1.84}\text{Sr}_{0.16}\text{CuO}_4$ [48], $\text{YBa}_2\text{Cu}_3\text{O}_{6.6}$ [49], $\text{YBa}_2\text{Cu}_3\text{O}_{6.5}$ [50, 51], $\text{Bi}_2\text{Sr}_2\text{CaCu}_2\text{O}_{8+\delta}$ [52]. The energy is scaled by the exchange coupling J of the AF parent material [44, 53]. From Fujita et al. [54].

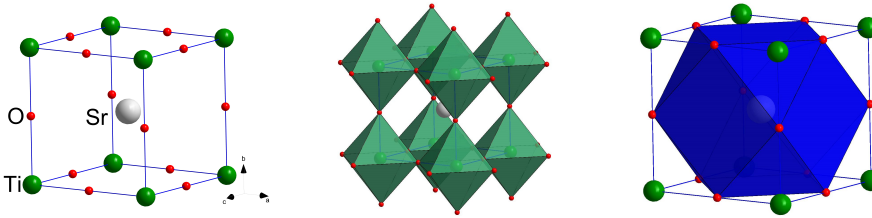


Figure 1.3: Structure of the perovskite SrTiO_3 *left*: Atom positions within the cubic unit cell. *middle*: Six-fold oxygen coordination of titanium. *right*: Oxygen coordination polyhedron of the twelve-fold coordinated strontium.

1.2 Crystal Structure of 214 Compounds

Transition metal compounds with the general formula A_2TX_4 often exhibit the common K_2NiF_4 structure (Figure 1.4 *left*) when A is a divalent alkaline earth or a trivalent lanthanide metal, T a transition metal and $\text{X} = \text{O}, \text{F}, \text{Cl}$. The structure consists of two simpler components, the perovskite and the rock salt structures, which are stacked alternating along the c-direction. A better understanding of the trends and properties of layered perovskites can be gained by examining these underlying components: Stoichiometric perovskites with the formula ATO_3 consist of corner-sharing TO_3 octahedra giving rise to a cubic unit cell where the transition metal T can be found at the corners while the oxygen atoms occupy all 12 edges. This arrangement of octahedra is known from the ReO_3 structure where it contains a large empty space in the center. This central hole can be filled with a cation which must be larger in size than a typical transition metal ion due to the 12-fold coordination with oxygen. The resulting perovskite structure is common among ternary transition metal compounds (Figure 1.3). Depending on the oxidation state of the A and T ions three categories of perovskites can be classified: $\text{A}^{\text{I}}\text{T}^{\text{V}}$, $\text{A}^{\text{II}}\text{T}^{\text{IV}}$ and $\text{A}^{\text{III}}\text{T}^{\text{III}}$. Systematic studies and tabulations of perovskites are available in the literature [55, 56].

Like most members of this class of materials not even its name giving mineral CaTiO_3 crystallizes in the ideal cubic form but, due to a mismatch in size, in an orthorhombic space group. To sufficiently fill the oxygen octahedra a first criterion for a stable perovskite is that the T-cation size is sufficiently large. If this is not fulfilled there is not enough space to attach all the oxygen atoms to the cation. Off centering of an undersized T cation within its octahedron reduces the coordination number to attain a stable bonding pattern. Introduction of the A cation generally leads to a distortion in the TO_3 array so as to optimize the A-O bonding. The coordination number can be decreased down to 8 by a tilting of the TO_6 octahedra. Goldschmidt [57] formulated a tolerance factor to define

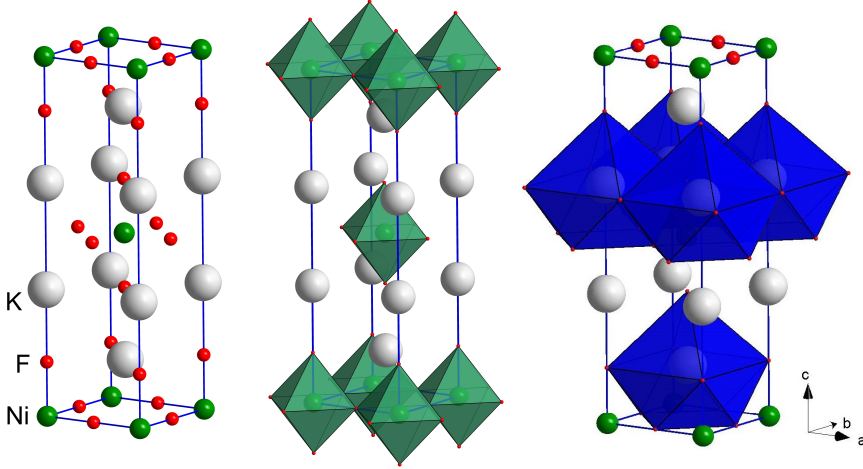


Figure 1.4: *Left:* The ideal tetragonal single layered perovskite structure of the reference compound K_2NiF_4 has the space group $I4/mmm$.

Middle: Alternating layers of nickelfluorite and potassiumfluorite. Oxygen coordination of nickel is six, like in the perovskite parent compound.

Right: Potassium coordination by oxygen is nine fold. Only half of the potassium oxide polyhedra have been made visible.

the sustainable limits of the A and T cation size:

$$t = \frac{r_A + r_O}{\sqrt{2}(r_T + r_O)} \quad (1.1)$$

where r_i are the empirical ionic radii which generally depend on oxidation state, coordination number, type of coordinating atoms, proportion of covalency, spin state, etc.. Empirical radii were tabulated by Shannon and Prewitt in 1968 [58, 59] based on the evaluation of 1000 interatomic distances. Their values were calculated starting from assumed oxygen and fluoride radii and take into account the coordination number and the spin state. From the geometric point of view the ideal cubic structure has a tolerance factor of $t \approx 1$ (e.g. SrTiO_3 which has $t = 0.98$) while the distorted perovskite structure is stable within the range $0.8 < t < 1.05$ [1].

Rock salt is the second simple structure contained in the K_2NiF_4 system. Compared with the corner-sharing oxygen octahedra in perovskites the cubic rock salt structure (eg. SrO) consists of edge-sharing oxygen octahedra. To understand how the two structures fit together one should envision a cut along the ab -plane at a height of $z = 1/2$ through the perovskite structure in Figure

1.3. It then becomes apparent that the distribution of strontium and oxygen in the plane resembles that of rock salt. Attaching the two structures in this plane leads to the K_2NiF_4 structure if they are stacked alternating (see Figure 1.4). Ruddlesden and Popper [60] found that a whole series of compounds can be described by a varying amount of perovskite layers between the intermediate rock salt layers. The general formula is:

$$(\text{ATX}_3)_n\text{AX} = \text{A}_{n+1}\text{T}_n\text{X}_{3n+1} \quad (1.2)$$

where n is an integer. In this series the K_2NiF_4 structure is the starting member with $n=1$ and is therefore often referred to as “single layer perovskite” or “214-perovskite”, while the simple perovskite ATO_3 represents the $n = \infty$ member. Examples for the series are $\text{La}_{n+1}\text{Ni}_n\text{O}_{3n+1}$, $\text{Sr}_{n+1}\text{Ti}_n\text{O}_{3n+1}$ [60] or $\text{La}_{n+1}\text{Cu}_n\text{O}_{3n+1}$. The latter being the system in which Bednorz and Müller observed high temperature superconductivity for the first time [15]. Except for the end member ATO_3 the compounds within the Ruddlesden-Popper series have a tetragonal crystal structure due to the stacking along the c -axis. The relation of the lattice constants between perovskite and rock salt is

$$a \approx a_{\text{perovskite}} \approx \frac{a_{\text{rocksalt}}}{\sqrt{2}} \quad (1.3)$$

$$c_n \approx 2(na_{\text{perovskite}} + \frac{a_{\text{rocksalt}}}{\sqrt{2}}) = a_p(2n + \sqrt{2}) = a_r(n\sqrt{2} + 1) \quad (1.4)$$

where a and c_n are the lattice constants of the n -layered perovskite.

Basal and apical oxygen positions in the octahedral coordination sphere of the central transition metal ion are subject to different coordination spheres in layered perovskites and usually no longer maintain their cubic (ideal perovskite) symmetry (see Figure 1.4). Oxygen octahedra in layered perovskites therefore usually exhibit a tetragonal distortion of the ideal octahedral symmetry. The layered 214-perovskites, discussed in this thesis, all exhibit a pronounced bond length mismatch at room temperature through to big A-site ions compared with the T-site ions. That places the A-O-bonds under tension and the T-O-bonds under compression. Strain can be released by decreasing the distance to the basal oxygens. The values of the tolerance factor are therefore not accurate as they are calculated for a symmetric coordination and are therefore closer to unity than suggested by Figure 1.5.

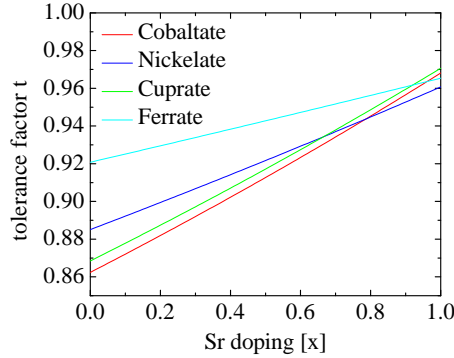


Figure 1.5: Doping dependence of the calculated Goldschmidt tolerance factor t for $\text{La}_{2-x}\text{Sr}_x\text{CoO}_4$, $\text{La}_{2-x}\text{Sr}_x\text{NiO}_4$, $\text{La}_{2-x}\text{Sr}_x\text{CuO}_4$ and $\text{La}_{1-x}\text{Sr}_{1+x}\text{FeO}_4$ at room temperature under the condition of the spin states drawn in Figure 1.14. The real values are expected to be somewhat higher as the tetrahedral distortion of the transition metal oxygen octahedra has not been accounted for.

1.3 Mutual Octahedra Tilting

Throughout this thesis the lattice values are expressed with respect to the tetragonal $I4/mmm$ unit cell, an index will be added only when referring to a different unit cell. The tetragonal unit cell (space group $I4/mmm$) of compounds with the K_2NiF_4 structure contains two formula units A_2TX_4 where neighboring planes of corner sharing TX_6 octahedra are shifted by half the body diagonal of the unit cell i.e. $(1/2 \ 1/2 \ 1/2)$ (Figure 1.4). The oxygen coordination of the transition metal is six-fold like in the perovskite structure but the coordination of the A-site is nine-fold which is the average between the 12-fold coordination in perovskite and the six-fold coordination in rock salt (see Figure 1.4 *left*). In two simultaneous studies of the structural distortions found in K_2NiF_4 materials it has been shown that all experimentally observed phase transitions can be described by considering the collective tilts of the TX_6 octahedra [61–63]. Taking into account the three possible tilting directions: a tilt around the normal to the ab -plane (Θ tilts) and two kinds of tilts (Φ and Ψ), that can occur around the a and/or b axes of the tetragonal unit cell, a total of 15 different variants of distortions within a single layer are possible [61, 62, 64]. For the compounds investigated here only four variants are of interest. These are listed in Table 1.1. Especially the Θ -tilts do not occur.

octahedral tilt	unit cell [V_{HTT}]	space group	notation
(0 0 0)	1	I4/mmm	HTT
(Φ - Φ 0)	$\sqrt{2} \times \sqrt{2} \times 1$	Bmab	LTO
(Φ 0 0)	$\sqrt{2} \times \sqrt{2} \times 1$	P4 ₂ /ncm	LTT
(Φ Ψ 0)	$\sqrt{2} \times \sqrt{2} \times 1$	Pccn	LTLO

Table 1.1: Structural distortions and their corresponding unit cells. HTT - high temperature tetragonal, LTO - low temperature orthorhombic, LTT - low temperature tetragonal, LTLO - low temperature less orthorhombic [61, 62, 64]

1.4 Structural Phase Transitions

In the undoped parent compounds La_2TO_4 with $T = \text{Co}, \text{Ni}$ and Cu the tetragonal K_2NiF_4 structure is only stable at high temperature. Phase diagrams, summarizing the results so far, can be found in Figure 1.6. The cause for the instability is a mismatch of the ionic sizes between the A-site and T-site atoms. According to the revised tables of Shannon [59] the radii of the T-site ions $r(\text{Co}^{+2} \text{ HS}) = 0.745$, $r(\text{Ni}^{+2}) = 0.69$ and $r(\text{Cu}^{+2}) = 0.73$ in octahedral coordination are quite similar, leading to the room temperature tolerance factors $t = 0.862, 0.885$ and 0.868 , respectively. In other words, the transition metal ions are too big for the T-site and it can be expected that the ideal tetragonal structure can be stabilized by a (partial) replacement with smaller ions. The tolerance factor has been calculated for the whole doping range $0 \leq x \leq 1$ and plotted in Figure 1.5. Lifting the strain through strontium doping leads to a reduced temperature of the HTT-LTO phase transition until it disappears around $x \approx 0.2$ for the nickelate and cuprate and $x \approx 0.3$ for the cobaltate.

Keeping in mind that the ionic radii used for the evaluation are averaged values determined from many different structures and that the tolerance factor was derived from geometrical arguments only, it is nonetheless a very useful tool. The HTT-LTO transition temperatures of the cobalt and nickel compounds are quite similar while it is slightly lower in the nickelate as to be expected for a tolerance factor closer to the ideal value. The situation is different in the cuprate because the $3d^9$ state of the Cu^{+2} ion is highly Jahn-Teller active [65], leading to a distortion of the ideal copper-oxide octahedra. While the distance between central atom and apical oxygen is increased, the distance to the equatorial oxygen is reduced. This effective reduction of the transition metal size within the ab-plane releases structural strain. In the phase diagram this effect becomes apparent in a reduced transition temperature. Nickel in the Ni^{+3} state is also expected to show a Jahn-Teller distortion but experiments were unable to find evidence for this effect on the NiO_6 octahedra. It was also argued that this kind

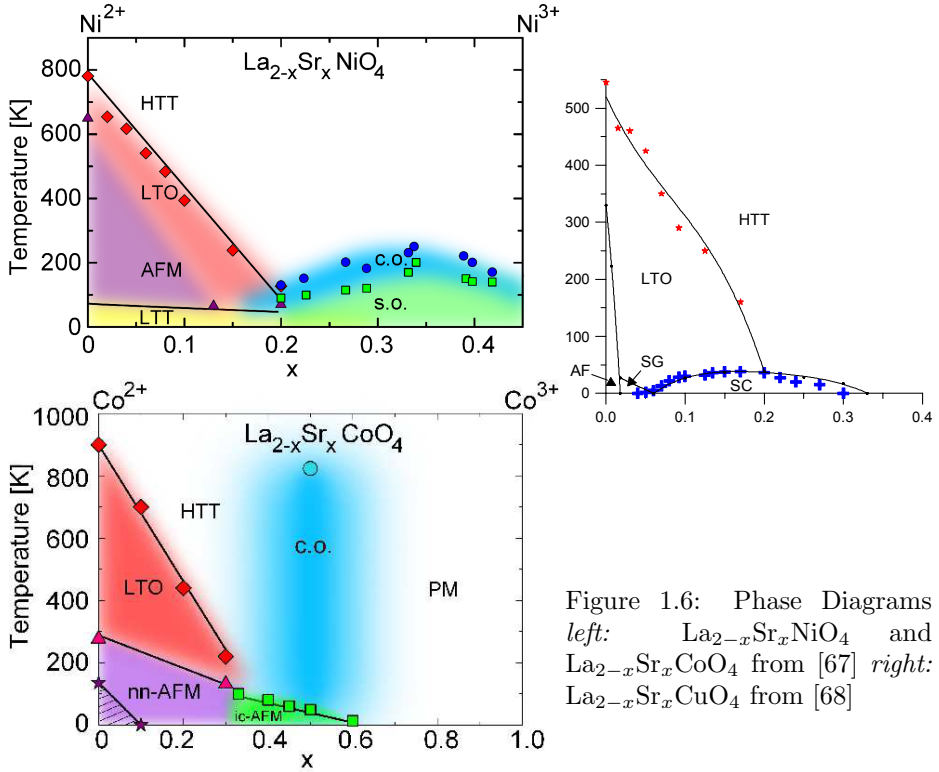


Figure 1.6: Phase Diagrams
left: $\text{La}_{2-x}\text{Sr}_x\text{NiO}_4$ and $\text{La}_{2-x}\text{Sr}_x\text{CoO}_4$ from [67] right:
 $\text{La}_{2-x}\text{Sr}_x\text{CuO}_4$ from [68]

of distortions are incompatible with local symmetry in $x = 1/3$ stripe ordered nickelates [66].

In the orthorhombic phase of all three systems the space group is Bmab (see Tabular 1.1) due to a collective tilt of the transition metal oxygen octahedra along the (1 -1 0)-direction (a-direction in the orthorhombic Bmab space group). Between two adjacent corner sharing octahedra the distortion direction is opposite leading to an antiferrodistortive ordering [69]. The reason for the phase transition is an increasing bond mismatch upon cooling. While the tolerance factor can be close to unity during the synthesis at above 1000° C, its value will decrease as the temperature is lowered due to the larger thermal expansion of the La-O bonds compared to the T-O bonds (T = Co, Ni, Cu) [70].

A further structural transition below room temperature was reported for the cobaltate [71, 72] and the nickelate [32] systems. For the nickelates structural refinements were not able to distinguish between the proposed $\text{P4}_2/\text{ncm}$ and

Pccn space groups because of a similar good agreement with the experimental data [73]. Finally Carvajal et al. [74] concluded that due to twinning the two phases are indistinguishable when regarding Bragg positions only. Evaluating the anisotropic broadening of the Bragg reflections due to correlated fluctuations of the cell parameters they found the low temperature phase to have tetragonal $P4_2/\text{ncm}$ symmetry [74]. Contrary results favoring the LTLO structure were obtained in a later neutron diffraction study on a twinned single crystal containing only two of the four possible twin domains [75]. The HTT to LTO transition is of second order with a continuous order parameter (orthorhombic strain = $2(b-a)/(a+b)$) and Bmab being a subgroup of $I4/\text{mmm}$ [74]. The second phase transition, LTO to LTT is of first order with a jump in the order parameter. $P4_2/\text{ncm}$ is a subgroup of $I4/\text{mmm}$ but not of Bmab [74]. For the cobaltate compound the same low temperature structure was proposed [67].

1.5 Oxygen Stoichiometry

Among the derivatives of the ATO_3 perovskites structure are also $\text{A}_2\text{T}_2\text{O}_7$ (eg. pyrochlore) and $\text{A}_2\text{T}_2\text{O}_5$ (eg. brownmillerite [76]). The former can be synthesized through oxidation, the latter through reduction of the stoichiometric perovskite. Especially for the compounds $\text{SrTO}_{2.5+\delta}$ ($\text{T} = \text{Fe}, \text{Co}$) and $\text{La}_2\text{TO}_{4+\delta}$ ($\text{T} = \text{Co}, \text{Ni}, \text{Cu}$) the oxygen content δ can be varied already at room temperature via electrochemistry in an aqueous alkaline electrolyte [77–79]. The transition from one compound to another proceeds through a variety of intermediate compositions with oxygen superstructure. The importance of the oxygen content for the physical properties in layered perovskites became obvious when high temperature superconductivity was found in $\text{La}_2\text{CuO}_{4+\delta}$. By electrochemistry at ambient temperature it is possible to oxidize this compound up to $\delta = 0.07$, turning it to a high T_c superconductor [80–82]. Similar studies on other 214 transition metal perovskites revealed ambient temperature oxygen conductivity also for the cobalt and nickel compounds [77, 83–85]. Attempts to label the position of the excess oxygen proved difficult due to the low occupancy of the interstitial site (e.g. $\delta = 0.07$ corresponds to one excess oxygen atom per seven unit cells, randomly distributed among all symmetry equivalent sites). Finally it appears that the excess oxygen is located at an interstitial position $(1/2\ 0\ 1/4)$ [71, 86, 87] (see Figure 1.7). This site provides a favorable coordination with four lanthanum atoms in tetrahedral coordination. But also the coordination with four oxygen in the first coordination sphere is unfavorable, especially with an oxygen-oxygen distance of about 2.3 \AA in comparison to the average ionic oxygen radius of 1.38 \AA [59]. The existence of a bonding between interstitial and apical oxygen, i.e. the formation of a superoxide O_2^{2-} was discussed controversial [88–93]. But it was finally dismissed after spectroscopic measurements

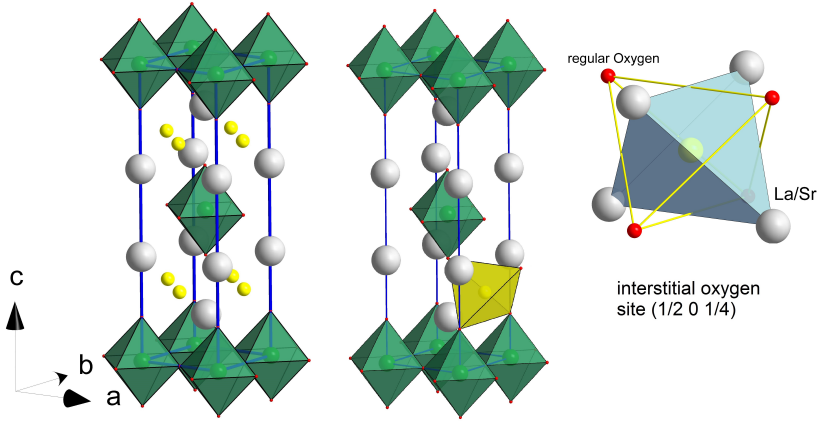


Figure 1.7: *left*: Interstitial oxygen position $(1/2\ 0\ 1/4)$ within the tetragonal $I4/mmm$ unit cell.

middle and right: Coordination of the interstitial oxygen. The nearest neighbors are four apical oxygen sites and four lanthanum sites, both at a distance of $\approx 2.3\ \text{\AA}$, forming tetrahedral coordinations.

were able to show that inter-oxygen bonds are due to a high surface oxygen concentration [94] and neutron diffraction experiments found the distance between interstitial and apical oxygen to be $\approx 2.7\ \text{\AA}$ [71, 95].

Occupancy of an interstitial oxygen site pushes the four closest oxygens away to widen the tetrahedral site. The result is a tilt of the whole rigid MO_6 octahedra in opposite directions. In contrast to the tilting along the (110) -direction, which corresponds to the orthorhombic Bmab structure, this leads to a displacement along the (100) direction. Such a distortion is incompatible with the orthorhombic as well as the tetragonal symmetry. The local disorder induced by the excess oxygen is propagated further than the first coordination sphere through the rigid corner sharing octahedra. Consequently for high enough δ this leads to a change in crystal symmetry. For $\text{La}_2\text{CuO}_{4+\delta}$ it was reported that the space group becomes Fmmm for $\delta \leq 0.04$ [96]. A phase diagram for the oxygen content in $\text{La}_2\text{NiO}_{4+\delta}$ has been published as a summary of several studies (see Figure 1.8). The white areas correspond to miscibility gaps [97] and the shaded areas to different oxygen ordered phases. Upon increasing δ the space group varies from $\text{Bmab} \rightarrow \text{P4}_2/\text{ncm} \rightarrow \text{F4}/\text{mmm} \rightarrow \text{Fmmm}$ [79]. So far only the Fmmm space group has been reported for the oxygen enriched cobalt compound [98].

Oxygen intercalation and deficiency in some 214 Ruddlesden-Popper com-

pounds can be induced over a remarkable range. For $\text{La}_{2-x}\text{Sr}_x\text{NiO}_{4+\delta}$ oxygen deficiency depends on the strontium content. Crespin et al. [99, 100] found that for $x = 0.4$, $\delta_{max} = -0.5$ while for $x = 1$, $\delta_{max} = -0.9$. On the other hand Grenier et al. used electrochemical oxidation to increase the excess oxygen of the undoped nickelate to $\delta = 0.26$ [78]. An even higher oxygen excess $\delta = 0.34$ was obtained for samples treated at 350° in an oxygen atmosphere of 20 MPa [101]. The related cobaltate compound exhibits similar interesting properties. According to [87], when grown with the floating zone technique in argon atmosphere, the undoped La_2CoO_4 already possesses a high amount of excess oxygen (about $\delta = 0.15$). It should be noted, that our results for the oxygen content of the as prepared floating zone grown single crystal suggest a stoichiometric composition (see Section 3.2.5). Under ambient conditions this compound shows spontaneous topotactic oxidation, leading to a significant oxygen excess incorporation up to $\delta = 0.19$ [102]. In the same study $\delta_{max} = 0.26$ for the undoped cobaltate was reported while an even larger value of $\delta_{max} = 0.32$ was claimed in a more recent publication for a sample treated at 300° in an oxygen atmosphere of 20 MPa [103].

Studies on the 214 cuprate revealed that excess oxygen stoichiometry leads to fast oxygen transport [104]. The enhancement of oxygen transport was reported to be two orders of magnitude higher, compared to the oxygen deficient material. At 500°C the oxygen self diffusion D^* and the activation energy E_A^D have been measured to be $D^* = 3.3 \cdot 10^{-9} \text{ cm}^2/\text{s}$ and $E_A^D = 0.56 \text{ eV}$ for $\text{La}_2\text{NiO}_{4+\delta}$ and $D^* = 2.5 \cdot 10^{-8} \text{ cm}^2/\text{s}$ and $E_A^D = 0.12 \text{ eV}$ for $\text{La}_2\text{CoO}_{4+\delta}$ [105]. Especially the low activation energy of the cobalt compound is remarkable. Together with the large oxygen storage capacity and high diffusion rates close to ambient temperature this properties are ideal for solid oxide fuel cells. Only the high resistivity of the cobaltates hinders their application.

Recent studies on the mechanism of oxygen transport, like the in situ nuclear density analysis at 1015°C from neutron data on $(\text{Pr}_{0.9}\text{La}_{0.1})_2\text{Ni}_{0.74}\text{Cu}_{0.21}\text{Ga}_{0.05}\text{O}_{4+\delta}$ [106] and molecular dynamics simulations on $\text{Ni}_2\text{NiO}_{4+\delta}$ [107], revealed that the oxygen migration path leads along the interstitial $(1/2 \ 0 \ 1/4)$ oxygen site. If the interstitial site is empty, the oxygen transport is hindered as the migration of an apical oxygen to the neighboring interstitial site implies strong displacements of the surrounding atoms. For $\delta > 0$ the lattice is already locally distorted, thus lower energies are involved. This explains the large difference in oxygen transport between the reduced and the oxidized cuprates and helps understanding why some compounds with a related layered structure have much smaller oxygen self diffusion coefficients.

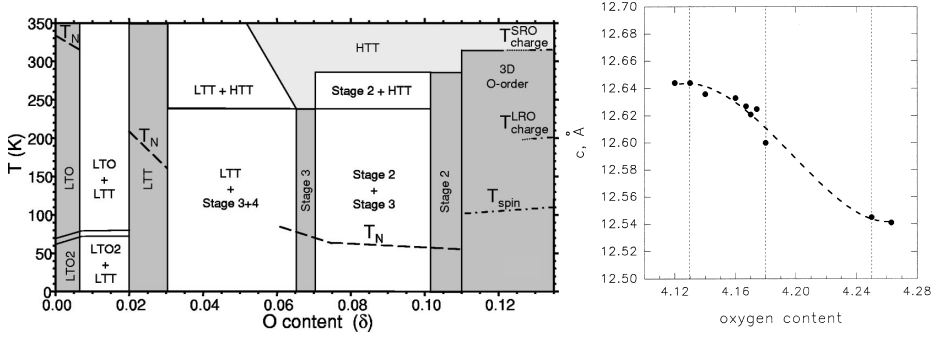


Figure 1.8: *left*: Oxygen content phase diagram of $\text{La}_2\text{NiO}_{4+\delta}$ [79]. *right*: Lattice constant dependency of oxygen content for $\text{La}_2\text{CoO}_{4+\delta}$ published by Nemudry et al. [102].

1.6 Mott-Hubbard

The large repertoire of properties observable in transition metal oxides is a consequence of the competition between different kinds of interactions with comparable magnitude. While strong electron interactions suppress charge fluctuations, the band width has a contrary effect and enhances the delocalization. Concepts like the band theory circumvent the calculation of the electron repulsion by introducing an average effective potential. In metals this works very well because the mobile electrons have good screening properties. However, this concept brakes down for narrow 3d bands. Electron correlations is the term that describes the way in which electrons alter their motion in order to avoid each other more effectively than an independent electron wavefunction can describe. Our current understanding of correlated electron systems is based on the fundamental ideas that were developed by N. F. Mott [108] and J. Hubbard [109]. Mott proposed an understanding for the insulating nature of NiO which, according to band theory, should be metallic due to its half filled d-orbital [108]. He compared the London-Heitler with the molecular orbital description and estimated the energy of a wave function containing n electron-hole pairs, responsible for electronic conduction, as a function of the inter-metallic spacing. He argued that in metals an absolute energy minimum exists at finite electron-hole pair concentrations while in the oxide the absolute minimum lies at the concentration of zero pairs [108]. Hubbard studied the suppression of charge fluctuations through large coulomb interactions considering also the electron spin and the case of large inter-atomic distances [109]. The opening of a correlation gap can be understood considering a system of two hydrogen atoms which are far enough apart that interactions are negligible. Each atom carries an electron in the 1s orbital. Band theory predicts a metallic system due to the half filled 1s-band.

To remove an electron from one hydrogen the ionization energy $E_I = 13.6 \text{ eV}$ has to be invested. Adding the free electron to the other hydrogen results in the energy gain $E_A = 0.7 \text{ eV}$ through electron affinity. The large energy difference through Coulomb repulsion $U = E_I - E_A = 12.9 \text{ eV}$ suppresses the hopping of electrons. Effectively separating the half filled band into two bands, the lower- and the upper-Hubbard bands, with a conductivity gap which is proportional to U .

In real materials the inter-atomic distances are smaller, so that hybridization effects broaden the Hubbard bands. The interplay between hybridization and on site Coulomb repulsion can be expressed in a Hamiltonian called the Hubbard model:

$$H = - \sum_{\langle i,j \rangle, \sigma} t_{ij} c_{j,\sigma}^+ c_{i,\sigma} + U \sum_i n_{i\uparrow} n_{i\downarrow} \quad (1.5)$$

which contains the minimum of features necessary to include band-like and localized behavior in suitable limits. Each ion contains only a single orbital which can be empty or occupied by a spin up/down electron or two electrons in the combination up-down. The first term destroys an electron at site i and creates one at site j , thus connecting states that differ by the hopping of only one electron without a change in spin. The second term is the Coulomb repulsion which only applies when an orbital is doubly occupied.

Already this simple model has proved to be difficult for an exact analysis when U and t are finite. For vanishing U it can be shown that the Hamiltonian leads to a conventional band spectrum with delocalized electrons. In the case of strong correlations, $U \gg t$, the hopping term can be treated as a perturbation. The expansion in powers of t/U then leads to the so called t - J Hamiltonian which includes the possibility for next nearest neighbor hopping.

In the case of half filled orbitals the t - J model reduces to the spin $1/2$ Heisenberg model. A sum over all pairs of two spin interactions scaled with the exchange coupling constants J_{ij} :

$$H_H = \sum_{\langle i,j \rangle} J_{ij} \vec{S}_i \cdot \vec{S}_j \quad (1.6)$$

Simple though it seems, the Heisenberg Hamiltonian H_H sufficiently represents the spin Hamiltonian in many cases of interest and is often used as starting point for profound investigations of magnetism in solids. [110, 111]

1.7 Zaanen-Sawatzky-Allen Model

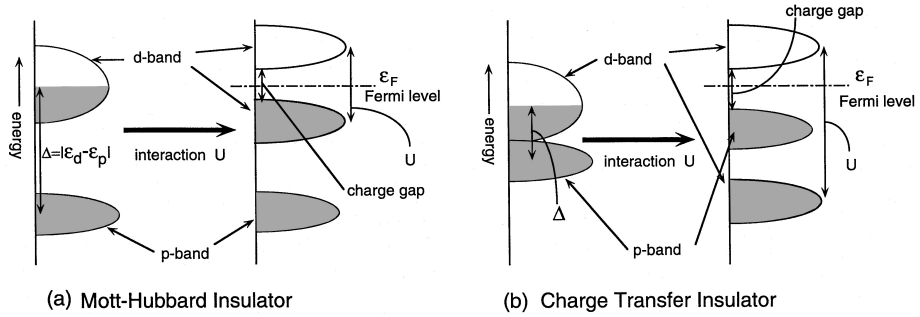


Figure 1.9: Energy level diagram for (a) a Mott-Hubbard insulator and (b) a charge-transfer insulator. [112]

According to the Mott-Hubbard model the band gap, which is determined by the on-site 3d-3d Coulomb interaction U , should not vary within a series of transition metal compounds containing the same transition metal, in contrast to experimental data [113, 114]. Similar discrepancies were observed for HTSC cuprates where the Coulomb interaction U on the copper site is larger than the energy cost for charge fluctuations that involve O 2p and transition metal 3d orbitals [115–117]. These observations indicate the importance to include the oxygen degrees of freedom within the low energy scale into the model. It follows for the cuprates that the O 2p band lies between the upper- and the lower-Hubbard bands.

Consequently, the charge transfer energy was identified as a fundamental parameter which determines the electronic structure of transition metal compounds [118, 119] (see Figure 1.9). A classification scheme based on the on-site Coulomb interaction U and the charge transfer energy Δ was proposed by Zaanen, Sawatzky and Allen [116] (see Figure 1.10).

The energy scale of charge fluctuations is the on-site Coulomb interaction U . It can be defined as the energy necessary to remove an electron from one atomic site and to add it on another far away site:

$$U = E(d^{n+1}) + E(d^{n-1}) - 2E(d^n) \quad (1.7)$$

where n is the number of electrons in the d-shell and the three energies correspond to the ionization energy, electron affinity and ground state, respectively. Similar, the charge transfer energy Δ is the energy cost to transfer an electron

from the O 2p band into a 3d transition metal orbital:

$$\Delta = E(d^{n+1}\underline{L}) - E(d^n) \quad (1.8)$$

where \underline{L} denotes a ligand hole.

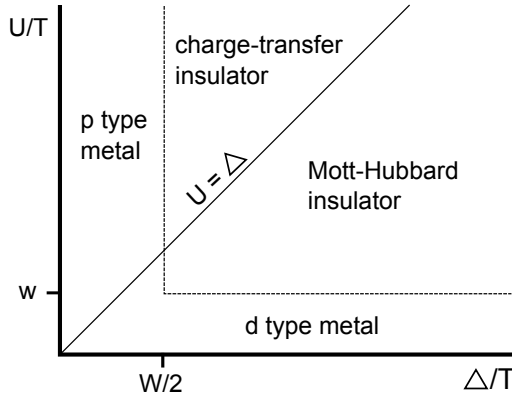


Figure 1.10: The Zaanen-Sawatzky-Allen phase diagram classifies four insulating and metallic possibilities that can be observed in transition metal oxides. [116]

Figure 1.9 is a sketch of the two different types of insulating transition metal oxides. In a) the Mott-Hubbard case is shown. Due to a larger charge transfer energy compared to the transition metal Coulomb interaction U the oxygen bands lie below the lower Hubbard band. Electron/hole doping (eg. chemically or by photoemission/ inverse photoemission) on such systems mainly concerns the 3d bands/exited states. In the right side b) of Figure 1.9 the charge transfer insulator case is drawn. Here the removed electrons originate from states with mainly O 2p character. The states where electrons can be added are mainly of 3d transition metal character.

The Zaanen-Sawatzky-Allen phase diagram can be found in Figure 1.10. Straight lines indicate the diffuse boundaries between four cases applicable for transition metal oxides. The width of the anion 2p band is W and the width of the transition metal 3d band is w . In addition to the two parameters U and Δ a third parameter T is used to account for hybridization between transition metal and ligand orbitals. For $U, \Delta \gg T$ the material is a Mott-Hubbard ($\Delta > U$) or a charge transfer ($U > \Delta$) insulator. Increasing the hybridization drives the system through an insulator-metal transition and results in a d-type or p-type metal, depending on the relative size of U and Δ . Compounds close to the line $U = \Delta$ will have strongly covalent binding. Plotting the charge transfer

energy and the Coulomb repulsion for the series of 3d transition metal oxides reveals the general trend that early 3d-metal oxides are better described by the Mott-Hubbard model while late 3d-metal oxides fall into the charge transfer regime.

1.8 Intersite Exchange Interactions

A classical approach to understand the origin of magnetic order in the absence of an external field is to employ the dipole-dipole interaction between magnetic moments of individual atoms. Using typical values for the distance $r = 1 \text{ \AA}$ and the magnetic moment $\mu = \mu_B$, the magnetostatic energy gain is $\Delta E \approx 0.05 \text{ meV}$ which corresponds to a temperature $T < 1 \text{ K}$. Apparently such a weak interaction can not be responsible for robust magnetic ordering phenomena at elevated temperatures, e.g. 848°C in magnetite [120].

It is one of the profound “surprises in theoretical physics” [121] that magnetism is an intrinsically quantum mechanical effect. Its origin is the interplay of electronic properties that are seemingly unrelated to magnetism: the Pauli principle in combination with the Coulomb repulsion (Coulomb exchange) and the (virtual) hopping of electrons (kinetic exchange).

1. **Direct Exchange:** The effects of a direct exchange can be understood using a two site Hubbard model (like the hydrogen molecule) as shown in Figure 1.11. While the Pauli principle forbids a hopping of electrons with parallel spin in case a) it is allowed for antiparallel spins in case b). It follows from the Heisenberg uncertainty principle that the configuration b) is favorable due to its decreased kinetic energy. Solving the Hamiltonian in equation 1.5 and with the approximation $U \gg t$ we can obtain the energies of the lowest singlet $E_1 = -4t^2/U$ and triplet states $E_2 = 0$. Note that the state in b) is not an eigenstate and the singlet state corresponding to E_1 can be expressed as $\sqrt{2}(c_{A\uparrow}^\dagger c_{B\downarrow}^\dagger |0\rangle - c_{B\uparrow}^\dagger c_{A\downarrow}^\dagger |0\rangle)$. The energy difference $J = E_2 - E_1$ is the interatomic exchange energy:

$$J \approx -\frac{4t^2}{U} \quad (1.9)$$

and the negative sign indicates an antiferromagnetic coupling. In the more general case where more than one orbital per atom is involved it becomes necessary to also account for the orbital degrees of freedom. Here the magnitude and sign of the exchange interaction depends on the orbital occupation.

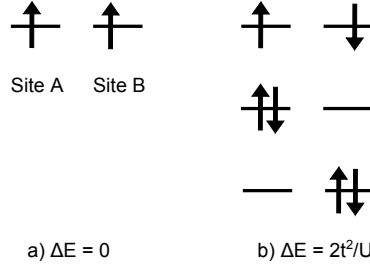


Figure 1.11: Direct exchange for two half filled orbitals. In b) the kinetic energy is reduced by the possible hopping of electrons.

2. **Superexchange:** In transition metal oxides the direct 3d-3d overlap is often small and the bandwidth is mainly a result of indirect interactions via the intermediate oxygen orbitals. The indirect overlap is also responsible for magnetic interactions and the mechanism is called superexchange. It is strongest for linear metal-oxygen-metal bonding (180°) which occurs for example in perovskite and rocksalt structures. In the simple case shown in Figure 1.12, where each metal contributes only a single half filled orbital, the interaction is antiferromagnetic. The reason is, similar to the direct exchange case, that the Pauli principle forbids (virtual) hopping for electrons with parallel spins. Under the assumption that $\Delta \ll U$ the resulting exchange coupling parameter can be estimated to:

$$J = -\frac{4t_{pd}^4}{\Delta^2} \left(\frac{1}{U} + \frac{2}{2\Delta + U_p} \right) \quad (1.10)$$

with U_p being the repulsion for two holes in the same oxygen 2p orbital. Again, the introduction of orbital degrees of freedom influences strength and sign of the exchange interaction.

Another simple case of superexchange, though generally weaker, occurs for a metal-oxygen-metal bonding at an angle of 90° . Here each 3d metal orbital interacts with a different 2p oxygen orbital and the kinetic term vanishes due to orthogonality. Although virtual interactions are possible for parallel and antiparallel spin configurations the resulting exchange is ferromagnetic. The driving force is Hund's rule which favors a parallel spin configuration for the two half filled oxygen 2p orbitals.

3. **Double Exchange:** This mechanism describes a ferromagnetic interaction in combination with a spin polarized conductivity in some mixed valence transition metal oxides. It is based on the fact that a spin conserving coherent tunneling of electrons between degenerated initial and

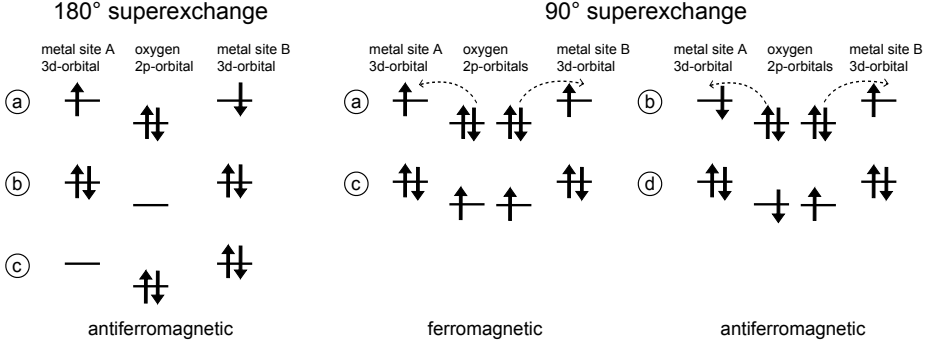


Figure 1.12: Superexchange interactions between two half filled transition metal orbitals. *left:* For the 180° metal-oxygen-metal bonding the spins align anti-parallel. The ground state configuration a) can lower its energy by mixing with the excited states b) and c). *right:* For a 90° bonding angle the parallel configuration a) mixes with c) and the anti-parallel configuration b) mixes with d). Hund's rule favors parallel spins in the two orthogonal oxygen 2p orbitals. Therefore the system has a ferromagnetic ground state.

final states reduces the total energy of the system by an amount proportional to the electron bandwidth [122]. As an example we consider the case of $\text{La}_{1-x}\text{Ca}_x\text{MnO}_3$ where Mn^{3+} and Mn^{4+} ions are present (see Figure 1.13). According to Hund's rule all four spins on the Mn^{3+} are parallel. The hopping of one electron from Mn^{3+} to Mn^{4+} via the oxygen only leads to a degenerate state if the moments are coupled ferromagnetically. As a consequence the resistivity becomes a function of the spin structure and an external magnetic field. The colossal magnetoresistance in $\text{La}_{1-x}\text{Ca}_x\text{MnO}_3$ is a good example for the consequences of a double exchange coupling [123, 124].

double exchange

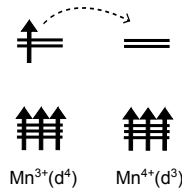


Figure 1.13: Double exchange mechanism in $\text{La}_{1-x}\text{Ca}_x\text{MnO}_3$: the electron spin is conserved upon hopping. The system's kinetic energy is lowered for parallel spins.

Exchange mechanisms are idealizations of characteristic situations found in real materials, and they provide a good basis for thinking about relevant effects. Especially the exchange coupling J is an important experimentally accessible parameter to quantitatively compare the strength of different couplings in solids. A set of empirical rules which is known as the Goodenough-Kanamori-Anderson rules [125] summarizes the different exchange interactions occurring in transition metal oxides with octahedral symmetry. Whether the coupling is ferro or antiferromagnetic depends on the d-orbital occupation, the bonding angle and the relative strength of the possibly competing interactions [126–128]. We can use these rules to estimate the effective interactions that could occur in our cobalt, nickel and iron systems:

- **$\text{Co}^{2+}\text{HS-O-Co}^{2+}\text{HS}$:** 180° -angle - AF interaction, 90° -angle - FM interaction; the larger overlap between the oxygen 2p and the e_g orbitals compared to the t_{2g} orbitals favors a superexchange via the e_g orbitals. Depending on the system either the $d(3z^2-r^2)$ or the $d(x^2-y^2)$ orbitals are suitable to mediate the exchange leading to a case which is analogous to the example in Figure 1.12.
- **$\text{Co}^{2+}\text{HS-O-Co}^{3+}\text{LS}$:** Co^{3+}LS is nonmagnetic.
In $\text{La}_{1.5}\text{Sr}_{0.5}\text{CoO}_4$ an antiferromagnetic coupling between the 180° bonded cobalt Co^{2+} sites occurs along the path $\text{Co}^{2+}\text{-O-Co}^{3+}\text{-O-Co}^{2+}$. For an interpretation we assume that $\text{Co}^{2+}\text{-O}$ forms a unit with hybridized orbitals. The superexchange between the two $\text{Co}^{2+}\text{-O}$ -units is then mediated via the nonmagnetic interstitial Co^{3+} , similar to the example in Figure 1.12.
- **$\text{Co}^{2+}\text{HS-O-Co}^{3+}\text{HS}$:** 180° -angle - AF, 90° -angle - FM; similar to the case of $\text{Co}^{2+}\text{HS-O-Co}^{2+}\text{HS}$
- **$\text{Ni}^{2+}\text{HS-O-Ni}^{2+}\text{HS}$:** 180° -angle - AF, 90° -angle - FM; similar to the case of $\text{Co}^{2+}\text{HS-O-Co}^{2+}\text{HS}$
- **$\text{Ni}^{2+}\text{HS-O-Ni}^{3+}$:** 180° -angle - FM, 90° -angle - AF; In the first scenario a simultaneous hopping of one electron from the O 2p orbital to each nickel is only possible for a ferromagnetic coupling. For the 90° case we estimate the consequences if each oxygen orbital contributes one electron to each nickel. In the case of AF interactions this results in two parallel spins at the Ni^{3+} -site and two parallel spins in the two oxygen orbitals.
- **$\text{Ni}^{3+}\text{-O-Ni}^{3+}$:** 180° -angle - The interaction between two degenerated orbitals on each metal which are filled by a single electron leads to orbital order. In the case of antiferro orbital order the exchange is FM and in the case of ferro orbital order it is AF.
- **$\text{Fe}^{3+}\text{HS-O-Fe}^{3+}\text{HS}$:** 180° -angle - AF, 90° -angle - FM; similar to the case of $\text{Co}^{2+}\text{HS-O-Co}^{2+}\text{HS}$

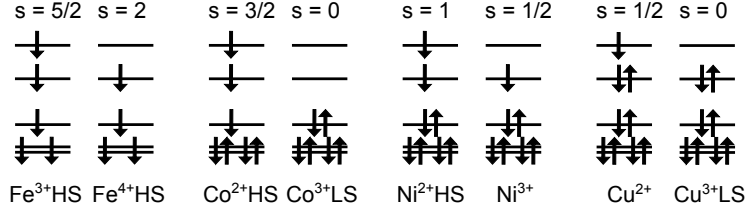


Figure 1.14: (*left to right*) Spin state diagrams for 3d transition metals: Iron, Cobalt, Nickel and Copper. The total spin angular momentum s is indicated above each diagram.

- **Fe³⁺HS-O-Fe⁴⁺HS**: 180°-angle - FM, 90°-angle - AF; similar to the case of Ni²⁺HS-O-Ni³⁺
- **Fe⁴⁺HS-O-Fe⁴⁺HS**: 180°-angle - AF, 90°-angle - FM; similar to the case of Ni³⁺-O-Ni³⁺

1.9 Spin blockade Mechanism

Within the family of $\text{La}_{2-x}\text{Sr}_x\text{TO}_4$ transition metal oxides with $T = \text{Co}, \text{Ni}, \text{Cu}$ all end members ($x = 0$) are insulators [129, 130]. In accordance with the general trend in the ZSA-diagram (Figure 1.10) measurements of the optical conductivity reveal an increasing charge transfer energy Δ_{CT} from Cu to Co which then decreases towards Mn [129, 131]. Upon decreasing the atomic number we expect a crossover from a charge-transfer to a Mott-Hubbard insulator. For the 214-perovskites it was claimed to be the case for the iron compound while the $T = \text{Co}, \text{Ni}$ and Cu compounds belong to the charge-transfer regime [129].

Element	Δ_{CT}
Fe	n.a.
Co	5-6 eV [129]
Ni	4 eV [132]
Cu	2 eV [133]

Table 1.2: Conductivity gaps in the 214-perovskites La_2TO_4 with $T = \text{Fe}, \text{Co}, \text{Ni}, \text{Cu}$.

Undoped La_2CuO_4 is a charge transfer insulator with a half filled band

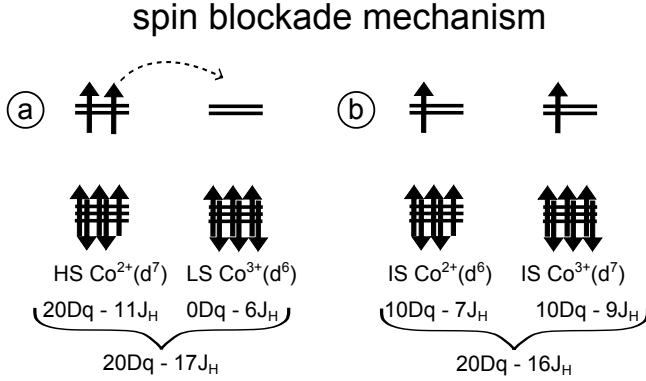


Figure 1.15: The spin blockade mechanism in $\text{La}_{2-x}\text{Sr}_x\text{CoO}_4$: hopping of one electron from Co^{2+} to Co^{3+} changes the total energy of the system by one Hund's coupling exchange J_H .

and an antiferromagnetically ordered ground state that is well described by a spin-1/2 Heisenberg model. Small strontium doping $x \approx 0.06$ turns the system metallic [112]. In contrast, in the nickelate metallic behavior can only be induced by very high doping $x \approx 1$ [134, 135]. The lower conductivity compared to the cuprate was attributed to the formation of small polarons (compared with those observed in cuprates) [136, 137].

Surprisingly, the cobaltate is an even stronger insulator. It remains insulating for a very wide range of x values with anomalously high activation energies for conductivity [112, 138]. Chang et al. [139] argued that the Co^{3+} within $\text{La}_{2-x}\text{Sr}_x\text{CoO}_4$ is in the nonmagnetic low spin state. At a doping of $x = 0.5$ the ratio between Co^{3+} and Co^{2+} is 1:1 and a checkerboard charge order (CBCO) develops at a transition temperature as high as 800 K [140]. In this specific situation the CBCO involves an ordering of the associated e_g^0 and e_g^2 which leads to a large difference in the Co-O bond length. The scheme in Figure 1.15 illustrates the spin-blockade mechanism in the 214-cobalt oxide. The spin moments of the Co^{2+}HS and the Co^{3+}LS are $S = 3/2$ and $s = 0$, respectively. Since hopping of one electron carries only the spin $s = 1/2$ from Co^{2+} to Co^{3+} it is clear that the final state differs from the initial state. A calculation for an idealized cubic symmetry is presented in the Figure 1.15 and indicates that electron hopping costs an energy of one Hund's exchange coupling J_H which is of the order of 1 eV.

1.10 Magnetic Order

It is not surprising that the three transition metal oxide systems, $\text{La}_{2-x}\text{Sr}_x\text{TO}_4$ with $T = \text{Co}, \text{Ni}$ and Cu , have a similar crystal structure and equal structural phase transitions at low doping concentrations. They share a stable oxidation state T^{2+} and are of similar size. In the low doping regime of all three phase diagrams exists an area where neighboring spins are coupled antiferromagnetic (AF) due to a nearest-neighbor exchange coupling J . Although the single-layer magnetic structure is identical, there exists a difference in the direction of the ordered moment in the orthorhombic structure and in the stacking of the magnetic layers. While the spins in La_2NiO_4 and La_2CoO_4 point along the $(1\ -1\ 0)$ direction (tilt axis of the octahedra), they align along $(1\ 1\ 0)$ perpendicular to the tilt axis in La_2CuO_4 [71, 141, 142]. Only for the cuprate this allows for a small out of plane canting due to Dzyaloshinski-Moria interaction [143]. In all three compounds the stacking of magnetic order is described by the $(1\ 0\ 0)$ vector [71, 141, 142]. But due to the rotation of the moments between the cuprate and nickelate/cobaltate this yields different magnetic structures. These two types of structures are common for compounds with K_2NiF_4 structure and may even coexist [144]. The antiferromagnetic coupling is hindered by strontium doping through a decrease of the average exchange parameter via the introduction of T^{3+} -ions into the ideal AF T^{2+} order. At higher strontium doping concentrations the bond-length mismatch decreases and the structural transition temperature drops to zero. Here electronic ordering phenomena like charge order, spin order as well as superconductivity occur. The electronic configuration shown in Figure 1.14 is very different for each transition metal and consequently the ordering phenomena observed may greatly differ.

While undoped La_2CuO_4 is a charge transfer insulator with a half filled band and an antiferromagnetically ordered ground state that is well described by a spin-1/2 Heisenberg model, small strontium doping $x \approx 0.06$ turns the system metallic [112].

1.10.1 $\text{La}_{2-x}\text{Sr}_x\text{CuO}_4$

Representative for the cuprate high T_c superconductors the phase diagram of $\text{La}_{2-x}\text{Sr}_x\text{CuO}_4$ (Figure 1.6 *right*) will be discussed to provide the basis for a comparison with the isostructural nickelate and cobaltate. Most cuprates exhibit AF order in their respective undoped parent compounds. Upon suppression of the magnetic order through hole or electron doping a superconducting phase appears. In between exists a doping range that sustains neither of the two phases. In $\text{La}_{2-x}\text{Sr}_x\text{CuO}_4$ this “spin-glass” phase is characterized by a disorder of static spins. Long range AF order disappears already at a small strontium concentration of $x = 0.02$. This phase can be observed most distinctly in μSR

experiments which are sensitive to spin fluctuations within a time window of about 10^{-9} - 10^{-6} s [145, 146]. Although the transition temperature decreases with hole concentration p it could be observed up to $p < 0.09$ [146]. The onset of superconductivity is at $p > 0.06$. A coexistence of frozen AF correlations and superconductivity has also been reported for $Y_{1-x}Ca_xBa_2Cu_3O_6$ [146].

Remarkably is the initial discovery of elastic incommensurate magnetic peaks in $La_{1.6-x}Nd_{0.4}Sr_xCuO_4$ [38, 147] with positions $(1/2 \pm \epsilon, 1/2)$ and $(1/2, 1/2 \pm \epsilon)$ with respect to the tetragonal unit cell. It was argued that the underlying magnetic order implies a modulation of the charge density in the form of charge stripes. Later incommensurate magnetism was also reported for other cuprates. In the superconducting phase of $La_{2-x}Sr_xCuO_4$ [148] magnetic peaks at similar positions were found around $x = 0.12$. A study on low doped samples revealed that incommensurate magnetism can also exist in the spin glass phase. In contrast to the observations for higher doping, the peaks appeared to be 45° rotated with respect to the AF wave vector $(1/2, 1/2)$ [149]. It can therefore be argued that the region is better described as diagonally-modulated incommensurate spin-density-wave phase [150]. Without clear evidence for the related charge order the nature of the incommensurate magnetism remains a matter of debate. Also alternative models like Fermi-surface effects [151, 152] and spiral magnetic order [153] exist for the spin glass phase of $La_{2-x}Sr_xCuO_4$.

For zinc co-doped cuprates it was reported, that already small concentrations can induce and increase elastic magnetic peaks, possibly by pinning the presumed fluctuating stripes [150]. At the same time an increased peak width was observed [154, 155]. Additionally, 1% or less Zn causes the appearance of excitations within the spin gap of the Zn-free cuprates [156, 157]. For $YBa_2Cu_3O_{6+\delta}$ zinc doping causes a shift in spectral weight from E_r into the spin gap [158, 159].

1.10.2 $La_{2-x}Sr_xNiO_4$

Hole doped La_2NiO_4 exhibits an exotic form of charge order first discovered in this system on an oxygen excess sample with the composition $La_2NiO_{4.125}$ [160] in 1993. The increased interest on this system due to its structural similarity with the cuprates and later also due to the new type of charge order led to numerous studies with a variety of techniques. The insulating properties of the nickelates distinguish them from the cuprates but have the advantage that electronic order can be static and therefore easier to detect. Less than three years after the discovery of combined incommensurate charge and magnetic order in the nickelates the basic nature of this phenomenon had been fairly well established by scattering studies [160–166]. At sufficient high levels of doping ($n_h \geq 0.2$ holes/Ni [167]) the holes which are localized in the NiO_2 plane order in a periodically spaced stripe pattern at low temperature. At again lower temperature the nickel spins order antiferromagnetically within the

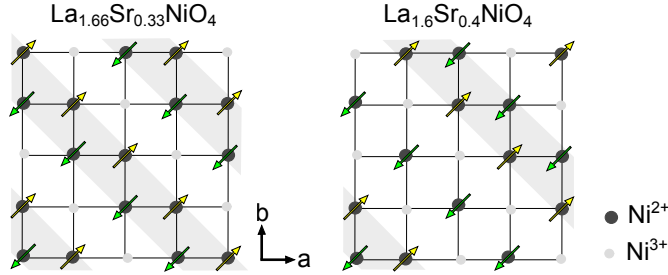


Figure 1.16: Microscopic model of charge stripe order in $\text{La}_{2-x}\text{Sr}_x\text{NiO}_4$.

stripes with an anti-phase relationship between neighboring stripe domains. The incommensurability ϵ is approximately linear in the hole doping $n_h = x + 2\delta$. This type of order has been observed over a wide doping range $0.20 \leq x \leq 0.5$ with the highest transition temperature of about 240 K at $x \approx 1/3$ [168]. For samples with incommensurability $0.25 \leq \epsilon < 1/3$ it was found in neutron [160, 166] and X-ray measurements [169] that the corresponding peak positions are drawn towards the value $\epsilon = 1/3$ with raising temperature. The enhanced stability of the $1/3$ phase is underlined by a decrease of correlation length of spin and charge order the further the hole doping is away from this ideal value. A special case is the half doped sample with $x = 0.5$ where stable CBCO up to 480 K was reported [170]. Surprisingly also at this doping the incommensurate charge order takes over at a lower temperature of about 180 K.

It is instructive to visualize how the holes introduced by doping can be arranged in stripes within the Ni-O planes in the incommensurate phase. The measured incommensurability roughly follows the hole concentration and consequently not only rational values appear. Obviously the incommensurate modulation required to explain the peak positions found in diffraction experiments can not be modulated on an atomic scale. Here the hole ordering can only occur at integer values of the intra nickel distances. For small hole concentrations $n_h \leq 1/3$, the distance between the hole stripes is wide enough to accommodate two or more Ni^{+2} stripes in between. This allows for nearest neighbor AF interactions inside the Ni^{+2} stripes with an antiphase AF spin ordering across the hole stripes. This can be observed also in the $x = 1/3$ doped sample where the modulation is shown in Figure 1.16. The situation changes for the doping range $1/3 < n_h \leq 1/2$. At $n_h = 1/2$ the ordering pattern for the spin order is a 2D checkerboard pattern where all the nearest neighbor sites of the spins are occupied by holes [168]. As the example for $n_h = 0.4$ in Figure 1.16 demonstrates, the stripe order in the regime between the two rational values consists of a mixture of the $1/3$ -type stripe order and the $1/2$ -type charge order. The measured peak positions reflect only the average crystal structure and incommensurability

might occur when two rational structures are mixed on the atomic scale.

In contrast to the horizontal stripes in the superconducting cuprates, the nickelates exhibit diagonal stripes. Such stripes cause a lattice modulation in only one direction while the lattice remains unchanged parallel to the stripes. This kind of superstructure causes additional Bragg reflections, called satellites, in diffraction experiments. The expected positions in the tetragonal notation with respect to a lattice reflection $(H\ K\ L)$ are $(H \pm \epsilon\ K \pm \epsilon\ L)$. Because the lattice directions a and b are equal in the tetragonal system, measurements always also find superstructure satellites at $(H \mp \epsilon\ K \pm \epsilon\ L)$ due to twinning. As the stripes act as antiphase domain walls for the antiferromagnetic order between two charge stripes, the wave length is twice as large for the magnetic modulation compared to the structural one. Consequently magnetic super structure reflections appear at $(\frac{H \pm \epsilon}{2}\ \frac{K \pm \epsilon}{2}\ L) = (H_{AF} \pm \frac{\epsilon}{2}\ K_{AF} \pm \frac{\epsilon}{2}\ L)$ and $(H_{AF} \pm \frac{\epsilon}{2}\ K_{AF} \mp \frac{\epsilon}{2}\ L)$ where the subscript AF denotes the magnetic Bragg peak of the commensurate nearest neighbor antiferromagnetic order. Apparently the in plane length of the spin correlations ϵ_s is only half as large as that of the charge ϵ_{ch} .

It should be noted that neutrons are not sensitive to the order of electronic charges. But such charges induce a modulation on the bond distances through the relation between bond length and bond strength. The resulting displacements of the oxygen atoms can be measured. Neutron scattering is more sensitive on oxygen than X-rays, which is why the precise determination of charge order related distortions can be performed more easily with neutrons [171].

1.10.3 $\text{La}_{2-x}\text{Sr}_x\text{CoO}_4$

An increased bond length mismatch compared to the nickelates is responsible for the even higher structural HTT to LTO transition temperature of 900 K [172] in the undoped La_2CoO_4 . The larger structural distortion in the cobaltates is also reflected in a larger amount of strontium doping needed to fully suppress the tilting of the octahedra (about $x = 0.2$ in the nickelate compared to about 0.33 in the cobaltate). The half doped sample was found to exhibit very robust CBCO with an exceptional high ordering temperature of about 800 K [140]. Two groups reported the possible discovery of incommensurate charge order, like in the nickelates [173, 174], but until now no unambiguous data is available for the intermediate doping region. At low temperatures an incommensurate magnetic phase appears (in the half doped compound at about 30K [175]). The difference in order temperature is extremely large (especially compared to the nickelate) and indicates an effective decoupling of the two phenomena, thus implying that in this cobaltate the charge order arises from electron-lattice coupling [175, 176].

1.11 Scope of this Thesis

Static charge stripe ordering reflections have also been observed in $\text{La}_{2-x}\text{Sr}_x\text{NiO}_4$ for hole concentrations $n_h > 0.2$ [161]. It remains an open question how to best describe the doping dependent transition from the commensurate AF order in the undoped parent compound to the incommensurate charge and magnetic order. Another interesting question is the effect of disorder in the charge sector which can be introduced by the co-doping of additional elements. The study of the charge stripe order in nickelates might help to better understand this peculiar phenomenon.

The magnetic excitations in the nickelates match well with the expectations from linear spin wave theory. While the magnon dispersion of the commensurate AF parent compound exhibits the characteristic spin wave cone emerging from the AF zone center, four cones appear in the excitation spectrum of the incommensurate stripe phase, each emerging from one of the four magnetic superstructure reflections [177, 178]. Apparent similarities to the excitation spectrum of the cuprates lead to the question whether the hourglass dispersion can be explained by the crossing of spin wave cones at an energy corresponding to the neck of the hourglass [179].

Incommensurate magnetism has also been observed in the isostructural cobaltates [174]. It appears that the position of the superstructure reflections depends linear on the effective hole concentration, similar to the nickelates and cuprates [174]. An nonmagnetic low spin Co^{3+} site [139] implies that magnetic stripe ordering would be inevitably connected to charge stripes. Some evidence for charge order superstructure reflections [174] together with the observed similarities to the stripe ordered nickelates led to the belief of a similar scenario in the cobaltates [180, 181]. Further investigations on the nature of the charge and magnetic order in the cobaltates are necessary to verify the proposed CSO.

In contrast to the nickelates, an hourglass dispersion has recently been reported for a cobaltate sample with nominal composition $\text{La}_{5/3}\text{Sr}_{1/3}\text{CoO}_4$ [181]. This peculiar shaped magnon dispersion was so far uniquely reported for the HTSC cuprates. The differences in conductivity between the metallic cuprates and insulating cobaltates raises the question whether the excitation spectra could have a common origin. It is therefore a necessary first step to comprehensively characterize the excitations in the cobaltates. With sufficient data it might be possible to understand the microscopic origin of the magnon dispersion in $\text{La}_{2-x}\text{Sr}_x\text{CoO}_4$.

- **Chapter 2** introduces crystal growth techniques and synthesis routes. Besides the growth of $\text{La}_{2-x}\text{Sr}_x\text{NiO}_4$ and $\text{La}_{2-x}\text{Sr}_x\text{CoO}_4$ single crystals the main focus of single crystal synthesis was on $\text{La}_{2-x}\text{Sr}_x\text{FeO}_4$. In order to increase the accessible doping range compared to previous (published)

works on ferrates we perform a systematic variation of the growth parameters and investigate the grown products. The remaining pages of this chapter are used to introduce some of the applied methods.

- **Chapter 3** summarizes results of the characterization of the sample properties. This step is important for the final data interpretation. Among the large number of publications on the nickelates are also some comprehensive studies. This enables us to compare basic properties like the lattice constants to verify the quality of our samples. References for the cobaltates are scarce and therefore not as reliable. Especially the oxygen concentrations have to be determined carefully because no data for strontium doped samples has been reported so far, while it is known that the system is capable of incorporating large amounts of excess oxygen (for $x < 1/2$).
- In **Chapter 4** we present neutron and synchrotron measurements on the $\text{La}_{2-x}\text{Sr}_x\text{NiO}_4$ system. We investigate the doping dependence of the structural and magnetic aspects within the less known part of the low doped LSNO phase diagram. Furthermore, we study the influence of co-doping in the LSNO system in order to determine the influence of structural changes and disorder within the charge sector on the magnetic excitations of LSNO.
- **Chapter 5** concerns measurements on cobaltate samples $\text{La}_{2-x}\text{Sr}_x\text{CoO}_4$ within the doping range $1/3 \leq x \leq 1/2$. Charge stripe order can be detected with neutron and X-ray diffraction. The combination of both techniques is used to determine the nature of charge order in cobaltates. Neutron spectroscopy was used to measure the magnetic excitation spectrum of cobaltate samples to study the impact of charge ordering on the cobalt-oxygen bond stretching phonon modes.

Chapter 2

Experimental Methods

Synthesis of new materials usually begins with carefully weighing the reactants in the calculated stoichiometry. Nonetheless, the product sometimes can deviate from this ideal composition and in the worst case the desired material is not formed at all. Methods to analyze the progress of a ceramic reaction or the quality of a floating zone grown single crystal are therefore essential. Particularly Laue backscattering and powder X-ray diffraction are useful methods. Powder X-ray diffraction is a fast way to track the decreasing fraction of the reactants after each synthesis step, while the product is formed. Impurity phases down to 5 % volume fraction are easily detectable. If no impurities are observed with powder X-ray diffraction more sensitive techniques can be applied. Inductively coupled plasma atomic emission spectroscopy (ICP-AES) on dissolved sample material can be used to measure the relative mass fraction of each metal. Energy-dispersive X-ray spectroscopy (EDX) and Wavelength-dispersive X-ray spectroscopy (WDX) can be applied on compressed powder pellets as well as single crystals. Transition metal oxides with K_2NiF_4 structure are well known to be stable in a wide range of oxygen content [102, 182]. The parent compound $\text{La}_2\text{NiO}_{4\pm\delta}$ was synthesized with $-0.9 \leq \delta \leq 0.26$ [78, 100] and $\text{La}_2\text{CoO}_{4+\delta}$ with $0 \leq \delta \leq 0.26$ [102]. Small oxygen off stoichiometry generally also results in a slight change in lattice constants. Larger variations can even lead to ordered superstructures of excess oxygen or vacancies and might give rise to new crystal structures, thus forming a rich phase diagram (see Section 1.5). In practice the oxygen content is very difficult to adjust because of the wide range of possible concentrations. Fortunately, in the investigated materials, small deviations δ smaller than 0.01-0.02 do not alter the crystal structure. During the synthesis reaction the final oxygen content is determined by the atmospheric conditions. Oxygen atoms can leave or enter the solid, depending on reaction temperature and oxygen partial pressure. For the discussed compounds this is further facilitated by the high oxygen permeability.

Determination of the oxygen content is the other half of the problem. Because of its low electron count, the oxygen atom does not contribute much in measurements with X-rays. At the same time a comparably high fraction of its electrons are located in the outer shell where the corresponding energy levels strongly depend on the chemical environment. This results in somewhat enlarged error bars for the determination with the X-ray based techniques EDX and WDX. Alternative approaches are the carrier gas hot extraction (CGHE) method and thermogravimetry (TG).

2.1 Sample Preparation

Experimental results can only be as good as the investigated sample quality and purity permits. Sample preparation can therefore be considered as the most important first step in the whole procedure.

Polycrystalline powder samples have been prepared by the “ceramic method”, so called after the process to produce “ceramics” in the common meaning, namely the burning of clay. The similarity to the ceramic method is obvious: reactants are ground together and burned at high temperatures in a furnace until the product is formed by solid state reaction.

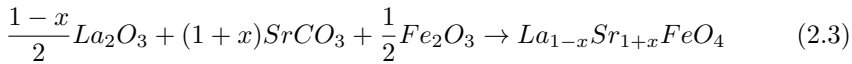
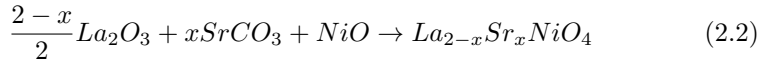
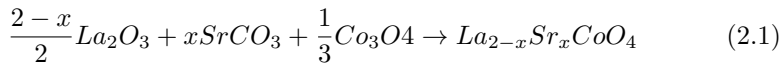
The combination of covalent, ionic and sometimes metallic contributions is responsible for the variety of ceramic materials. In contrast to polymers, ceramics consist of arrays of interconnected atoms, not discrete molecules. A definition for ceramics was proposed by Kingery [183]: “A ceramic is a non-metallic, inorganic solid.” Apart from this general definition it is not possible to define ceramics in terms of specific properties. For every generality exceptions can be found.

Our frequent neutron measurements as well as X-ray absorption spectroscopy performed by colleagues generate a strong demand for high quality single crystals with several cubic centimeter in size. To satisfy this demand we used the floating zone technique on a vertical four mirror furnace. This crucible free method is capable of producing large single crystals without impurities from crucible or flux. The molten zone is formed by contact-less heating and held between the feed and seed rods by surface tension only. The benefits of this method, like quality, size and well defined stoichiometry are very convincing, but at the same time it is one of the most difficult and time consuming techniques because the growth process is highly dependent on the skills of the crystal grower.

2.1.1 Polycrystalline Samples

Depending on the desired product a variety of synthesis routes are available, such as ceramic, sol-gel, flux and self-flux method. The simplest and by far the most employed is the ceramic method. Starting materials are weighted according to the desired sample composition and ground until they are well intermingled. Then filled into a crucible, in our case mostly Al_2O_3 , and fired in a furnace according to a well planned temperature profile. Thereafter the product is ground again and tested by powder X-ray diffraction to establish whether a single phase has formed. If the final single phase composition has not been reached, the specimen has to be fired and ground again. This procedure can be repeated until no more changes are visible between the diffractograms of two consecutive measurements. If the final product is not stoichiometric the synthesis route has to be adapted.

The starting materials used for the synthesis were chosen to be as stable as possible under standard conditions. Oxidation or incorporation of water leads to false molecular masses and consequently to wrong sample compositions. Using the most stable compounds has the benefit that materials can be produced at very high purity for much lower prices. According to the chemical reaction in equations 2.1 - 2.3 we used La_2O_3 (Alfa Aesar and ACROS Organics, 99,99%), SrCO_3 (Alfa Aesar, 99,994%), NiO (Alfa Aesar, 99,995%), Fe_2O_3 (Alfa Aesar, 99,998%), Co_3O_4 (Alfa Aesar, 99,9985%). For some codoped samples we also used ZnO (Alfa Aesar, 99,99%) and TiO_2 (Alfa Aesar, 99,99%).



In a first step in the crystal growth process the rods have to be prepared from the products. High amounts of polycrystalline material are needed as a single grows process can use up to 30 g of the starting materials. La_2O_3 is well known to react with water from the atmosphere to form $\text{La}(\text{OH})_3$. Before weighting this component the correct composition has to be ensured. To prevent the formation of lanthanum hydroxide, La_2O_3 was kept at 900°C in the furnace. Removing it from the hot furnace and weighting the still warm powder avoids the problem.

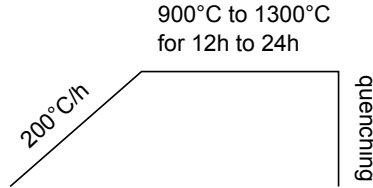


Figure 2.1: Typical temperature diagram applied to prepare the rods for the mirror furnace.

Weighted and mixed reactants were heated to temperatures between 900°C and 1300°C according to the temperature diagram in Figure 2.1. Synthesis time at lower temperatures can be decreased by increasing the contact surface of the components by compressing the loose powder to pellets. At the end of the firing, the product is removed from the hot furnace and ground again as soon as the temperature permits it. The resulting powder is filled into an empty balloon with a diameter of about 1 cm and a length of up to 12 cm. A hydrostatic press is used to apply pressures up to 60 MPa. If the powder in the balloon was uniformly distributed the result is a 8 cm to 10 cm long rod with a diameter of about 8 mm. The same procedure has to be applied to the seed rod. Finally the rods are fired again under similar conditions to sinter the pressed powder. This prevents a breaking of the feed or seed rod during the growth process.

Depending on the system and the desired composition it can become necessary to perform the described reaction under a special atmosphere. In the case of low doped $\text{La}_{2-x}\text{Sr}_x\text{CoO}_4$ we used a flow of pure argon 6.0 or active vacuum. Cobalt is in a mixed valence state between pure Co^{2+} and Co^{3+} . This is not by itself problematic regarding that the most stable cobalt oxide is Co_3O_4 with a mixed valence and an average oxidation $\text{Co}^{2.66+}$. But especially at low doping the Co^{2+} becomes unstable in the sense that samples become more likely to incorporate excess oxygen to increase the average oxidation number. The stoichiometric parent compound La_2CoO_4 is known to incorporate excess oxygen up to the composition $\text{La}_2\text{CoO}_{4.2}$ [87] when left in atmosphere, corresponding to an oxidation number of $\text{Co}^{2.4+}$. A second reason for choosing a reducing atmosphere for the low doped cobaltates is that the excess oxygen introduced by Co_3O_4 should be removed before the growth process.

In $\text{La}_{1-x}\text{Sr}_{1+x}\text{FeO}_4$ the oxidation number of iron varies between +3 and +4. The most stable iron oxides are $\text{Fe}_2^{3+}\text{O}_3$ and $\text{Fe}_3^{2.66+}\text{O}_4$ with oxidation numbers between +2 and +3. Consequently the undoped LaSrFeO_4 compound can be easily prepared as a single phase in air. In contrast stabilizing the oxygen concentration in the doped compounds proved to be very challenging. Synthesis with temperatures from 900°C to 1300°C in air and in oxygen flow at ambient

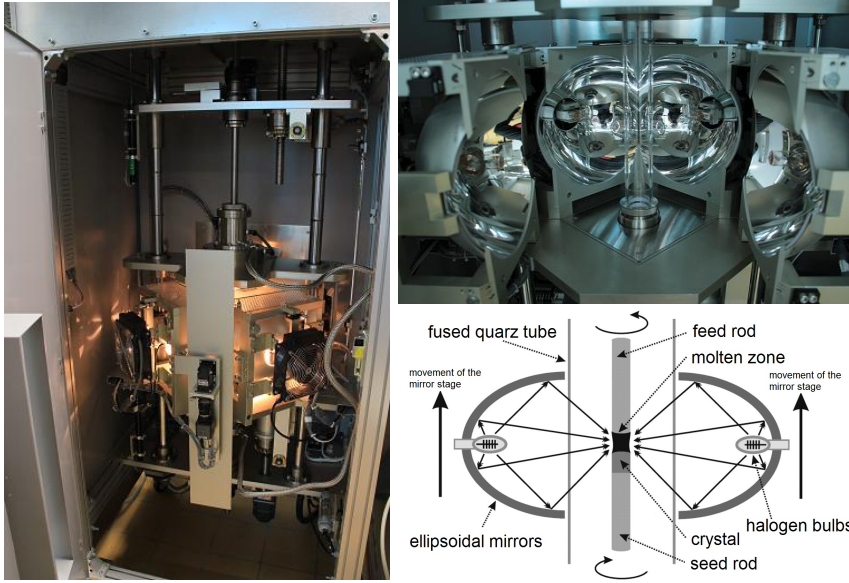


Figure 2.2: Four mirror floating zone image furnace, Model: FZ-T-10000-H-VII-VPO-PC by CSC Japan.

left: View inside the furnace housing during the growth process. The whole mirror stage is moved upwards to create a traveling of the floating zone relative to the fixed crystal.

right: The top image shows the inside of the growth chamber with the fused quartz tube in the center. Below is a sketch of the same view illustrating the working principle.

pressure have been applied. Single phase powder samples were prepared for strontium doping concentration up to $x = 0.2$. At higher doping impurities of the 113 infinite layer Ruddlesden-Popper phase appear in the X-ray diffractograms.

2.1.2 Floating Zone Technique

Image furnaces have become the best choice to create large high quality single crystals mainly due to the advantages of the floating zone technique but also due to improvements in furnace design. Nonetheless the tasks to stabilize the melt and get the crystal to grow are still very challenging. A main challenge is that every crystal has to be grown individually and the success mainly depends on the experience of the operator. Specialized furnaces are built by small companies and in small quantities. These companies ensure that every system is adapted according to the preferences of the customer but they can not perform

long term tests. One parameter that is difficult to control and reproduce is the temperature of the melt as it depends on too many factors, like type of lamps and their age, atmosphere pressure, heat absorption, rod diameter, thermal conductivity of the sample, transparency of the glass, and so on. Measuring the temperature on the running system is difficult as it has to be contact less, in front of the lamp background, on different sample materials and through the quartz glass tube. Consequently temperature measurements are inaccurate or it is necessary to switch of the lamps for the duration of the measurement. This is highly impractical during a growth process as a temperature drop greatly changes melt properties and can even lead to total solidification. Many customized image furnaces, like our CSC four mirror optical floating zone furnace even have no such sensors. A successful synthesis route on a specific image furnace might therefore need adaptation in order to work on a different system.

The predecessor of the image furnace was the flame-fusion method first described by A. Verneuil in 1902 [184]. It was used to produce synthetic rubies from alumina oxide powder. A mixture of oxygen and hydrogen gas was used to blow the powder through a tube above the crystalline product where it was burned. The liquefied powder crystallized on the seed crystal which was slowly moved downwards to keep constant conditions.

In the 1950s the floating zone technique was developed for the growth of single crystal semiconductors which also belong to the large family of ceramics. High melting points up to 3000°C and strongly corrosive properties of many ceramic melts make it difficult to find crucible materials. The floating zone technique is the ideal choice: it reaches such high temperatures and, equally important, it is crucible free. Nowadays also metallic and inter-metallic crystals are successfully grown with the floating zone technique.

The principle of the floating zone image furnace is shown in Figure 2.2. Feed and seed rods are made of compressed and sintered polycrystalline powder as described in Section 2.1.1. The seed rod is fixed on the stationary part of the furnace below the mirror focus and the seed rod on a movable bar above. A fused silica tube has to be placed around the rod setup to prevent damage to the mirrors from hot spraying sample material and to enable the use of a controlled atmosphere with pressures up to 0.95 MPa. The lamp and mirror setup varies between different furnaces. Heating can be achieved with high frequency coils, multiple lasers or with infrared, halogen or xenon arc lamps placed in one focal point of up to four elliptical mirrors where the melting zone is in the other focal point. An increased number of light sources provides a much smoother temperature profile at the potential cost of focus. The procedure to adjust the position of four lamps is lengthy and the focus can never be as good as on a single mirror furnace. On the other hand is a single lamp often not sufficient

to reach the highest temperatures and the inhomogeneous temperature profile might affect the growth process.

During the growth process the melt can be observed through a camera. The controllable parameters are lamp power, rotation speed and direction of the upper and lower shafts where the feed and seed rods are fixed. Usually the growth rate was chosen between 0.8 mm/h and 4 mm/h for our samples. Gas composition, pressure and flow rate can be adjusted manually. For our purposes argon 6.0, nitrogen 6.0 and oxygen 5.0 pressurized steel bottles (20 MPa) were connected to the furnace, as well as a low pressure 0.05 MPa air compressor for air flow and chamber flushing. The manufacturer specifies the working temperature of the used four mirror furnace to 1850°C with a maximal temperature of 2200°C .

At the bottom of the melt the new crystal is formed where the material recrystallizes on the seed rod, while new material is melted at the top. The length of the molten zone depends on the furnace type, the adjustment of the lamps in their foci and also on the size of the lamp filaments. It can be theoretically calculated to $l = \lambda\sqrt{\sigma/\rho g}$ and depends on the surface tension σ , the density ρ and the gravitational acceleration g . The constant λ has been calculated to be about $\lambda = 2.7(1)$ [185–187].

It is always best to start the growth with an oriented single domain seed crystal (see Figure 2.5 middle). If no mistakes happen during the heat and contact-procedure, the growth of a single domain starts immediately. The crystal growth direction can be controlled by the orientation of the seed crystal. Since this approach is only accessible if growing the same sample multiple times it has been used mainly to produce a large amount of LaSrFeO_4 crystals.

A more general approach is the use of a poly-crystalline seed rod which provides multiple seed grains. Most of which will have unfavorable orientations. Normally one domain will steadily increase in size until, after a growth one to three centimeter length, it is the only domain left. This can be supported by the so called “necking”, a technique where the seed rod is moved at a higher speed then the feed. This results in a narrower diameter of the grown crystal, thus supporting the formation of a single domain. During the necking the molten zone considerably changes shape and size. This potentially changes heat absorption and heat dissipation due to the smaller diameter. It is therefore not without risk to apply this procedure and it has been rarely used. Even without necking one domain usually quickly suppresses the others. Finally, setting the correct growth rate is crucial. If chosen too fast, defects will be introduced into the crystal. On such defects new crystal domains can start growing. Even if starting with a single domain seed rod the growth product will become a polycrystal when using too high growth speeds.

The large number of parameters, a poor reproducibility due to slightly changed sample density and diameter, lamp conditions and glass transparency

makes it difficult to develop growth recipes for a concrete material. Consequently the success of a crystal growth depends largely on experience and it is not unjustified to think of this process as a form of alchemy.

2.1.3 Growth of Incongruent Melting Crystals

The simple crystal growth process as described above applies only to congruent melting systems. These are materials where the liquid phase has the same composition as the solid phase. Elements are single component systems and naturally belong to this group. Two or more component systems usually melt incongruent except for some specific compositions. Heating an incongruent melting material will result in decomposition at the temperature where part of the material becomes liquid while the rest remains a solid with a different composition.

In Figure 2.3 a qualitative phase diagram for the pseudo binary system La_2O_3 - CoO is presented. This diagram is not able to illustrate the continuous melting and re-crystallization process of the traveling floating zone technique which also implies two solid-liquid interfaces. In fact it is only valid for a system without temperature gradient. Nonetheless, the phase diagram represents a good starting point.

Heating a finite amount of La_2CoO_4 increases the sample temperature along the vertical line until point 1) in the phase diagram is reached. Here the temperature remains constant while the material decomposes into a liquid consisting of CoO and La_2O_3 and a solid La_2O_3 phase. The composition of the liquid phase corresponds to the point in the phase diagram where the horizontal solidification line intersects with the liquidus line (between 3) and 4)). When the temperature is increased, the remaining La_2O_3 will start to melt and the composition of the melt changes according to Gibbs phase rule along the liquidus line until point 2) is reached. Gibbs phase rule calculates the degrees of freedom f at a certain point in the phase diagram with the amount of independent particle types, $C = 2$ in our binary phase diagram, and the number of adjacent phases Ph : $f = C - \text{Ph} + 2$. For a constant pressure the equation simplifies to $f = 3 - \text{Ph}$.

To discuss the re-crystallization process we choose the idealized case of a stoichiometric melt above a stoichiometric crystal. Starting at a point in the phase diagram somewhere above 2), the melt at the liquid/solid interface will cool down as the floating zone moves on. In the pure liquid phase the composition will remain constant upon cooling until the solidus line is intersected at point 2). Further decrease in temperature will result in change of composition ($f = 1$) along the path 3) and, more specific, in the solidification of La_2O_3 . When the melt reaches a composition in the range of 4) the final product La_2CoO_4 will be formed. Continuous crystallization of the stoichiometric product increases the CoO concentration until the eutectic point 5) is reached. Here, three phases are in equilibrium and no degrees of freedom remain. The result is a characteristic two phase solid consisting of a mixture of CoO and La_2CoO_4 . Reaching

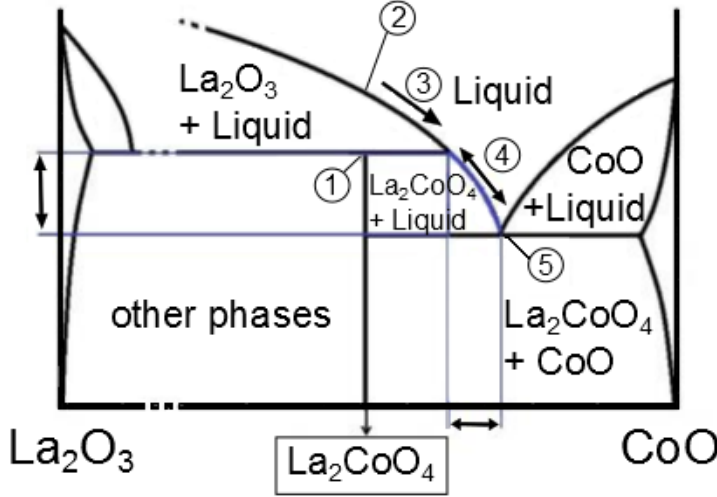


Figure 2.3: Ideal qualitative phase diagram of the La_2O_3 - CoO pseudo binary system (after [87])

the eutectic point of the phase diagram during a crystal growth can be severe. Escape is only possible by increasing the temperature, but simultaneously the decreased surface tension will destabilize the melt. In contrast to the described static case, floating zone is a dynamic technique where new material with the composition according to 2) is continuously provided. Cooling the melt with a composition in the range of 4) results in formation of La_2CoO_4 at the seed rod, while the feed rod is simultaneously melted. If conditions can be kept constant, the melting feed will replenish material with the same composition as the produced crystal and thus the melt composition can reach an equilibrium.

For the description of the crystal growth process with the binary phase diagram two unjustified simplifications have been made: a homogeneous temperature and a homogeneous melt composition [188–190]. Indeed according to the phase diagram it would be impossible to melt the entire feed rod at the low crystallization temperature necessary to form single phase La_2CoO_4 . Material transport from the feed to the seed is another crucial process. If both rods are rotated in the same direction a large convection current will form. Material is transported upwards on the outside and downwards on the inside, resulting in a quick connection of feed and seed rods. As the feed rod melts the mentioned fraction of La_2O_3 remains solid and forms small grains that fall into the melt. Through the quick connection they sink down and deposit on the seed. This

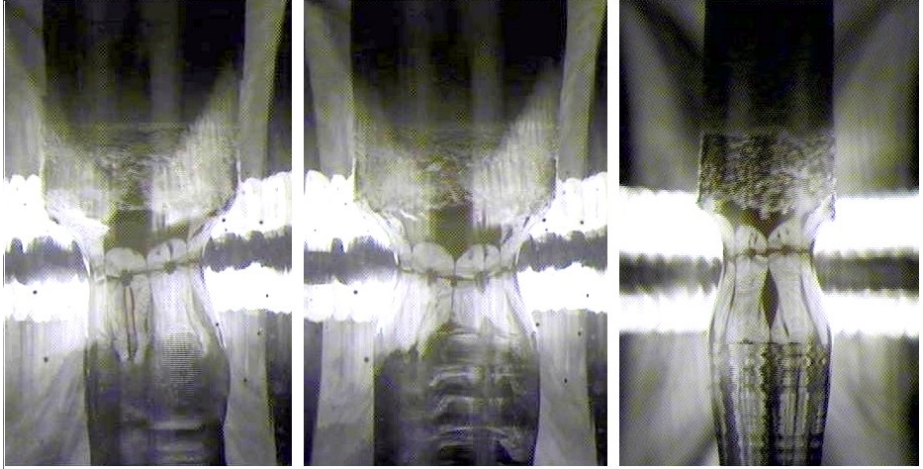


Figure 2.4: View into the chamber during the crystal growth of LaSrFeO_4 .
left and middle: The two pictures have been taken during the same growth, demonstrating the large anisotropy of the product.
right: With a different growth direction the crystal grows perfectly symmetric.

pollutes the crystal and changes melt composition. To prevent this, the rods are rotated in different directions. The result is two convection zones, the upper one moving downwards on the outside and the lower one moves upwards on the outside. The interface is quite turbulent and prevents fast connection from top to bottom. La_2O_3 grains have enough time to be completely solved during the slow propagation of material through the hottest part of the melt.

It is very important to know the phase diagram when growing incongruent crystals. Unfortunately phase diagrams for the systems La_2O_3 - CoO or La_2TO_4 - LaSrMeO_4 with $T = \text{Fe, Co, Ni}$ are not available. Only for the iron system a SrO - LaFeO_3 and a La_2O_3 - Fe_2O_3 phase diagram have been published [191–193]. It can be inferred, that the composition $\text{La}_2\text{SrFe}_2\text{O}_7$ melts incongruent while the compounds La_2FeO_4 and $\text{La}_3\text{Fe}_2\text{O}_7$ might not form at all. Also in literature the two latter compositions have not yet been reported.

Growth of $\text{La}_{1-x}\text{Sr}_{1+x}\text{FeO}_4$ -system crystals has been extensively studied for this thesis in order to produce samples within the whole doping range x . For a neutron measurement of the excitations in LaSrFeO_4 a large amount of sample mass was required to reduce counting time. Surprisingly the grown crystals can exhibit quite different shapes. Half the time the product is perfectly round, in the other half an elliptical shape can be observed with the long axis up to two times as long as the short axis. Figure 2.4 shows the formation of LaSrFeO_4 , left

and middle images are taken during the same growth. The large anisotropy can be best observed at the bottom of the image. The irregular shape is not able to support the large melt above and often material leaks over the edge, preventing a further increase of the anisotropy. In comparison the right image was taken during a symmetric growth of LaSrFeO_4 . Laue camera images revealed that the growth direction is (100) in the elliptical and (111) in the symmetric crystal. When (100) is the growth direction the directions (010) and (001) will be perpendicular where the latter is the direction of the short axis. This means that the growth along the (001) direction is much slower than along (100). This can be observed for all 214 compounds: generally the growth direction lies in a 30° cone around the (110) direction, preferably between (110) and (100), e.g. (120) and (130). Most of the crystals exhibit two 180° facets with the (001) direction lying within the plane spanned by the facet normal and the growth direction, but always close to the facet normal (within 30°). The facets are not only an indication for a good crystal as they imply that the same domain reaches through the whole crystal, but also prove that the growth process along the (001) direction is hindered in the 214-system. Especially the $\text{La}_{1-x}\text{Sr}_{1+x}\text{FeO}_4$ compounds cleaves very easy perpendicular to (001), leaving the ab-plane as a shining surface. This demonstrates the quasi two dimensional character of the unit cell in this compounds. While interactions within the ab-plane are strong, neighboring planes are only loosely bound along the c-direction.

Growth of the strontium doped LaSrFeO_4 proved to be rather difficult for $x \geq 0.2$, where the system becomes more and more incongruent melting with rising strontium concentration. As mentioned above, during crystal growth the melt has a different composition than the feed and seed rods, because it is enriched with a flux component. The flux has a lower melting point than the feed rod while the temperature in the upper part of the melt is high enough to melt the feed rod. Capillary climbing along the grain boundaries inside the feed rod is then possible. This has two unwanted effects: the feed rod can be heavily enlarged (see Figure 2.5 middle) while at the same time the melt is depleted of flux and therefore in danger of solidifying due to the increasing melting point. Finally the flux will solidify inside the seed rod at a height corresponding to its melting temperature, forming a ditch that effectively separates upper and lower part of the feed rod. As the molten zone moves upwards, the whole ditch can liquefy at once (see Figure 2.5 right). The probability that a large piece or even the whole unmelted material falls into the melt is very high and this usually breaks the melt.

If smaller pieces of solid fall into the melt they might be quickly dissolved. But sometimes this fast melting can lead to the evaporation of a gaseous phase inside the melt. The excess gas will form a bubble that floats between the upper and lower convection zones (see Figure 2.5 left). This bubble will burst eventu-

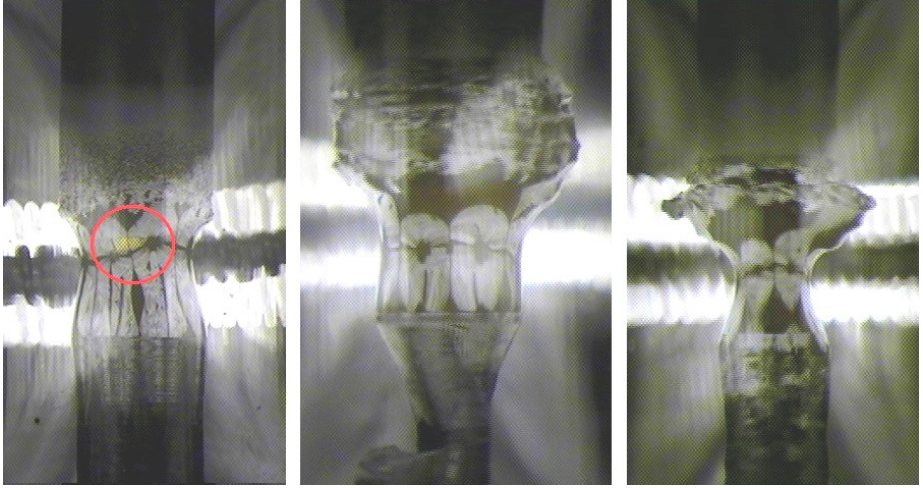


Figure 2.5: Exemplary complications during the growth process:
left: A gas bubble formed inside the melt of $\text{La}_{1.67}\text{Sr}_{0.33}\text{CoO}_4$.
middle and right: Severe ditches formed during the growth of $\text{La}_{1-x}\text{Sr}_{1+x}\text{FeO}_4$.

ally. If it was small, the damage (overflowing material, change of temperature, change of melt composition) can be repaired but the burst of a large bubble breaks the melt. The size of such bubbles can be decreased with increasing pressure in the sample environment. For that reason even crystal growth in argon atmosphere was performed at elevated pressures. For the same reason growth in active vacuum has not been done as it amplifies the formation of bubbles in these oxygen rich compounds.

For our systematic studies on the $\text{La}_{2-x}\text{Sr}_x\text{CoO}_4$ and $\text{La}_{2-x}\text{Sr}_x\text{NiO}_4$ systems, a variety of floating zone single crystals had been grown. Only few crystals of the 214 cobaltate and nickelate series have been made by the author. They are labeled with the first letters “YD”. Most samples were prepared by A. Komarek and can be recognized from the “ACK” label. “ZL” denotes samples made by Z. Li.

Low doped cobaltates have been grown in argon atmosphere to stabilize the low oxidation number of the cobalt. Indeed it was claimed in a study on the end member La_2CoO_4 [87] that a crystal grown in argon atmosphere has an oxygen excess of $\delta = 0.15$. Only post annealing in an argon/hydrogen atmosphere leads to the stoichiometric compound. In the same study it was reported that the excess oxygen content rises up to $\delta = 0.19$ when the sample is left in air. The cobalt valency in the oxidized compound is $\text{Co}^{2.38+}$, similar to a strontium

doped sample with $x = 0.38$. Samples with smaller strontium doping concentration should therefore be grown and stored with care as they might tend to incorporate excess oxygen.

Rods for the cobaltate samples YD_070 and YD_071 have been sintered under active vacuum at 1150°C . Growth has been performed under argon or nitrogen atmospheres with small flow rates of about 50 ml/min. YD_070 with a strontium doping $x = 1/3$ grew very stable at a speed of 2 mm/h. Rotation speed of the feed/seed rods was 110/220 rotations per minute. The crystal has a shining surface and 2 facets at an angular distance of 180° (see Figure 2.6). In comparison, the growth of a cobaltate with $x = 1/4$ proved more difficult. The preparation procedure was similar to YD_070. In both cases gas bubbles formed in the melt, but no ditches due to raising flux appeared. Still the zone broke a few times without obvious reason during the growth of YD_071. Probably this can be attributed to a change in flux concentration during the beginning of the growth. The more a system melts incongruent the more the temperature has to be adjusted during the enrichment of the melt with flux. Inaccurate temperature changes can decrease viscosity until the surface tension is insufficient to hold the melt. Finally a 3 cm large single domain single crystal could be extracted from the boule.

The last growth to be mentioned is YD_051. The undoped La_2NiO_4 sample was grown from a rod of compressed starting materials without any pre-reaction. This was possible because no carbonate was used for this crystal. The growth was very stable and a high growth speed of 3.6 mm/h was possible. Evaporation of nickel is a serious problem for the growth of nickelates. If the process takes too long the entire quartz glass tube will be covered with evaporated material, preventing the heat from reaching the melt. This can terminate the growth through solidification of the melt. Therefore the growth has to be finished before too much light is blocked. After the growth, the evaporated material was collected and weighted. It amounts to about 3% of the initial NiO used for the rods. The resulting single crystal was about 7 cm long and of black color. A post treatment of the whole crystal in Ar/ H_2 flow of concentration 95%/5% for one week at 400°C removed the excess oxygen. The result was a red, opaque crystal.

2.2 Powder X-ray Diffraction Technique

This powerful method is the first choice to investigate the result of a synthesis and is especially useful to track the progress of a reaction under different conditions in order to find the best synthesis route. It can also be used to exclude impurities above 1 % - 5 % volume fraction and determine the unit cell param-

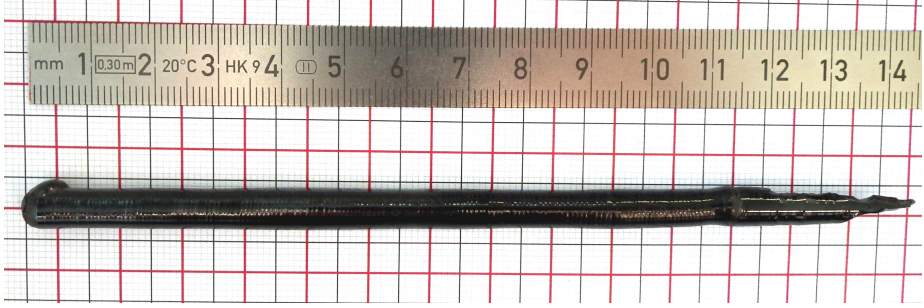


Figure 2.6: The “as grown” boule $\text{La}_{1.67}\text{Sr}_{0.33}\text{CoO}_4$. The lower part from 11.5 cm to 14.5 cm is the seed crystal.

eters of a crystal structure. Even the unknown structure of a new material can be determined, but to identify the exact atom positions, single crystal X-ray diffraction is much better suited.

Our routine sample analysis in house powder X-ray diffractometers operate in an asymmetric Guinier geometry. A metal ring serves as sample holder where a thin ($5\text{ }\mu\text{m}$) polyimide (Kapton) foil can be tightly fixed on. Especially crushed single crystals have to be ground well in order to provide crystallites of the order of $50\text{ }\mu\text{m}$ and smaller to avoid false peak intensities, resulting from big crystallites in reflection position.

An example of a powder pattern can be found in Figure 2.7. A structure model was fitted to the data with the Fullprof software [194]. All refinements were done with the Rietveld method [195]. This routine minimizes χ^2 , the sum of the squared difference between the measured and a calculated intensity for each data point, weighted by the variance. For the pattern calculation a user defined set of parameters is varied with the least squares method until convergence is reached. The minimized parameter χ^2 is a measure for the deviation between calculated and the measured pattern only but contains no information on the reliability of a fit. To express the reliability of a structure model, usually the profile factor R_P , the weighted profile factor R_{WP} or the Bragg factor are used. y_i and $y_{c,i}$ are the measured and calculated intensities and $I_{Obs,\mathbf{h}}$ is the integrated intensity of reflection \mathbf{h} [196].

$$R_p = 100 \frac{\sum_{i=1}^n |y_i - y_{c,i}|}{\sum_{i=1}^n y_i} \quad (2.4)$$

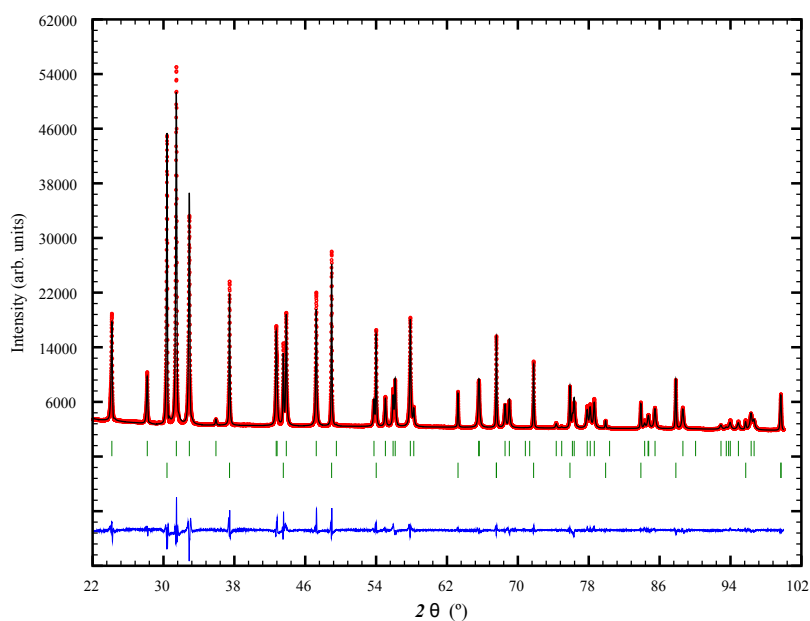


Figure 2.7: Powder X-ray pattern of ACK269 - $\text{La}_{1.79}\text{Sr}_{0.21}\text{NiO}_4$ mixed with a LaB_6 standard and measured at room temperature. Data in red color, Rietveld refinement fit in black, difference between experimental and calculated intensities in blue. The green vertical bars mark calculated Bragg positions (upper bars for the nickelate, lower ones for the standard).

$$R_{wp} = 100 \left[\frac{\sum_{i=1}^n w_i |y_i - y_{c,i}|^2}{\sum_{i=1}^n w_i y_i^2} \right]^{1/2} \quad (2.5)$$

$$R_{Bragg} = 100 \frac{\sum_{\mathbf{h}} |I_{Obs,\mathbf{h}} - I_{calc,\mathbf{h}}|}{\sum_{\mathbf{h}} |I_{Obs,\mathbf{h}}|} \quad (2.6)$$

The final results of a refinement procedure with the I4/mmm space group on a $\text{La}_{1.79}\text{Sr}_{0.21}\text{NiO}_4$ sample are shown in Figure 2.7. The difference curve between measured and calculated intensities shows only minor deviations from a neutral line, indicating that the structure model is in good agreement with the measured data.

2.3 Energy-dispersive and Wavelength-dispersive X-ray Spectroscopy

A high energy electron or X-ray beam is used to remove core electrons from the atom or excite them to higher states. When electrons from higher shells fill the vacancies a characteristic electromagnetic radiation, corresponding to the energy difference between initial and final state, is emitted that can be detected by an energy dispersive detector. As every element has a different nuclear charge, the energy of the electronic shells and, more important, the energy difference between them vary from one element to the next. Unique peak positions have been tabulated and can be used to qualitatively determine the elements contained in the sample.

One of the limiting factors of this technique is the peak to noise ratio, because the interaction of the primary beam with matter creates a variety of secondary radiation. The excitation of core electrons by the electron beam, and therefore the peak intensity, is proportional to the electron density which is high in heavy elements. A second reason why the method is better suited for heavier elements is the influence of the chemical environment on the valence electron shells. While electronic transitions between inner shells are mostly independent of the chemical surrounding and therefore characteristic for every atom, this is not true when valence electrons are involved. Their energy levels strongly vary between different coordinations. When no core electrons are left to excite the method fails. The lightest detectable element is boron.

The density of atoms of a certain type is proportional to the overall electron density attributed to this element and therefore proportional to its peak intensities. It is then a first approach for a quantitative analysis to compare the intensity of an element specific peak with the the same peak of an element pure sample (standard). This direct approach is obscured by other effects on the peak intensity, e.g. material density, chemical environment, peak broadening due to

interaction of the emitted radiation with the crystal. The best results can be obtained when using a standard with a chemical composition and structure as close as possible to that of the specimen.

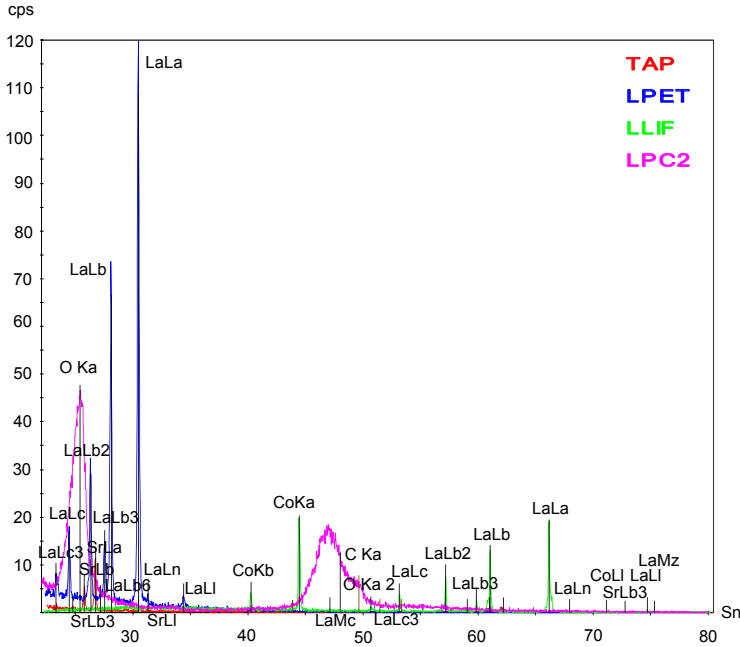


Figure 2.8: WDX spectrum of ACK343, vertical black bars mark the expected peak positions, colors correspond to different analyzer crystals.

Energy-dispersive spectroscopy (EDX) and wavelength-dispersive X-ray spectroscopy (WDX) differ only in the detection process. In the first case the emitted x-rays are analyzed by an energy dispersive detector measuring the whole spectrum at once and providing a typical resolution of 150 eV. Additional energy resolution can be gained with an analyzer crystal mounted between sample and detector. Because now monochromatic X-rays are measured for every position of the analyzer crystal, recording the whole spectrum takes much more time. The employed WDX device uses a set of four different analyzer crystals, as each only covers a narrow energy range (different colors in the WDX spectrum in Figure 2.8). The gain in energy resolution is roughly a factor 10, greatly decreasing inaccuracies due to peak overlap. WDX also has a better signal to noise ratio that enables the detection of trace elements down to concentrations in the order of 10-100 ppm [197]. At the time when the measurements were done, no other technique to determine the oxygen content was available. This method is capable to evaluate the oxygen concentration. A typical WDX measurement

can be found in Figure 2.8. The x-axis corresponds to the scattering angle of the analyzers. The large uncertainties in the oxygen content determination are directly connected to the broadness and irregular surface of the oxygen peak (pink color). Additional information can be found in [197].

2.4 ICP-OES and CGHE

A complementary method to determine sample compositions is the combination of Optical-Emission-Spectrometry with Inductively-Coupled-Plasma (ICP-OES) and Carrier Gas hot Extraction Method (CGHE). Measurements were performed by the team of G. Auffermann. The ICP-OES method can be used to determine the mass fraction of metals. First the sample has to be dissolved, e.g. in acid. Then a nebulizer introduces the liquid into the chamber filled with an inductively coupled argon plasma. The excited metal ions emit characteristic radiation that is collected by a high resolution spectrometer. For light non-metal elements the CGHE method is used. The specimen is heated (up to 3000°C) inside a graphite crucible in a stream of helium. The oxygen content is measured indirectly as it reacts with the crucible. At high temperatures the resulting CO and CO₂ emit IR radiation that can be detected with selective IR-cells. Similarly hydrogen can be detected from the IR spectrum of H₂O. If both methods are applied on the same material the individually measured mass fractions should add up to 100±1%. A larger deviation could mean that additional elements are present. Similar to the WDX/EDX measurement the measured mass fractions have to be normalized. Here the normalisation factor was chosen so that the lanthanum concentration in La_{2-x}Sr_xTO₄ matches the nominal values. See [198] for further insight.

2.5 Triple Axis Spectrometer

A new scattering technique was developed after the discovery of the neutron, by J. Chadwick in 1932 [199, 200]. The difficulty to produce a neutron beam of sufficient intensity for experiments is the main drawback of this technique. In the decade between the neutron discovery and the construction of the first fission source (CP-1 in 1942) the general properties of the new particle had been mapped. A white neutron beam emitted from a fission source finally had the necessary intensity to do diffraction experiments. The first structure determination ever performed with neutrons was done for NaCl on a two-axis diffractometer in 1946.

Neutrons generated in a research reactor are called thermal neutrons because their kinetic energy of about 25 meV is the most probable in the Maxwell-

Boltzmann distribution at ambient temperature. Their wavelength in the typical range of distances in condensed matter 1-4 Å makes them ideal for diffraction experiments. The neutron intensity maximum can be shifted to a lower value of about 5 meV using a liquid hydrogen environment at 25 K or to higher values in a 2000 K graphite moderator. Due to the relation between neutron energy and moderator temperature, experimentally used neutron sources are classified as cold, thermal and hot. While cold neutrons allow a better resolution in momentum and energy transfer, hot neutrons provide an increased accessible range.

Most neutron data presented in this thesis was collected with triple axis spectrometers (TAS) at fission reactor based neutron sources. This type of instrument allows the measurement of scattered intensity in the four dimensional space generated by momentum transfer \vec{Q} and energy transfer $\hbar\omega$. Of the six angles that can be found in the schematics of the IN22 spectrometer in Figure 2.9, two belong to each of the three axis of monochromator, sample and analyzer. A strong Bragg reflection of the monochromator crystal is used to select neutrons with a specific energy out of the white beam produced by the reactor. According to Bragg's law this energy can be varied by changing its angle a_1 . The whole spectrometer together with the large shielding has to follow the monochromator at double its angle $a_2 = 2a_1$. Depending on the sample environment the sample can be rotated freely in space. In our experimental setup usually a cryostat was used which restricts sample rotation a_3 to the scattering plane. The neutrons are diffracted by the sample at an angle a_4 which defines the position of the bulky analyzer and detector housing. Finally the analyzer selects a specific energy according to its angle a_5 which is led through to the detector at $a_6 = 2a_5$. Neutron spectrometer are large and bulky due to their shielding and the need to mount various heavy sample environments.

Our samples were always pre-oriented at our in house X-ray Laue Camera and mounted on alumina sample holders so that the a-b-plane coincided with the scattering plane of the neutron spectrometer. On TAS instruments the measurement of the scattering function $S(\vec{Q}, \omega)$ is essentially limited to only two dimensions in \vec{Q} . To measure at a specific point in Q space the angles a_3 and a_4 can be varied. Changing a_3 moves the point on a circle around the origin, a_4 moves it outwards on a curved line that originates in the center. This can be well observed in the scans performed at the IN8 (see Section 4.3) with a flatcone detector. The measured maps in \vec{Q} space have a border consisting of four sections. The two segments of circle correspond to scans at different a_3 angles while the two connecting sections correspond to the 31 different a_4 positions of the detectors for a single a_3 value. According to scattering terminology a_3 and a_4 are also called ω' and 2θ , respectively. To perform a scan along a straight line both angles have to be changed simultaneously. For elastic scans the wave vectors of the incoming and outgoing neutrons, are of equal absolute value

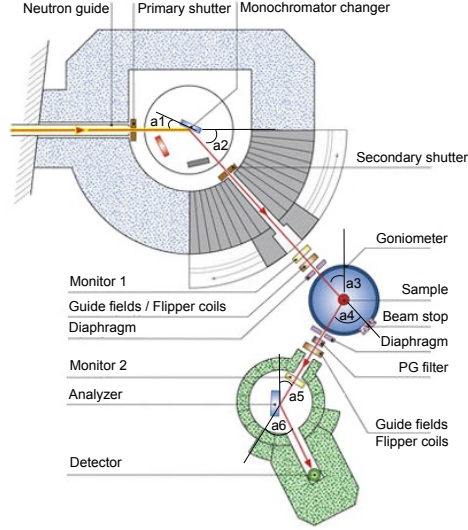


Figure 2.9: Revised schematic of the thermal neutron Triple Axis Spectrometer IN22 taken from [201]

$|\vec{k}_i| = |\vec{k}_f|$. For inelastic scans either k_i or k_f has to be varied corresponding to the energy transfer.

The sample environment is mounted on a goniometer which allows titling in two orthogonal directions for a final sample alignment and to provide the a_3 rotation. Some other essential components of a TAS instrument are also labeled in the figure. The incoming neutron beam generally has a diameter of about 5 cm. Diaphragms before the sample decrease the beam size roughly to the sample geometry to prevent unnecessary neutrons from scattering on the cryostat and air. The diaphragms after the sample blocks neutron not scattered by the sample.

Pyrolytic graphite has the property that neutron transmission probability is highly energy dependent. This can be used to significantly reduce neutron intensity resulting from higher order scattering. For thermal neutrons energy windows corresponding to the neutron wave numbers $k = 2.662 \text{ \AA}^{-1}$, $k = 3.81 \text{ \AA}^{-1}$ and $k = 4.2 \text{ \AA}^{-1}$ exist. The value $k = 2.662 \text{ \AA}^{-1} \equiv 14.7 \text{ meV}$ is commonly used as it provides the largest flux for thermal neutrons. All parts of the TAS are equipped with air buffers to allow individual movement on the tanzboden type floor.

Although a triple axis spectrometer is a very flexible instrument the need to obey the scattering triangle $\vec{Q} = \vec{k}_i - \vec{k}_f$ combined with limited space places

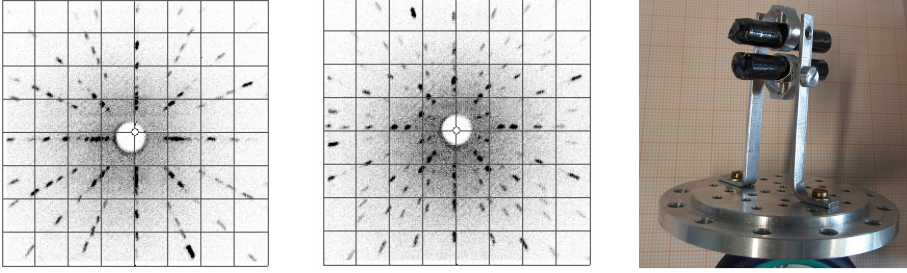


Figure 2.10: *Left to Right:* 1.) Laue image with four fold rotational symmetry centered at the (001) direction 2.) Laue image with vertical and horizontal mirror planes through the (1 1 0) reflection, the ab-plane is horizontal. 3.) Crystals co-aligned and mounted on a sample holder for neutron measurements. c direction is vertical.

restrictions on the accessible (\vec{Q}, ω) -space. For elastic scans at the IN22 on our layered perovskites with lattice constants of about $a = b = 3.85 \text{ \AA}$ and $c = 12.6 \text{ \AA}$ this affects the large scattering vectors \vec{Q} . The maximal value of 2θ is 110.5° , corresponding to $|\vec{Q}| = 2.67 \text{ r.l.u.}$ in the ab plane at $k_i = k_f = 2.662 \text{ \AA}^{-1}$. Similarly for an energy scan at (0.5 0.5 0) the 2θ value decreases with increasing energy until the scattering triangle can not be fulfilled any more. Before that point is reached, the vicinity to the direct beam results in a large background at angles $2\theta \leq 7.5^\circ$ for typical instrument configurations.

2.5.1 Sample Orientation and Mounting

A real time Laue Camera was used for sample orientation and alignment. The disadvantage of a poor resolution of the built in multi-wire detector compared to e.g. image plate instruments is compensated by the possibility to orient crystals in real time with a remotely controlled motorized goniometer. This feature is particularly useful when scanning along a 10 cm long floating zone grown crystal to determine size and position of single domains. For most of our neutron experiments on TAS instruments one or two crystals were oriented, so that the a-b-plane coincides with the scattering plane. Typically the c-direction was determined prior to the mounting on a sample holder (Figure 2.10, left). The whole setup, including the screws, is made of alumina and can be fixed on the bottom plate of an alumina can. The right image in Figure 2.10 is a picture of two co-aligned crystals, ready to be mounted on a TAS. The last step to complete the three dimensional sample orientation is to mark the (1 0 0) or (1 1 0) direction in the scattering plane on the sample holder.

Chapter 3

Sample Characterization: Results

3.1 $\text{La}_{2-x}\text{Sr}_x\text{NiO}_4$

3.1.1 Powder X-ray Diffraction

The whole series of strontium doped and co-doped nickelates has been characterized by powder X-ray diffraction together with a LaB_6 standard. Several diffractometers were used for sample characterization, each regularly calibrated. Nonetheless, systematic errors can occur due to slightly different calibrations. A standard was used to ensure the determination of absolute lattice parameter values.

A systematic evaluation of the powder X-ray data has been done. Because the results of a structural refinement may vary significantly depending on the route taken during the refinement process, it is best to choose a similar approach for all samples. First a good structural refinement had been done for one sample thus obtaining the starting values to be used for all other samples. The route then was as follows: 1. all parameters fixed except background and scaling parameter 2. additional refinement of the lattice constants 3. refinement of all other reasonable fit parameters.

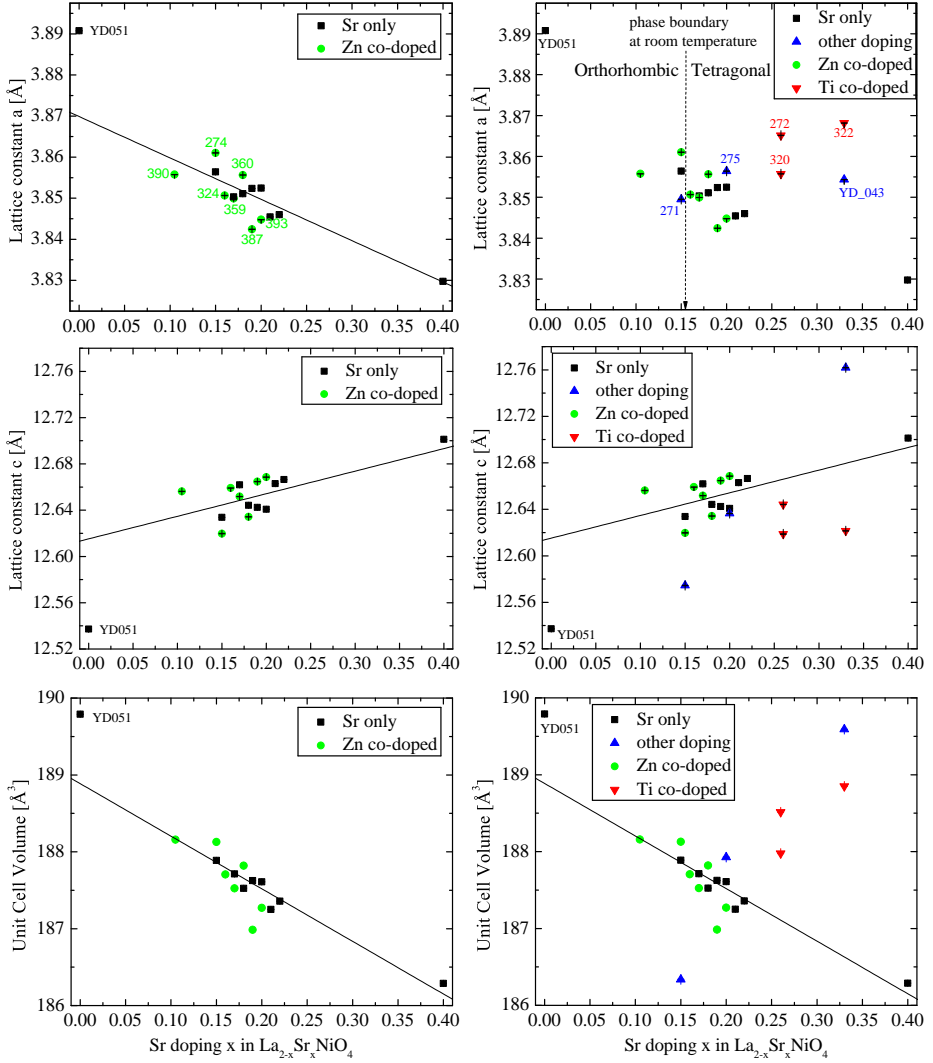


Figure 3.1: *left*: Doping dependence of the lattice parameters of $\text{La}_{2-x}\text{Sr}_x\text{NiO}_4$ and $\text{La}_{2-x}\text{Sr}_x\text{Zn}_y\text{Ni}_{1-y}\text{O}_4$ samples at room temperature.

right: Comparison of the lattice parameters for all nickelates.

Note, that the co-doped samples were in some cases also voluntarily oxygen co-doped.

The fitted lattice parameters of all measured nickelate samples are listed in Table 3.1. All samples have been evaluated with the tetragonal $I4/mmm$ space group except for YD051- $\text{La}_2\text{NiO}_{4\pm\delta}$ which shows a too large orthorhombic splitting for a reasonable fit. In fact all samples with strontium doping of $x \leq 0.15$ show a weak orthorhombic splitting at room temperature which is too small to be reflected in the R-values. The plots on the right side of Figure 3.1 place the lattice constants of the co-doped samples in the frame set by the systematic study of the pure strontium doped samples. EDX and ICP-OES measurements (see Sections 3.1.3 and 3.1.2) proofed that zinc concentrations are very small in the zinc co-doped samples. Therefore, their lattice constants have been plotted together with those of the undoped samples on the left side of Figure 3.1. The plots on the right side include the data from all characterized nickelate samples. The black line is a linear fit to the purely strontium doped samples and only meant as a guide to the eye.

A comparison with published data qualitatively confirms the observed doping dependencies [202–204]. Especially in the region of interest with $0.15 \leq x \leq 0.22$ the evaluated lattice constants also quantitatively coincide with literature data [202–204]. Apparent in our plots (Figure 3.1) is the deviation of the parameters of the undoped sample YD051 from the linear fit. Such a discontinuity within the low doped region was also reported in [203, 204]. In a more recent systematic study of the lattice constants in strontium doped nickelates the oxygen content dependency was also investigated [202]. The absence of such a discontinuity in their data suggests that a strong deviation from a stoichiometric oxygen content is present in our undoped sample YD051. Therefore this data point was excluded from the fit.

Replacing the 1.22 \AA sized La^{3+} by the larger 1.31 \AA Sr^{2+} in LaNiO_4 results in a smooth and virtually linear decrease in cell volume (see 3.1) with increasing Sr^{2+} concentration x . The increase in A cation size in A_2TO_4 is overcome by the accompanied substitution of the low-spin Ni^{3+} with 0.56 \AA for the larger high-spin Ni^{2+} with a radius of 0.69 \AA [59]. According to the evaluated tolerance factor a strong mismatch exists between the lattice dimensions of the rock salt component compared to the perovskite. The resulting internal strain is strongest in the undoped parent compound La_2NiO_4 and results in a pronounced orthorhombic distortion already above room temperature. Strontium doping releases this strain so that at a doping above $x = 0.15$ the tetragonal phase is stabilized down to ambient temperature (see vertical line in Figure 3.1).

While the development of the in plane lattice constants coincides with the unit cell volume an anomaly appears in the out of plane constant, which increases with strontium content. This trend in the c-lattice parameter has been explained in literature in terms of a Jahn-Teller distortion due to orbital ordering in the low-spin $t_{2g}^6 e_g^1$ nickel(III) cation [205]. A look at the $3d^7$ electron configuration of Ni^{+3} shown in Figure 1.14 gives a hint. In Ni^{+3} the orbital with

Name	Sr		a [Å]	c [Å]	V [Å ³]	R _F , R _B
YD051	0		3.89077(4)	12.5372(1)	189.789(3)	7.3, 10
ACK270	0.15		3.85642(5)	12.6337(1)	187.889(4)	5.8, 11
ACK264	0.17		3.85033(6)	12.6618(2)	187.712(5)	5.1, 9.0
ACK265	0.18		3.85110(5)	12.6441(2)	187.525(4)	4.5, 6.3
ACK266	0.19		3.85238(4)	12.6424(1)	187.625(4)	7.2, 12
ACK268	0.2		3.85246(5)	12.6408(2)	187.608(4)	5.5, 9.6
ACK269	0.21		3.84543(3)	12.6628(1)	187.250(3)	4.4, 6.2
ACK273	0.22		3.84600(4)	12.6664(1)	187.358(4)	6.8, 9.8
ACK326	0.4		3.82974(3)	12.7012(1)	186.288(3)	5.6, 9.3
YD043	0	0.33 Ba	3.85434(3)	12.7619(1)	189.590(2)	5.1, 7.6
ACK271	0.15	0.39 Nd	3.84949(2)	12.5745(7)	186.336(2)	5.1, 8.3
ACK275	0.2	0.05 Fe	3.85639(4)	12.6365(1)	187.927(3)	5.3, 7.2
ACK274	0.15	0.03 Zn	3.86103(7)	12.6197(2)	188.128(6)	3.9, 7.5
ACK359	0.17	0.04 Zn	3.84994(4)	12.6518(1)	187.525(3)	3.8, 5.4
ACK360	0.18	0.05 Zn	3.85564(4)	12.6342(1)	187.819(4)	5.6, 5.6
ACK387	0.19	0.05 Zn	3.84242(4)	12.6647(1)	186.985(4)	6.8, 5.7
ACK393	0.2	0.05 Zn	3.84478(4)	12.6685(1)	187.269(3)	5.7, 8.2
ACK324	0.16	0.05 Zn	3.85066(4)	12.6591(1)	187.704(4)	4.0, 6.5
ACK390	0.105	0.05 Zn	3.85574(4)	12.6562(1)	188.156(4)	5.2, 8.9
ACK320	0.26	0.05 Ti	3.85573(6)	12.6441(2)	187.976(5)	4.1, 6.5
ACK272	0.26	0.05 Ti	3.86513(4)	12.6187(1)	188.514(4)	3.8, 6.6
ACK322	0.33	0.08 Ti	3.86817(7)	12.6214(2)	188.851(5)	4.8, 6.8

Table 3.1: Nominal sample composition, lattice parameter and reliability factors of the nickelates determined by powder XRD.

the highest energy, (x^2-y^2) , is empty while the $(3z^2-r^2)$ is filled by one electron. In contrast to Ni^{+2}HS where both orbitals are half filled, this Ni^{+3}LS configuration considerably benefits from a tetrahedral elongation which is responsible for the splitting of the two initially degenerated orbitals. Upon increased strontium doping the growing fraction of Ni^{+3} therefore stabilizes a larger tetragonal distortion in the transition metal oxygen octahedra through the occupation of the $(3z^2-r^2)$ orbital.

3.1.2 EDX and WDX

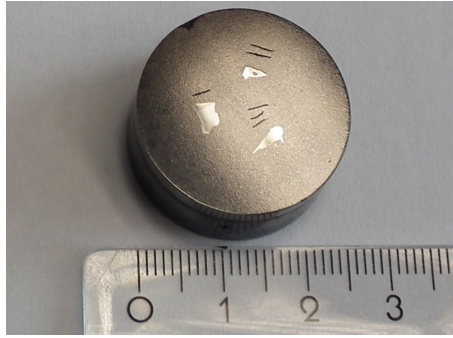


Figure 3.2: Cobaltate single crystals embedded in a polymer and polished for WDX measurements.

Our in house material analysis group provides sample characterization with both techniques using a scanning electron microscope to excite the core electrons. Electron beams have a very low penetration depth and therefore the sample surface has to be prepared prior to the measurement. Small single crystals (ca 1 mm^3) are plunged in a hot polymer liquid which solidifies upon cooling to room temperature. The block is then polished until the sample exhibits a clean shiny surface (Figure 3.2). Nickelates exhibits large enough electronic conductivities and to prevent charge accumulation on the sample the polymer has a descent conductivity.

Prior to the spectroscopy measurement the crystal surface is probed with different visualization techniques, each suited to reveal irregularities in the grown crystal. The standard procedure is to take images with direct light, polarized light, secondary electrons and with backscattered electrons. Our high quality single crystals usually exhibit no anomalies. Some rare examples are shown in Figure 3.3: 1) A network of a lanthanum rich phase present in a LaSrFeO_4 single crystal. 2) Domain boundary in a LaSrFeO_4 where both domains have correct stoichiometry but different orientation. 3) Backscattered electron image

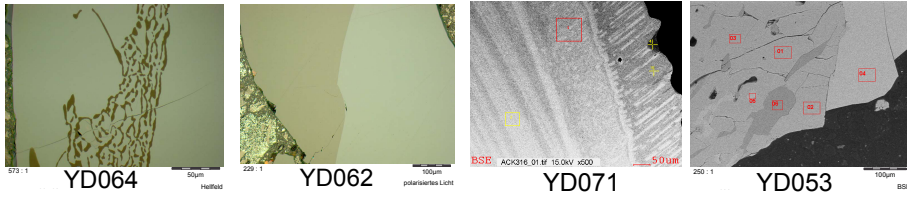


Figure 3.3: *left to right*: 1. lanthanum rich impurity phase 2. domain boundary in polarized light 3. and 4. areas of different stoichiometry in BSE

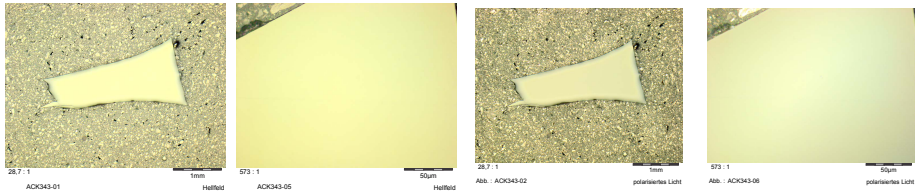


Figure 3.4: Light microscope images of the cobaltate sample ACK343. *left side*: bright field *right side*: polarized light

taken from a bottom piece of a cobaltate crystal. On the right side the crystal surface is visible. The bright and dark areas correspond to different stoichiometry although the sample consists of a single domain solely. The features on the left are ring like structures comparable to the annual rings in trees and originate from the crystal growth process. In a traveling floating zone furnace the crystallization starts at the cooler middle of the melt and continues outwards. Unstable growth conditions in the beginning of the growth process caused the observed inhomogeneities. 4) A part from the beginning of the floating zone grown CoV_2O_6 is shown. An excess of V_2O_5 was used in this self flux synthesis and deposits of V_2O_5 are indicated by the bright areas 04 and 06. The area in intermediate color corresponds to the stoichiometric phase (areas 01, 02 and 03) and the darker color corresponds to a phase where vanadium and cobalt occur in similar concentrations.

Apart from the above mentioned examples, where imperfections can be attributed to the unstable conditions at the beginning of the growth process, impurities are rare in macroscopic floating zone grown samples. Figure 3.4 shows an example of a featureless clean surface that is indicative for a single domain, impurity free single crystal. Images recorded from secondary emitted electrons (SE) are very surface sensitive because of the small penetration depth of low energy electrons. In comparison backscattered electrons (BSE) have a high energy and are emitted from a depth of the order of $1\text{ }\mu\text{m}$. Typical SE and BSE images can be found in Figure 3.5.

High accuracy in WDX measurements is gained if the reference material

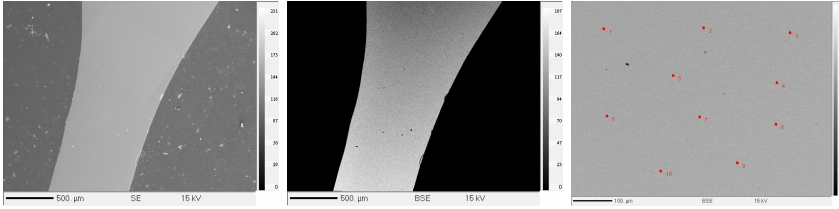


Figure 3.5: Scanning electron microscope images of the cobaltate sample ACK343. *left*: secondary electron image *middle*: backscattered electron image *right*: distribution of the ten spots where the WDX measurement was performed.

is trustworthy. The best choice are reference materials with the same elemental composition and crystal structure as the measured sample. For the $\text{La}_{2-x}\text{Sr}_x\text{TO}_4$ system with $T = \text{Fe, Co, Ni}$ no established standards exist. We therefore chose the most stable compounds out of this series as standard materials. While this method is valid to test specific crystals for deviations from the common behavior one needs to keep in mind that systematic errors can not be excluded if the stoichiometry of the standards is not confirmed by other methods. As standard materials we used $\text{La}_{1.5}\text{Sr}_{0.5}\text{CoO}_4$ (ACK353), LaSrFeO_4 (YD062) and $\text{La}_{1.6}\text{Sr}_{0.4}\text{NiO}_4$ (ACK326).

Co-doped nickelate samples have been measured with WDX and EDX. Results can be found in Table 3.2. EDX values were averaged from only three measurements compared to the ten used in WDX. In contrast to the cobaltates the oxygen contents match the expectations quite well. The sample ACK390 was intended to be slightly over oxidized with an expected value of $\delta = 0.05$, in good agreement with the measurement. Also the other samples exhibit oxygen contents close to stoichiometry within their margin of error. Given the uncertainty for oxygen determination inherent to this method, these results are rather good. The same is true for the co-doped titanium concentrations. Although the statistical error bars are too small to be trustworthy the measured titanium concentrations for ACK272 and ACK320 match the nominal values of 0.05 very well.

The element zinc could not be detected in EDX measurements on the zinc co-doped samples. For all six samples the nominal value of the zinc concentration is 0.005. It is questionable whether this value is high enough to be detected in the EDX measurement. The sublimation point of zinc oxide is around 1800°C but the vapor pressure is already of the order of 100 Pa at a temperature as low as 1400°C [206]. Consequently, an accurate doping with zinc is difficult. It is possible that the entire zinc content evaporated during the growth process. (See next Section 3.1.3 for further discussion.)

All measured nickelates exhibit a nickel deficiency with concentrations be-

Name	Strontium		Lanth.	Nickel	Oxygen	Co-doping
	nom.	meas.				
ACK390	0.105	0.103(1)	1.858(6)	0.992(4)	4.047(9)	
ACK272	0.26	0.225(1)	1.788(6)	0.953(3)	3.976(9)	Ti 0.057(1)
ACK320	0.26	0.242(1)	1.764(6)	0.956(3)	3.982(8)	Ti 0.056(1)
ACK322	1/3	0.311(5)	1.700(9)	0.891(6)	3.977(12)	Ti 0.122(4)
ACK271	0.15	0.142(2)	1.449(21)	0.999(7)	4.034(38)	Nd 0.376(8)
ACK275	0.15	0.181(3)	1.811(11)	0.968(4)	4.015(15)	Fe 0.025(1)
ACK274	0.15	0.146(3)	1.859(7)	0.969(9)	4.025(22)	Zn 0
ACK324	0.16	0.179(3)	1.820(2)	0.975(4)	4.026(36)	Zn 0
ACK359	0.17	0.196(2)	1.819(23)	0.982(12)	4.002(20)	Zn 0
ACK360	0.18	0.169(3)	1.822(12)	0.993(14)	4.016(36)	Zn 0
ACK387	0.19	0.208(6)	1.820(6)	0.953(22)	4.019(21)	Zn 0
ACK393	0.20	0.215(3)	1.797(1)	0.963(9)	4.025(13)	Zn 0

Table 3.2: Nickelate sample composition determined with WDX (top) and EDX (bottom). The measured values were normalized so that the sum corresponds to the seven atoms per formula unit.

tween 0.953 and 0.999. Deviations of similar size are also observed for the lanthanum and strontium content. Summarizing the results, we proofed that all samples exhibit element ratios consistent with the 214-phase and consist of the expected elements and element ratios. Except for the mentioned oxygen discrepancies, deviations from the nominal values are of the order of 5% or smaller.

3.1.3 ICP-OES

The titanium concentrations in the co-doped nickelates confirm the measurements in the previous section quite well. This is also true for the neodymium and iron co-doped samples. Surprisingly the ICP-OES measurement was sensitive enough to reveal traces of zinc in the Zn-0.005 nickelates. Instead of the deficiency found in EDX/WDX measurements the ICP-OES results show a pronounced nickel excess. It can be excluded that this is an artifact of the different normalization methods because the resulting lanthanum content is similar in both cases. The oxygen content has not been measured for the nickelate samples. Similar to the EDX/WDX measurements the displayed error bars refer only to the local sample homogeneity and statistical evaluation. Most of the discrepancies in the results lie within the enhanced error bars of 5%.

Name	Lanth.	Strontium	Nickel	co-doping
ACK390	1.895	0.106(1)	1.038(6)	Zn 0.004(1)
ACK272	1.74	0.217(2)	0.960(10)	Ti 0.055(1)
ACK320	1.74	0.232(3)	0.964(10)	Ti 0.051(1)
ACK322	1.66	0.312(5)	0.918(14)	Ti 0.102(2)
ACK271	1.46	0.142(1)	1.025(15)	Nd 0.360(5)
ACK275	1.80	0.168(3)	0.990(12)	Fe 0.031(3)
ACK274	1.85	0.123(1)	1.020(7)	Zn 0.004(1)
ACK324	1.84	0.150(1)	1.029(7)	Zn 0.006(1)
ACK359	1.83	0.159(1)	1.032(9)	Zn 0.004(1)
ACK360	1.82	0.144(1)	1.024(10)	Zn 0.004(1)
ACK387	1.81	0.180(2)	1.025(9)	Zn 0.005(1)
ACK393	1.80	0.164(1)	1.017(4)	Zn 0.004(1)

Table 3.3: Co-doped nickelate sample composition determined with ICP-OES. Values normalized according to the nominal Lanthanum content. Error bars result from the statistical treatment of three measurements.

3.2 $\text{La}_{2-x}\text{Sr}_x\text{CoO}_4$

3.2.1 Powder X-ray Diffraction

For our systematic studies on the cobaltate system a large number of samples had been grown. Although many of the crystals developed well visible facets on their skin during the growth process a careful analysis of the composition is necessary (see Section 2.1). We performed powder X-ray diffraction on every sample as a standard procedure to exclude additional phases. Only phase pure samples were considered for further characterization and experiments.

In the data plotted in Figure 3.6 a monotone decrease of lattice constants a and c upon strontium doping can be observed. The sample YD071 with $x = 0.25$ shows a considerable orthorhombic splitting already at room temperature. For comparison the sample has also been fitted with the tetragonal structure. This explains the much higher R values for this sample (see 3.4). All samples with doping $x \geq 0.33$ had the tetragonal space group $I 4/m m m$. Apparently, strontium doping into the parent compound has sizable effects on the lattice constants. The strong influence can not be explained by the size difference between La^{3+} and Sr^{2+} only [59].

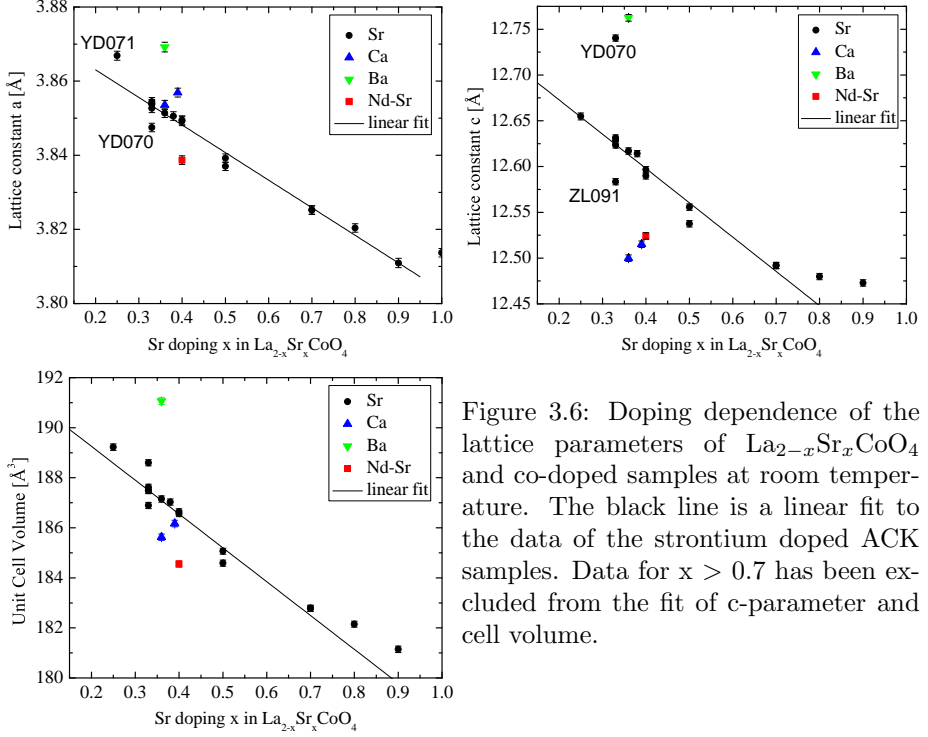


Figure 3.6: Doping dependence of the lattice parameters of $\text{La}_{2-x}\text{Sr}_x\text{CoO}_4$ and co-doped samples at room temperature. The black line is a linear fit to the data of the strontium doped ACK samples. Data for $x > 0.7$ has been excluded from the fit of c -parameter and cell volume.

To discuss further influences we have to remember that the crystal structure is composed of two different simple structures. Perovskite and rock salt layers are piled up along the c direction. To form a stable crystal it is therefore not only necessary that the ionic sizes within each crystal structure match together, but also, that the a/b lattice constants of the two structures are of similar size. Some uncertainties arise from the ability of cobalt to be stabilized in different spin states with considerably different ionic radii. According to Hollmann et al. the cobalt(III) cation is in the low spin and cobalt(II) in the high spin state for the doping range $0.4 \leq x \leq 0.8$ [207]. Replacing lanthanum by strontium reduces the mismatch between the A and T sites in two ways. According to the tables [59] the ionic lanthanum(III) radius is $r(\text{La}^{3+}) = 1.22 \text{ \AA}$ for nine fold coordination and $r(\text{Sr}^{2+}) = 1.31 \text{ \AA}$ for strontium. On the other hand, the decreased electron density in the perovskite layer leads to a decrease of the effective transition metal radius. For cobalt in six fold coordination the radii are $r(\text{Co}^{3+} \text{ LS}) = 0.545 \text{ \AA}$ compared to $r(\text{Co}^{2+} \text{ HS}) = 0.745 \text{ \AA}$.

Doping dependent plots of the a and c lattice constants and the unit cell volume can be found in Figure 3.6. Error bars correspond to the sum of the

Name	doping	a [Å]	c [Å]	V [Å ³]	R _F , R _B
YD071	0.25 Sr	3.866(2)	12.654(4)	189.20(13)	13, 15
YD070	0.33 Sr	3.847(2)	12.740(4)	188.59(12)	7.6, 10
ACK312	0.33 Sr	3.852(2)	12.631(4)	187.48(12)	5.2, 7.0
ACK183	0.33 Sr	3.853(2)	12.623(4)	187.49(12)	6.1, 7.8
ACK315	0.33 Sr	3.854(2)	12.628(4)	187.62(12)	7.4, 9.1
ACK317	0.36 Sr	3.851(2)	12.617(4)	187.14(12)	9.0, 11
ACK318	0.38 Sr	3.850(2)	12.614(4)	187.02(12)	7.5, 10
ACK305	0.4 Sr	3.849(2)	12.596(4)	186.63(12)	5.9, 6.1
ACK343	0.4 Sr	3.849(2)	12.589(4)	186.56(12)	6.8, 7.7
ACK353	0.5 Sr	3.837(2)	12.537(4)	184.58(12)	6.9, 9.0
ACK184	0.5 Sr	3.839(2)	12.555(4)	185.06(12)	6.8, 9.7
ACK308	0.7 Sr	3.825(2)	12.491(4)	182.78(12)	7.2, 9.1
ACK349	0.7 Sr	3.825(2)	12.491(4)	182.78(12)	6.6, 8.6
ACK316	0.8 Sr	3.820(2)	12.479(4)	182.14(11)	7.8, 9.6
ACK157	0.9 Sr	3.810(2)	12.472(4)	181.10(12)	6.2, 7.4
ZL091	0.33 Sr	3.853(2)	12.583(4)	186.89(12)	6.9, 8.9
ACK342	0.36 Ca	3.853(2)	12.500(4)	185.62(12)	8.4, 10
ACK346	0.39 Ca	3.856(2)	12.515(4)	186.17(11)	5.2, 7.5
ACK370	0.4Sr,0.4Nd	3.838(2)	12.524(4)	184.55(12)	8.1, 13

Table 3.4: Nominal sample composition, lattice parameter and reliability factors of $\text{La}_{2-x}\text{Sr}_x\text{CoO}_4$ determined by powder XRD

statistical contribution taken from the fit routine and a systematic contribution Δ due to measurements without standard. A powder sample has been measured five times to estimate the systematic error. $\Delta = 1.1 \cdot 10^{-3} \text{ Å}$ corresponds to the statistical deviation of the a-lattice parameter from its mean value. The black lines in the diagram indicate linear fits to the strontium doped sample data in the range $0.33 \leq x \leq 0.9$. All samples grown by A. Komarek show almost perfectly linear doping dependence apart from the highly hole-doped samples where the stabilization of the Co^{3+} oxidation state requires very high oxygen partial pressures. The general development of the lattice constants upon strontium doping x ($0.3 \leq x \leq 0.9$) is a shrinkage of about 1.2% in the a/b direction and 1.5% in c direction. This linear dependency is consistent with the expectations for a scenario in which the replacement of $\text{Co}^{2+}(\text{HS})$ with $\text{Co}^{3+}(\text{LS})$ plays the major role. Indeed the tolerance factor (see section 1.4) implies that the lanthanum-oxygen-bonds are under tension while the cobalt-oxygen-bonds are under compression at room temperature in the undoped compound. In this sense strain is decreased through both effects, the increased lattice parameter in the rocksalt layer through a larger strontium and the decreased lattice pa-

parameter in the perovskite layer through the smaller cobalt(III). Apparently the decreased atomic distances within the perovskite govern the overall behavior of the cell parameters.

Especially the lattice parameter c shows a saturation behavior for $x \geq 0.7$ while the unit cell volume decreases further until $x = 0.9$. Hollmann et al. saw a deviation from the calculated magnetic moments in their SQUID measurements on a $x = 0.8$ doped sample [207]. They mentioned the possibility of a temperature driven spin state transition of the cobalt(III) low spin to an intermediate or high spin state, slightly above room temperature. In a full multiplet calculation for Co^{3+} Hollmann et al. estimated that the IS spin state is favored for a splitting $\Delta e_g > 1.5 \text{ meV}$ [208]. Already the thermal population of the antibonding e_g orbitals could increase the average cobalt size at ambient temperature. The saturation of the c -lattice constant at lower strontium doping could be an indication for the intermediate spin state which, in contrast to the high spin state, benefits from the tetragonal elongation of the oxygen octahedron. Nonetheless, a closer look at the involved atomic distances contradicts this interpretation. While the equatorial oxygen to cobalt distance in the high doped regime $x \geq 0.7$ is about $d(\text{O}_{eq}\text{-Co}) \approx 1.91 \text{ \AA}$ the distance to the apical oxygen $d(\text{O}_{ap}\text{-Co}) \approx 2.14 \text{ \AA}$ is only slightly larger. The cuprate $\text{La}_{2-x}\text{Sr}_x\text{CuO}_{4+\delta}$ is well known to exhibit a quasi square planar oxygen coordination of the central copper atom. Due to the strong Jahn-Teller activity of this compound the apical and basal oxygen atoms distance is much larger than the equatorial one, resulting in a ratio between the two distances of about $d(\text{O}_{ap}\text{-Cu})/d(\text{O}_{eq}\text{-Cu}) = 1.28$ in the $x = 0.14$ doped compound [209]. In contrast, the ratio is much smaller in the highly doped cobaltates $d(\text{O}_{ap}\text{-Co})/d(\text{O}_{eq}\text{-Co}) = 1.12$ which makes the IS state less probable.

An increased doping dependent oxygen deficiency in the high doping regime could also cause the observed saturation of the lattice constant c . We can exclude this through our oxygen determination measurements, which neither indicated a pronounced nor a systematic oxygen deficiency (see Section 3.2.5).

Alternatively, we can consider a scenario with a doping dependent partially occupied Co(III)HS state. The small size difference between lanthanum and strontium prevents an ordering of these two cations. The statistical distribution leads to strontium rich and lanthanum rich regions on short length scales. A locally increased strontium concentration might then be sufficient to stretch some cobalt-oxygen octahedra, stabilizing the much larger Co(III)HS state. Indeed X-ray absorption spectroscopy measurements on LaSrCoO_4 performed by Z. Hu indicate a partial occupation of the high spin state of about 25 % [210].

According to Figure 1.5 the pronounced size difference between the Co(III)LS and the Co(II)HS cations causes the strongest raise of the tolerance factor upon doping throughout the investigated materials. The layered perovskites struc-

ture can be thought of as a lattice of oxygen anions packed at closest possible distances while the cations occupy the intermediate pockets. The Co(II)HS cation is too large for its pocket, therefore expanding the lattice. In contrast, the Co(III)LS cation might be too small to adequately fill its oxygen lattice pocket. Consequently, at a certain Co(III)LS concentration the oxygen anions are at their smallest possible distance. Further strontium doping then decreases the overlap between oxygen and transition metal orbitals, also decreasing the binding energy. A partial occupation of the larger Co(III) high spin state could stabilize the crystal structure. In accordance with our experimental data we would expect a decreased slope in the strontium doping dependence of the unit cell volume in the high doped regime.

Publication numbers on the $\text{La}_{2-x}\text{Sr}_x\text{CoO}_4$ system were steadily increasing in the past ten years, but so far not much data on the lattice constants has been published. The whole doping range $0 \leq x \leq 1$ was covered in the PhD thesis of M. Cwik [140]. In contrast to our nice linear doping behavior of the lattice parameters in the for this thesis most interesting region around $x = 0.33$ a strange anomaly in the c lattice constant was observed in [140]. Instead of the monotone decrease with strontium content, they found a greatly enlarged c constant for the samples $0.2 \leq x \leq 0.45$ and interpreted an increased distance between the cobalt atoms and their apical oxygen determined with single crystal X-ray diffraction, to be the cause [140]. But no explanation for this anomalous behavior was provided. However, no such anomaly could be observed in our single crystals. It has been mentioned in Section 1.5 that oxygen stoichiometry is difficult to obtain in many transition metal perovskites. The data on the c -lattice constant for oxygen rich undoped cobaltates in Figure 1.8 shows a decrease for increasing oxygen content. Although data on oxygen off stoichiometric strontium doped samples is not available, it seems likely that oxygen deficiency is responsible for the anomalies reported in Ref. [140].

3.2.2 EDX and WDX

Oxide samples often have an extremely high resistivity. This is especially problematic for the investigated cobalt oxides. To allow the charges to leave the sample it is necessary to evaporate a few (around 20) layers of carbon atoms onto the sample surface.

The measurement provides the relative element composition. To estimate absolute values assumptions have to be made for the rescaling. The straight forward assumption would be to set the number of atoms per formula unit to seven (stoichiometric composition). Our initial measurements have shown, that evaluation of the cobaltate measurements yielded unrealistic high amounts of excess oxygen throughout the whole doping range. Therefore these measurements have a systematic problem. The results for the oxygen content are included in

Figure 3.8. Due to the rescaling an excess of oxygen implies a deficiency for all other elements. To understand the unrealistic oxygen content results, different normalization approaches and also a variation of standard materials were tried. Although the peculiar high oxygen content is most likely a result of some kind of systematic error we were unable to identify its source with WDX measurements only. This will be discussed further in Section 3.2.4.

WDX measures the mass volume fraction for each element individually. Even if the oxygen content is incorrect, the metal concentration ratios are unaffected by the removal of oxygen from the calculation. For the evaluation the number of metal atoms has been normalized to three per formula unit and the results are summed in Table 3.5.

Each sample was measured ten times and the error bars result from statistical evaluation. Standard deviations are small and reflect the homogeneity of our samples. In many cases nominal and experimental compositions match within their uncertainties, but an over all tendency to smaller strontium concentration is apparent. As the deviations from stoichiometry are significant for some samples the possibility of systematic errors has to be considered. This could be caused by a poor standard for the lanthanum-strontium ratio (with a slightly to high strontium concentration). Another possibility is the correction to all measured mass fractions applied by the evaluation program. Three effects are accounted for: 1.) Average order number Z - influences the surface reflectivity for the electron beam. Therefore a higher lanthanum content will also decrease the cobalt peak intensity. 2.) Absorption - peak intensity emitted from a specific element can be absorbed by the surrounding atoms, depending on their type and concentration. 3.) Fluorescence - especially for neighboring elements in the periodic table the radiation from the heavier element can excite the lighter element, increasing its emitted intensity. The parameters for the ZAF correction are taken from a database and could therefore be faulty if the wrong sample composition is assumed. Oxygen would be the main suspect to cause such an error. But with its low electron count it barely influences peak intensities of the other elements. Another possible source for systematic errors from the instrument is the calibration that is carried out in regular intervals. The influence was observed for a comparison between two sample groups measured on different days. While the three samples from the first group all exhibited a to large sum of the individual weight fractions of about 104%, in the second group the values were around 101%. This indicates the poor reliability of this measurement technique where systematic errors have a major influence on the results.

Name	Strontium content		Lanthanum content		Cobalt content	
	nominal	measured	nom	measured	nom	measured
ACK163	0		2.00	2.006(30)	1	0.994(11)
ACK354	0		2.00	2.014(10)	1	0.986(3)
YD071	0.25	0.242(1)	1.75	1.739(8)	1	1.019(9)
YD070	1/3	0.327(1)	1.67	1.656(4)	1	1.018(11)
ACK183	1/3	0.323(2)	1.67	1.668(6)	1	1.009(4)
ACK315	0.33	0.319(1)	1.67	1.675(7)	1	1.006(4)
ACK312	0.33	0.317(1)	1.66	1.668(8)	1	1.014(10)
ACK317	0.36	0.352(3)	1.64	1.637(11)	1	1.011(2)
ACK318	0.38	0.353(1)	1.62	1.646(4)	1	1.001(1)
ACK305	0.40	0.382(1)	1.60	1.618(7)	1	0.999(4)
ACK343	0.40	0.380(1)	1.60	1.615(3)	1	1.005(1)
ACK184	0.50	0.483(3)	1.50	1.508(8)	1	1.009(5)
ACK353	0.50	0.500(1)	1.50	1.500(6)	1	0.999(3)
ACK349	0.70	0.670(2)	1.30	1.313(6)	1	1.016(4)
ACK308	0.70	0.688(7)	1.30	1.297(7)	1	1.015(9)

Table 3.5: Cobaltate sample composition determined with WDX. Only metal ratios are evaluated and normalized to three, the nominal amount of metal atoms per formula unit.

Name	Lanthanum	Strontium	Cobalt	co-doping
ACK354	2.00		0.997(9)	
ACK163	2.00		1.001(15)	
ACK356	2.00		1.001(7)	
YD071	1.75	0.224(1)	0.999(5)	
YD070	1.67	0.320(1)	1.008(3)	
ACK315	1.67	0.325(3)	0.993(10)	
ACK312	1.67	0.313(3)	0.989(8)	
ACK445	1.67	0.339(2)	1.017(3)	
ACK317	1.64	0.354(1)	1.006(3)	
ACK318	1.62	0.351(1)	0.997(4)	
ACK305	1.60	0.408(2)	1.003(7)	
ACK343	1.60	0.350(1)	0.986(3)	
ACK184	1.50	0.483(3)	1.005(5)	
ACK353	1.50	0.484(3)	1.000(7)	
ACK349	1.30	0.656(6)	0.976(8)	
ACK308	1.30	0.657(5)	0.978(6)	
ACK370	1.20	0.407(2)	0.995(6)	Nd 0.382(2)
ACK342	1.64		0.966(16)	Ca 0.310(6)
ACK346	1.61		0.927(7)	Ca 0.255(3)
ACK344	1.64		0.979(5)	Ba 0.283(4)

Table 3.6: Cobaltate sample composition determined with ICP-OES. Values normalized according to the nominal Lanthanum content. Error bars result from the statistical treatment of three measurements.

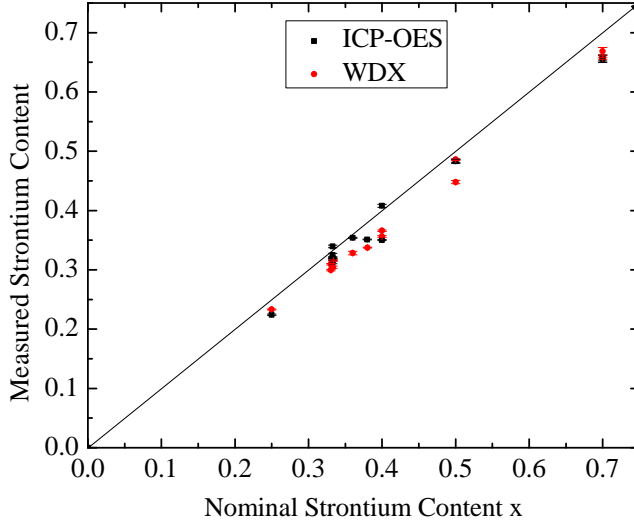


Figure 3.7: Doping dependent deviation of the strontium content in cobaltates. Comparison of the values obtained with ICP-OES and WDX methods. The black line corresponds to the nominal compositions. Error bars represent only the statistical deviations.

3.2.3 ICP-OES and CGHE

Similar to the WDX results, the oxygen content was found to be very high with $0.1 \leq \delta \leq 0.35$ in the cobaltate samples (discussed in the next Section 3.2.4). The strontium doping concentrations in Table 3.6 vary around the nominal values with deviations up to $\Delta x = 0.05$.

Figure 3.7 shows that the nominal stoichiometry of all samples could be confirmed by WDX and ICP-OES measurements. For an estimation of error bars that include systematic influences we can compare the determined sample compositions with those from WDX measurements. The sizable differences up to $\Delta x = 0.05$, observed for all elements, indicate the large influence of systematic errors. A resulting error bar of 5% of the measured value for both methods seems appropriate. Within this range most sample compositions match very well with their nominal values.

Single crystal X-ray diffraction measurements performed by A. Komarek confirmed the nominal stoichiometry with even higher precision than WDX and ICP-OES measurements [211]. Our considerations justify the further use of the nominal sample compositions.

3.2.4 Oxygen Content Determination

Oxygen intercalation can significantly change the physical properties of 214 perovskites. Some general trends and examples like the superconductivity in cuprates were discussed in Section 1.5. Determining the oxygen content is crucial for a correct interpretation of results acquired with different methods. The field of oxygen storage and conduction has taken some interest in the 214 cobaltates and nickelates. In literature, most publications concerning these compounds include some information on the oxygen content determination, but detailed insight on the procedure is missing.

We have analyzed samples within the whole doping range $0 \leq x \leq 1$ of $\text{La}_{2-x}\text{Sr}_x\text{CoO}_4$. One thing that became apparent during our studies is, that the samples do not decompose under ambient conditions at least in the range $1/3 \leq x \leq 0.9$. Nonetheless all samples were stored in a desiccator under active vacuum to be on the safe side.

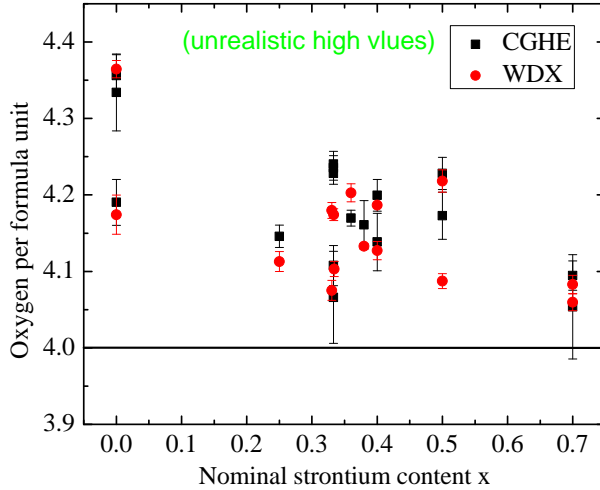


Figure 3.8: Strontium doping dependency of the oxygen content. Comparison of the values obtained with CGHE and WDX methods. The determined oxygen content is unrealistic high, thus, revealing systematic problems of the used methods.

The oxygen content of the cobaltate samples measured with CGHE and WDX are plotted in Figure 3.8 for comparison. Error bars result from statistic data treatment of multiple measurements. According to the discussion about the oxygen content in 214 perovskites (see Section 1.5), $\text{La}_2\text{CoO}_{4+\delta}$ grown by other groups exhibits an oxygen excess between $\delta \approx 0.15$ and $\delta \approx 0.26$ [102].

According to the obtained data, our measured cobaltate samples exhibit even larger oxygen excess and many of them even unrealistic values as high as $\delta \geq 0.30$. The large oxygen excess is even more questionable in the high strontium doping range $x \approx 0.7$ as it implies an average cobalt oxidation number towards Co^{+3} and Co^{+4} . Another peculiarity is the large spreading of the results even for samples with similar nominal composition grown under identical conditions. It is therefore more than doubtful that the oxygen content was determined correctly with the two applied methods.

It has been mentioned in Section 1.5 that cuprates and possibly nickelates [94] have been found to exhibit superoxide bonded oxygen content in surface sensitive measurements. The standard procedure for preparing a CGHE sample is to grind it to a fine powder before handing it over to the analysis team. For the WDX measurement a single crystal piece is polished under ambient conditions before it is introduced into the vacuum chamber for the measurement. Both methods are sensitive to surface oxygen excess.

In contrast to the results on the cobaltates, the oxygen content in the nickelate samples measured with WDX/EDX was found to be in rather good agreement with a stoichiometric oxygen content. The mentioned superoxide was found in cuprates and proposed in nickelates [94]. Surprisingly a comparison of our results for the nickelates with those for the cobaltates indicate a much more pronounced effect in the cobaltates. Since it could not be explained why CGHE and WDX completely fail in determining the oxygen content in cobaltates and why they even yield absolute unrealistic values, other methods had to be applied.

3.2.5 Thermogravimetric

The method applied in thermogravimetry (TG) follows a rather simple principle. A specimen is introduced into the device consisting of a high accuracy balance inside a chamber to control the atmosphere. Heater and thermometer grant a controlled temperature variation. A standard procedure then is to heat the sample and measure the change in weight as it partly evaporates. To determine the oxygen content with this method the popper gas flow is required. To help solving the question of the oxygen content in the cobaltates M. Schmidt and his team implemented the possibility to introduce a mixture of argon and hydrogen. For each sample a single crystals of around 80 mg was measured with TG by M. Schmidt and his team. The specimen were crushed to a rough powder just before it was weighted and introduced into the device. This step is generally necessary to speed up the reduction by an increasing the surface area. The results of measurements performed in a flow of Ar/H_2 with a ratio of 80/20 and a flow rate of 21/min are presented in Figure 3.9. The samples were heated at a rate of 10 K/min up to 1200°C where they remained for five hours, followed by a

controlled cooling with 10 K/min. The sample weight decreased mostly during the heating process and became stable soon after the temperature plateau was reached, indicating that the reduction of the cobalt component to cobalt metal was complete.

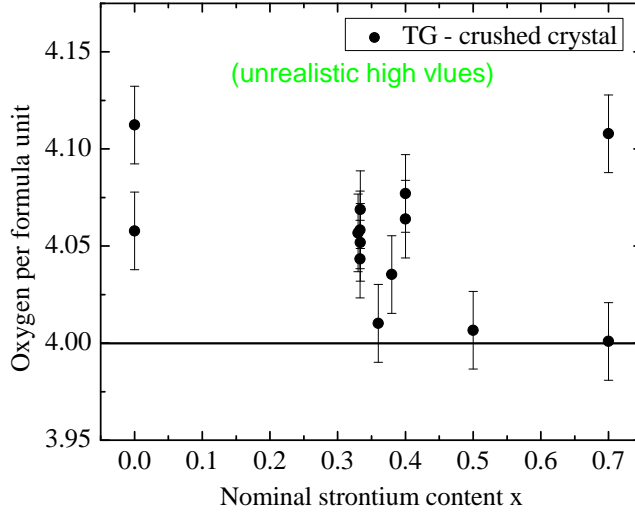


Figure 3.9: TG measurements on crushed single crystals. Error bars were calculated by Gaussian error propagation of the balance accuracy. The determined oxygen content is significantly improved compared to Figure 3.8 but still unrealistic high for many samples.

Besides all the already mentioned difficulties to determine the oxygen content there is the additional issue that we can not measure the excess oxygen only. Consequently the relative accuracy needed to decrease the error bar below $\Delta\delta \leq 0.01$ is 0.25% or better. The mass loss during the hydrogen reduction amounts to 4-5% of the total sample mass (around 4 mg). Although the TG instrument is equipped with a high precision balance, the obtained oxygen loss values deviated from those determined by hand. For calibration, an empty sample container is measured first. During the measurement the instrument calculates the difference curve between the current measurement and the reference. Surprisingly the results deviate by up to 10% from those obtained by weighting the sample container before and after the TG treatment on an external balance. It finally turned out that the discrepancy is caused by turbulences in the gas flow that influence the measured weight. Consequently only values determined by hand are used for the presented oxygen content evaluation. The accuracy of the balance is 0.01 mg and it was zeroed with the sample container including the

expectations for most samples. The sample ACK315 was intended as an oxygen doped sample, in good agreement with the TG measurements.

Finally, the problem of detecting far too high oxygen concentrations could be solved by a decrease of the measured sample surface to sample volume ratio. In principle the WDX measurement is capable of probing samples to a depth of the order of μm . Due to the low lying K-edge of oxygen the emitted X-ray fluorescence has a low energy and consequently a small penetration depth. Therefore, oxygen atoms that are far from the surface do not contribute to the measured intensity. On the other hand, an increased oxygen concentration close to the surface will contribute disproportionate. Also in the CGHE method the large sample surface was involved. Here the powder samples had an unfavorable volume to surface ratio because the crystals had been crushed to a fine powder.

Compared to the fine powder that was used for CGHE, our initial TG measurements on crushed crystals had a better volume to surface ratio because the crystal was only crushed but not ground to a fine powder. Additionally the time that the crushed sample was exposed to ambient conditions was kept as short as possible. The further decreased oxygen content that was observed in TG measurements on bulk crystals indicates that already a short air exposure in the order of minutes is sufficient to contaminate the sample surface with oxygen.

Such effects are also known for other materials. Resonant X-ray reflectivity was used to characterize the surface-vacuum interface of SrTiO_3 and PrNiO_3 [212]. An oxygen rich light element coating in the order of nm was observed on the sample surface. C. F. Chang et al. [213] reported in a resonant soft x-ray diffraction study on Fe_3O_4 that measurements on a sample that was polished under ambient conditions were obscured by a “dead” layer in the order of $1/4\ \mu\text{m}$. This dead layer was found to absorb X-ray intensity without contributing to the scattered signal. Samples cleaved in situ did not show this peculiarity. They concluded that the dead layer might consist of polycrystalline sample material or of a material with a different chemical composition. On the background of such studies it seems likely that surface contamination is responsible for the observed oxygen excess in measurements where the surface plays a great role. Systematic studies are necessary to determine the real surface contamination. A very rough sample surface or cracks in the crystalline structure are two ways to explain the large excess oxygen. Remarkable is the fact that the high doped cobaltates suffer much less from this effect while it was not observed for the isostructural nickelates and iron oxides. Since the encountered difficulties in oxygen determination were, to our knowledge, not yet reported in literature our findings cast serious doubt on the reported oxygen contents determined on cobaltate powder samples in literature.

Our final TG measurements on bulk crystals proved that the oxygen content of all strontium cobaltates is stoichiometric with only minor deviations (see Appendix Tabular 6.3). The only remaining discrepancies could be observed for

La_2CoO_4 that is probably most sensitive to oxygen. S. Subakti applied a titration method where Co^{3+} ions are reduced by a known amount of Fe^{2+} [214]. The remaining iron(II) can then be determined by a potentiometric titration with potassium dichromate (see next Section). S. Sarapulova used iodometric titration to determine the Co^{3+} content directly [215]. The specimens have been crushed under argon atmosphere to avoid oxygen contamination and the titration was performed under flowing argon. Details on the titration procedure and the formula used to calculate the oxygen content can be found in [216]. In addition, X-ray absorption spectroscopy (XAS) measurements have been performed on the undoped parent compound by Z. Hu. This method can be used to determine the energy that is necessary to excite a core electron (here 2p) to an unoccupied state (here 3d). For a sample with mixed valency (here Co^{3+} and Co^{2+}) two peaks appear in the XAS measurement, one for each oxidation state. In the XAS measurement performed on a specimen without strontium doping ($x = 0$) showed no peak intensity at the energy corresponding to the excitation in Co^{3+} [217]. Therefore we can exclude any oxygen excess with a good accuracy of $\Delta\delta = 0.01$. The result is in agreement with titration measurements that reveal a vanishing small Co^{3+} contribution of the order of 1% [214]. This is remarkable because all La_2CoO_4 samples reported in literature were reported to be grown with oxygen excess only. In the final Figure 3.10 the results obtained with different methods are presented together.

3.3 $\text{La}_{1-x}\text{Sr}_{1+x}\text{FeO}_4$

3.3.1 Powder X-ray Diffraction

The doping dependency of the lattice constants in the iron oxides is similar to that discussed for the nickelates. This is not surprising since the electron configuration in the (x^2-y^2) and ($3z^2-r^2$) orbitals which are most sensitive to a tetrahedral distortion is the same in both cases. The refined lattice constants can be found in Figure 3.3.1 and in Table 3.7. The black line is a linear fit to the black data points. Deviation from the linear behavior is small except for the samples ACK224 and YD068, which reflects the difficulties encountered during the growth of samples with higher strontium doping (see Section 2.1.2). Few reference data is available for the $\text{La}_{1-x}\text{Sr}_{1+x}\text{FeO}_4$ system and we were probably investigating the first single crystals ever made in this doping region. The doping dependence of the lattice constants is similar to that found in the nickelates. A comparison with the effects of oxygen off stoichiometry in the cobaltates and nickelates suggests that the sample ACK224 is oxygen deficient while YD068 is oxygen rich. The truth has been uncovered with titration measurements on the iron oxides in Section 3.3.2. We found that all samples are oxygen deficient and almost no Fe^{4+} is present except in YD068, which was

grown with 12 MPa oxygen pressure in our new high pressure image furnace (HKZ). In our iron oxides the driving factor for the observed lattice constants is the increasing oxygen deficiency with strontium doping. Undoped LaSrFeO_4 seems to be especially stable due to the pure Fe^{+3} content. The refined lattice constants fall well on top of each other for all synthesized single crystals. For this reason this compound has been chosen as a standard material in WDX measurements.

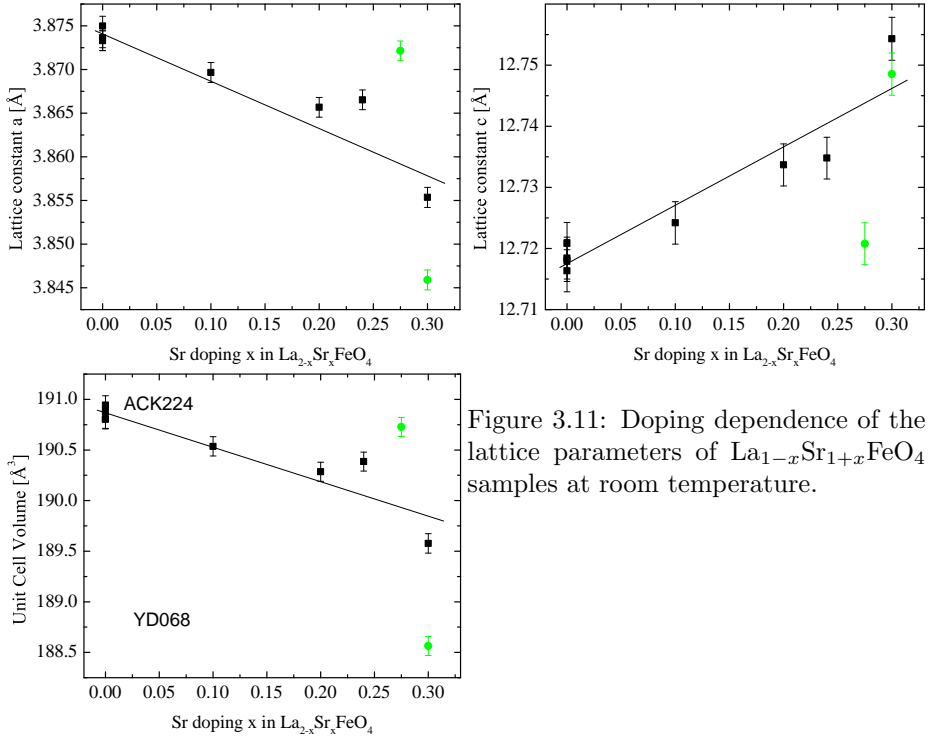


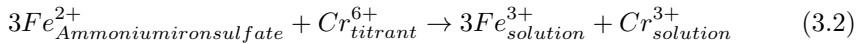
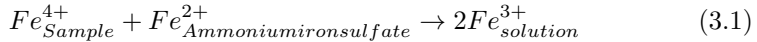
Figure 3.11: Doping dependence of the lattice parameters of $\text{La}_{1-x}\text{Sr}_{1+x}\text{FeO}_4$ samples at room temperature.

Name	Sr-doping	a [Å]	c [Å]	V [Å ³]	R _F , R _B
YD001	1.3	3.8553(12)	12.754(5)	189.57(11)	6.9, 11
YD002	1.2	3.8656(12)	12.733(4)	190.28(9)	7.6, 9.5
YD027	1	3.8749(12)	12.716(4)	190.94(10)	8.6, 11
YD062	1	3.8733(12)	12.718(4)	190.80(10)	6.9, 8.3
YD064	1	3.8733(12)	12.718(4)	190.80(10)	7.0, 8.2
YD065	1	3.8736(12)	12.720(4)	190.87(10)	7.9, 9.8
YD068	1.3	3.8459(12)	12.748(4)	188.56(10)	6.6, 9.4
ACK195	1.1	3.8696(12)	12.724(4)	190.53(11)	8.1, 10
ACK224	1.275	3.8749(12)	12.729(4)	190.72(10)	8.6, 8.6
ACK276	1.24	3.8665(12)	12.734(4)	190.38(10)	6.9, 6.9

Table 3.7: Nominal sample composition, lattice parameter and reliability factors of $\text{La}_{2-x}\text{Sr}_x\text{FeO}_4$ determined by powder XRD.

3.3.2 Titration of $\text{La}_{2-x}\text{Sr}_x\text{FeO}_4$

Samples of 214 iron oxide have been grown with the traveling floating zone technique with strontium concentrations $1 \leq x \leq 1.3$. It was found that the growth process became more difficult the higher the strontium content. Despite numerous attempts to grow crystals with higher strontium concentration no success was granted. Increasing the oxygen partial pressure from ambient conditions at a doping $x = 1$ to 9 bar at higher strontium concentrations could not stabilize the growth process for high strontium concentrations. It seems that a very high oxygen pressure would be necessary to stabilize the high oxidation state Fe^{4+} . To quantify the amount of Fe^{4+} ions in our samples the titration method was chosen because of its simplicity combined with a high accuracy. The sample was ground and weighed before it was mixed with a known amount of ammonium iron(II) sulfate. Then the powders were dissolved in 40 ml desalted H_2O and 10 ml concentrated HCl . As titrant we used a 0.0125 molar potassium dichromate standard solution. The chemical reactions are as follows:



The iron(IV) ions react with the solved iron(II) ions to iron(III) (equation 3.1). The next step is to titrate the remaining amount of iron(II) in the solution by adding strongly oxidizing Cr(VI) ions until all iron(II) ions are oxidized to iron(III). A platinum electrode in the solution and another in a standard solution were linked with a volt meter to continuously monitor the electromotive force

during the titration. The electromotive force of the solution is sensitive to the ion concentrations and exhibits a jump at the equivalence point where the iron(II) concentration suddenly changes by several orders of magnitude.

$$n(Fe_{Sample}^{4+}) \stackrel{\text{eq. point}}{=} n((NH_4)_2Fe(SO_4)_2 \cdot 6H_2O) - 6n(K_2Cr_2O_7) \quad (3.3)$$

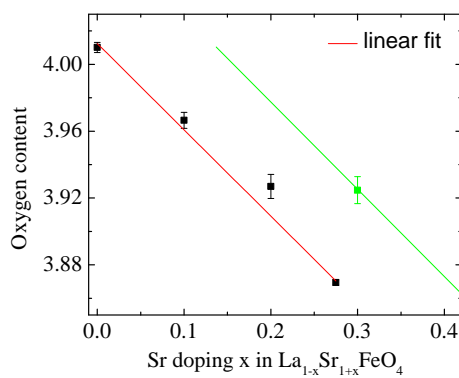
$$O_y = 4 - \frac{x-1}{2} + \frac{n(Fe_{Sample}^{4+}) \cdot M(La_{2-x}Sr_xFeO_4)}{2m(La_{2-x}Sr_xFeO_4)} \quad (3.4)$$

Formula 3.3 was used to calculate the iron(IV) content $n(Fe^{4+})$ in [mol]. The oxidation numbers of lanthanum(III) and strontium(II) are extremely stable. Upon doping strontium for lanthanum the iron atoms have to provide more and more electrons to maintain stoichiometry. The deviation between the calculated and measured Fe^{4+} concentration can only be identified with oxygen vacancies. These were calculated using equation 3.4 where O_y is the oxygen content per formula unit. Results for all measured samples are given in Tabular 3.8 and the doping dependence of the oxygen content is plotted in Figure 3.12. The data shown is the average of five titrations and the error bars represent the statistical deviation.

Apparently the oxygen pressure up to 9 bar, that was used during growth process for samples with strontium content up to $x = 1.275$, was insufficient to stabilize the Fe^{4+} ion in this compound. Consequently the amount of highly oxidized iron is nearly zero in these samples and the oxygen per unit cell shows a linear decrease with doping (Figure 3.12). The observed change in lattice constants in powder X-ray measurements is therefore probably mostly due to the increasing oxygen deficiency (see 3.3). When the oxygen content decreases to the value of approximately $y = 3.85$ the crystal structure is no longer stable and single crystals can not be grown. An attempt to create a sample with higher Fe^{4+} concentration was conducted using our high pressure mirror furnace with an oxygen pressure of 120 bar. We successfully grew a small single crystal with a Fe^{4+} concentration of 14.9(17) % which is significantly higher than for all the other samples but still only half of what would be expected for the stoichiometric compound. This leads to the conclusion that much higher oxygen pressures would be necessary to grow samples with higher strontium doping. Linear extrapolation from the existing data suggests that it should be possible to grow an oxygen deficient crystal with the high pressure mirror furnace for strontium doping up to $x = 0.4$.

Name	Sr-doping x	oxygen content y	Fe ⁴⁺ content [%]
YD027	1	4,010(4)	2,0(7)
ACK195	1.1	3,967(5)	3,3(1)
YD002	1.2	3,927(8)	5,4(15)
ACK224	1.275	3,869(2)	1,4(4)
YD068	1.3	3,925(9)	14,9(17)

Table 3.8: Ferrate oxygen content

Figure 3.12: Oxygen off-stoichiometry in $La_{2-x}Sr_xFeO_y$ upon strontium doping.

Chapter 4

$\text{La}_{2-x}\text{Sr}_x\text{NiO}_4$

Two decades after the initial discovery of incommensurate magnetic ordering in strontium doped [161] and oxygen deficient [218] nickelates their properties have been mapped over a wide hole-doping range. The proposed charge modulations [162] have been claimed to be a quite common ordering phenomenon in layered transition metal oxides and may rather be considered as the rule [67] than an exception. The term “stripe phase”, nowadays commonly used for this type of ordering, was first introduced by Tranquada et al. [219] when they found static spin and charge correlations in $\text{La}_{1.46}\text{Nd}_{0.4}\text{Sr}_{0.12}\text{CuO}_4$. The following debate about the interplay of superconductivity and stripe order is one reason for the extensive study of the nickelates. Among the strontium doped nickelates, a major focus was placed on research of the compounds exhibiting stable stripe ordering (around $x = 1/3$) as well as the undoped parent compound. The intermediate doping regime is much less studied. In the phase diagram presented in Section 1.4 it becomes apparent that no data was available for the doping region $0.15 \leq x \leq 0.2$. The doping concentration at which the nearest neighbor antiferromagnetic order is first completely suppressed remains unknown. Similarly it is an open question whether there exists a doping region where it can coexist with stripe order. At a strontium doping of about $x = 0.2$ the authors of the phase diagram [67] claim the coexistence of charge and magnetic stripe order with the orthorhombic and LTT distortions of the undoped parent compound. Whether this results from phase separation is unclear while a microscopic picture for a coexistence of phases is missing.

The observation of an hourglass shape [49, 49] magnon dispersion in the superconducting cuprates raises the question whether the dispersion in nickelates can be tuned to such a shape. The idea was first proposed by Batista et al. [179] who argued that the magnon dispersion of a stripe phase could explain the resonance mode observed in high T_c cuprates. The parent com-

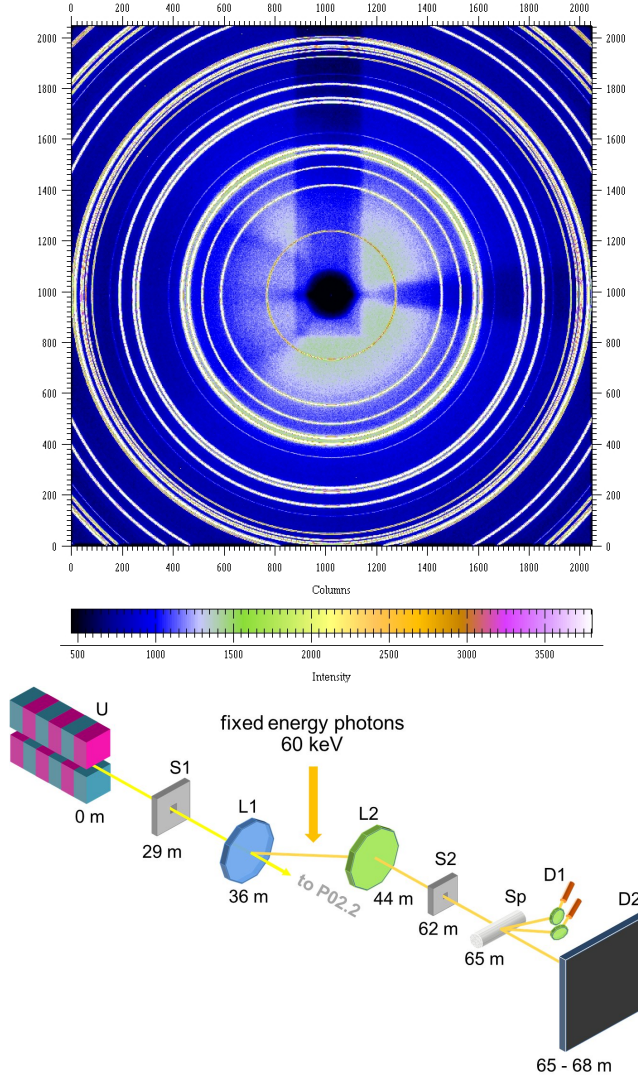


Figure 4.1: *Top*: Raw 2-d diffractogram of ACK269 recorded at room temperature with an area detector PerkinElmer XRD1621 (amorphous Si sensor with CsI scintillator). The shadow from top to center is due to the beam stop that protects the detector from damage by the intense direct beam.

Bottom: Schematic of the HRPD P02.1 optical train. U - undulator U23, L1,L2 - Laue monochromator crystals (C(111) and Si(111)), S1,S2 - slit systems, Sp - sample (e.g. powder in capillary), D1,D2 - detectors (multi-analyzer or flat panel) [220]

pound La_2NiO_4 exhibits a very steep magnon dispersion with a spin wave velocity $\hbar c_s = 320(10) \text{ meV\AA}$ [177]. Studies on the strontium doped nickelate $\text{La}_{1.69}\text{Sr}_{0.31}\text{NiO}_4$ revealed a similar value for the spin excitation spectrum in the stripe phase, $\hbar c_s = 300(20) \text{ meV\AA}$ [221]. Both dispersions can be well described by the simple expression $\omega(\vec{Q}) = \omega_0 |\sin(3\pi H)|$ along the (HH0) direction [221].

An optimally strontium doped $x = 0.33$ sample exhibits a magnon dispersion similarly steep as in the undoped parent compound [222]. Also for $\text{La}_{1.825}\text{Sr}_{0.175}\text{NiO}_{4+\delta}$ a similar spin wave velocity was reported [223]. In contrast, a by 40% decreased spin wave velocity was reported for a stripe phase in a strontium free but oxygen rich sample with an excess oxygen of $\delta = 0.133$ [167].

4.1 Temperature Dependence of the Lattice Parameter in Low Doped Nickelates

Located at the synchrotron facility DESY in Hamburg, Germany in the instrument building for the new storage ring PETRA III is the High Resolution Powder Diffraction Beamline P02.1 (HRPD P02.1). The key features of the 2.3 km long storage ring are its world leading brilliance and the top-up operation mode which allows a steady positron current through frequent injections and therefore a constant X-ray intensity.

The multi purpose beamline HRPD P02.1 operates at a high fixed energy of 60 keV ($\lambda = 0.207 \text{ \AA}$). As the attenuation factor decreases exponentially with photon energy, this enables the measurement of thick and/or absorbing samples in transmission geometry. For our measurements a nitrogen cooled cryostream was used to reach temperatures down to 80 K. Samples taken from our floating zone grown single crystals were crushed and ground before filling borosilicate capillaries of 0.4 mm diameter. Together with a sample spinner for the cryostream setup and the two dimensional detector this helps to avoid the measurement of false Bragg intensities due to large crystallites in reflection position. Collimation was used to decrease the beam size to 1 mm times 1 mm and calibration measurements ensured a constant intensity over the whole cross section. For a reliable data evaluation at least 15 Bragg reflections should be captured in the diffractogram. Additionally it is useful to measure peaks at high 2Θ -values when expecting structural phase transitions as the peak splitting is more pronounced at higher angles. A compromise between resolution and covered angular range is necessary. To access the (1 11 3) reflection with the 40 cm times 40 cm detector at an energy of 60 keV the sample-detector distance was chosen to be 154 cm. Binning of the three dimensional data images to two dimensional diffractograms was done with the program Fit2d provided by the ESRF [224].

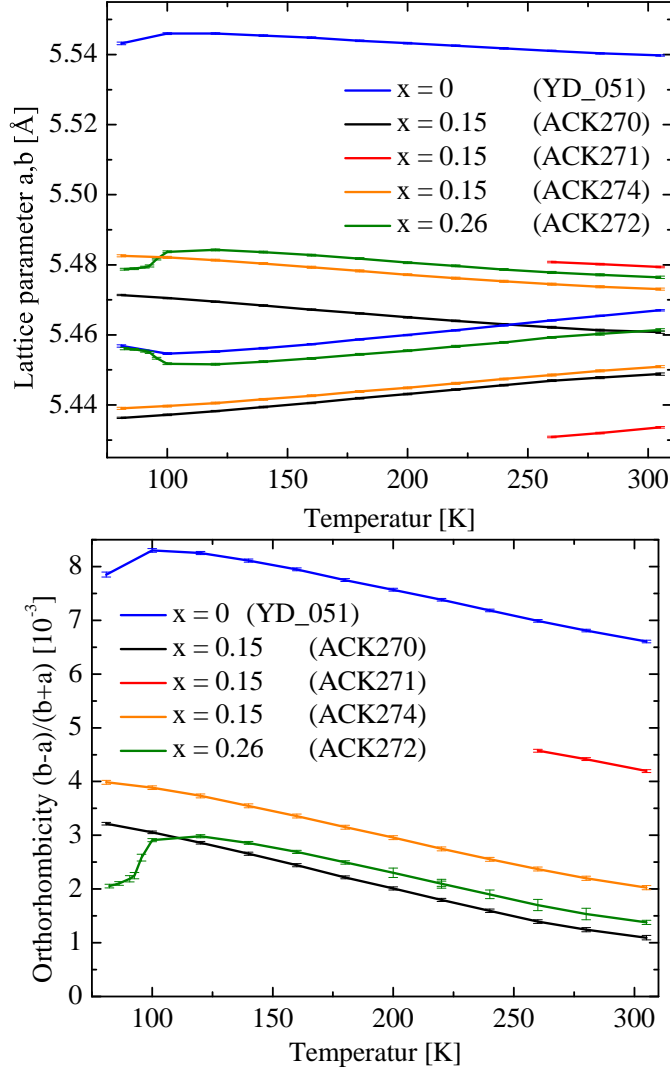


Figure 4.2: *Top*: Temperature dependence of the orthorhombic a-b-lattice parameters, *Bottom*: Temperature dependence of the order parameter for the tetragonal to orthorhombic phase transition.

In preparation for further studies we measured the lattice constants of our strontium doped nickelate samples as a function of temperature. The strontium doping concentration has been chosen to cover the whole range between the ambient temperature orthorhombic compound ACK270, which might still show

antiferromagnetic order, and the regime where the tetragonal to orthorhombic phase transition is completely suppressed down to low temperatures. Similar to the procedure described in Section 2.2 the obtained diffractograms were fitted with the Rietveld refinement method. Error bars obtained from the refinement are included in the graphs. The higher resolution of this measurement compared to our in house instrumentation allowed the observation of an orthorhombic peak splitting for characteristic reflections.

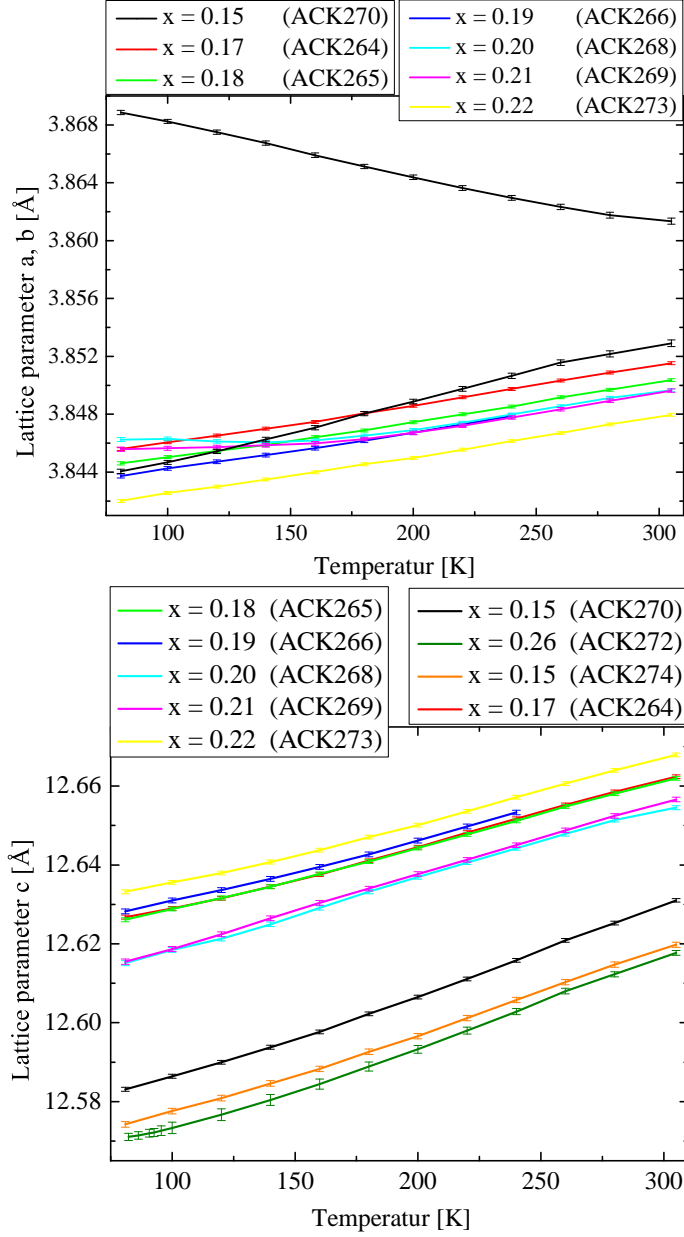


Figure 4.3: *Top*: Temperature dependence of the tetragonal a-lattice parameter, *Bottom*: Temperature dependence of the tetragonal c-lattice parameter.

The structural phase transition in the undoped parent compound is expected above room temperature and consequently the a and b lattice constants of YD051 exhibit the largest splitting at ambient temperature (see Figure 4.2). Below 100 K a second structural transition to a low temperature tetragonal phase, apparent in the deviation from the monotone development of the lattice constants, appears (see Section 1.4). The $x = 0.15$ strontium doped sample has also been fitted with an orthorhombic model. A common problem when applying a model with a lower symmetry than necessary is that the deviation between measured and calculated pattern can still be decreased due to the increased number of refinement parameters. Without data at higher temperature it is therefore not possible to determine the transition temperature accurately. Upon cooling the deviation of the a - b lattice parameters increases very subtle. This is also visible in the orthorhombicity $O = (a-b)/(a+b)$, which is the order parameter of the tetragonal to orthorhombic phase transition. The subtle onset is in agreement with a phase transition of second order. Similar to the parent compound, the measured co-doped samples all adopt the orthorhombic structure already at room temperature. The low temperature phase transition of ACK272 has been measured in more detail. As can be seen from the order parameter the structure changes abruptly at around 100 K. In Section 1.4 it has been discussed that this transition might be of first order, in accordance with a sudden change in lattice parameters observed here.

In Figure 4.3 the temperature dependence of the lattice parameters a and c between 80 K and 305 K is presented. A silicon standard measurement has been used to determine the wavelength and the sample-detector distance. To avoid the overlap of reflections that are characteristic for a structural phase transition only the pure samples have been measured. A comparison of the more accurate lattice constants at ambient temperature can be found in the sample characterization Section 3.1.1. Thermal expansion is rather small in the nickelates in the measured temperature range. Between 305 K and 80 K the c -parameter only shrinks about 0.38% and the a -parameter about 0.13%. Surprising is the deviation from the monotone decrease in the samples with doping $x = 0.2$ and $x = 0.21$ at low temperature. A fit with an orthorhombic lattice did not yield significant better R values. Probably the orthorhombic distortion is too small in these samples. As an alternative to the orthorhombicity a temperature dependent comparison of the full width at half maximum (FWHM) of a reflection that splits upon an orthorhombic distortion can be discussed. High indexed peaks show larger splitting but are superimposed with other reflections in these samples. In Figure 4.4 the splitting of the $(211)_{Tetragonal}$ into the $(311)/(131)_{Orthorhombic}$ peaks is compared. Plotted is the FWHM ratio $(211)/(200)$, normalized to the ambient temperature value. The increased values for ACK268 and ACK269 are indicative for an orthorhombic distortion at low temperature in these samples. Another peculiarity can be observed for ACK272. The transition to the low

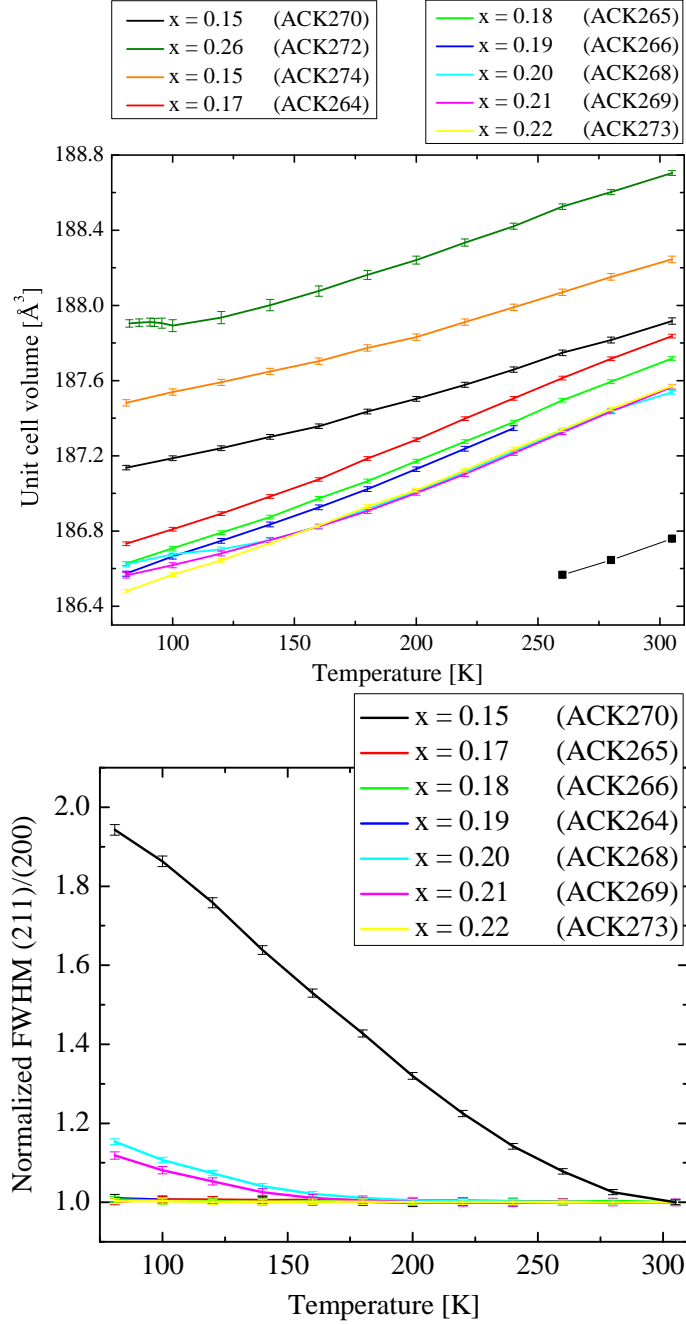


Figure 4.4: *Top*: Temperature dependence of the unit cell volume, *Bottom*: Comparison of temperature dependence of the (211)-FWHM.

temperature phase seems to prevent a further shrinkage of the unit cell volume in this sample.

4.2 Incommensurate Magnetic Order

Magnon dispersions have been measured for the magnetically ordered parent compound and also for the stripe phases found in strontium doped and oxygen excess samples. While the doping of strontium seems to have only minor effect on the spin wave velocity a value decreased by a factor of 5 has been found in a $\text{La}_2\text{NiO}_{4+\delta}$ with $\delta = 0.105$ sample which is still in the antiferromagnetic regime [167]. At a higher oxygen excess of $\delta = 0.133$ the sample already exhibits the stripe phase at low temperature and the value for the spin wave velocity recovers to about half the size found in the undoped compound. The overall shape of the spin wave excitations which have the expected appearance of two branches dispersing away from the magnetic wave vector does not change for the two mentioned hole doping mechanisms. In order to study the effect of different types of doping on the magnetic excitations several large single crystals have been grown by the floating zone method. We used the triple axis spectrometer IN3 to search for incommensurate magnetism in our samples. Collimation before and after the sample was chosen to be $60' - 60'$. The instrument is equipped with a pyrolytic graphite (PG) monochromator and analyzer ((002)-reflection) and in principle capable of performing inelastic measurements. Due to the low flux the counting times involved are very long and this feature is therefore rarely used. Elastic scans have been performed with $k_i = k_f = 2.662 \text{ \AA}^{-1}$ corresponding to a neutron energy of about 14.7 meV. The instrumental resolution was derived from a Gaussian fit to the peak width of a (1 1 0) Bragg reflection to be 0.0074(10) r.l.u.. Results for some co-doped nickelate samples can be found in Figure 4.5.

Out of the two possible diagonal scan directions we chose the one from (0 1 0) to (1 0 0). This avoids the direct beam and the strong structural Bragg reflection at (1 1 0) which is too intense to be measured directly as the detector starts to saturate around 10000 counts/sek. For the sample alignment an attenuator is used, which decreases beam intensity by a factor of seven. Clearly visible in our scans (Figure 4.5) are the sharp peaks at the half indexed position (0.5 0.5 0) which are due to $\lambda/2$ scattering from the fundamental (1 1 0) Bragg reflection. Their width is limited by the low point density. Error bars in all counting statistics are the square root of the absolute counts and have been omitted for clarity. Three Voigt functions have been fitted to the data with a fixed FWHM of the Gaussian contribution according to instrumental resolution. The results for the peak positions are included in the graphs.

With the observation of hourglass shaped dispersions in the cuprates and recently also in a cobaltate [181] there naturally raises the question whether

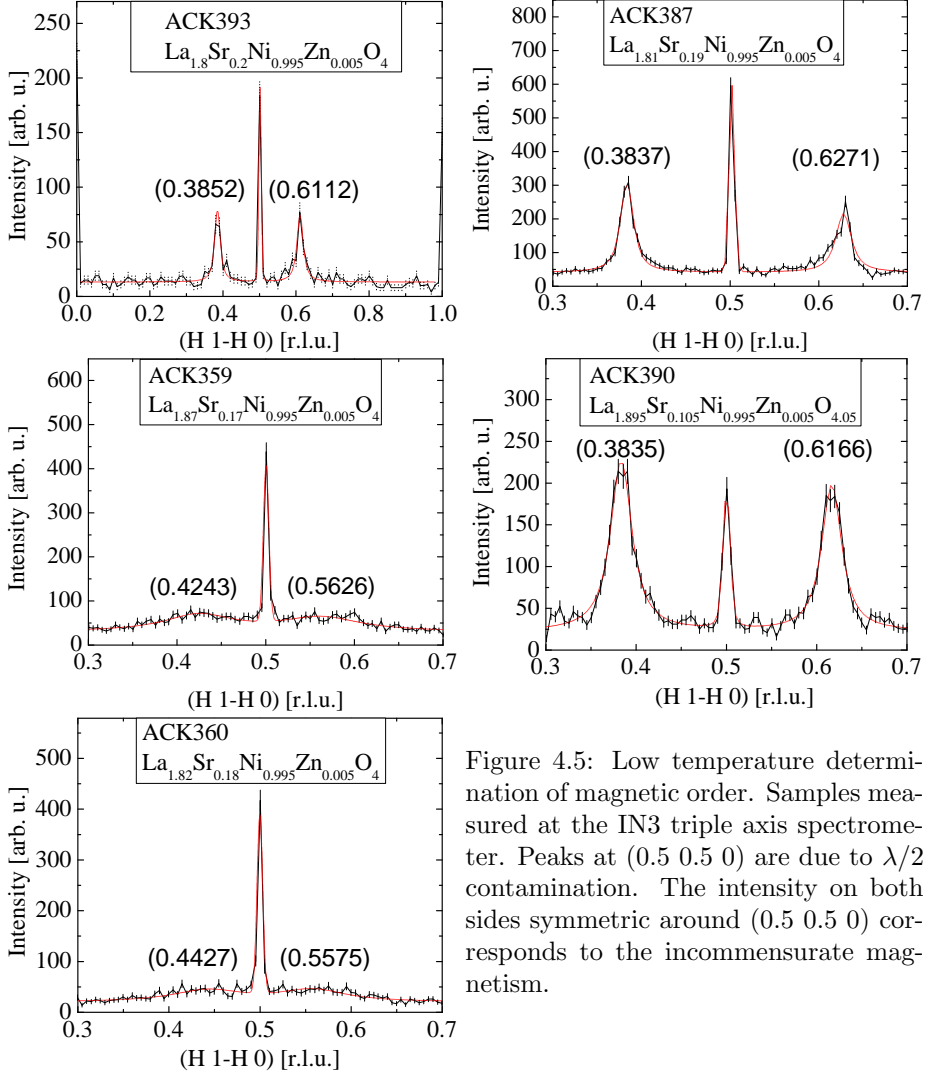


Figure 4.5: Low temperature determination of magnetic order. Samples measured at the IN3 triple axis spectrometer. Peaks at $(0.5 \ 0.5 \ 0)$ are due to $\lambda/2$ contamination. The intensity on both sides symmetric around $(0.5 \ 0.5 \ 0)$ corresponds to the incommensurate magnetism.

dispersions in nickelates can also be tuned to such a shape. Most convenient would be a sample in which the merging of the spin wave branches appears at intermediate energies up to 30 meV, at which it could easily be measured with a standard TAS setup at a reactor based neutron source. The co-doping in our samples might significantly increase the disorder as has been found in the two previous studies on samples in the intermediate strontium doping range [161, 225], causing a general peak broadening of elastic and inelastic magnetic peaks.

The low doped $\text{La}_{2-x}\text{Sr}_x\text{Ni}_{1-y}\text{Zn}_y\text{O}_{4+\delta}$ samples ACK359 and ACK360 with strontium contents $x = 0.17$ and $x = 0.18$, receptively, and a very small zinc co-doping, show a very broad peak at incommensurate positions. This is indicative for a strong disorder in the magnetic phase. The incommensurability in these samples is very small, $\epsilon = 0.138(7)$ and $\epsilon = 0.115(13)$, respectively. Together with the steep dispersion found in other nickelates this could result in a merging at very low energy. But with the pronounced disorder it is questionable whether it can be resolved and measured in a reasonable time. Upon increasing strontium doping the peaks suddenly sharpen at $x = 0.19$ (ACK387) and $x = 0.2$ (ACK393) but at the same time also the incommensurability drastically increases to $\epsilon = 0.243(11)$ and $\epsilon = 0.226(4)$, respectively. A similar result has been obtained for ACK390 which has a combined doping of strontium $x = 0.105$, oxygen $\delta \approx 0.05$ and zinc and exhibits an incommensurability of $\epsilon = 0.2331(1)$.

The large difference in magnetic order between the two groups of samples rises the question whether it is possible at all to obtain a sample with small incommensurability and well ordered magnetism. Apart from the two mentioned publications around twenty years ago [161, 225] on samples $\text{La}_{1.8}\text{Sr}_{0.2}\text{NiO}_{3.96}$ and $\text{La}_{1.865}\text{Sr}_{0.135}\text{NiO}_4$ with incommensurabilities $\epsilon \approx 0.16$ and $\epsilon \approx 0.12$, respectively, there are no reports of samples with $\epsilon \leq 0.25$. In fact, for $\text{La}_{1.8}\text{Sr}_{0.2}\text{NiO}_{3.96}$ the magnetic intensities had a very low peak to background ratio and the broadness is comparable to that in our samples with similar incommensurability. In the measurement on $\text{La}_{1.865}\text{Sr}_{0.135}\text{NiO}_4$ the measured magnetic intensity had in fact the shape of a single peak and the proposed incommensurability was derived from a scan that integrated over elastic as well as inelastic signal, yielding a broad feature that was interpreted as two peaks [161]. Two more recent X-ray studies on samples with strontium doping down to $x = 0.2$ found only incommensurabilities above $\epsilon = 0.25$ [169, 226]. It was argued that the weaker and broader magnetic peaks found in the $x = 0.2$ and $x = 0.25$ doped samples compared to the ideally doped $x = 0.33$ sample are due to the formation of a charge stripe glass phase in the lower doped compounds [226].

In preparation of an inelastic neutron measurement at the IN22 (ILL) we determined the magnetism of further samples at low temperature. Scans can be found in Figure 4.6. Using a setup with two PG filters we made sure that

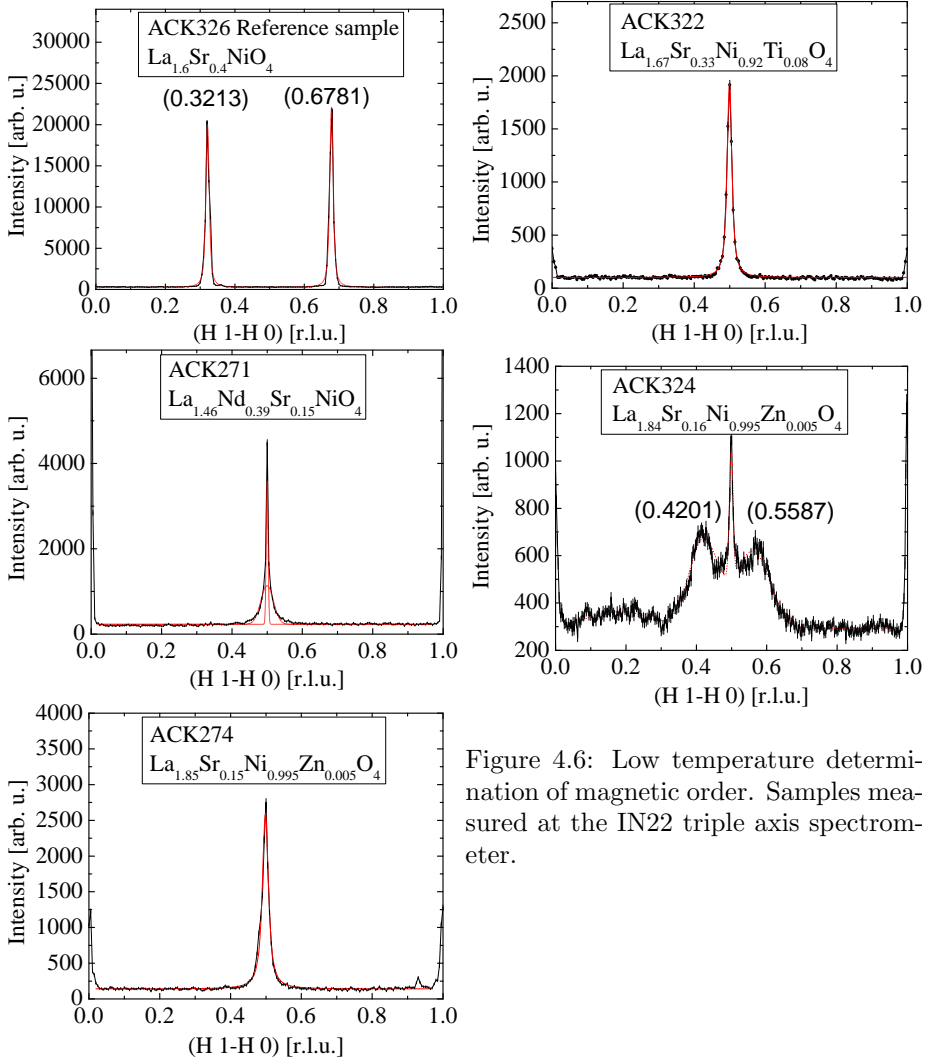


Figure 4.6: Low temperature determination of magnetic order. Samples measured at the IN22 triple axis spectrometer.

no $\lambda/2$ contamination is present in the elastic scans. For our beamtime we used the vertically focusing PG monochromator and an PG analyzer with a fixed vertical focus and adjustable horizontal focus. Elastic scans have been performed with horizontally flat analyzer. Compared to the IN3 where a factor seven attenuator is sufficient to decrease a strong fundamental reflection below an intensity where its detector starts to saturate at 10000 counts/sec, at the IN22 a factor 35 attenuation is not sufficient to orient a large crystal, although its detector has a linear characteristic up to 30000 counts/sec.

Apparently the co-doping with neodymium in $\text{La}_{1.46}\text{Nd}_{0.39}\text{Sr}_{0.15}\text{NiO}_4$ did not lead to an incommensurate magnetic structure in the low strontium doped sample ACK271. Instead it proofed impossible to arrive at a good agreement when fitting the central peak with a single Gaussian or Voigt function. In the orthorhombic phase the positions (1 0 0), (0 1 0) and (0.5 0.5 0) are allowed for superstructure reflections associated with an octahedral tilting. A fit of two superimposed Gaussian functions is well suited to account for the broader magnetic contribution below the sharp and possibly structural intensity and is plotted above the measured data.

The doping of 8% titanium in $\text{La}_{1.67}\text{Sr}_{0.33}\text{Ni}_{0.92}\text{Ti}_{0.08}\text{O}_4$ (ACK322) was sufficient to completely suppress the stripe order which is most stable in the pure strontium $x = 0.33$ doped compound with a transition temperature $T_N \approx 250$ K. Similar to ACK274 the sample exhibits structural reflections at (1 0 0) and (0 1 0) and a broader magnetic contribution at (0.5 0.5 0). Measurement of the samples ACK320 and ACK272 will clarify whether a titanium doping of $y = 0.05$ is low enough to not completely suppress the incommensurate magnetism or if samples with even lower titanium content need to be prepared.

Sample ACK274 is another specimen of the zinc co-doped series measured at the IN3 with the composition $\text{La}_{1.85}\text{Sr}_{0.15}\text{Ni}_{1-y}\text{Zn}_y\text{O}_4$. In contrast to the above mentioned samples with slightly higher strontium doping this sample is still in the antiferromagnetic regime with no incommensurate magnetism present. In the low temperature powder X-ray measurements on the pure strontium doped samples in Section 4.1 we found that the $x = 0.15$ doped sample also showed the tetragonal to orthorhombic phase transition while it was missing in the $x = 0.17$ sample. In this measurement we did not explicitly look for the structural phase transition but at the end points of the scan in Figure 4.6 an orthorhombic peak intensity is observable. The peak at (0.5 0.5 0) is significantly broader than the pure structure reflections. Considering the sample ACK324 with slightly higher strontium content, this sample composition marks the phase boundary of the commensurate antiferromagnetism.

Finally our sample ACK324 with the nominal composition $\text{La}_{1.84}\text{Sr}_{0.16}\text{Ni}_{0.995}\text{Zn}_{0.005}\text{O}_4$ provided some unexpected results. Instead of disappearing together with the commensurate magnetism, an orthorhombic structure coexists with incommensurate magnetism in this sample. The magnetic modulation with the

Name	Strontium	co-doping	ϵ	FWHM [r.l.u.]	ξ [Å]
ACK274	0.15	Zn 0.005	0	0.0170(14)	102(9)
ACK322	0.33	Ti 0.08	0	0.0127(4)	137(5)
ACK360	0.18	Zn 0.005	0.115(13)	0.151(31)	12(3)
ACK359	0.17	Zn 0.005	0.138(7)	0.136(19)	13(2)
ACK324	0.16	Zn 0.005	0.139(11)	0.081(4)	21(1)
ACK393	0.20	Zn 0.005	0.226(4)	0.017(2)	102(12)
ACK390	0.105	Zn 0.005	0.2331(1)	0.025(2)	69(6)
ACK387	0.19	Zn 0.005	0.243(11)	0.015(2)	116(16)
ACK326	0.40	-	0.3568(3)	0.0073(3)	238(10)

Table 4.1: Modulation ϵ and peak width of the magnetic intensities.

value $\epsilon = 0.139(11)$ is favorable for a determination of the magnon dispersion while the magnetic peaks are quite well developed. In Table 4.1 the values for ϵ and FWHM are listed for all measured samples (except ACK271). The FWHM values belong to the Lorentzian part of the Voigt functions that were fitted to all evaluated peaks. The Gaussian FWHM was fixed to the instrumental resolution which was $0.0072(2)$ r.l.u. in the IN22 measurement for $k_i = k_f = 2.662 \text{ \AA}^{-1}$. Indeed, of the three samples with small incommensurability the sample ACK324 exhibits much sharper magnetic peaks. The correlation length in scan direction (H 1-H 0) which corresponds to a scan perpendicular to the stripes, or along the stripe modulation, has been calculated with the formula:

$$\xi = \frac{d}{\pi\omega} \quad (4.1)$$

where ω is the full width at half maximum of the reflection in reciprocal lattice units and d is the Bragg plane spacing normal to the scattering vector [226]. Samples can be classified in four groups: 1) pure antiferromagnetism, 2) incommensurability $\epsilon \approx 1/8$ with low correlation length, 3) incommensurability $\epsilon \approx 1/4$ with intermediate correlation length and 4) incommensurability $\epsilon \approx 1/3$ with large correlation length. Samples of group 2) only exist in the narrow strontium doping range $0.16 \leq x \leq 0.18$. The magnetic modulation $\epsilon = 0.16$ in $\text{La}_{1.8}\text{Sr}_{0.2}\text{NiO}_{3.96}$ [225] places the sample in between the groups two and three. The magnetic intensities were already barely visible, comparable to those in our samples with much lower ϵ . With the over all trend to broader magnetic signals in samples with smaller ϵ it raises the question whether strontium doping alone would be sufficient to prepare a sample that belongs to group two. A final conclusion can not be reached from the scarce data on pure strontium doped samples in the low ϵ regime. Poor sample quality might be one explanation, but possibly the zinc co-doping in our samples is a necessary ingredient to stabilize

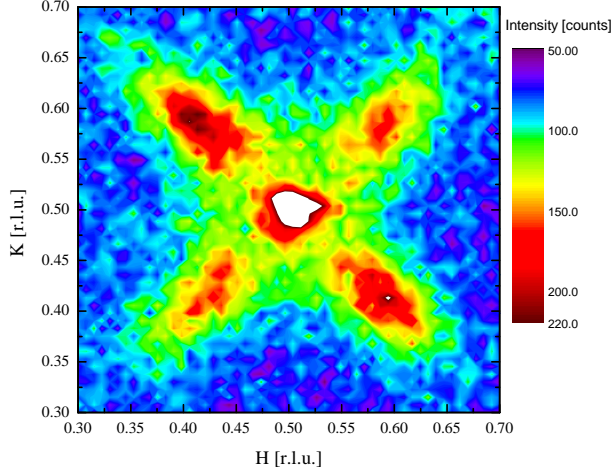


Figure 4.7: Map of the (HK0)-plane in ACK324 measured on IN3.

the incommensurate magnetism.

In another IN3 measurement the sample ACK324 has been mapped in the HK0 plane in the range from (0.3 0.3 0) to (0.7 0.7 0). The result is presented in Figure 4.7. The magnetic intensities have a pronounced anisotropy between the (1 1 0) and the (-1 1 0) directions. In the previously discussed measurement correlations along the stripe modulation have been found to be only $21(1) \text{ \AA}$. In contrast the mapped peak shape suggests a correlation length about a factor three larger along the stripes. On the local scale the distance between two charge stripes can only amount to an integer multiple. On the larger scale these distances have to vary to produce the observed incommensurate scattering, generating some diffuse scattering. Along the stripes no such restriction exists and the order can, in principle, be perfect [168].

4.3 Magnetic Excitations

All scans on the IN22 have been performed with a constant $k_f = 2.662 \text{ \AA}^{-1}$ if not defined otherwise. When the titanium doped sample ACK322 was mounted on this instrument we also performed some inelastic scans to check whether the magnon dispersion exhibits an anomalous behavior. (H 1-H 0)-Scans around the antiferromagnetic wave vector (0.5 0.5 0) at three different energies can be found in Figure 4.8. The scan at 14 meV already shows a clear plateau characteristic for the onset of a splitting into two dispersion branches. As this can be expected

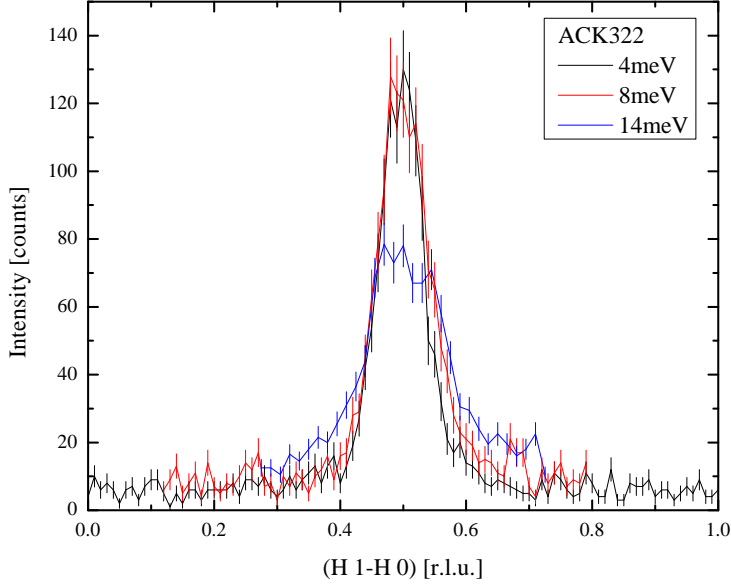


Figure 4.8: Constant energy scans of sample ACK322 with composition $\text{La}_{1.67}\text{Sr}_{0.33}\text{Ni}_{0.92}\text{Ti}_{0.08}\text{O}_4$ measured in (H 1-H 0) direction through (0.5 0.5 0).

for an antiferromagnet this sample was not studied any further. Similarly the neodymium (ACK271) and zinc (ACK274) co-doped samples mentioned above have been measured with inelastic neutron scattering. Both show no anomalies and the data can be found in the Appendix, Figure 6.1.

In contrast, the zinc co-doped sample ACK324 with the composition $\text{La}_{1.84}\text{Sr}_{0.16}\text{Ni}_{0.995}\text{Zn}_{0.005}\text{O}_4$ was found to belong to a newly characterized regime between the pure antiferromagnetic and the intermediately ordered incommensurate phases. We chose this sample for our detailed inelastic neutron study because of its enhanced correlation length compared with the two other samples in this group. Constant energy scans in (H 1-H 0) direction through the commensurate magnetic Bragg point (0.5 0.5 0) are plotted in Figure 4.9. We would expect to see four magnon branches in the inelastic scans, two dispersing from each incommensurate magnetic reflection. In this respect it is not surprising to find a very broad feature in the low energy scans due to the overlap of four broad intensity profiles. In contrast the high temperature scans deviate from the expectations. Similar to the 14 meV scan on ACK322 we would expect a decrease in peak intensity and a simultaneous increase in peak width

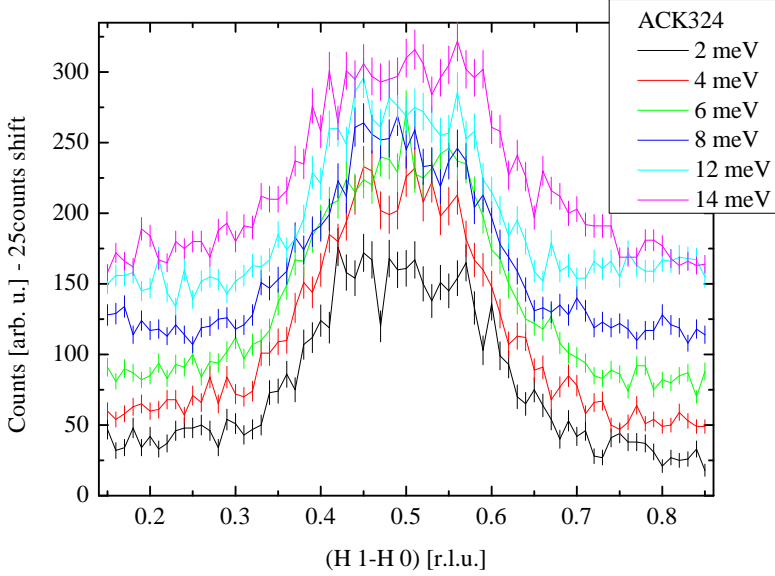


Figure 4.9: Constant energy scans of sample ACK324 with composition $\text{La}_{1.84}\text{Sr}_{0.16}\text{Ni}_{0.995}\text{Zn}_{0.005}\text{O}_4$ measured in (H 1-H 0) direction through (0.5 0.5 0).

due to the dispersing branches. Since the two inner branches are expected to disperse both towards the center an intensity increase at this point should be observable. Instead we find an almost constant plateau intensity with only a very subtle FWHM increase in the order of the error bar of a single Gauss fit. For comparison the scans at 2 meV and 14 meV are plotted directly on top of each other in Figure 6.2 in the Appendix.

Higher energy transfer in inelastic scans can be achieved by choosing a larger Q . For those scans a horizontally focusing analyzer has been used. Although the resolution is slightly better with a flat analyzer this should play only a minor role when measuring broad inelastic signals. Comparison of two scans with and without focusing analyzer at an energy transfer of 24 meV gave a factor of three for the intensity gained per monitor. The improved statistics justify the usage of a focusing analyzer. To measure at energy transfers above 32 meV at the same Q -points it was necessary to change to $k_f = 4.1 \text{ \AA}^{-1}$ for those scans. Five points have been measured at similar points in \vec{Q} space for both k_f values to normalize the scans. All scans are normalized by monitor. Measuring magnon dispersions at higher Q points has two major disadvantages. The magnetic form factor decreases rapidly with increasing Q due to the general dependence

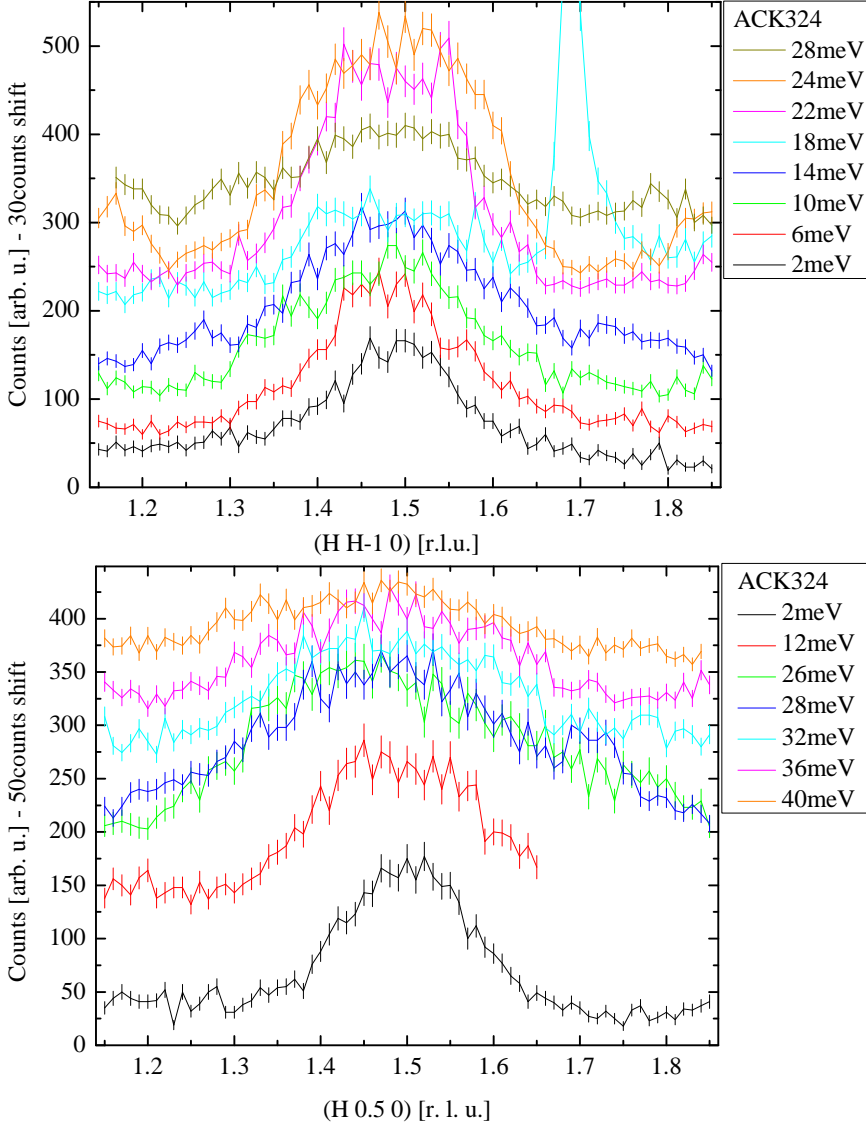


Figure 4.10: Constant energy scans of sample ACK324 with composition $\text{La}_{1.84}\text{Sr}_{0.16}\text{Ni}_{0.995}\text{Zn}_{0.005}\text{O}_4$. *Top:* $(H \ H-1 \ 0)$ direction through $(1.5 \ 0.5 \ 0)$. *Bottom:* $(H \ 0.5 \ 0)$ direction through $(1.5 \ 0.5 \ 0)$.

of $\sin(\theta)/\lambda$. At the same time the phonon structure factor is highly direction and Q dependent but in average it increases quadratic in \vec{Q} .

Diagonal constant energy scans in (H H 0) direction through (1.5 0.5 0) in the energy range 2 meV to 28 meV have been done (see Figure 4.10, top). Scans have been shifted along the vertical by 30 counts. The sharp feature at (1.7 0.7 0) in the 18 meV scan is a spurious contribution. Similar to the diagonal scans through (0.5 0.5 0) the intensity of the inelastic signal does not decrease between 2 meV and 14 meV. Instead there is an observable over all increase in intensity in contrast to the usual decay observed for higher energies. Especially the 14 meV scan shows a peak broadening while the central intensity is increased, in accordance with the expectations for four dispersing branches. At 18 meV the peak shape resembles a plateau, contradicting the 14 meV scan. The largest anomaly in the whole series can be found in the 22 meV and 24 meV scans where the intensity suddenly exhibits a jump to very high values while the 22 meV scan is considerably narrower than the one at 24 meV. This somehow resembles the resonance in the high T_c cuprates [227]. At even higher energies the peak still exhibits a plateau but it is very weak. From these scans it appears difficult to derive a consistent picture of the character of the excitations. A possible phononic contribution can not be excluded to be responsible for the large and unexpected variations in peak shape and intensity.

To get a better overview and because for some cuprates it was found that they exhibit a strongly anisotropic dispersion above and below the resonance we also performed scans in the (H 0 0) direction through (1.5 0.5 0), plotted in Figure 4.10 in the bottom. The right side of the 12 meV scan was removed due to strong spurious contributions. Scans have been shifted vertically by 50 counts. Compared to the low energy scans a broadening of the inelastic signal at higher energies up to 40 meV can be observed. There is also a pronounced decrease in peak height between 28 meV and 40 meV. The general trend can be compared with the observations in the diagonal scans where a similarly low intensity was measured for 28 meV compared to the low energy peaks.

According to measurements and calculations on spin wave dispersions we would expect the measured intensities to be a superposition of four individual magnon branches. In fact the measured intensities appear like one single peak in most of the scans. This is not especially surprising for our excitation spectrum when we consider the broadness and the proximity of the peaks. A similar broadness of the spin wave dispersion has been observed for $\text{La}_{1.825}\text{Sr}_{0.175}\text{NiO}_{4+\delta}$ in [223].

Due to the shape of our peaks it is not directly obvious how they can be fitted. Different approaches to fit Gaussian functions to the data were tested and it appears that in many cases a single Gaussian function leads to the best agreement. In these cases a refinement of two or four Gaussian functions converges with all peaks centered at the antiferromagnetic wavevector. Restrictions

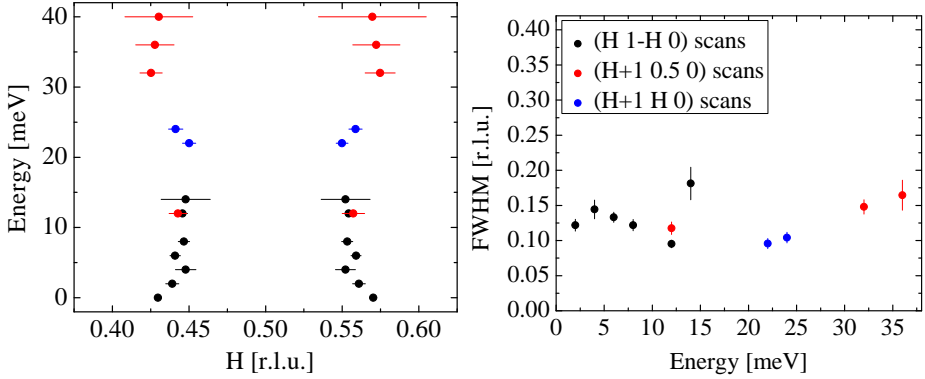


Figure 4.11: Dispersion of $\text{La}_{1.84}\text{Sr}_{0.16}\text{Ni}_{0.995}\text{Zn}_{0.005}\text{O}_4$. *Left*: Peak positions obtained by a fit of two Gaussian functions to the data. *Right*: The energy dependence of the corresponding FWHM.

to the fit parameters like combined FWHM and peak area and symmetric peak positions could not solve this issue. To include further restrictions seems inappropriate. It appears that some of the peaks measured at higher Q have an asymmetric intensity distribution. Finally only two Gaussian functions were fitted to the data with the mentioned dependences where it was possible. The resulting dispersion is plotted in Figure 4.11. All scans around (0.5 0.5 0) could be included but for the diagonal scans through (1.5 0.5 0) only 22 meV and 24 meV scans allowed a fit. In the (H 0.5 0) direction the peak positions of the 2 meV and 12 meV scans have not been plotted. At low energy the magnetic signal has a strong anisotropy between diagonal and horizontal directions due to its origin in the incommensurate Bragg positions. This results in a much narrower peak in the horizontal direction as can be also observed in the reciprocal space maps in the next section (Figure 4.14). In these maps also an increased isotropy at higher energies can be observed which justifies the comparison of peak positions in the two different directions. The resulting dispersion does not match the expectations for a spin wave dispersion as only two peak positions were used. If the compound indeed exhibits some kind of spin wave dispersion we should be able to observe a pronounced broadening of the peak intensity with increasing energy transfer. The FWHM obtained from the peak fits are plotted in the right graph in Figure 4.11. The expected steady increase in peak width can not be observed. On the other hand it is not possible to find an over all trend within the margin of errors from the plotted data. But since a clear broadening is absent a fit of four Gaussian functions to obtain a spin wave dispersion is not justified. In Section 4.5 we will discuss polarized neutron measurements to further elucidate this peculiarity.

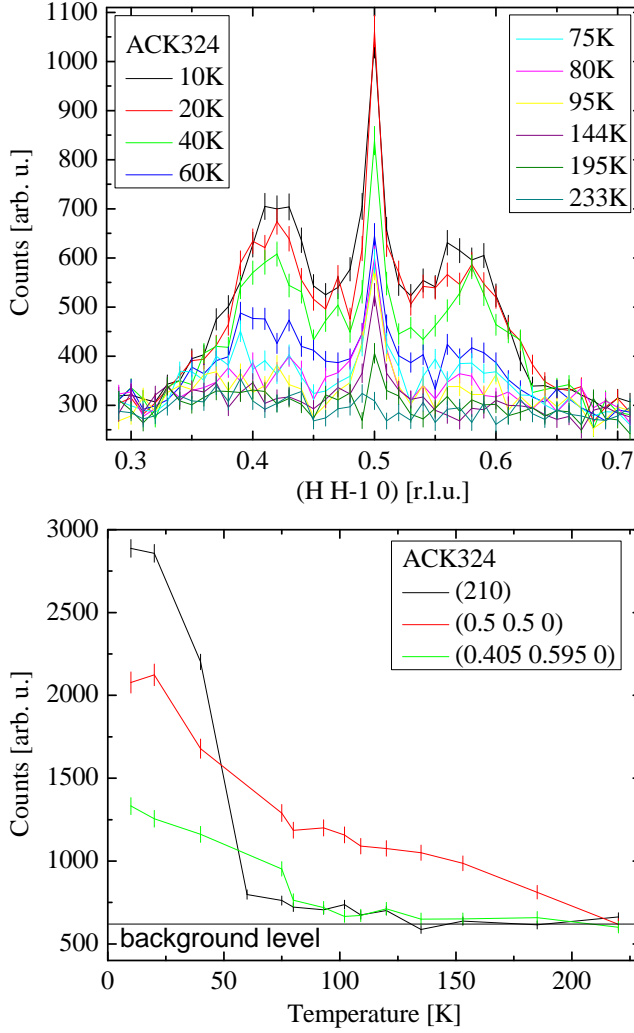


Figure 4.12: Temperature dependence of structural and magnetic intensities in ACK324. *Top*: Scan in $(H H-1 0)$ direction through $(0.5 0.5 0)$. *Bottom*: Determination of the transition temperatures for the magnetic and structural phase transitions: $\text{HTT} \rightarrow \text{LTO} \rightarrow \text{LTT}$.

While warming the sample back to ambient temperature we measured the temperature dependence of the magnetic intensities as well as of the two structural superstructure reflections $(0.5\ 0.5\ 0)$ and $(2\ 1\ 0)$. The evolution in a diagonal scan in $(H\ 1-H\ 0)$ direction through $(0.5\ 0.5\ 0)$ can be found in Figure 4.12, top. In the bottom figure the peak intensities are compared directly. It appears that the two reflections that are connected to the octahedral distortions due to a tilting of the CoO_6 -octahedra exhibit very different temperature dependences. The strong $(2\ 1\ 0)$ intensity decreases rapidly below 60 K while a tiny contribution is still detectable up to 120 K. In contrast, the $(0.5\ 0.5\ 0)$ peak decreases constantly and vanished only at 220 K. Although the low temperature decrease of the magnetic intensity is better comparable to that of the $(0.5\ 0.5\ 0)$ reflection, it disappears at a temperature of about 80 K. We can assume that at the second transition the structure changes to the low temperature tetragonal phase.

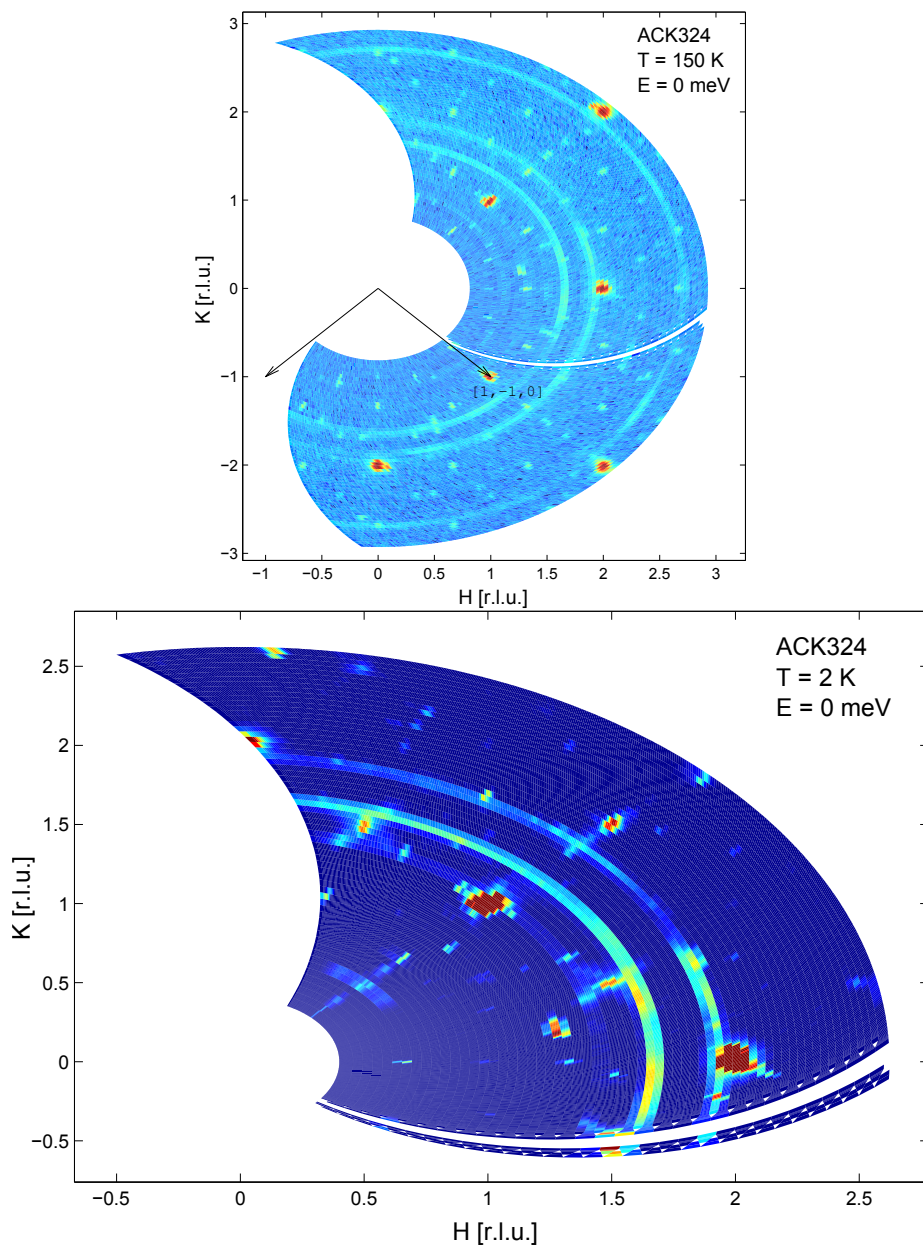
4.4 Reciprocal Space Maps with FlatCone

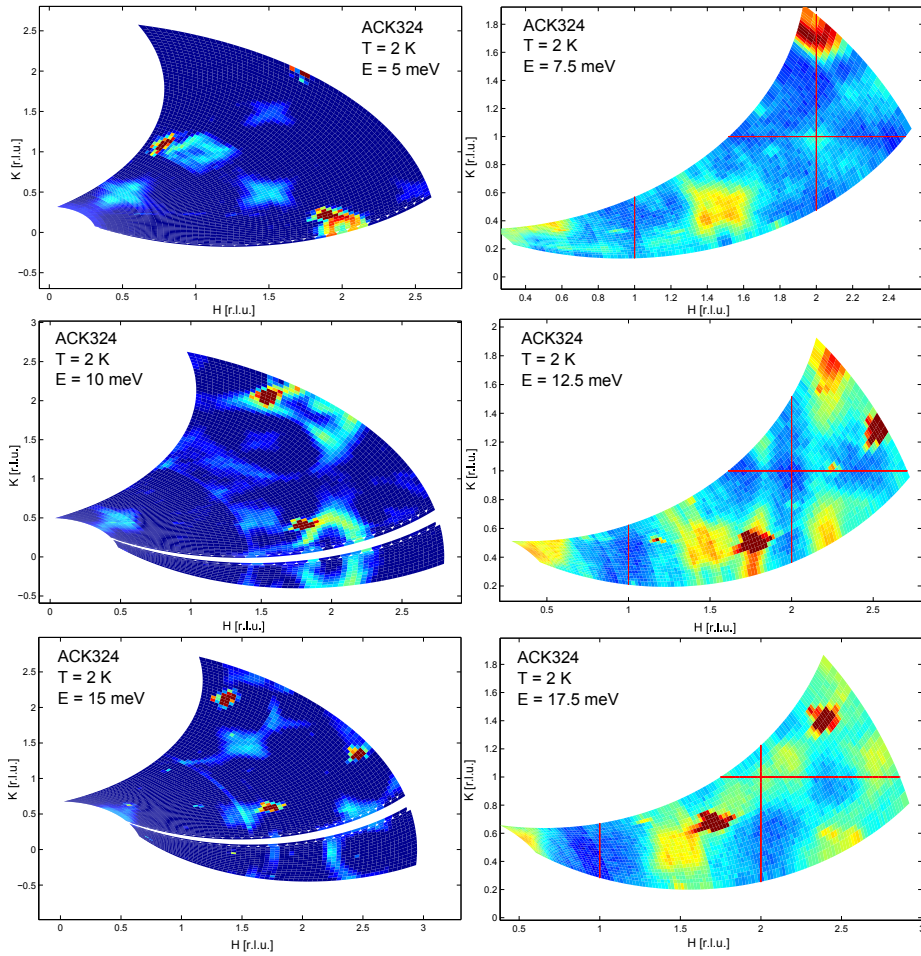
Instrumentation is always developing and a new trend on TAS instruments is to collect as many data points simultaneously as possible. The flatcone option accessible at the high flux thermal TAS IN8 is a good example. It makes it possible to map large regions of the reciprocal space without an increase in measuring time. In a large shielding a total of 31 detector channels are placed besides each other. This multi detector covers the whole 2θ range of 75° at once. As mentioned in Section 2.5 a measurement at a certain sample angle ω' produces 31 data points in (\vec{Q}, ω) space along a curved line and an ω' scan records a whole map. To increase the point density of the map the detector position can be varied slightly. Due to the spacing between two channels of 2.5° in 2θ we changed the detector position by half the value for a second scan in all our maps. The first detector was placed at $2\theta = 7.5^\circ$ to include the lowest Q points possible in our maps. This channel corresponds to the most inner circle around the center at zero r.l.u.. ω' scans were performed with a step size of 1° . To normalize the detector channels a scan on a vanadium powder sample taken at the beginning and end of the measurement were used in the data refinement. The monochromator and analyzer crystals were silicon with the $(1\ 1\ 1)$ Bragg peak in reflection position. We used $k_f = 3\ \text{\AA}^{-1}$ for our measurements which is advertised on the ILL web page [228] to provide a signal free contamination with higher harmonics. While the second order higher harmonics are suppressed because the $(2\ 2\ 2)$ reflection is forbidden in silicon, the third order should play a minor role because the neutron flux decreases rapidly at such high energies.

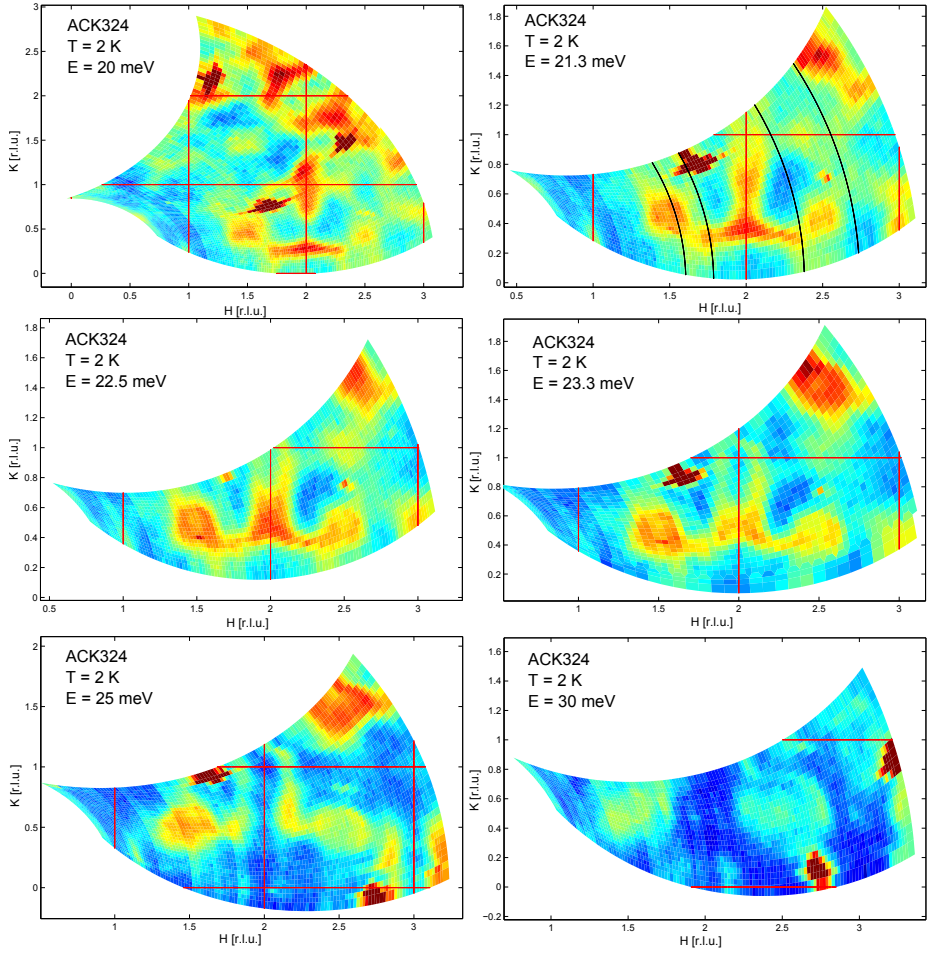
Intensity maps in the $(H\ K\ 0)$ plane were measured elastically on the zinc co-doped sample ACK324 with the composition $\text{La}_{1.84}\text{Sr}_{0.16}\text{Ni}_{0.995}\text{Zn}_{0.005}\text{O}_4$ in

Figure 4.13. The map denoted with 150 K was recorded while cooling in the range 180 K - 80 K. Clearly visible are the three alumina lines which form concentric circles at $|\vec{Q}| \approx 1.7$ r.l.u., 1.9 r.l.u. and 2.7 r.l.u.. The strong structural Bragg intensities for the characteristic pattern where reflections with $H + K = 2n + 1$ are absent due to the body centering of the I 4/m m m unit cell used for indexing. Unfortunately a second pattern of weak intensities can be observed which clearly index with 1/3 of the structure. Since we did not observe these reflections in our IN22 measurement they must be attributed to third harmonics scattering. In the 2 K map the appearance of additional intensities due to the orthorhombic distortion at half integer Bragg points and the incommensurate magnetic satellites appear. All inelastic maps have been scaled by the same color-intensity relation except the 5 meV, 10 meV and 15 meV maps which have a common but different scaling. Sharp high intensity spots can be found in many maps and are spurious. A very unfortunate spurious intensity appears in many scans due to poorly shielded elastic scattering from the alumina sample environment. Although space is scarce inside the flatcone detector, two different monochromators have been installed. This leaves only room for a radial collimator which seems insufficient to reduce the alumina background. The powder lines are well visible in e.g. the 12.5 meV scan where they superimpose with the magnetic signal we are interested in. The four alumina lines intersecting with our reciprocal space maps are indicated by black lines in the 21.3 meV scan. Since their scattering angle does not change they are always detected by the same channel. But the higher the energy transfer the larger the absolute Q value of the detector. Consequently it appears as if the alumina lines move outwards in momentum-energy space.

The evolution of the magnon dispersion with increasing energy transfer was thoroughly mapped and is presented in the Figures 4.14, 4.15 and 4.16. In the low temperature 5 meV map a monotone decrease of the magnetic scattering with raising Q can be observed. Around the structural Bragg points the acoustic phonons emerge and their intensity has an opposite Q dependency. We focused the maps on the region around the (1.5 0.5 0) because at higher energy transfer the scattering triangle can not be closed for Q points around (0.5 0.5 0). Initially the symmetry of the sum of magnon dispersions emerging from the magnetic Bragg points is four fold. At 17.5 meV this symmetry is almost lost and the magnetic excitations acquire a ring like shape with smaller intensity in the center. We chose a smaller energy step width around 22.5 meV where the pronounced intensity increase appeared in the IN22 measurement. In the range between 20 meV and 23.3 meV the magnon maintains its ring shape. But at 25 meV it appears to be elongated along the crystal axis, 45° rotated compared with the elastic signal. In contrast, the magnon measured at (2.5 0.5 0) still exhibits a ring like shape. At higher energies the magnetic signal decays quickly. The stronger intensity around (2.5 0.5 0) compared to (1.5 0.5 0) suggests that there

Figure 4.13: Elastic maps in the $(H K 0)$ plane of ACK324.

Figure 4.14: Constant energy maps in the $(H K 0)$ plane of ACK324.

Figure 4.15: Constant energy maps in the $(H\ K\ 0)$ plane of ACK324.

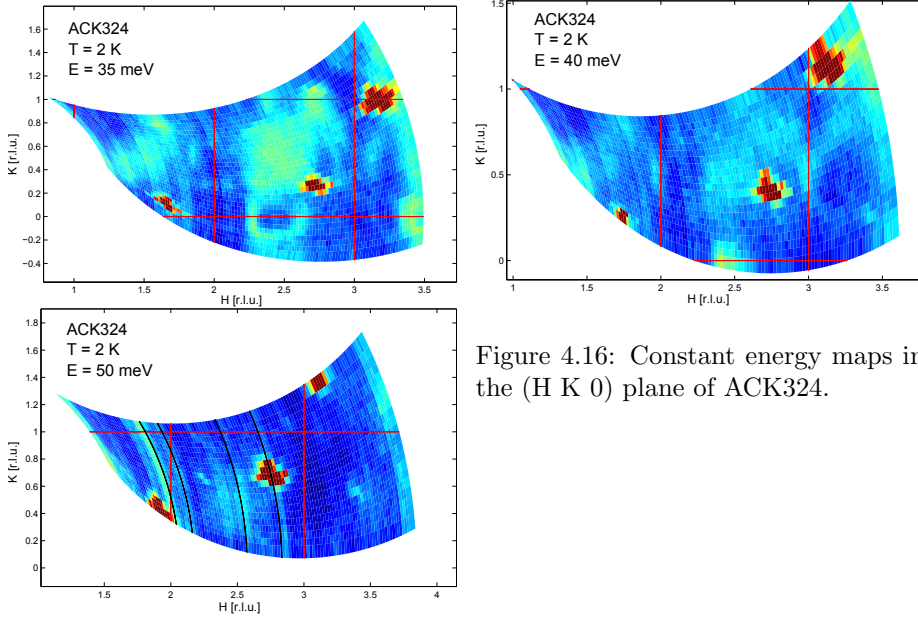


Figure 4.16: Constant energy maps in the $(H\ K\ 0)$ plane of ACK324.

is also some phonon contribution.

In the low energy range the acoustic phonon originating in $(2\ 0\ 0)$ disperses symmetrically at first but at 12.5 meV it becomes anisotropic. In the 17.5 meV map it seems to have already reached the zone boundary and only a small intensity is left over. Regarding the region around the magnon where the phonon should intersect a decreased intensity is observable. This suggests that the phononic contribution to the IN22 constant energy scans in this region is small. At 20 meV new phonon branches appear. Namely a vertical bar around $(1\ 2\ 0)$ and a horizontal one around $(2\ 0.3\ 0)$. They are connected at 21.3 meV but still separated from the magnon intensity. In the range around 22.5 meV magnonic and phononic intensities are connected and possibly superimpose. And at 25 meV the phonon signal lost already most of its intensity. The small energy range in which this phonon branch extends over a wide area in the HK-plane implies a very flat phonon dispersion.

Sample ACK390 with the composition $\text{La}_{1.895}\text{Sr}_{0.105}\text{Ni}_{0.995}\text{Zn}_{0.005}\text{O}_{4.05}$ belongs to group three defined in the previous section. Out of the three samples in this group it exhibits the smallest ϵ and the lowest intensity at $(0.5\ 0.5\ 0)$ in the IN3 scans. The absence of any intensity at this \vec{Q} -point in the elastic map 4.18 measured at the IN8 with the flatcone detector proves that this sample remains tetragonal even at 2 K. The part of the map above $K = 0$ has been measured with four different 2θ positions and the lower part only with one.

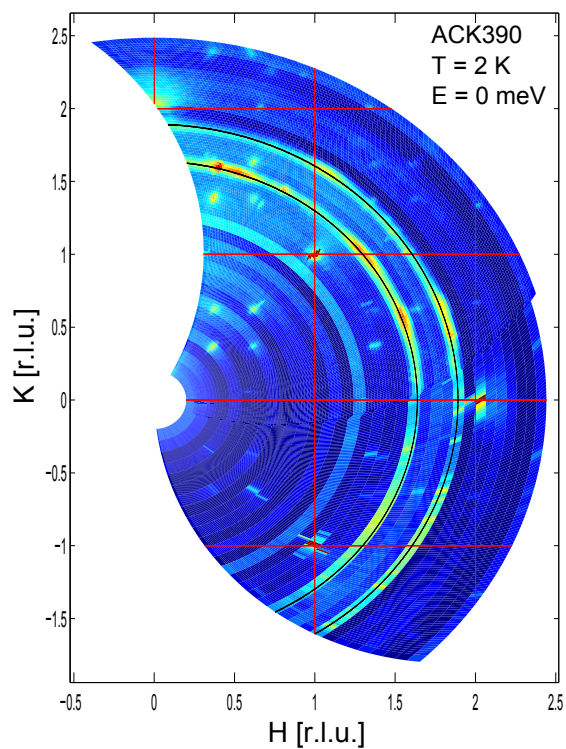
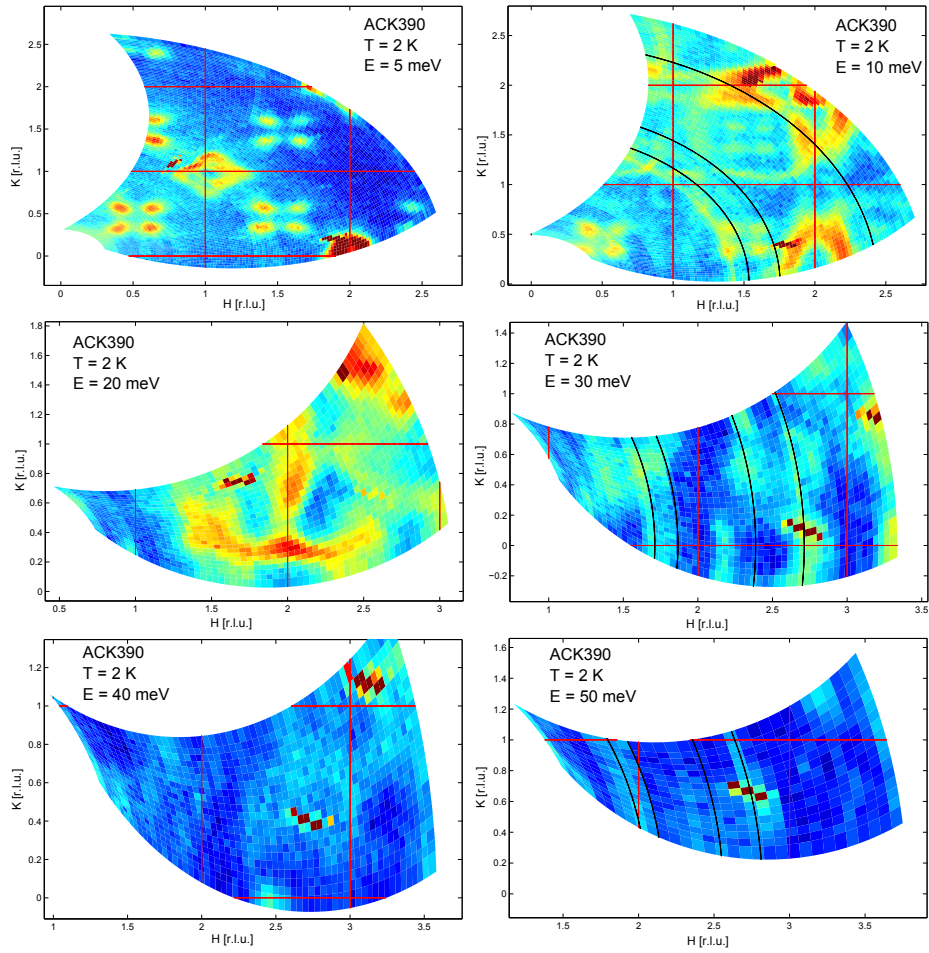


Figure 4.17: Elastic maps in the $(H K 0)$ plane of ACK390 with the composition $La_{1.895}Sr_{0.105}Ni_{0.995}Zn_{0.005}O_{4.05}$.

Figure 4.18: Constant energy maps in the $(H K 0)$ plane of ACK390.

Magnetic peaks are well separated as to be expected for the larger epsilon compared to ACK324. At 5 meV and 10 meV the intensities remain well separated. The higher energy transfer maps are not reliable for evaluation. The optical phonon intersects with the magnon already at 20 meV implying a softening of this branch of about 2.5 meV compared to the sample ACK324. At 30 meV the magnon seems to split into two vertical bars with decreased intensity in between but the signal is possible superimposed with the spurious alumina lines. At the highest energies the magnon becomes too feint to be detectable above the background.

4.5 Polarized Neutrons

In the previous sections we made use of the neutrons ability to interact with the magnetic structure and excitations due to its spin moment. But to take full advantage of this property a polarized neutron beam is necessary. To separate magnetic from nuclear intensities we need both, a polarized incident beam and polarization analysis of the scattered neutrons [229]. Polarization of the incident neutrons and polarization analysis at the IN22 is achieved by scattering on the (1 1 1) plane of a heusler crystal. In an external field magnetic and nuclear scattering can be constructive for one spin state while being destructive for the opposite spin state. The field is also necessary to keep a single magnetic domain. To counter the loss of neutron flux large array of crystals are used for the fixed vertically focusing monochromator and analyzer. Horizontal focusing can be adjusted according to the neutron energy. Permanently installed guide fields prevent the loss of polarization along the flight path. A setup of three horizontal coils and a vertical Helmholtz pair is used to continuously select the polarization. Spin flippers before and after the sample can reverse the polarization of the beam and make it possible to measure the four partial cross sections (+,+), (-,-), (+,-) and (-,+) directly. In this short notation the first and second position in the bracket correspond to the flipper before and after the sample. The signs “+” and “-” denote whether the flipper is turned off (+) or on (-).

The neutron polarization was chosen parallel to the scattering vector \vec{Q} in our experiment. Only the component of the magnetic density which is perpendicular to \vec{Q} contributes to the scattering. The four formulas for the partial cross sections then collapse into only two expression [230]:

$$\left(\frac{d^2\sigma^{\pm\mp}}{d\Omega d\omega}\right)_X = \frac{k_f}{k_i} [\langle M_{\perp Y} M_{\perp Y}^* \rangle_\omega + \langle M_{\perp Z} M_{\perp Z}^* \rangle_\omega] \mp i [\langle M_{\perp Y} M_{\perp Z}^* \rangle_\omega - \langle M_{\perp Z} M_{\perp Y}^* \rangle_\omega] + \frac{2}{3} SS_{incoh}(\vec{Q}, \omega) \quad (4.2)$$

and for non-spin-flip:

$$\left(\frac{d^2\sigma^{\pm\pm}}{d\Omega d\omega}\right)_X = \frac{k_f}{k_i}[\langle NN^* \rangle_\omega + NN_{incoh}(\vec{Q}, \omega) + \frac{1}{3}SS_{incoh}(\vec{Q}, \omega)] \quad (4.3)$$

In the coordinate system defined by the scattering vector \vec{Q} on a TAS instrument X is parallel to \vec{Q} , Y is perpendicular to \vec{Q} and in the scattering plane and Z is perpendicular to \vec{Q} and the scattering plane. $M_{\perp Y}$ and $M_{\perp Z}$ are the components of the spacial Fourier transform of the real space magnetic density $\vec{M}(\vec{r})$ perpendicular to \vec{Q} and along Y and Z, respectively [230]. The angle brackets $\langle \dots \rangle_\omega$ are the correlation functions which correspond to the thermal average of the double Fourier transformation [230]. Incoherent scattering due to the distribution of isotopes $NN_{incoh}(\vec{Q}, \omega)$ only contributes to the non spin-flip (NSF) channel while the scattering due to the completely disordered nuclear spins $SS_{incoh}(\vec{Q}, \omega)$ contributes to both channels differently [230]. The equations have been taken from [230] where also a complete derivation of the formulas is provided.

From the equations 4.3 and 4.2 it is apparent that in this special configuration with the polarization along the scattering vector magnetic and nuclear scattering can be measured separately. The NSF cross section is only nuclear while the spin-flip (SF) cross section is purely magnetic. The mixed terms in the SF cross section are the chiral terms.

In real experiments the beam polarization is never perfect. This is expressed by the flipping ratio $R(\vec{Q}) = I^+/I^-$. We measured the (2 0 0) Bragg reflection in the NSF (+, +) and SF (+, -) channels at $k_f = 2.662 \text{ \AA}^{-1}$ to obtain I^+ and I^- . The resulting flipping ratio is $R(2\ 0\ 0) = 16.0(8)$ in our experiment. Consequently 1/16 of the NSF signal will also contribute to the background in the SF channel. This can be important if the nuclear scattering is strong compared to the magnetic scattering.

In the previous sections it turned out that the evaluation of the magnon dispersion of ACK324 with the composition $\text{La}_{1.84}\text{Sr}_{0.16}\text{Ni}_{0.995}\text{Zn}_{0.005}\text{O}_4$ is difficult. One reason being the superposition of the magnetic signal with several phonon branches. Polarized neutrons are the ideal tool to separate nuclear and magnetic scattering. Figure 4.19 is a comparison of the SF and NSF channels in an energy scan at (1.5 0.5 0). The intensities were normalized by monitor. Around 21 meV a strong phonon intensity appears while an increased phononic background of a similar size as the magnetic signal can be observed in the range from 14 meV to 32 meV. Two peaks appear in the SF channel. The one at 40 meV is not unambiguous and could also result from the increased background at small 2θ values. Over all, the magnetic contribution at the central

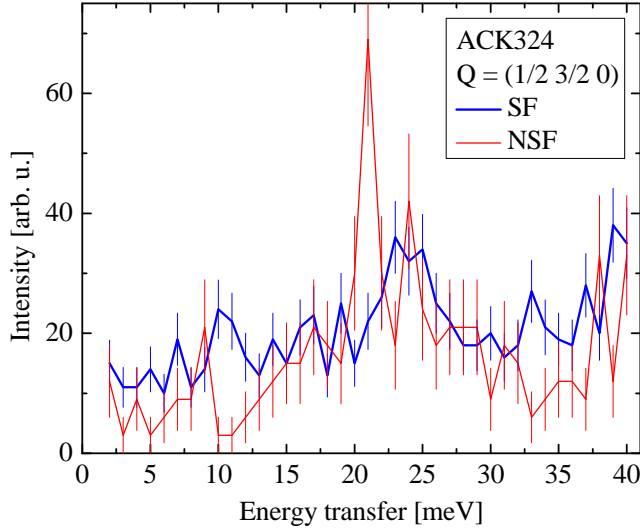


Figure 4.19: Energy scan of SF/NSF channels at $(1.5 \ 0.5 \ 0)$ in ACK324.

Q point shows a monotone increase with energy. This is in contrast to the general observation in neutron spectroscopy that magnon and phonon intensities decrease with increasing energy transfer. In expectation of a spin wave dispersion a merging of the two inner branches should occur. Three interpretations are possible: either one of the peaks in the SF channel could correspond to the merging or it appears at much higher energies. For the latter scenario the increasing proximity of the branches would explain the observed magnetic intensity raise.

Constant energy scans with polarized neutrons at several energies can be found in Figure 4.20. The intensity has been normalized by monitor. The peaked intensities in the SF channel prove that our previous measurements indeed followed the magnon dispersion. On the left side of the figure are diagonal scans at three different energies. At 20 meV and 24 meV the NSF contribution has a peak at similar Q points as the SF. The strong anisotropy in the NSF channel is obviously responsible for the pronounced intensity raise observed in the unpolarized scans at this energy (compare Figure 4.10, top). An opposite situation can be observed at 30 meV. Here the superposition of SF and NSF channels results in a broad peak due to a minimum in the NSF channel at half integer Q. Also the other scans in Figure 4.20 show a strong phononic background but it is more isotropic and therefore less influential on the peak position and broadness. In the $(H \ K \ 0)$ plane maps in Figure 4.15 a ring shaped intensity could be observed around $(2.5 \ 0.5 \ 0)$. The scan in the bottom right of

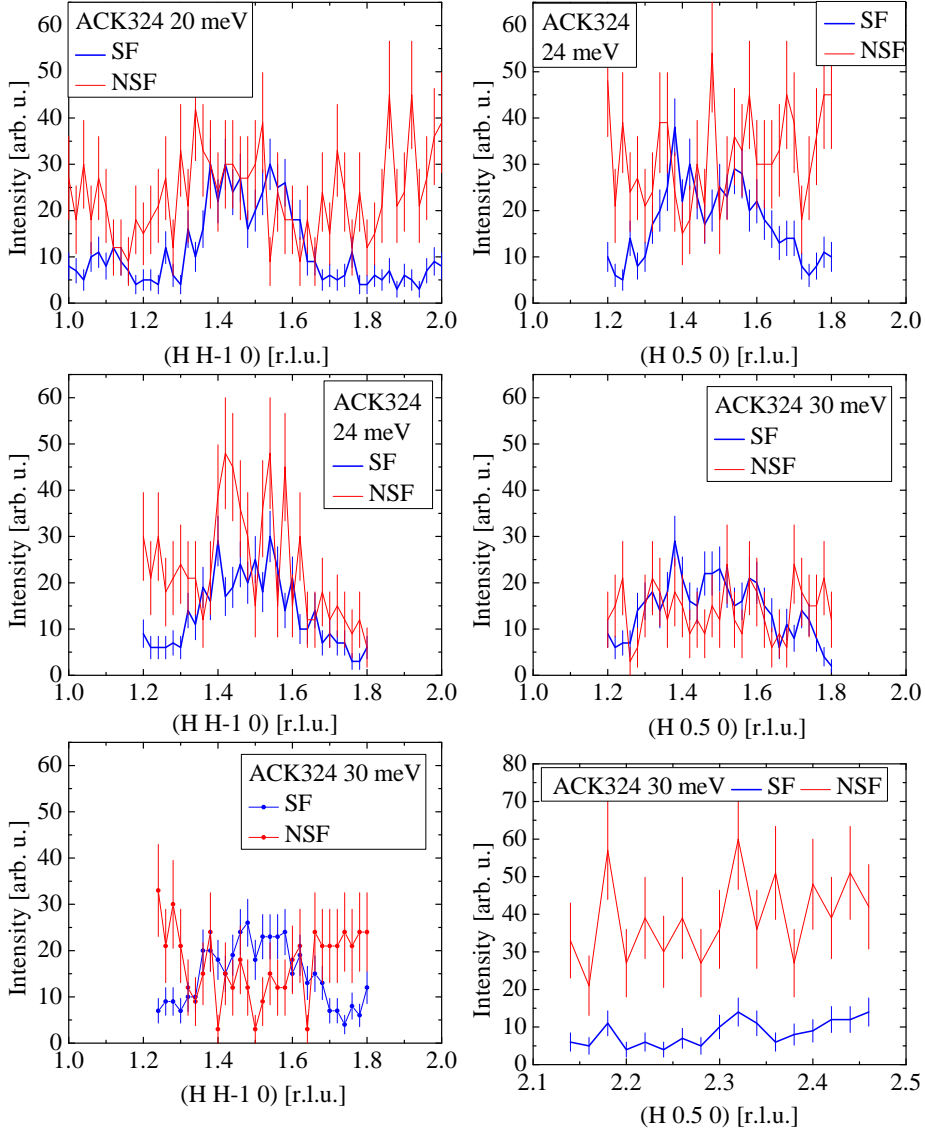


Figure 4.20: Constant energy scans of SF/NSF channels in ACK324.

Figure 4.20 uncovers this signal as purely phononic in nature.

For the final version of the refined peak positions in Figure 4.21 the results obtained from unpolarized neutron scans through (1.5 0.5 0) have been replaced by those from polarized neutrons. The 14 meV results have been removed as it is apparent from the flatcone maps that this scan is already contaminated by a phonon. Instead of the expected broadening due to the development of spin wave cones, we find that the intensity weight in a symmetric fit of two Gaussian peaks, moves inward with increasing energy up to 12 meV. At higher energy the peak positions recover to the elastic incommensurate values but neither dispersion nor a significant peak broadening can be observed.

Linear spin-wave theory (LSWT) has been used to calculate spectra of ideal commensurate stripe structures [231, 232]. For the undoped parent compound the calculations with a 2D spin wave model for the antiferromagnet with $J \approx 30$ meV are in agreement with experimental data for energies $E \leq 30$ meV [233]. At lower energies deviations in the form of excitation gaps appear due to uniaxial spin anisotropy and weak interlayer couplings [231]. The decreased spin wave velocity parallel to the stripes $v_{||} = 0.6v_{AF}$ compared to the parent compound in an oxygen doped sample as well the isotropic velocity in a strontium doped sample with an upper edge at 80 meV could be well reproduced. Our findings for the spin excitation spectrum of ACK324 - $\text{La}_{1.84}\text{Sr}_{0.16}\text{Ni}_{0.995}\text{Zn}_{0.005}\text{O}_4$ disagree with expectations from LSWT. In the energy range of our measurements the characteristic dispersion of a spin wave cone is absent.

In a different theoretical approach within LSWT the dynamical spin structure factor of spin waves for weakly coupled stripes $|J_b| \ll |J_a|$ was calculated [234]. J_a is the nearest neighbor exchange coupling and J_b the coupling across the domain walls. The authors argue that doped holes create line dislocations in the antiferromagnetic matrix, but in between the defects the antiferromagnet is more or less intact. For our low doped sample with small hole concentration this approach seems reasonable. Assuming a weak coupling $J_b = 0.05J_a$ across the stripes the authors of [234] find that in a constant energy map centered at the AF wave vector four strong incommensurate peaks are visible at low energy. Although the expected spin wave cone emanating from each reciprocal lattice vector is also visible in their calculated intensity maps, the intensity is not uniform. Due to the weak coupling between stripes the intensity is strongly peaked on the inner side of the cones. Therefore, as energy is increased the weight of the measured intensity moves inward. At E_{res} a resonance peak appears at the AF wave vector. The energy E_{res} increases with increasing $|J_b/J_a|$. Above the resonance a rotated square shaped continuum can be observed. The calculations are based on vertical stripes with $\epsilon = 0.2$ which can be seen as a 4-leg ladder or period-5 stripes. In our sample with $\epsilon = 0.139(11)$ the regions of pure antiferromagnetism are even larger but stripes are diagonal. The calculations were based

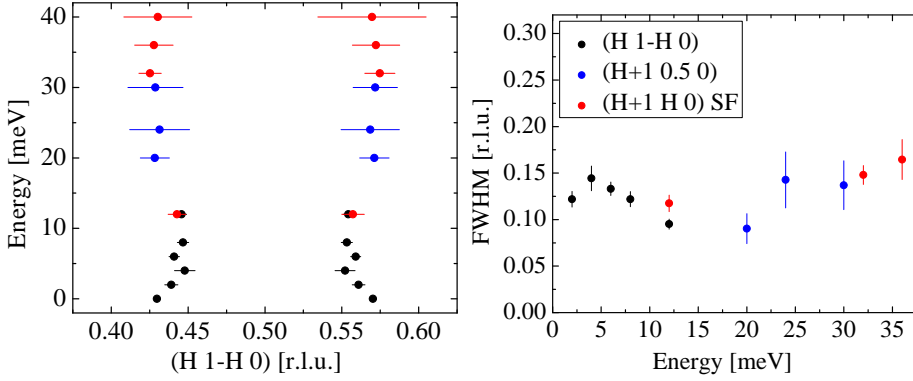


Figure 4.21: Dispersion of $\text{La}_{1.84}\text{Sr}_{0.16}\text{Ni}_{0.995}\text{Zn}_{0.005}\text{O}_4$. *Left*: Peak positions obtained by a fit of two Gaussian functions to the data. *Right*: The energy dependence of the corresponding FWHM.

on a perfectly ordered structure. In contrast to this assumption we observed a very small correlation length $\xi_{\perp} = 21(1) \text{ \AA}$ along the stripe modulation. Strong disorder present in our sample might therefore be the reason why our measured intensities are rather broad compared to calculations.

An energy scan of the sample $\text{ACK390-La}_{1.895}\text{Sr}_{0.105}\text{Ni}_{0.995}\text{Zn}_{0.005}\text{O}_{4.05}$ at $(1.5 \ 0.5 \ 0)$ shows similarities to the one performed on ACK324. SF and NSF channels are plotted in Figure 4.22. In the SF channel a broad peak appears around 20 meV. At higher energies the magnetic intensity remains constant. Around 22 meV the already mentioned optical phonon branch crosses the scan where it contributes the majority to the cross section. In the remaining energy range magnetic scattering exceeds the nonmagnetic contributions.

A series of constant energy scans (Figure 4.23) through $(1.5 \ 0.5 \ 0)$ reveals a quite similar energy dependence of the magnetic intensities compared to ACK324. With increasing energy transfer the lower Q points in the scans could not be reached any more. Two Gauss functions symmetric around $(1.5 \ 0.5 \ 0)$ and with a shared peak width have been fitted to the data and are included in the figure. The corresponding NSF scans and two scans in K direction can be found in the Appendix Figure 6.3. Two distinct peaks can be observed up to 15 meV in the SF channel. At higher energies additional intensity in between the peaks appears. Although at 20 meV also the NSF channel shows a peak, the additional SF intensity over a wide energy range can not be explained with a phononic background. A flipping ratio of ≈ 16 due to a not perfectly polarized beam results in a NSF background in the SF channel that corresponds to the measured NSF signal, but reduced by the factor ≈ 16 .

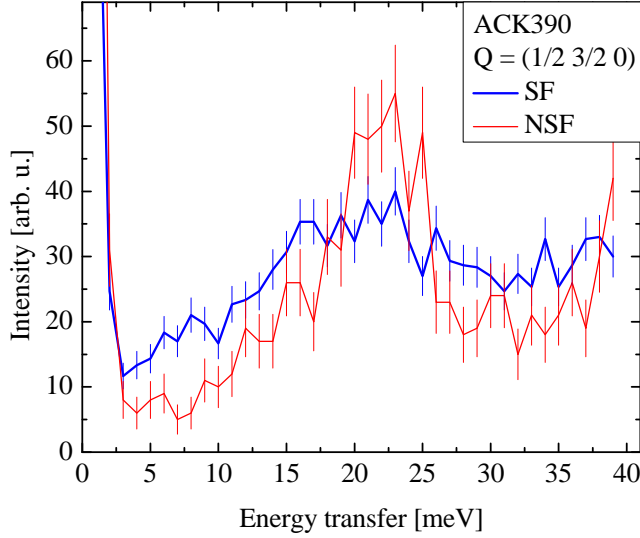


Figure 4.22: Energy scan of SF/NSF channels at $(1.5 \ 0.5 \ 0)$ in ACK390.

LSWT predicts spin wave cones emerging from the incommensurate elastic peak positions. These should be visible in our diagonal scan as four peaks, one pair dispersing away from each magnetic Bragg peak. In previous work on strontium doped samples with $x = 0.275, 0.31, 1/3$ [221, 222] and an oxygen doped sample with $\delta = 0.11$ [177] such excitations have indeed been observed.

The incommensurability of our sample is comparable to that published for a sample with composition $\text{La}_{1.825}\text{Sr}_{0.175}\text{NiO}_{4+\delta}$ [223]. For the inelastic scans on that sample it was possible to fit four Gaussian peaks to the measured intensity by reducing the free fit parameters from twelve to three. The author determined the low energy peak positions by a fit of two Gaussian functions. For the four peak fit two sets of peaks were assumed, each symmetric with respect to the low energy peak position and the center of the two sets symmetric with respect to the AF wave vector. The two additional parameters were a common width and a common intensity. The result was a spin wave dispersion with a similar spin wave velocity as in the undoped parent compound and the $x = 1/3$ doped nickelate [223]. It should be noted that the peak positions also show deviations from the fitted spin wave dispersion at energies $E \leq 20$ meV. Using this approach and the peak positions of our 5 meV scan resulted in a very poor agreement with the experimental data. For most scans the fit converged to a common peak width of about 0.3 r.l.u..

The condition that individual peaks could not be resolved at elevated energies strongly complicates data analysis. Assumptions have to be made to justify

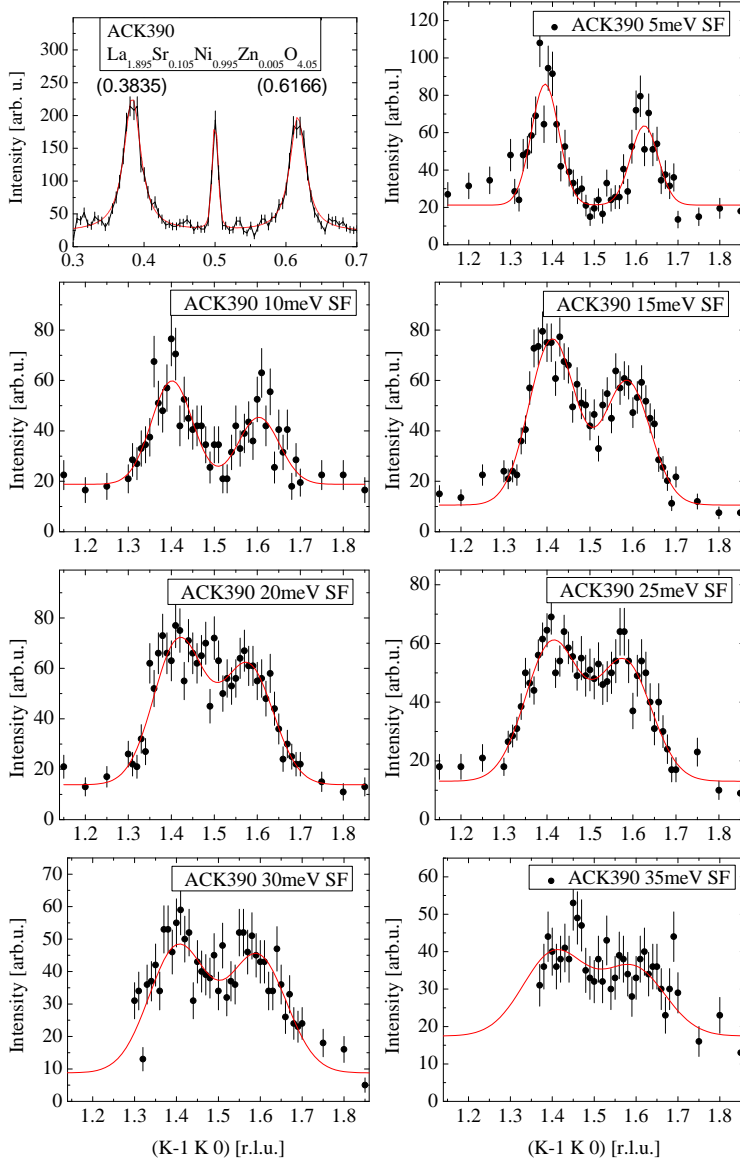


Figure 4.23: Spin flip intensities in ACK390 measured with constant energy scans at the IN22. Red curve is a fit of two Gaussian functions with a common width to the data.

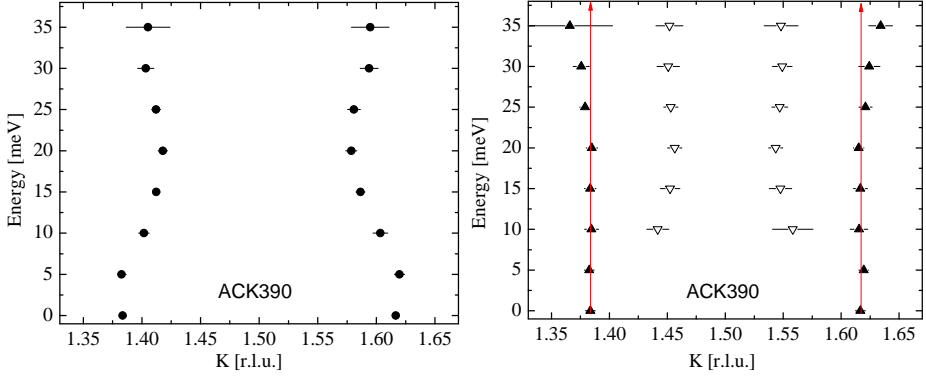


Figure 4.24: Dispersion of ACK390- $\text{La}_{1.895}\text{Sr}_{0.105}\text{Ni}_{0.995}\text{Zn}_{0.005}\text{O}_{4.05}$. *Left*: Peak positions obtained by a fit of two Gaussian functions to the data. *Right*: Peak positions obtained by a fit of four Gaussian functions to the data. Vertical red lines are a guide for the eye.

whether two, three or four peaks should be fitted to the data. The first case corresponds to the approach used for the cuprates where spin wave cones are absent. The second approach would account for the additional intensity appearing in between the two peaks. A fit of four peaks would imply the assumption that the dispersion does indeed follow the predictions of LSWT.

Similar to previous publications we fitted four Gaussian peaks to the data (see Figure 4.24, *right*). The restrictions were a single shared peak width and symmetric peak positions with respect to the AF wave vector for the pairs of inner and outer peaks. Clearly, the dispersion obtained by our four peak fit does not result in a finite spin wave velocity for the outward peaks between 0 meV and 20 meV. Similarly the inward peak positions deviate from a monotone development expected at small energy transfers. No spin wave velocity can be fitted to the obtained peak positions. This demonstrates that LSWT for a perfectly ordered stripe phase is inadequate to describe the observed magnon dispersion.

Alternatively a fit of only two symmetric Gaussian functions has been applied. The obtained peak positions are summed in Figure 4.24, *left*. While our 5 meV peaks show an increased incommensurability compared to the elastic data, the dispersion is strongly curved towards the center for higher energies (see Figure 4.23). The resulting inward shift between 5 meV and 20 meV is about 30%. In this scenario the outward curved branches are absent.

4.6 Conclusions

For the two peak case we obtain a dispersion with a peculiar shape. In order to compare any similarities with the hourglass dispersions reported in the cuprates [49, 49], the fitted peak positions are overlaid on a measured intensity map in Figure 4.25. The incommensurability $\epsilon = 0.2331(1)$ in our sample ACK390 places it in between the four-leg and the three-leg ladder systems discussed in [234]. Similar to the previously discussed sample ACK324 the outward dispersing intensity is also suppressed in ACK390. Compared to ACK324 the effect of the inward curvature is much stronger in this sample. This difference might be caused by a decreased spin wave velocity in ACK390. Studies on the pure strontium doped samples report a velocity comparable to that of the undoped parent compound for $x = 0.175, 0.275$ and 0.333 [222, 223, 233]. In contrast, the spin wave velocity was reported to be a factor 5 smaller in an oxygen doped sample with $\delta = 0.105$ which is still in the AF regime. For an incommensurate sample with higher oxygen doping $\delta = 0.133$ the value recovered to 40% compared to that of the undoped material [167]. While strontium doping seemingly has no effect on the spin wave velocity, it appears that oxygen doping can induce a pronounced decrease. This is in accordance with our observations since only ACK390 is oxygen doped.

Both types of hole doping, oxygen excess and strontium doping, can be used to induce charge stripe order in the nickelates. The two families share many commonalities, like the general trend $\epsilon \approx n_h = x + 2\delta$, but also differences can be observed. While the incommensurability jumps from zero to $\epsilon = 0.27$ at an oxygen doping of about $\delta \approx 0.11$ in $\text{La}_2\text{NiO}_{4+\delta}$ [167], also intermediate values for ϵ can be reached with strontium doping (see e.g. the overview in [166]).

Despite the large publication numbers for nickelates, only one study reports a similarly peculiar dispersion. For a purely oxygen doped sample with $\delta = 0.11(1)$ which is already in the incommensurate regime, Freeman et al. found an inward curvature of the spin excitation spectrum between 10 meV and 20 meV [235]. They compared their data with an excitation spectrum calculated with LSWT for period-4 stripes, Dubbed DS4 in [232]. The corresponding incommensurability $\epsilon = 0.25$ is close to their experimentally observed value. Only two exchange parameters are required for the minimal DS4 model, the nearest-neighbor Ni^{2+} coupling within a stripe domain J_a and the coupling of Ni^{2+} spins through the Ni^{3+} hole stripe J_b . The authors argue [235] that this model is justified by the successful description of the magnetic dispersion of the strontium doped sample $\text{La}_{5/3}\text{Sr}_{1/3}\text{NiO}_4$ [178, 222]. In both studies the simple model was insufficient to describe the low energy excitation spectrum [178, 222]. While additional assumptions were made to increase the agreement of the model with the low energy data [222], in [178] only data for $E \geq 30$ meV was considered for a comparison with the calculated intensities.

To reproduce the observed inward curvature of the dispersion between 10 meV

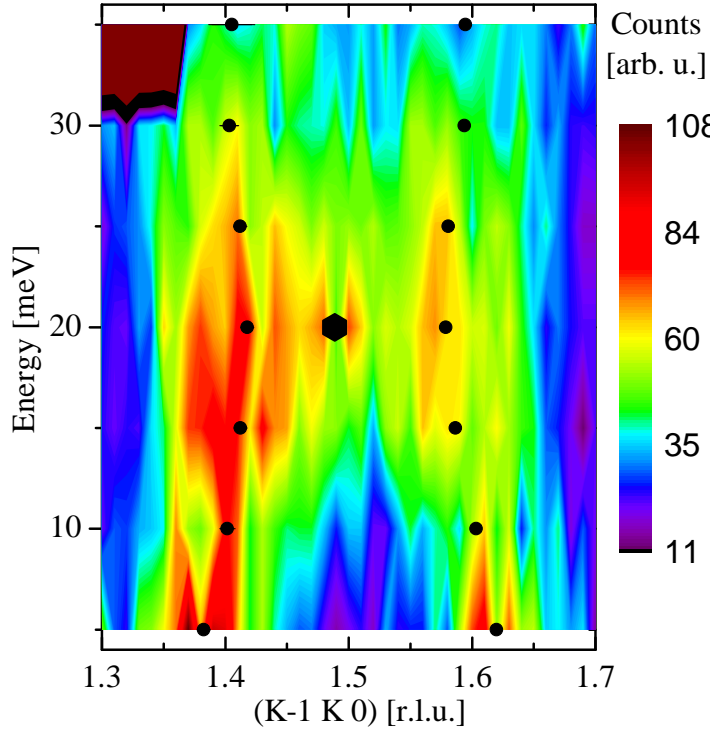


Figure 4.25: Magnon dispersion in ACK390. The map was obtained by interpolation between the constant energy scans in the SF channel that can be found in Figure 4.23. Peak positions obtained by a double Gaussian fit are indicated (black circles). The larger hexagon symbol at 20 meV corresponds to a single Gaussian fit.

and 20 meV the authors [235] also applied the before mentioned LSWT model for $|J_b| \ll |J_a|$ [234]. They found this model incompatible with the derived values of $J_a = 28(3)$ meV and $J_b = 17(3)$ meV for their sample [235]. Also the introduction of additional exchange parameters, for a diagonal next nearest neighbor coupling between - J_c and within - J_d stripe domains did not enable them to reproduce the observed inward shift [235].

Regarding this, a comparison of the low energy excitation spectra with the predictions of LSWT seems inadequate, since this theory predicts cones of spin excitations which are absent in the studied nickelate samples. At the same time there is little doubt that these cones generally exist at higher energies $E \geq 30$ meV, as has been confirmed by experiments on charge-stripe ordered samples. Also the sample with the reported inward dispersion exhibits a pronounced spin-wave-cone-like dispersion already between 30 meV and 40 meV [235]. For our samples we did not observe such a shape in the constant energy maps up to 35 meV. Instead, the measured intensity at this energy range is already quite weak and no final conclusion for the high energy spectrum is possible. Compared to the sample studied in [235] our samples exhibit a much smaller incommensurability. This might be attributed to the different doping method. Our measurements suggest a relation between the lowest reachable incommensurability and the amount of strontium doping compared to oxygen doping. The smallest ϵ within the series of nickelate samples was obtained for a pure strontium doped sample while the mixed doped sample already exhibits a much higher value.

A striking similarity between the studied samples within the $\epsilon \leq 0.25$ regime is, that they all exhibit a large amount of disorder. This is expressed through a limited in plane correlation length ($\xi_{\perp} \approx 50$ Å, 69 Å and 21 Å for the pure oxygen, mixed and pure strontium doped samples, respectively) and a significant broadening of the inelastic intensities. For the oxygen doped sample in [235] the authors argue that their sample is close to the border between stripe and AF order. The same is probably true for our samples.

It seems doubtful that the small amount of co-doped nonmagnetic zinc has a strong direct influence on the magnetic properties of our nickelates. Instead, the observed low energy deviations from the ideal LSWT could be induced by the increasing disorder in the intermediate doping range between commensurate and incommensurate magnetism. Zinc co-doping then further increased the disorder already present in strontium doped nickelates.

Recently, M. Rotter and A. Komarek [236] successfully modeled an hour-glass dispersion for a locally disordered spin configuration in the isostructural cobaltates (see Chapter 5). Due to the high intrinsic disorder present in the here measured nickelates a similar approach would be justified. Instead of the disordered checkerboard charge order present in the cobaltates, a disordered stripe scenario might similarly be applied to explain the observed spectra. A

necessary condition to simulate the hourglass spectrum in the cobaltates is the large difference between the nearest neighbor coupling J and the next nearest neighbor coupling J' . Within the nickelates the coupling constants only differ by less than a factor two. This might be responsible for the differences in the observed dispersion relations and the absence of an hourglass spectrum within the nickelates.

Ideally a microscopic model should also be able to explain the low energy deviation from LSWT in the ordered charge stripe regime. But this is a task for the future. It would be interesting to measure the high energy spectrum to answer the question whether spin wave cones are also present in our samples. Ideally this could be done with a time of flight spectrometer where it is possible to map the whole (\vec{Q}, ω) space in a single magnetic Brillouin zone at a small Q value. Another important task is to test with high accuracy whether charge stripe peaks can still be observed in our disordered samples.

Chapter 5

$\text{La}_{2-x}\text{Sr}_x\text{CoO}_4$

Results partially published as:

Hour-glass magnetic spectrum in a stripeless insulating transition metal oxide
Y. Drees, D. Lamago, A. Piovano & A.C. Komarek
Nat Commun **4**, 2449 (2013)

DOI: 10.1038/ncomms3449

URL: <http://dx.doi.org/10.1038/ncomms3449>

and:

Hour-glass magnetic excitations induced by nanoscopic phase separation in cobalt oxides
Y. Drees, Z.W. Li, A. Ricci, M. Rotter, W. Schmidt, D. Lamago, O. Sobolev, U. Rütt,
O. Gutowski, M. Sprung, A. Piovano, J. P. Castellan, & A. C. Komarek
Nat Commun **?**, ???? (2014)

DOI: 10.1038/ncomms6731

URL: <http://dx.doi.org/10.1038/ncomms6731>

An hourglass magnetic excitation spectrum has been observed in most high-temperature superconducting cuprates and appears to be a unifying property of these materials [47–49, 52, 150, 237–243]. Fluctuating charge stripes or alternative band structure approaches are able to explain the origin of these spectra. The charge stripe scenario is the one with the largest support [47, 244, 245]. An alternative scenario involves spin excitations arising from umklapp-scattering [246]. Surprisingly an hour-glass spectrum was recently also reported for a layered cobaltate with the composition $\text{La}_{5/3}\text{Sr}_{1/3}\text{CoO}_4$ [181]. The absence of a Fermi surface in this insulating compound indicates that band structure effects are not needed for the appearance of the hour-glass spectrum. Very recently theoretical calculations based on a disordered charge-stripe model have succeeded in reproducing the basic features of the hour-glass dispersion in the $x = 1/3$

doped cobaltate [247].

Incommensurate magnetic superstructure reflections at diagonal positions in reciprocal space have been reported for the $\text{La}_{2-x}\text{Sr}_x\text{CoO}_4$ system [174]. It is believed, that charge stripes are also present in cobaltates [67, 181]. Weak direct evidence for the expected charge order peaks has been reported for a sample with composition $\text{La}_{1.6}\text{Sr}_{0.4}\text{CoO}_4$ [140]. However, whereas the incommensurate magnetic peaks can be clearly observed in the cobaltates, the corresponding unambiguous observation of sharp and well separated charge-stripe ordering superstructure reflections is missing. Also disordered magnetic contributions spread around half integer positions in reciprocal space could be an alternative explanation for the reported features in $\text{La}_{1.6}\text{Sr}_{0.4}\text{CoO}_4$.

According to the phase diagram that has been established for the strontium doped 214-cobaltates low temperature incommensurate magnetism only occurs in the doping range $0.33 \leq x \leq 0.6$ (see Section 1.4) with incommensurabilities $\epsilon \lesssim 0.5$ [67]. At low doping a structural transition to an orthorhombic phase occurs with nearest neighbor AF ordering at even lower temperatures. In the doping range around $x = 0.5$ a very robust checkerboard charge order (CBCO) appears with incommensurate (IC) magnetism at comparably such low temperatures that it can be viewed as essentially decoupled from the charge order [176]. No magnetic order has so far been reported for the high doped region $x > 0.6$. This is probably related to the difficulties arising for the floating zone single crystal growth with very high strontium concentrations.

Apart from the important question whether charge-stripe order (CSO) also exists in the cobaltates also other issues are not yet treated conclusively. Obviously the boundary of the CBCO has not yet been established. While it seems clear that half doping $x = 0.5$ is the ideal composition for its occurrence, the stability of this phase, which can be inferred from the high transition temperature, suggests that it should continue away from ideal doping to some extent. Another peculiarity is the linear decrease of the magnetic phase transition temperature with doping, even across the phase boundary between commensurate and incommensurate antiferromagnetism. It also seems that the suppression of the orthorhombic phase has no effect on the magnetic ordering whatsoever. If the structural and magnetic ordering phenomena are fully decoupled it appears unlikely that both are suppressed at the same doping concentration. Z. Li, A. Komarek and the author synthesized $\text{La}_{2-x}\text{Sr}_x\text{CoO}_4$ cobaltates in the whole doping range $0 \leq x \leq 1$ to perform a comprehensive study and shed some light on the open questions. The main focus in this thesis was placed on the samples with IC magnetic order where the ongoing debate about the nature of this phase will be conclusively addressed.

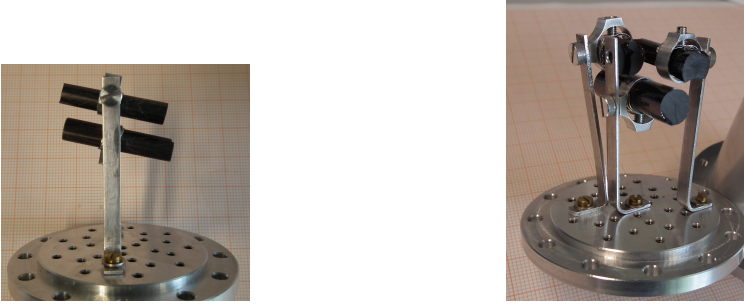


Figure 5.1: Co-aligned cobaltate crystals $\text{ACK183-La}_{5/3}\text{Sr}_{1/3}\text{CoO}_4$ and $\text{ACK305-La}_{1.6}\text{Sr}_{0.4}\text{CoO}_4$.

5.1 Sample and TAS Instrument Setup

Neutron spectroscopy measurements on HTSC cuprates are regularly difficult to interpret. The small static magnetic moment ($0.6 \mu_B$ in La_2CuO_4 [241]) results in low peak intensities. Due to small incommensurabilities the measured magnon dispersion branches are often too close to be resolved at low and intermediate energies. In contrast, the insulating cobaltates exhibit larger magnetic moments and incommensurabilities. In addition, they are free of obscuring effects from itinerant electrons and arising superconductivity and are therefore well suited as a toy model for further investigations into the mechanics behind the hourglass dispersion.

Similar to the nickelates discussed in Chapter 4 our cobaltate samples were mounted so that the ab-plane coincided with the scattering plane of the TAS instruments. Mostly two or three cylindrical pieces with a length up to 3.5 cm and a diameter of about 0.8 cm were co-aligned at our real time Laue camera (see Figure 5.1). Elastic and inelastic neutron scattering (INS) at low temperature has been performed with the TAS instruments at the Laboratoire Leon Brilluin (LLB) in Saclay and the at the Institute Laue Langevin (ILL) in Grenoble. Where possible, all elastic and inelastic scans at thermal TAS have been performed in constant- k_f -operation mode with $k_f = 2.662 \text{ \AA}^{-1}$. Only when it was necessary to reach higher energies at a given small scattering vector \vec{Q} the final wavenumber was changed to $k_f = 4.1 \text{ \AA}^{-1}$. Error bars of neutron scattering intensities are calculated by the square root of the neutron counts.

The individual TAS instrument setup was as follows:

1T1 LLB, thermal neutrons, two PG filters, fixed focusing PG-002 monochromator and analyzer.

- 2T1** LLB, thermal neutrons, two PG filters, vertical focusing PG-002 monochromator and flat PG-002 analyzer.
- IN8-magnons** ILL, thermal neutrons, two PG filters, double- focusing PG-002 monochromator and analyzer.
- IN8-phonons** ILL, thermal neutrons, two PG filters, double-focusing Cu-200 monochromator and PG-002 analyzer.
- IN8-Flatcone** ILL, thermal neutrons, Flatcone detector (see Section 4.4)
- IN22** ILL, thermal neutrons, PG filter, fixed vertical focusing (125mm) and flat horizontal Heusler(111) monochromator and analyzer, Spherical polarization analysis with the installed CRYOPAD polarimeter, flipping ratio ≈ 16 .
- IN12** Cold neutrons, velocity selector, double focusing PG-002 monochromator and horizontal focusing Heusler(111) analyzer, incident beam polarization with a polarizing cavity, for longitudinal polarization analysis a setup of three 120° shifted horizontal coils and a vertical Helmholtz coil were used, flipping ratio ≈ 17.4 .
- 4F.2** LLB, Cold neutrons, Be-filter at 77K, $k_f = 1.55 \text{ \AA}^{-1}$, vertical focusing PG-002 double monochromator and flat PG-002 analyzer.

5.2 HTT-LTO Phase Transition

5.2.1 High Resolution Powder X-ray Diffraction

Situated at the ID31 beam tube at the synchrotron ESRF in Grenoble, France, this high-resolution powder diffraction beamline is optimized for powder samples in a borosilicate capillary. It uses a cryogenically cooled Si(111) double-crystal monochromator and nine single counter detectors at an angular distance of 2° , each equipped with its own Si(111) analyzer. For our measurements with 31 keV X-rays the cryostream environment was mounted. The ideal capillary diameter to prevent strong absorption effects was calculated to 0.2 mm. A fast sample spinner ensured a smooth diffractogram despite the small amount of crystallites in the beam.[248]

For the two samples ACK305- $\text{La}_{1.6}\text{Sr}_{0.4}\text{CoO}_4$ and ACK317- $\text{La}_{1.64}\text{Sr}_{0.36}\text{CoO}_4$ powder diffractograms were recorded at ambient temperature and at 80 K. The ambient temperature measurement of ACK317 is plotted in Figure 5.2. While powder diffractograms measured with conventional in house diffractometers contain many overlapping peaks, especially at high angles, the patterns recorded

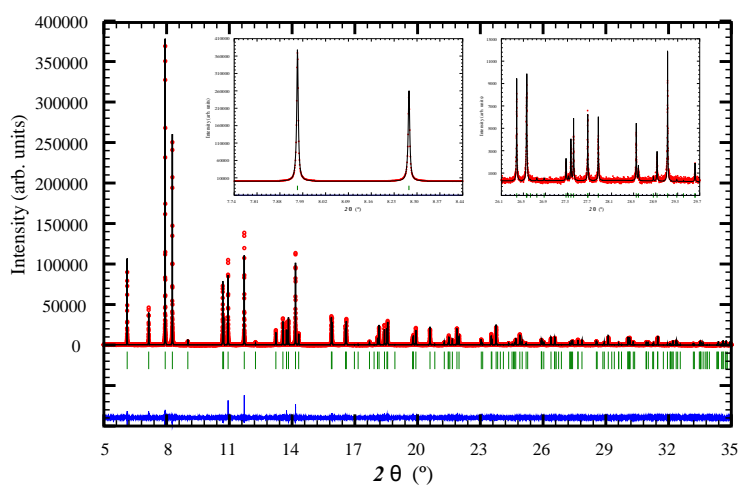


Figure 5.2: Diffractogram of the $x = 0.36$ doped sample ACK317 at room temperature. Data recorded at beamline ID31 in red color. Rietveld fit to the data in black. Bragg positions are indicated by green vertical bars. Difference between data and fit plotted in blue color. *Left inset*: enlarged peaks (1 0 3) (left) and (1 1 0) (right) around 8° . *Right inset*: peak profile at high scattering angles.

sample	doping	(110) 80K	(200) 80K	(110) 305K	(200) 305K
ack305	x = 0.4	0.00418(7) $^\circ$	0.00432(7) $^\circ$	0.00403(6) $^\circ$	0.00461(9) $^\circ$
ack317	x = 0.26	0.00633(10) $^\circ$	0.00554(3) $^\circ$	0.00613(9) $^\circ$	0.00554(6) $^\circ$

Table 5.1: Temperature dependence of the FWHM determined by Lorentz fits to the Bragg reflections (110) and (200).

at the ID31 consist of Bragg peaks standing out like delta functions (see insets in Figure 5.2). Due to the high instrumental resolution of about 0.003° at a diffraction angle $2\theta \approx 10^\circ$ [248] even tiny changes in lattice constants can be resolved at the ID31. A Rietveld refinement of an orthorhombic model was applied to the low temperature data but no improvement compared to the ambient temperature data fit could be observed.

A direct comparison of the peak width at different temperatures is more sensitive to small structural distortions. A splitting of the (1 1 0) reflection is indicative for the HTT to LTO transition that was observed in the low doped cobaltates. The fitted peak widths are summed in Table 5.1. While a transition temperature of 227 K was reported for the HTT to LTO transition in a x = 0.3 doped sample [174] it appears that the transition is already fully suppressed down to 80 K at a doping of x = 0.36. The small peak width close to the resolution limit of the instrument confirms the high quality of our floating zone grown single crystals.

5.2.2 Neutron Diffraction

As mentioned in Section 1.3 the HTT to LTO phase transition is related to the coordinated tilting of oxygen octahedra. We can benefit from the sensitivity of neutron measurements to oxygen order which results in comparably strong superstructure reflections even for small structural distortions. The (1.5 1.5 0) reflection, apparent at low temperature in our sample ACK312- $\text{La}_{1.67}\text{Sr}_{0.33}\text{CoO}_4$, is not a valid reflection for the tetragonal unit cell. Consequently it vanishes upon heating. The temperature dependent measurement is shown in Figure 5.3. From the disappearance of the peak intensity between 191 K and 211 K we can estimate the structural phase transition temperature to $T_S \approx 200(10)$ K.

Our value is remarkable close to the one reported for a x = 0.3 doped sample, $T_S = 227$ K in [174]. Together with our observation that no structural transition occurs in the x = 0.36 doped sample above 80 K this suggests a kink in the slope of the boundary between the HTT and LTO phases. An alternative scenario is, that the sample measured in [174] had a somewhat different composition than the nominal values. A discrepancy between the measured lattice constants on our samples compared to those investigated in [140], which are the same as

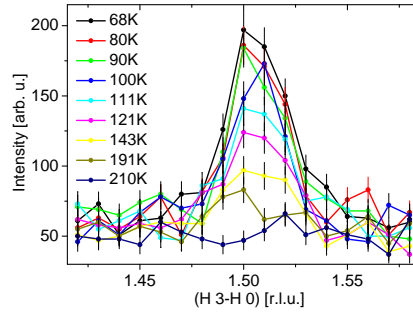


Figure 5.3: Temperature dependence of the $(1.5\ 1.5\ 0)$ orthorhombic superstructure reflection in our $x = 0.33$ doped sample ACK312.

in [174], has also become apparent in Section 3.2. As discussed in Section 1.5 especially the oxygen content in these layered perovskites is difficult to control.

5.3 Spin and Charge Order

5.3.1 Low Energy Synchrotron Diffraction

One possibility to probe charge order in our cobaltate samples is the measurement with X-rays. In contrast to neutrons that are only sensitive to the expected charge superstructure through resulting atomic displacements, X-rays are directly sensitive to a modulation in the charge density. We used the MPI beamline at ANKA in Karlsruhe to probe our cobaltates in reflection geometry. To avoid the strong cobalt fluorescence at about 8 KeV we used an X-ray energy of 10 keV, corresponding to a wavelength of about $\lambda = 1.2398\text{ \AA}$. The instrument operates in vertical geometry. A double crystal monochromator with a pair set of Si(111) crystals ensures monochromatic radiation. A set of two slits before and after the sample was used to reduce the beam size to 1 mm^2 .

To access charge order reflections with different L values we cut our samples, so that the $(1\ 1\ 1)$ direction was normal to the largest surface our cuboid with dimensions $2.5 \cdot 2.5 \cdot 1.5\text{ mm}^3$ (see Figure 5.4, *Left*). One of the other two surfaces was perpendicular to $(1\ -1\ 0)$. Because the system is orthorhombic the third direction was only roughly the $(-1\ -1\ 2)$ direction. One of the $(1\ 1\ 1)$ planes was polished on a textile mesh using $1\text{ }\mu\text{m}$ sized diamond crystallites.

The sample was glued with silver paint on a copper sample holder so that the $(1\ -1\ 0)$ direction coincided with the ω' rotation. This way the accessible scattering plane perpendicular to ω' contained the $(0\ 0\ 1)$ and $(1\ 1\ 0)$ reflections and consequently all linear combinations of those two vectors were also reachable (as long as both, incoming and outgoing beam remain above the crystal surface).

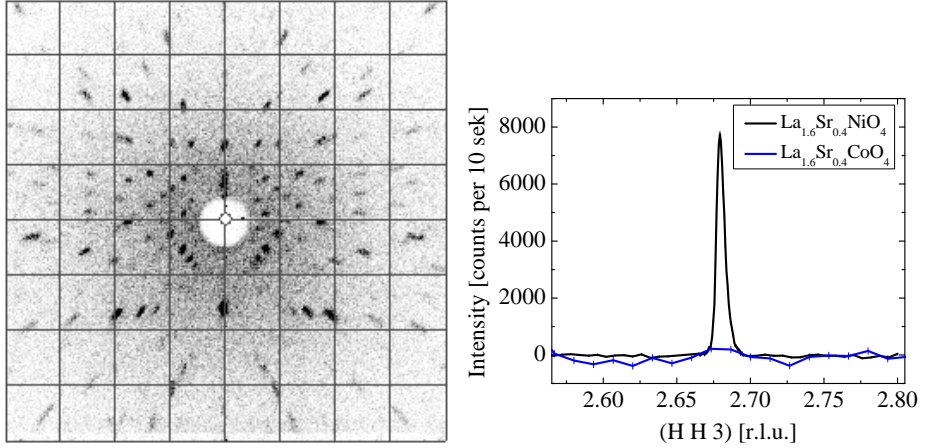


Figure 5.4: *Left*: Laue image of the (1 1 1) crystal surface. *Right*: Comparison of the measurements on the $x=0.4$ nickelate reference sample and a $x=0.4$ doped cobaltate. Both scans have been corrected by a linear background.

While the (1 1 1) surface of our samples was determined with an accuracy better than 0.5° , the other directions had an uncertainty of about 3.5° from cutting and gluing the sample. In combination with a much better resolution (FWHM of the (2 2 2) reflection with opened slits between sample and detector was 0.034° in ω' for the $x=0.4$ sample ACK305) the reciprocal space becomes quite vast, compared to TAS experiments, when searching for structural Bragg reflections to determine the orientation matrix.

Finally we could observe the charge superstructure reflections at low temperature (7.8 K) in our $x=0.4$ nickelate reference sample ACK326. As expected the intensities appeared at incommensurate positions in our scans with odd L values. This proved the general suitability of this method to search for charge modulations also in cobaltates. Despite much effort we did not succeed in finding similar charge order peaks in the cobaltate. In Figure 5.4, *Right* two scans are plotted for direct comparison between the reference nickelate and a similarly doped cobaltate sample. While the nickelate clearly shows an incommensurate charge order peak, it is absent in the cobaltate.

5.3.2 Elastic Neutron TAS Measurements

The incommensurability ϵ in charge stripe ordered nickelates $\text{La}_{2-x}\text{Sr}_x\text{NiO}_{4+\delta}$ was found to follow the trend $\epsilon = n_h = x + 2\delta$ with the hole concentration n_h , strontium doping concentration x and oxygen off stoichiometry δ . This dependency can be naturally understood considering charge stripe phases since the

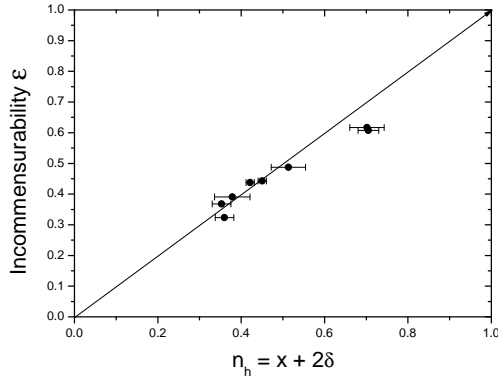


Figure 5.5: Relation between hole concentration and incommensurability in $\text{La}_{2-x}\text{Sr}_x\text{CoO}_{4+\delta}$ samples. ϵ error bars are smaller than the symbol size. The hole concentration was calculated based on the oxygen concentrations determined in Chapter 3 and the nominal strontium concentrations. The black line is a guide to the eye and indicates the ideal values according to $\epsilon = n_h$. Data has been collected on the instruments 1T1, 2T1, IN22 and IN8.

stripe spacing is directly related to the hole concentration (see Section 1.10.2). The fact that this trend was also observed in cuprates and cobaltates can be used as an argument that charge order must be present in these systems, too.

As a standard procedure we characterized the low temperature magnetic Bragg intensities of all samples prior to further investigations. The incommensurability was estimated from Gaussian fits to the two symmetric peaks apparent in the $(H\ 1-H\ 0)$ scans. Similar to the nickelates we determine the incommensurability with respect to the structural unit cell for better comparison: $\epsilon = \epsilon_{ch} = 2\epsilon_{mag}$. Where ϵ_{mag} is the distance between the magnetic satellite and the AF wave vector $(0.5\ 0.5\ 0)$ in units of the reciprocal lattice.

Results for the evaluated incommensurability of the characterized cobaltates are plotted in Figure 5.5. An overall relation between hole concentration and incommensurability could be confirmed for our samples. The comparably large error bars of the hole content n_h are due to uncertainties in the oxygen (and strontium) concentration determination (see Chapter 3). The deviation from the ideal relation $\epsilon = n_h$ can be quite large for individual samples. A systematic study on the relation between holes and incommensurability would be useful since the hole concentration could be determined much more accurate via the incommensurability.

Charge stripes in the nickelates have been found to be most stable around the doping $x = 1/3$ (see e.g. Sections 1.10.2 and 4.2). Note, that due to the stripe

periodicity of three lattice constants, this phase is actually commensurate with the lattice. For our sample ACK312 with nominal composition $\text{La}_{1.67}\text{Sr}_{0.33}\text{CoO}_4$ the diagonal scan to characterize the incommensurability shows only a broad peak at the commensurate AF position (0.5 0.5 0). This is in accordance with the results published in [174] for a $x = 0.3$ doped sample where also a broad AF peak was observed at low temperature. Consequently their sample was assigned to the commensurate regime.

To gain further insight into the transition from commensurate to incommensurate magnetic order the whole area around the AF wave vector has been measured at 10 K and at 150 K above the magnetic ordering temperature of about 127 K (see Appendix Figure 6.4). The high temperature data was subtracted from the 10 K data and the resulting map is shown in Figure 5.6.

Surprisingly the shape of the measured intensity exhibits a pronounced anisotropy. A diagonal scan through the structural (1 1 0) reflection is plotted on the right side for comparison (the peak is resolution limited and no additional intensity can be observed). Therefore, the observed diagonally enhanced magnetic intensity can not be attributed to a poor sample quality. Apparently we found a sample at the edge of the AF phase which is still in the orthorhombic regime (see Section 5.2.2). The AF nearest neighbor ordering at this doping concentration is already sufficiently disturbed to allow incommensurate magnetic ordering and we observe a highly disordered antiferromagnetic state which is close to the incommensurate regime.

In the nickelates the magnetic transition temperature drops significantly in the intermediate region between nn-AF and 1/3-stripe order. This is in good agreement with the stripe scenario and the observation of a maximized stability for 1/3-stripe phase. In contrast, the magnetic ordering temperature exhibits a monotone decrease in the cobaltates, even across the transition from commensurate to incommensurate order. While this would be totally accidental in the stripe scenario, the frustration scenario naturally implies a continuous transition.

Representative for our efforts to identify charge order superstructure reflections with neutron diffraction in the cobaltates within the doping range $0.33 \leq x \leq 0.4$, a concluding study on the sample ACK305 with composition $\text{La}_{1.6}\text{Sr}_{0.4}\text{CoO}_4$ is presented in Figure 5.8. In contrast to other studied cobaltates within the incommensurate magnetic regime our sample exhibits comparably sharp incommensurate magnetic peaks. This implies that much less disorder is present compared to previously studied compounds. It has been shown in [247] that the sharpness of the charge stripe order (CSO) signal should be roughly equal to the sharpness of the IC magnetic peaks in a CSO scenario for $\text{La}_{2-x}\text{Sr}_x\text{CoO}_4$. Hence, our $\text{La}_{1.6}\text{Sr}_{0.4}\text{CoO}_4$ material seems to be an ideal system to study any possible relation between IC magnetic peaks and charge

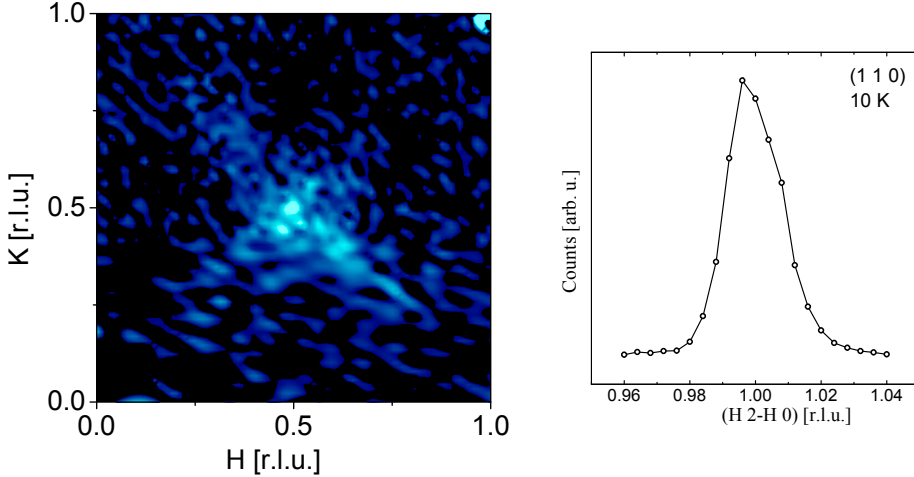


Figure 5.6: *Left:* Reciprocal space map in the HK0-plane for ACK312 measured on the 1T1 at 10 K (150 K background subtracted). *Right:* Shape of the (1 1 0) structural Bragg reflection for Comparison.

stripes in layered cobaltates.

To calculate the expected intensity of the presumed CSO peak we used the relation:

$$I_{calc\ CSO}^{x=0.4} = \alpha \cdot I_{magn}^{x=0.4} \cdot \frac{I_{CSO}^{LSNO}}{I_{magn}^{LSNO}} \quad (5.1)$$

with

$$\alpha = \frac{m_{Ni}^2}{m_{Co}} \cdot \frac{u_{Co}^2}{u_{Ni}} \approx 1 \quad (5.2)$$

Finally we were not able to detect any signal indicative for CSO in $\text{La}_{1.6}\text{Sr}_{0.4}\text{CoO}_4$ (see Figure 5.8). Instead, only one broad peak at half-integer positions appears that is indicative for a (disordered) CBCO state persisting up to high temperatures, very similar to the optimum half-doped compound $\text{La}_{1.5}\text{Sr}_{0.5}\text{CoO}_4$ (dashed line in the Figure). Thus, we managed to find a $\text{La}_{2-x}\text{Sr}_x\text{CoO}_4$ sample within the CBCO ordered regime which exhibits clearly incommensurate magnetism.

5.3.3 Hard X-ray Single Crystal Measurements

The synchrotron radiation single crystal X-ray diffraction measurements have been performed at the beamline P07 at PETRA-III at DESY using 100 keV hard

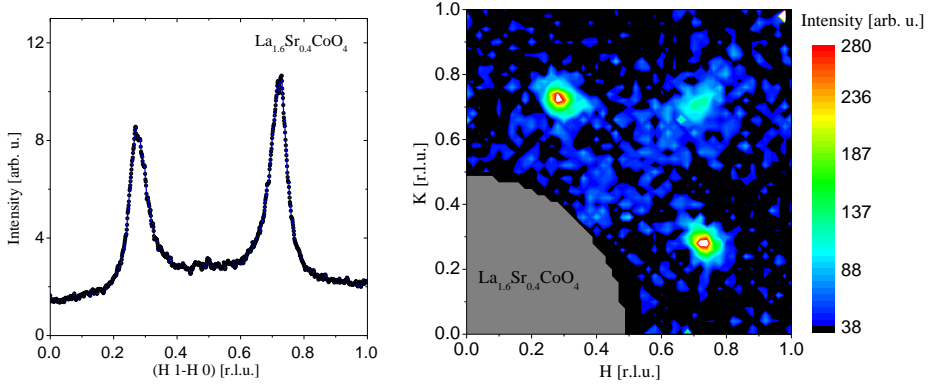


Figure 5.7: Elastic neutron diffraction measurements of incommensurate magnetic intensities in $\text{La}_{1.6}\text{Sr}_{0.4}\text{CoO}_4$ measured at the 2T1. *Left:* Magnetic peaks measured in a diagonal scan across $(1/2 \ 1/2 \ 0)$. *Right:* Low temperature neutron-scattering intensities in the $\text{HK}0$ -plane. The 200 K background has been subtracted from the 12 K data.

X-rays monochromatized by a bent Si(111) double monochromator. We measured in transmission geometry and the signal was analyzed with a Si-Ge(111) gradient crystal analyzer and detected with a point detector. The measured samples were roughly mm^3 -sized single crystals with the (001)-direction along the longer axis. The other directions were (100) and (010). Slits before the sample were used to decrease the beam profile to 1.1 mm times 1.15 mm with a roughly square shaped homogeneous intensity distribution. The samples were fixed on copper sample holders using silver glue before mounting inside the dilplex cryostat.

Here we mainly studied the charge and magnetic correlations in $\text{La}_{5/3}\text{Sr}_{1/3}\text{CoO}_4$, which is distinctly away from the checkerboard charge order regime. In [181] this composition was labeled to be within the “diagonal stripe phase” of $\text{La}_{2-x}\text{Sr}_x\text{CoO}_4$. In Figure 5.9 the commensurate magnetic peaks of this compound are shown and compared with a $\approx 1/3$ hole-doped charge stripe ordered LSNO reference sample. The charge stripe ordered nickelate exhibits extremely sharp magnetic peaks which is in contrast to the observations for $\text{La}_{5/3}\text{Sr}_{1/3}\text{CoO}_4$ (inset in Figure 5.9 (d)).

Since magnetic and charge stripe ordering reflections fully overlap in these $\approx 1/3$ hole-doped layered materials, we studied the charge correlations at the

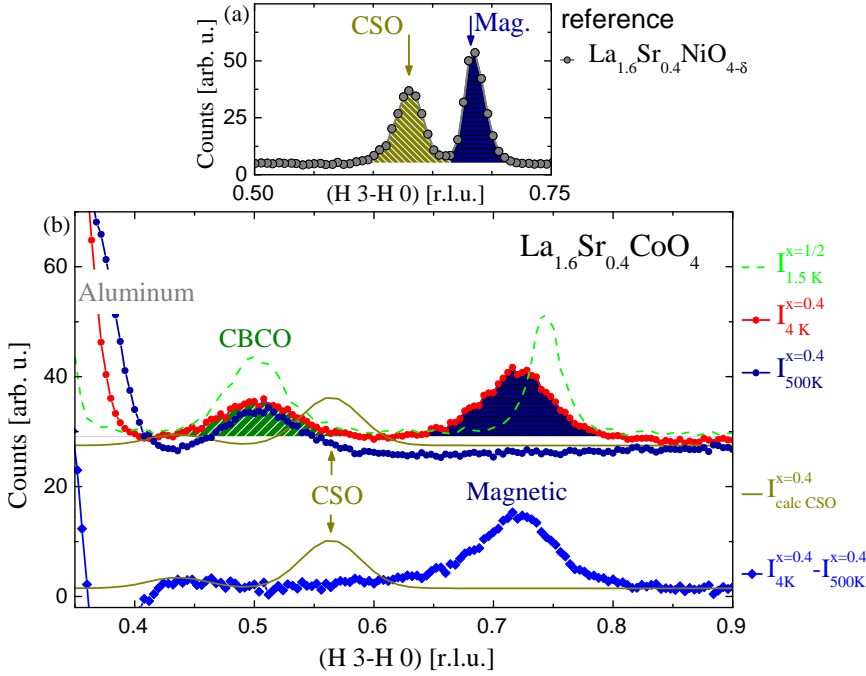


Figure 5.8: Elastic neutron diffraction study of charge and magnetic correlations in $\text{La}_{1.6}\text{Sr}_{0.4}\text{CoO}_4$ measured at the 2T1. (a) The reference sample $\text{La}_{1.6}\text{Sr}_{0.4}\text{CoO}_{4+\delta}$ exhibits incommensurate magnetic well as CSO superstructure intensities in the diagonal $(H \ 3-H \ 0)$ scan at 1.5 K. (b) A similar scan at 1.5 K on the reference sample $\text{La}_{1.5}\text{Sr}_{0.5}\text{CoO}_4$ reveals a CBCO peak at $(0.5 \ 2.5 \ 0)$ and a magnetic peak at $\approx(0.75 \ 2.25 \ 0)$ (green dotted line). For $\text{La}_{1.6}\text{Sr}_{0.4}\text{CoO}_4$ the scan has been performed at 4 K (dark blue circles) and at 500 K (cyan circles). In the lower part the difference intensity (4 K - 500 K) is plotted (blue diamonds). For comparison the expected CSO intensity has been calculated (light brown line, calculations see text).

synchrotron using hard X-rays. In these highly precise synchrotron measurements we were not able to detect any indications for charge stripe ordering reflections in $\text{La}_{5/3}\text{Sr}_{1/3}\text{CoO}_4$ with an extremely high accuracy of roughly 10^{-9} of a strong Bragg reflection.

According to [168, 249] charge-order superstructure scattering in LSNO always peaks at $(\epsilon \in L)$ with odd L , whereas the magnetic scattering exhibits peaks for odd and even L . The unit cell used to describe the K_2NiF_4 structure is $I4/mmm$. Due to the body centering the reflection $(0\ 0\ 1)$ is not a valid Bragg point and propagation vectors $(\epsilon \in L)$ with odd and even L are not equivalent but refer to 180° or zero phase shift for the modulation of the two nickel sites at $(0\ 0\ 0)$ and $(0.5\ 0.5\ 0.5)$. The coulomb forces require always anti-phase stacking of the charge ordering, which is also in agreement with the finite dispersion of phonons perpendicular to the planes [250]. In contrast, both, in-phase and anti-phase, magnetic stacking is possible.[67]

In Figure 5.9 (a) and (b) we show the measured intensities together with the intensities observed for a $\approx 1/3$ hole-doped nickelate reference sample. As can be seen in the direct comparison, charge stripes can be excluded for the cobaltate system. Especially since the Co^{+2} and Co^{+3} -ions exhibit distinctly bigger differences in their ionic radii than the corresponding Ni-ions such that any occurring stripe phases should be easier to detect in cobaltates than in nickelates. Also for propagation vectors with odd L -values we find no indications for charge stripes. Instead we observe weak intensities at half-integer H and K positions for even values of L which survive up to room-temperature (see Figure 5.9 (c) and (d)). This important finding indicates that the checkerboard charge ordering correlations still survive also far away from half doping, i.e. down to $1/3$ -doping in the $\text{La}_{2-x}\text{Sr}_x\text{CoO}_4$ system and that there are simply no disordered charge stripe phases in this entire incommensurate magnetic regime of the cobaltate system. Instead, checkerboard charge ordered regions with roughly $7(2)\text{ \AA}$ correlation length, estimated from Lorentzian peak fits, appear. The remaining Co^{+2} -ions have to be distributed somewhere into the cobalt oxygen planes since the hole-doping in $\text{La}_{5/3}\text{Sr}_{1/3}\text{CoO}_4$ is far below half-doping. Hence, checkerboard charge ordered regions have to be interspersed with La_2CoO_4 -like undoped islands within a nano-phase separation scenario.

5.4 Electron-Phonon Coupling

Charge stripes in single layered perovskites have been found to induce an electron-phonon coupling in related compounds. In the isostructural cuprates giant electron-phonon anomalies have been established for the high-energy Σ_1 CuO bond-stretching phonon modes [251]. The wave vectors at which the anomaly was observed correspond to the incommensurability of the charge order. Similar,

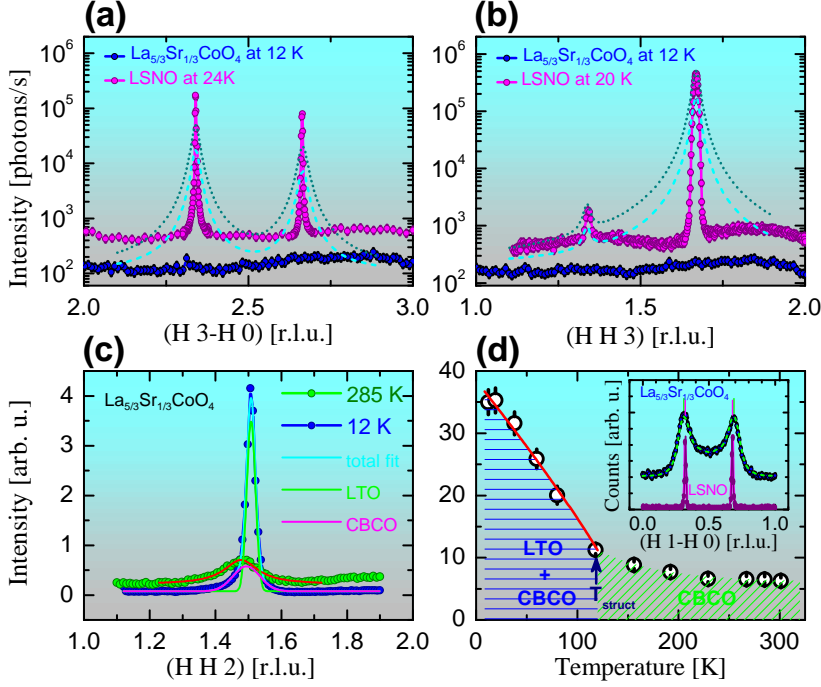


Figure 5.9: Hard X-ray synchrotron radiation single crystal diffraction at beamline P07 at Petra-III. (a) and (b) Intensities measured in (H 3-H 0) and (H H 3)-scans for La_{5/3}Sr_{1/3}CoO₄ and a $\approx 1/3$ hole-doped LSNO reference sample. Strong fundamental Bragg reflections are of the order of 10^{10} counts per second. Intensities have been normalized to the monitor in order to enable a comparison of cobaltate and nickelate reference sample. The dashed lines are Lorentzian peaks with the same integrated intensity as fitted to the charge stripe ordering peaks of the LSNO reference sample but with peak widths that have been multiplied by the width ratio derived from incommensurate magnetic peaks of both compounds measured with neutrons (see inset of (d)). The dotted lines are additionally normalized to the (200) peak intensities in order to take also account for the measured sample volume. Apparently no diagonal CSO like in the nickelates could be observed for La_{5/3}Sr_{1/3}CoO₄. (c) Instead, weak CBCO reflections appear at half integer positions for even values of L already at ambient temperature. Below the structural transition $\text{HTT} \rightarrow \text{LTO}$ additional sharp octahedral tilting reflections appear on top of the broad CBCO reflections. (d) Temperature dependence of the total integrated intensity around the half integer peak position. A neutron diffraction measurement across magnetic satellites in $\approx 1/3$ doped cobaltates and nickelates measured at the thermal triple axis spectrometer IN8 is shown in the inset.

it has been demonstrated on a $x = 0.2$ Sr-doped nickelate sample that an anomalous phonon softening occurs at phonon propagation vectors that perfectly agree with the propagation vector of the CSO in that compound [223]. Consequently we have measured the high-frequency Σ_1 phonon dispersion on our cobaltate samples in order to search for signatures of charge ordering. Diagonal charge stripes with a periodicity of three ($\epsilon = 1/3$) would couple to the Co-O bond-stretching phonon mode at the corresponding propagation vector ($\vec{Q} = \vec{q}_{\text{Bragg}} + (\epsilon \in 0)$). Analogous, the polarization pattern for CBCO with a periodicity of two, leads to an anomaly at the zone boundary ($\text{H}_{\text{Bragg}} + 1/2 \text{ K}_{\text{Bragg}} + 1/2 \text{ L}$). Some exemplary phonon scans of $\text{La}_{1.6}\text{Sr}_{0.4}\text{CoO}_4$ and $\text{La}_{1.6}\text{Sr}_{0.4}\text{NiO}_4$ are presented in Figure 5.10. Intensity energy maps have been interpolated from the constant-Q scans performed on the $x = 0.4$ doped cobaltate and nickelate (see Figure 5.11). Some spurious intensities are also present. The scans intersecting with the spurion have therefore not been used for data evaluation. Clearly, an anomalous phonon softening can be observed in the fitted phonon dispersion. Rather than appearing at positions indicative for charge stripes (indicated by black arrows), a softening is observable at $\zeta = 0.5$. In contrast, the nickelate reference with robust diagonal CSO exhibits a phonon softening at the position connected to the measured propagation vector. In fact, even an upturn is observable for $\zeta \rightarrow 0.5$. Our resulting high-frequency Σ_1 phonon dispersion for different doping concentrations ($x = 0, 1/3, 0.4, 0.5$) are summarized in Figure 5.12 for comparison. The data of the undoped compound has also been shifted to higher energies (black dash-dotted line). In contrast to the undoped Co^{2+} compound the strontium doped samples within the CBCO regime with incommensurate magnetism all show a substantial softening of the topmost CoO bond-stretching phonon dispersion towards the zone boundary ($\zeta = 0.5$). Clearly, no dependence between the phonon softening propagation vector and the incommensurability that could be attributed to CSO can be observed. Our results perfectly agree with the scenario obtained from elastic neutron and X-ray diffraction. The anomalous phonon softening at the zone boundary, that is present in the whole doping range $1/3 \leq x \leq 1/2$, is consistent with a robust CBCO persisting at least down to strontium concentrations where the HTT to LTO phase transition is present. This raises the question whether the CBCO and LTO phases are competing ordering phenomena or if they can coexist.

5.5 Magnetic Excitations

We studied the magnetic excitations in the cobaltates on samples with strontium doping $x = 1/3$ and $x = 0.4$. The magnetic excitation spectra of $\text{La}_{1.6}\text{Sr}_{0.4}\text{CoO}_4$ and the reference sample $\text{La}_{1.5}\text{Sr}_{0.5}\text{CoO}_4$ are presented in Figure 5.13. Neutron-scattering intensities determined from different constant-energy scans have been

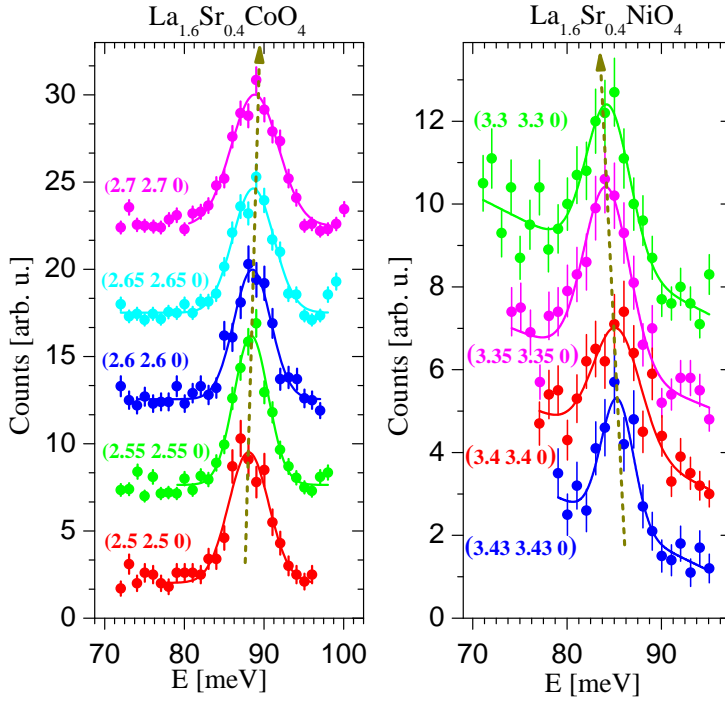


Figure 5.10: Inelastic neutron scattering study for high-frequency Σ_1 CoO bond-stretching phonon modes measured at 1.5 K at the IN8. *Left*: Constant Q-scans for $\text{La}_{1.6}\text{Sr}_{0.4}\text{CoO}_4$ measured at $(3-q \ 3-q \ 0)$. Data has been shifted vertically and colored lines correspond to Gaussian fits to the data. *Right*: Constant Q-scans for the reference sample $\text{La}_{1.6}\text{Sr}_{0.4}\text{NiO}_4$ measured at $(3+q \ 3+q \ 0)$. Data has been shifted vertically and colored lines correspond to Gaussian fits with a sloped background to the data. Dotted lines are guides to the eye.

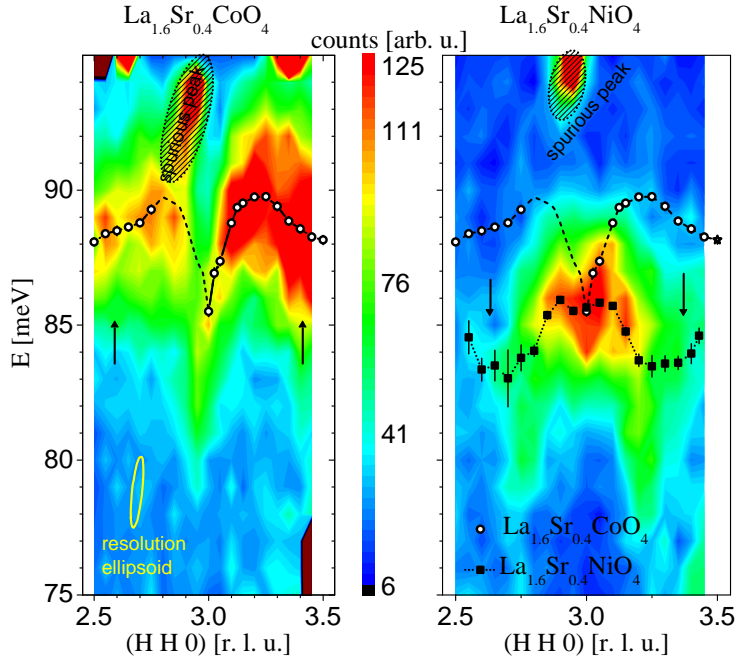


Figure 5.11: Inelastic neutron scattering intensity maps of the Σ_1 CoO bond-stretching phonon modes have been generated from constant Q -scans by interpolation. *Left:* The phonon dispersion for $\text{La}_{1.6}\text{Sr}_{0.4}\text{CoO}_4$ according to Gaussian fits is indicated. *Right:* Phonon dispersion in the reference sample $\text{La}_{1.6}\text{Sr}_{0.4}\text{NiO}_4$ for comparison.

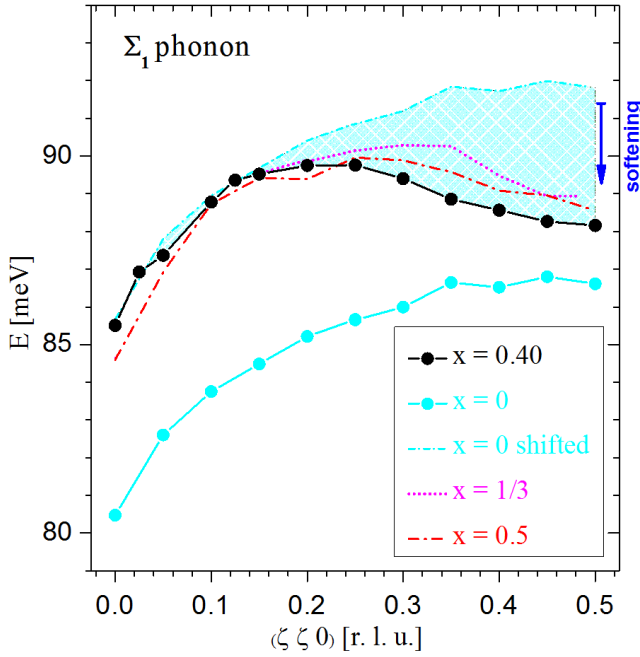


Figure 5.12: High-frequency Σ_1 CoO bond-stretching phonon modes in $\text{La}_{2-x}\text{Sr}_x\text{CoO}_4$ for different sample compositions measured at 1.5 K at the IN8. For better comparison the dispersion for $x = 0$ has also been shifted (cyan circles and cyan line). The softening upon strontium doping is indicated by a blue arrow.

scaled with energy to counter the decreasing scattering cross section. Diagonal scans across $(1/2 \ 1/2 \ 0)$ -Figure 5.13 *right* and $(3/2 \ 1/2 \ 0)$ -Figure 5.13 *left* are indicated by circle symbols. To reach the energies 15 meV - 20 meV in the scans on $\text{La}_{1.6}\text{Sr}_{0.4}\text{CoO}_4$ the final energy was changed to $k_f = 4.1 \text{ \AA}$. A scan at 12.5 meV was performed with both k_f to rescale the intensities. Square symbols correspond to $(\text{H} \ 0.5 \ 0)$ scans plotted as a function of H-1 and H for $x = 0.4$ and $x = 0.5$, respectively. Intensity maps in Figure 5.14 are plotted as a function of Q and energy transfer through $(3/2 \ 1/2 \ 0)$ from scans in $[1 \ 0 \ 0]$ direction (upper panels) and $[1 \ 1 \ 0]$ direction (lower panels). Circle and square symbols correspond to peak positions determined by Gaussian fits to the constant-energy scans in Figure 5.13. In $\text{La}_{1.6}\text{Sr}_{0.4}\text{CoO}_4$ all basic features of an hourglass magnetic spectrum can be observed. That is, an inwards-dispersion of low-energy branches towards the planar AF wave vector while the outward-dispersing branches are suppressed, an increased intensity at the merging around $\approx 20 \text{ meV}$ and an outward dispersion of the high energy branches. Note that the high-energy magnetic excitations in our $x = 0.4$ doped sample resemble on the isotropic high-energy excitations that have been reported for $\text{La}_{1.96}\text{Sr}_{0.04}\text{CuO}_4$ [252]. A constant-Q scan in Figure 5.15 *left*, performed at $\vec{Q} = (3/2 \ 1/2 \ 0)$, shows the energy dependence of the magnetic scattering from a different perspective. At the magnon-merging point an increase of intensity is clearly observable.

To elucidate the low energy dispersion we have studied the magnetic excitations at the cold triple-axis spectrometer 4F.2. In Figure 5.15 *right* a constant Q-scan at an incommensurate magnetic peak position $(1/2 - \epsilon/2 \ 1/2 + \epsilon/2 \ 0)$ measured at $\approx 10 \text{ K}$ is shown. The scan indicates the possible presence of a gap in the spin excitation spectrum which is about $\approx 1.8 \text{ meV}$ wide. Apparently the suppression of inelastic magnetic intensities below this possible gap is not fully complete. An intrinsic peak width of the magnetic modes that arises from short-lived damped magnetic excitations could be the reason. Those damped excitations are probably induced by the high degree of disorder resulting from a random doping of electrons into the ideal CBCO matrix. The vicinity of our $x = 0.4$ Sr-doped sample to the half-doped parent compound $\text{La}_{1.5}\text{Sr}_{0.5}\text{CoO}_4$ suggests a similar origin of the gap which was reported to result from a single ion or small exchange anisotropy within the ab plane [253].

During our studies on the magnetic excitations in $\text{La}_{5/3}\text{Sr}_{1/3}\text{CoO}_4$ we surprisingly observed a so far unknown high-energy magnon band above the entire classical hourglass dispersion (see Figure 5.16 and Figure 5.17). Constant-Q scans at the planar AF wave vector have been measured with polarized neutrons (see Figure 5.16 (a)). The three directions used for longitudinal polarization analysis are: $x \equiv$ polarization along the scattering vector \vec{Q} , $y \equiv$ in plane but $\perp \vec{Q}$ and $z \equiv \perp$ scattering plane and $\perp \vec{Q}$. In-plane polarized excitations that can be detected in the Spin-Flip (SF) channel $\parallel z$ emerge at the “neck” of the

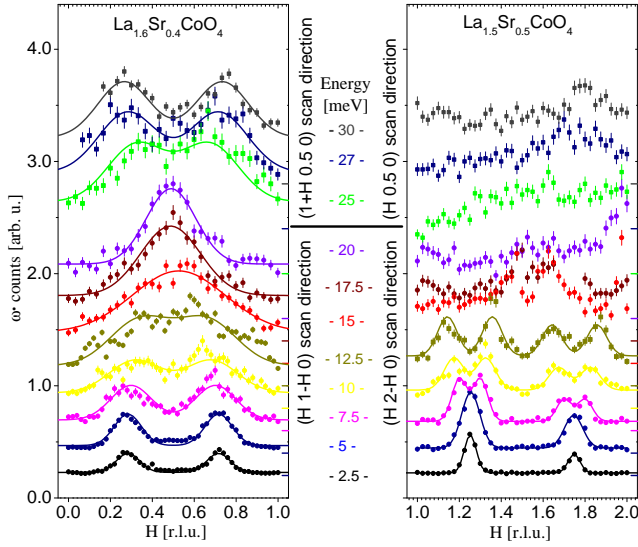


Figure 5.13: Energy dependence of the magnetic excitations measured at ≈ 10 K with INS. Intensities measured for *left*: ACK305- $\text{La}_{1.6}\text{Sr}_{0.4}\text{CoO}_4$ and *right*: the reference sample ACK184- $\text{La}_{1.5}\text{Sr}_{0.5}\text{CoO}_4$ at the 2T1 spectrometer. Scans have been shifted vertically according to the colored horizontal markings. For both samples the three high energy scans (square symbols) have a different direction than the low energy scans (circle symbols). Solid lines are symmetric Gaussian fits to the data.

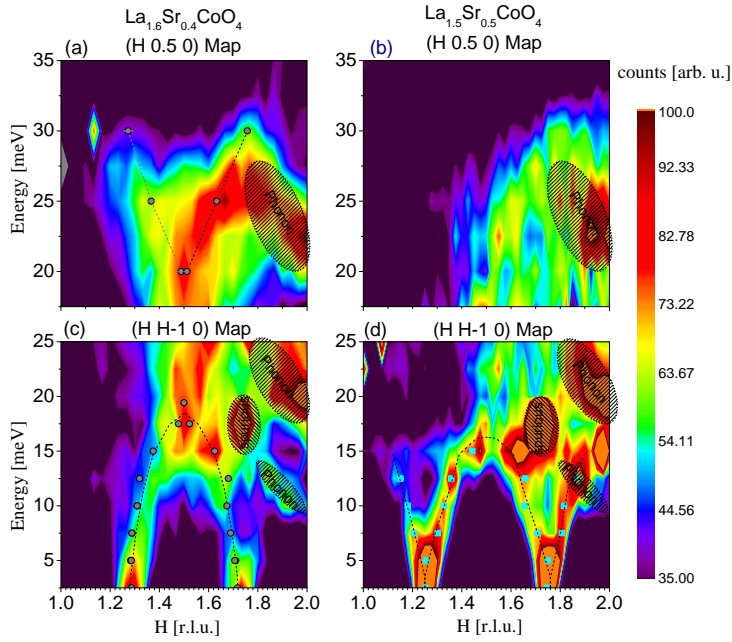


Figure 5.14: Energy dependence of the magnetic excitations measured at ≈ 10 K with INS. Colored intensities maps for *left*: ACK305- $\text{La}_{1.6}\text{Sr}_{0.4}\text{CoO}_4$ and *right*: ACK184- $\text{La}_{1.5}\text{Sr}_{0.5}\text{CoO}_4$ have been generated by interpolation between the scans presented in Figure 5.13. Peak positions obtained from symmetric Gaussian fits to the 2T1 data have been included (circle symbols). Dashed lines are guides to the eye.

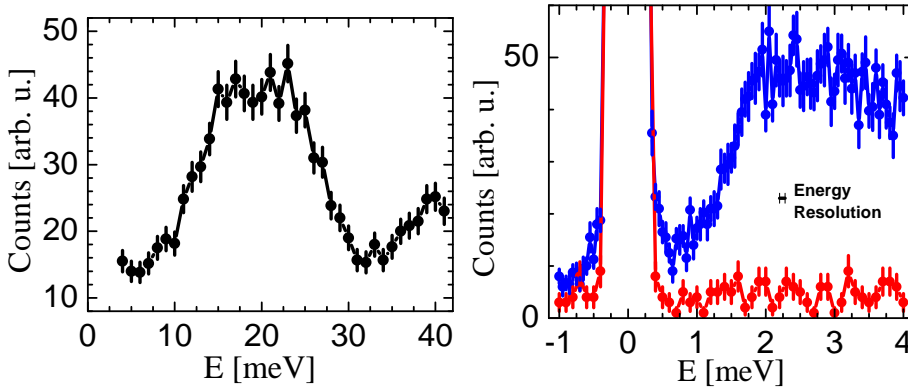


Figure 5.15: INS scans for ACK305- $\text{La}_{1.6}\text{Sr}_{0.4}\text{CoO}_4$ *Left*: Constant-Q scan at $(3/2\ 1/2\ 0)$ measured at the 2T1. *Right*: Spin gap measured in a constant-Q scan at $(1/2-\epsilon\ 1/2+\epsilon\ 0)$ at $\approx 10\text{ K}$ at the 4F.2 (blue circles). For comparison the background has been measured at $(0.9\ 0.1\ 0)$ (red circles).

hourglass (red data points). The additional excitation mode appears in the SF channel $\parallel y$, indicating the out-of-plane character of these high energy excitations (blue data points). For comparison, also the results of unpolarized neutron scattering experiments of $\text{La}_{5/3}\text{Sr}_{1/3}\text{CoO}_4$ measured at the IN8 spectrometer (dark cyan data points) and La_2CoO_4 taken from Ref. [254] (dark yellow data points) are shown. As can be seen, the small additional 20 meV feature belongs to a phonon whereas the increase of intensity at the neck of the hour glass is located around 15 meV which is close to the in-plane anisotropy gap of La_2CoO_4 . Due to polarization analysis we can confirm that this additional high-energy mode is magnetic in origin. The significance of this observations is underlined by the fact that this is the first report of an additional separated high-energy magnon band which is present completely above an entire hour-glass dispersion. Generally one would expect optical modes in a magnon dispersion without hour-glass shape or that the optical magnon mode merges with the low-energy dispersion. In the second case both together are forming the hour-glass-shaped dispersion [178, 253, 255].

For our $\text{La}_{1.6}\text{Sr}_{0.4}\text{CoO}_4$ sample we similarly find an additional high-energy mode in a constant-Q scan at the planar AF wave vector (see Figure 5.16 (c)). The plotted scan was measured with neutron polarization parallel to the scattering vector, i.e. in the channel SF_{xx} with $x \parallel \vec{Q}$. In this channel both contributions, in plane and out of plane, can be detected simultaneously. In contrast, the SF_{zz} channel measured on the $x = 1/3$ doped sample exhibits no upturn at high energies as it is only sensitive to in plane excitations. With our polarized neutron measurements we can uncover the interesting nature of these

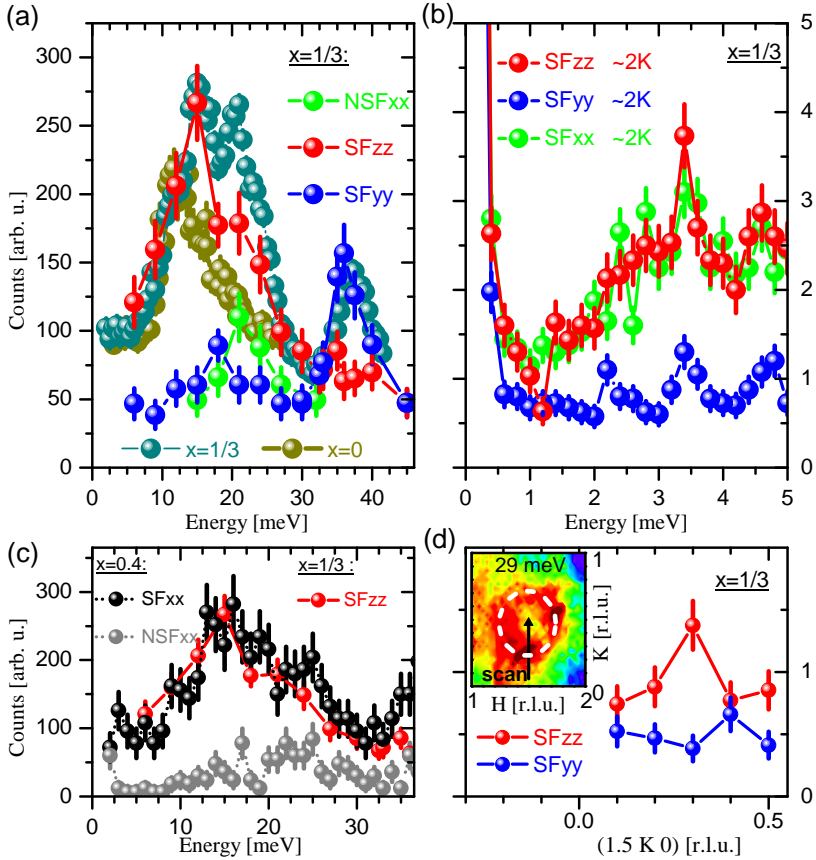


Figure 5.16: Polarization analysis of the spin excitations in $\text{La}_{5/3}\text{Sr}_{1/3}\text{CoO}_4$ measured at the IN22. (polarization directions defined in the text.) (a) Constant-Q scans at $(3/2, 1/2, 0)$. For comparison, unpolarized INS data of $\text{La}_{5/3}\text{Sr}_{1/3}\text{CoO}_4$ measured at the IN8 (dark cyan data points) and La_2CoO_4 taken from Ref. [254] (dark yellow data points) are included. (b) Low-energy excitations at $(1/2 - \epsilon/2, 1/2 + \epsilon/2, 0)$ measured at the IN12. (c) Comparison of the SF_{zz} channel in (a) with the data obtained for $\text{La}_{1.6}\text{Sr}_{0.4}\text{CoO}_4$. (d) Constant energy scan at 29 meV to demonstrate the magnetic contribution to the constant-energy map of the outward dispersing branches shown in the inset.

magnetic excitations: while all low-energy spin excitations that belong to the classical hour-glass dispersion are mostly in-plane excitations, the newly discovered high-energy magnon mode consists of out-of-plane excitations. The in-plane nature of the low-energy excitations can also be observed in Figure 5.16 (b). Because no out-of-plane contribution is present at these energies (only background intensity in the SF_{yy} channel) the intensity measured in the SF_{zz} channel resembles the one measured in the SF_{xx} channel.

Taking only the low-energy excitations below the merging point in $\text{La}_{5/3}\text{Sr}_{1/3}\text{CoO}_4$ into account, they apparently resemble on the excitations of the half doped cobaltate $\text{La}_{1.5}\text{Sr}_{0.5}\text{CoO}_4$. Similarly, the high-energy excitations above the merging point including the additional out-of-plane high-energy mode resemble on the excitations of the undoped parent compound La_2CoO_4 . These observations suggest, that the observed dispersion is not a single dispersion, but instead consists of two dispersions with distinct origin. While the low-energy dispersion arises from magnetic excitations of hole-doped regions which are governed by frustration and exhibit a chiral or non-collinear magnetic phase, the high-energy part can be attributed to magnetic excitations in undoped islands and therefore strongly resembles on the dispersion of the undoped parent compound La_2CoO_4 which exhibits a spin gap and a similar additional high-energy magnon mode.

An enhanced intensity at the magnon merging point or the neck of the hour-glass can be traced with constant-Q scans at the planar AF wave vector. The energy dependence of the intensity in $\text{La}_{5/3}\text{Sr}_{1/3}\text{CoO}_4$ is surprisingly similar to the one observed in La_2CoO_4 (dark yellow dots in Figure 5.16 (a)). This points to a related origin of the merging energy in the $x = 1/3$ doped sample and the spin gap in the undoped parent compound.

Compared to the dispersion for pure La_2CoO_4 , the high-energy part of the hour-glass-shaped dispersion in $\text{La}_{5/3}\text{Sr}_{1/3}\text{CoO}_4$ does not exceed to that high energies. Taking into account the structural changes and the amount of disorder in the charge sector with extremely short-ranged La_2CoO_4 -like correlations that are induced by strontium doping, some deviations can be expected. On the other hand, the difference in the peak energy clearly proves that our sample is not simply subject to a conventional macroscopic phase separation.

For the outward dispersing branches above the neck of the hour-glass also in-plane excitations can be detected in the SF channel $\parallel z$ (see Figure 5.16 (d)). The inset shows the corresponding scan in reciprocal space within a 29 meV constant-energy map. Our findings are underlined by the polarized neutron study. The discovered high-energy magnon mode clearly belongs to an out-of-plane excitation while the outward dispersing contributions above the magnon merging energy are mostly in-plane excitations. Both fully compatible with the excitation spectrum reported for La_2CoO_4 [254]. Regarding Figure 5.16 (c) we

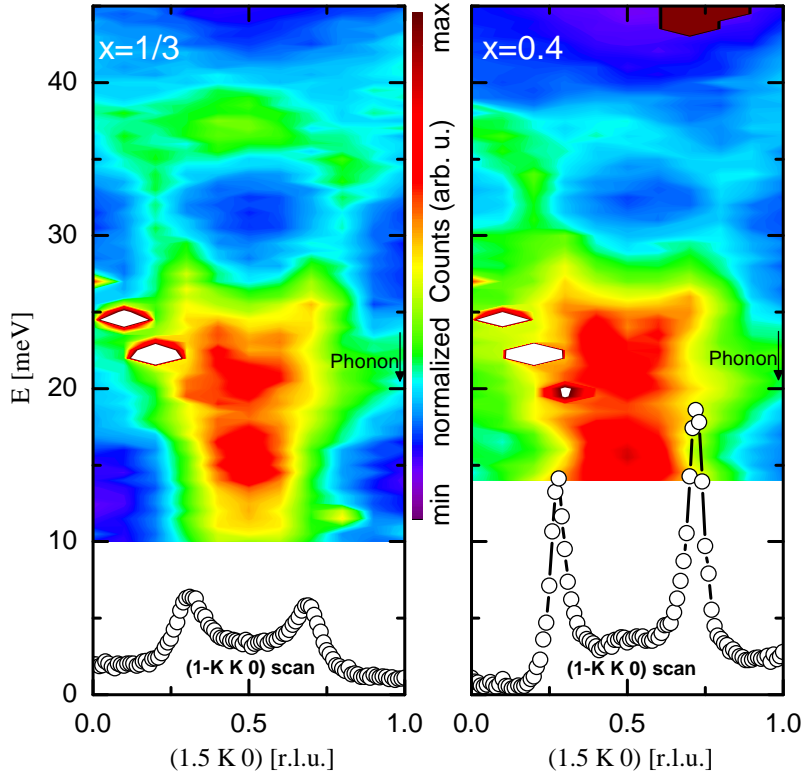


Figure 5.17: Comparison of the high-energy magnetic intensities for different Sr-doping measured at the IN8 spectrometer on the samples ACK183 ($x = 1/3$) and ACK343 ($x = 0.4$). Intensities have been normalized to the phonon peak intensity (black arrow). In the lower part the corresponding elastic incommensurate peaks can be found.

find a qualitatively similar energy scan at the planar AF wave vector for the $x = 0.4$ doped sample. This perfectly agrees with our scenario in which the spin gap within the undoped islands is responsible for the increased intensity at the magnon merging point. The spin gap energy can be expected to be much less doping dependent than the (low-energy) dispersion which starts from different incommensurate magnetic peak positions in samples with different doping concentration. The fact that the intensity of the additional high energy mode is strongest for low Sr-doping (see Figure 5.14) where larger undoped regimes can be expected further corroborates our scenario.

5.6 Discussion

Incommensurate magnetic order in the system $\text{La}_{2-x}\text{Sr}_x\text{CoO}_4$ was recently revealed with neutron scattering [140]. The ongoing discussion about the role of fluctuating charge stripes in the isostructural high temperature superconducting cuprates (HTSC) and the evidence of stable CSO in nickelates $\text{La}_{2-x}\text{Sr}_x\text{NiO}_4$ [225] readily led to the belief that CSO is also responsible for the observed magnetic order in cobaltates. Consequently, a broad magnetic intensity with multi-peak character was interpreted as evidence for stripe phases [140]. It is widely believed that electrons freeze out in a complex “stripe” pattern” [180] and “magnetic dynamics can conclusively be ascribed to stripes” [181].

With our comprehensive search for charge correlations in $\text{La}_{2-x}\text{Sr}_x\text{CoO}_4$ we were finally able to show that CSO is absent in the whole doping range $1/3 \leq x \leq 1/2$. We also show that CBCO is stable over a much wider doping range than previously thought (compare the phase diagram in Section 1.4).

The discovery of an hour-glass magnetic spectrum in $\text{La}_{5/3}\text{Sr}_{1/3}\text{CoO}_4$ [181] together with the assumption of CSO led to misinterpretations on the consequences for the HTSC. It was argued recently, that the absence of any gap in the hour-glass-shaped excitations of the cobaltates with static CSO and the presence of a gap in the excitations of the HTSC cuprates suggests a “collective quantum melting of stripe-like electronic order” in the cuprates [180]. Also our observation of an hour-glass magnetic excitation spectrum together with the indication for a gap in our $\text{La}_{1.6}\text{Sr}_{0.4}\text{CoO}_4$ and $\text{La}_{5/3}\text{Sr}_{1/3}\text{CoO}_4$ samples suggests that implications for the HTSC that have been proposed so far were based on wrong assumptions.

Starting from our observations, a new model for the IC magnetic order in cobaltates has to be developed which could also stimulate new theories for the HTSC. A decisive hint can be found in Figure 5.18 and Figure 5.19: the sharpest magnetic peaks can be observed in the optimum doped CBCO compound $\text{La}_{1.5}\text{Sr}_{0.5}\text{CoO}_4$. With decreasing strontium doping concentration a pronounced broadening can be observed. Similar observations reported in [140]

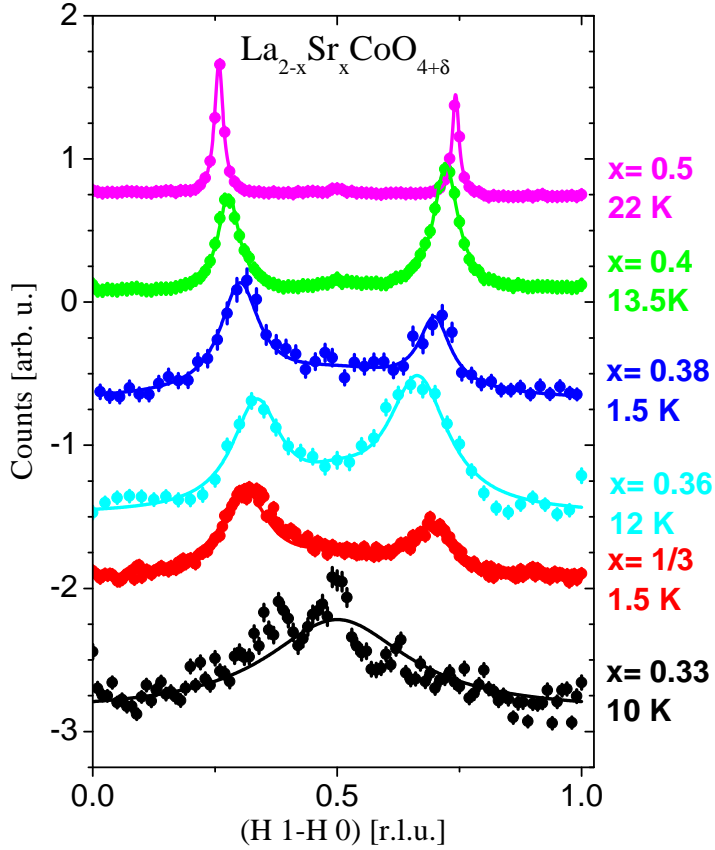


Figure 5.18: Doping dependence of the magnetic peak shape and the incommensurability in $\text{La}_{2-x}\text{Sr}_x\text{CoO}_4$ determined with elastic neutron scattering at the 3T1, 1T1 and IN8. Peak positions have been fitted with two symmetric Lorentzian functions of equal width and a third Gaussian for the additional intensity at the AF wave vector. Only one Lorentzian was used for the fit to the $x = 0.33$ data.

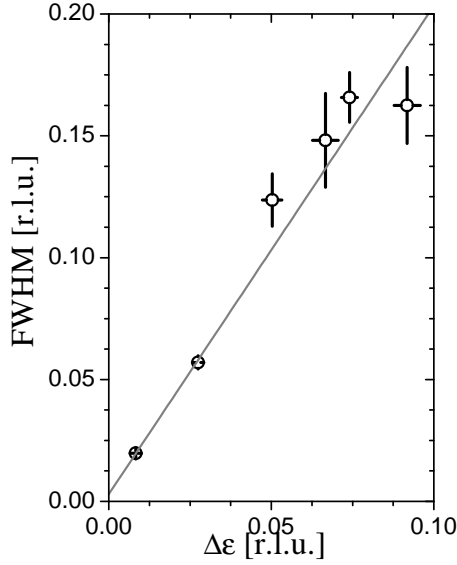


Figure 5.19: Dependence between the width and the incommensurability of the magnetic intensities for different doping x in $\text{La}_{2-x}\text{Sr}_x\text{CoO}_4$. Data obtained from the Lorentzian fits in Figure 5.18 and error bars are standard deviations. The incommensurability has been shifted: $\Delta\epsilon = \epsilon - 1/4$. The black line is a linear fit to the data as a guide to the eye.

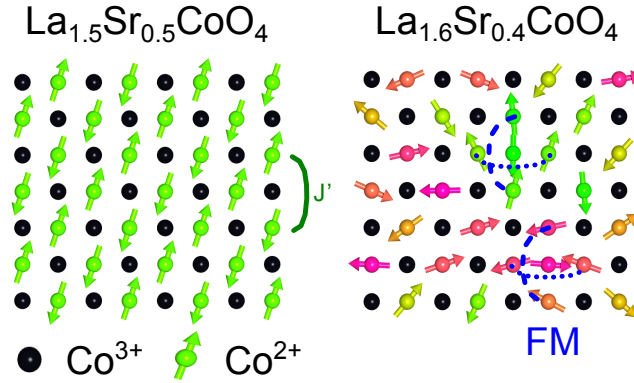


Figure 5.20: Schematic drawing of the frustration scenario in $\text{La}_{2-x}\text{Sr}_x\text{CoO}_4$. *Left*: Ideal model of the CBCO and AF structure in the half doped parent compound $\text{La}_{1.5}\text{Sr}_{0.5}\text{CoO}_4$. *Right*: Sketch of the mechanism that induces frustration in the under-doped cobaltates with $1/3 \leq x \leq 1/2$ (see text). Electron doping causes effective FM interactions (blue dotted/dashed lines) in the ideal CBCO ordered antiferromagnet. Frustration can be released by a canting of spins (directions are color coded). Graph taken from [256]

already led to an understanding that the strontium concentration $x = 0.5$ is the most stable composition for charge and spin order in cobaltates but further implications are missing. Obviously the peak broadening away from the half doped composition is inconsistent with the assumption of a CSO scenario which would imply the most stable stripe phase at a doping of $x = 1/3$, similar to the nickelates and opposite to the observations in cobaltates.

In an alternative scenario with chiral or non-collinear magnetic order the observed destabilization away from half doping can easily be understood as a result of an increasing amount of frustration. A sketch of the ideal CBCO in $\text{La}_{1.5}\text{Sr}_{0.5}\text{CoO}_4$ can be found in Figure 5.20. The low temperature magnetic order is antiferromagnetic, mediated via a next next nearest (nnn) neighbor interaction J' . Strontium doping introduces additional electrons into the Co-O layer resulting in the substitution of a Co^{2+} for a nonmagnetic Co^{3+} (see Figure 5.20). Therefore, each doped electron introduces a strong nearest neighbor AF interaction J , like in the undoped parent compound. Due to $J \gg J'$ (with $J \approx 9.7 \text{ meV}$ and $J' \approx 1.4 \text{ meV}$ [253, 254]) the AF ordering of neighboring spins like in the undoped parent compound is locally recovered. This induces a strong frustration into the CBCO AF-order where the nnn neighbor interaction across a Co^{2+} is now forced to be ferromagnetic (blue dotted/dashed lines in Figure 5.20 *right*). An expected consequence to release such a frustration is, that the magnetic moments start twisting/spiraling. An alternative scenario of a spin

density wave seems less likely in cobaltates with strongly localized electrons.

In this scenario the observed dependence between doping concentration and incommensurability as well as the direction of the IC satellite reflections follow naturally. Upon increasing electron doping more and more centers of frustration are introduced and consequently more spiraling occurs in order to release frustration. In the tetragonal structure of the cobaltates these spiraling effects may appear similarly in a and b directions. It was shown for the half doped compound that it in fact contains two independent AF sublattices [253]. Both sublattices are affected simultaneously by the electron doping and when averaging over a sufficiently large distance, the total modulation along a and b will be similar. The propagation then appears to be along the diagonal directions, i.e. $[\pm 1 \pm 1 0]$.

Predictions of the magnetic excitations spectra that are based on spin-wave theory for perfect stripes are not able to reproduce the observed hour-glass intensity distribution nor the anomalous broadening [247]. With the introduction of quenched disorder in the charge sector which causes frustration in the spin interactions it was finally possible to calculate an excitation spectrum that exhibits the basic features of an hour-glass dispersion [247].

For the insulating spin glass phase of low doped $\text{La}_{2-x}\text{Sr}_x\text{CuO}_4$ which also exhibits diagonal magnetic satellites and magnetic excitations with the characteristics of an hour-glass spectrum [237] spiral spin correlations have been proposed in Refs. [255, 257, 258]. This model also involves frustration which arises from the doping of charges into the ideal AF order of the parent compound La_2CuO_4 [255, 257, 258]. It could be that both isostructural systems share a common mechanism in which frustration is generated by the doping of additional charges (electrons for cuprates and holes for cobaltates) in interstitial sites, resulting in a ferromagnetic exchange interaction inside the ideal AF spin structures.

Chapter 6

Appendix

6.1 List of Grown Single Crystals

Name	composition	atmosphere	Lamp [W]	speed [$\frac{mm}{h}$]
YD001	La _{0.7} Sr _{1.3} FeO ₄	air	500	3.5
YD002	La _{0.8} Sr _{1.2} FeO ₄	4 bar O ₂	500	3.7
YD010	LaCaCoO ₄	7.5 bar O ₂	1000	1.6 + 0.4
YD027	LaSrFeO ₄	5 bar Ar	1000	1.2 + 2.4
YD028	Nd _{0.75} Sr _{1.25} FeO ₄	9 bar O ₂	1000	3.2
YD029	La _{0.7} Ba _{1.3} FeO ₄	8 bar O ₂	1000	3.2 + 0.6
YD037	NaCaFeO ₄	9 bar O ₂	1000	2.5
YD043	La _{1.67} Ba _{0.33} NiO ₄	4.5 bar O ₂	1000	3
YD051	La ₂ NiO ₄	2 bar Ar	1000	3.6
YD052	Ba ₂ CoO ₄	8 bar O ₂	1000	2.2
YD053	CoV ₂ O ₆	2.2+0.3 bar Ar/O ₂	150	0.8
YD061	LaSrFeO ₄	air flow 2l/min	1000	4 + 1
YD062	LaSrFeO ₄	air flow 2l/min	1000	4 + 1
YD063	LaSrFeO ₄	air flow 2l/min	1000	4 + 1
YD064	LaSrFeO ₄	air flow 2l/min	1000	4 + 1
YD065	LaSrFeO ₄	air flow 2l/min	1000	4 + 1
YD066	NdCaFeO ₄	4.5 bar O ₂	1000	2.5 + 0.5
YD068	La _{0.67} Sr _{1.33} FeO ₄	120 bar O ₂	3000	3
YD069	Pr _{1.3} Ca _{0.7} NiO ₄	8 bar O ₂	1000	1.5 + 0.5
YD070	La _{1.67} Sr _{0.33} CoO ₄	5 bar Ar, 50 ml/min	1000	2 + 0.5
YD071	La _{1.75} Sr _{0.25} CoO ₄	4 bar N ₂ , 50 ml/min	1000	2 + 0.5

Table 6.1: List of single crystals grown by the author.

6.2 List of Measured Crystals

Name	nominal Sr doping	nominal co-doping
ACK163	0	
ACK354	0	
ACK356	0	
YD071	0.25	
YD070	0.33	
ACK312	0.33	
ACK183	0.33	
ACK315	0.33	
ACK317	0.36	
ACK318	0.38	
ACK305	0.4	
ACK343	0.4	
ACK353	0.5	
ACK184	0.5	
ACK308	0.7	
ACK349	0.7	
ACK316	0.8	
ACK157	0.9	
ACK381	1	
ZL091	0.33	
ACK342	0	0.36 Ca
ACK346	0	0.39 Ca
ACK370	0.4	0.4 Nd
ACK344	0	0.36 Ba

Table 6.2: Measured cobaltate samples with composition $\text{La}_{2-x-y}\text{Sr}_x\text{Ln}_y\text{CoO}_4$ with $\text{Ln} = \text{Nd}, \text{Ca}, \text{Ba}$.

Name	nominal Sr doping	nominal co-doping
YD051	0	
ACK270	0.15	
ACK264	0.17	
ACK265	0.18	
ACK266	0.19	
ACK268	0.2	
ACK269	0.21	
ACK273	0.22	
ACK326	0.4	
YD043	0	0.33 Ba
ACK271	0.15	0.39 Nd
ACK275	0.2	0.05 Fe
ACK274	0.15	0.005 Zn
ACK359	0.17	0.005 Zn
ACK360	0.18	0.005 Zn
ACK387	0.19	0.005 Zn
ACK393	0.2	0.005 Zn
ACK324	0.16	0.005 Zn
ACK390	0.105	0.005 Zn
ACK320	0.26	0.05 Ti
ACK272	0.26	0.05 Ti
ACK322	0.33	0.08 Ti

Table 6.3: Measured nickelate samples with composition $\text{La}_{2-x-y}\text{Sr}_x\text{Ln}_y\text{Ni}_{1-z}\text{Me}_z\text{O}_4$ with $\text{Ln} = \text{Nd}, \text{Ba}$ and $\text{Me} = \text{Ti}, \text{Zn}$, and Fe .

Name	nominal Sr doping
YD001	1.3
YD002	1.2
YD027	1
YD062	1
YD064	1
YD065	1
YD068	1.3
ACK195	1.1
ACK224	1.275
ACK276	1.24

Table 6.4: Measured iron oxide samples with composition $\text{La}_{2-x}\text{Sr}_x\text{FeO}_4$

6.3 List of TG Results in the Cobaltates

Name	Sr doping	Oxygen content
ACK356	0	4.080(10)
YD071	0.25	4.006(11)
YD070	0.33	3.992(10)
ACK315	0.333	4.048(10)
ACK317	0.36	4.009(10)
ACK318	0.38	3.999(21)
ACK343	0.4	3.997(14)
ACK305	0.4	4.025(10)
ACK353	0.5	4.022(13)
ACK308	0.7	4.003(12)
ACK316	0.8	3.970(10)
ACK157	0.9	4.015(10)
ACK354	0	4.080(10)
ACK163	0	4.06(2)
ACK356	0	4.11(2)
ACK183	0.333	4.06(2)
ZL091	0.333	4.07(2)
ACK312	0.33	4.06(2)
ACK305	0.4	4.08(2)
ACK184	0.5	4.01(2)
ACK349	0.7	4.00(2)
ACK381	1	3.99(2)

Table 6.5: Oxygen content in the cobaltates determined with TG. Data in the upper part of the table has been measured on bulk crystals of about 80 mg and data in the lower part has been measured on samples that have been crushed to smaller crystallites prior to the TG measurement.

6.4 Additional Neutron Data in the Nickelates

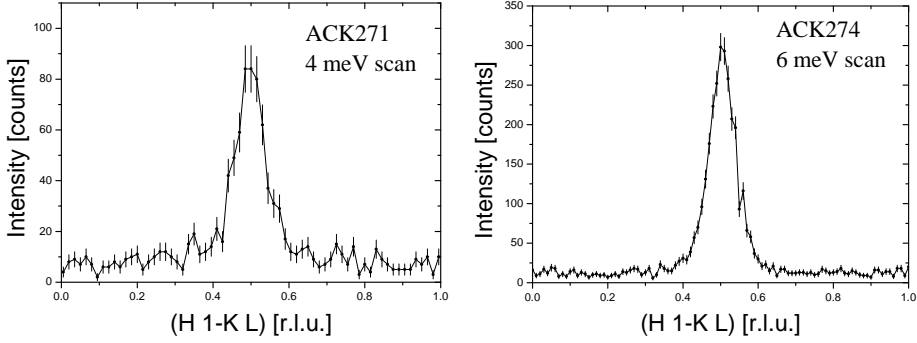


Figure 6.1: Diagonal constant energy scans probing the magnetic dispersion of ACK271 and ACK271.

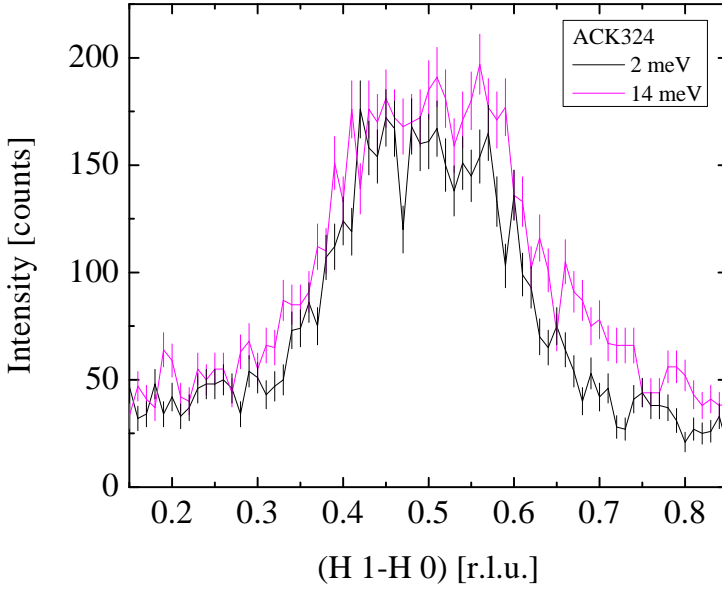


Figure 6.2: Comparison of the 2 meV and 14 meV constant low energy scans in (H 1-H 0) direction through (0.5 0.5 0) of sample ACK324 - $\text{La}_{1.85}\text{Sr}_{0.15}\text{Ni}_{1-y}\text{Zn}_y\text{O}_4$

QH	QK	EN	SF	NSF
2.05	1.05	24	6(2.4)	21(7.9)
2.2	1.2	24	5(2.2)	18(7.3)
2.35	1.35	24	4(2.0)	18(7.3)
2.5	1.5	24	12(3.5)	60(13)
2.65	1.65	24	9(3.0)	18(7.3)
2.2	1.2	26	4(1.4)	19.5(5.4)
2.3	1.3	26	3(1.2)	27(6.4)
2.4	1.4	26	11(2.3)	28.5(6.5)
2.5	1.5	26	7(1.9)	16.5(5.0)
2.6	1.6	26	10.5(2.3)	40.5(7.8)
2.45	1.45	25	13(2.5)	30(6.7)
1.22	0.22	38	15.5(2.8)	27(6.4)
2.5	0.5	20	12(3.5)	21(7.9)
2.3	0.3	24	5(2.2)	18(7.3)
2.5	0.5	24	15(3.9)	12(6.0)
2.7	0.7	24	7(2.6)	9(5.2)
2.9	0.9	24	0(0)	18(7.3)
2.1	0.1	24	5(2.2)	21(7.9)
2.1	0.1	22.5	3(1.7)	9(5.2)
2.3	0.3	22.5	13(3.6)	33(9.9)
2.5	0.5	22.5	11(3.3)	21(7.9)
2.7	0.7	22.5	5(2.2)	33(9.9)

Table 6.6: ACK324 - Polarized neutron measurement at different Q points for comparison with the IN8-flatcone data normalized for a monitor of 1500

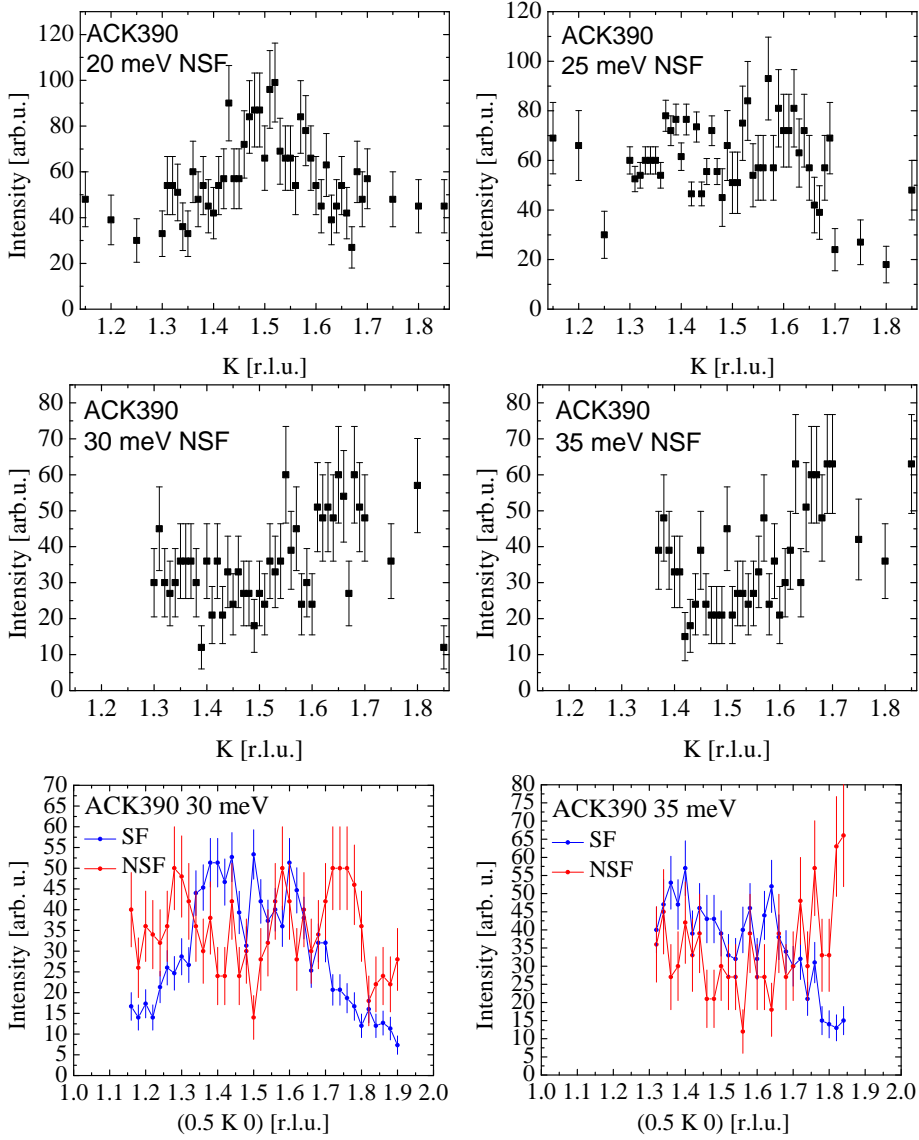


Figure 6.3: Diagonal constant energy scans of ACK324 in the NSF channel. And vertical constant energy scans of ACK324 in the SF/NSF channel.

6.5 Temperature Dependence of the Magnetic Order in $\text{La}_{4/3}\text{Sr}_{1/3}\text{CoO}_4$

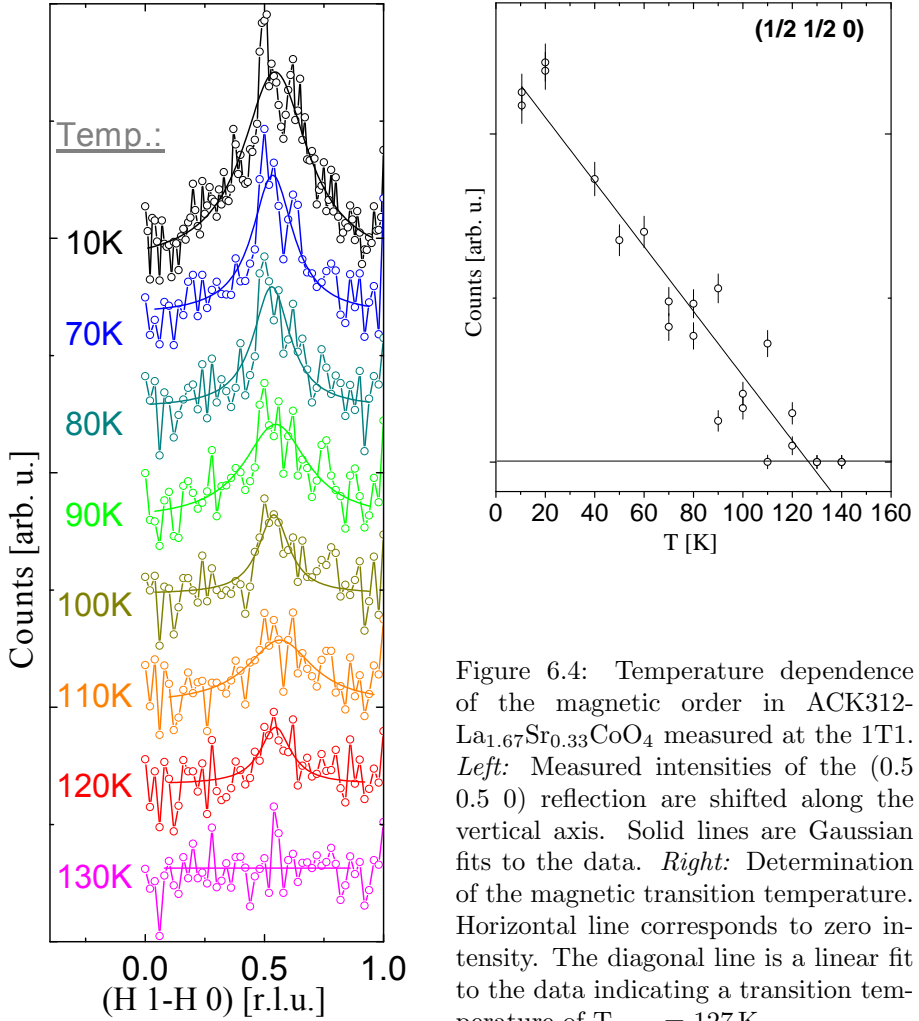


Figure 6.4: Temperature dependence of the magnetic order in ACK312- $\text{La}_{1.67}\text{Sr}_{0.33}\text{CoO}_4$ measured at the 1T1. *Left:* Measured intensities of the (0.5 0.5 0) reflection are shifted along the vertical axis. Solid lines are Gaussian fits to the data. *Right:* Determination of the magnetic transition temperature. Horizontal line corresponds to zero intensity. The diagonal line is a linear fit to the data indicating a transition temperature of $T_{mag} = 127$ K.

Bibliography

- [1] C. N. R. Rao and B. Raveau. *Transition Metal Oxides*. Wiley-VCH, 1998.
- [2] W.D. Ryden, A.W. Lawson, and C.C. Sartain. Temperature dependence of the resistivity of RuO_2 and IrO_2 . *Physics Letters A*, 26(5):209 – 210, 1968.
- [3] T. P. Pearsall and C. A. Lee. Electronic transport in ReO_3 : dc conductivity and Hall effect. *Phys. Rev. B*, 10:2190–2194, Sep 1974.
- [4] K.P. Rajeev, G.V. Shivashankar, and A.K. Raychaudhuri. Low-temperature electronic properties of a normal conducting perovskite oxide (LaNiO_3). *Solid State Communications*, 79(7):591 – 595, 1991.
- [5] D. B. McWhan, T. M. Rice, and J. P. Remeika. Mott Transition in Cr-Doped V_2O_3 . *Phys. Rev. Lett.*, 23:1384–1387, Dec 1969.
- [6] H. Eschrig. Metal-insulator transition. *Crystal Research and Technology*, 26(6):788–788, 1991.
- [7] G. Travaglini, I. Mörke, and P. Wachter. CDW evidence in one-dimensional $\text{K}_{0.3}\text{MoO}_3$ by means of Raman scattering. *Solid State Communications*, 45(3):289 – 292, 1983.
- [8] E. J. W. Verwey. Electronic Conduction of Magnetite (Fe_3O_4) and its Transition Point at Low Temperatures. *Nature*, 144:327–328, August 1939.
- [9] R. A. Mashelkar. *Solid State Chemistry: Selected Papers of C N R Rao*. World Scientific, 1995.
- [10] G. H. Kwei, A. C. Lawson, S. J. L. Billinge, and S. W. Cheong. Structures of the ferroelectric phases of barium titanate. *The Journal of Physical Chemistry*, 97(10):2368–2377, 1993.
- [11] G. Shirane, H. Danner, A. Pavlovic, and R. Pepinsky. Phase Transitions in Ferroelectric KNbO_3 . *Phys. Rev.*, 93:672–673, Feb 1954.

- [12] K. Aizu, A. Kumada, H. Yumoto, and S. Ashida. Simultaneous Ferroelectricity and Ferroelasticity of $\text{Gd}_2(\text{MoO}_4)_3$. *Journal of the Physical Society of Japan*, 27(2):511–511, 1969.
- [13] M. N. Baibich, J. M. Broto, A. Fert, F. Nguyen Van Dau, F. Petroff, P. Etienne, G. Creuzet, A. Friederich, and J. Chazelas. Giant Magnetoresistance of (001)Fe/(001)Cr Magnetic Superlattices. *Phys. Rev. Lett.*, 61:2472–2475, Nov 1988.
- [14] P. Grünberg, R. Schreiber, Y. Pang, M. B. Brodsky, and H. Sowers. Layered Magnetic Structures: Evidence for Antiferromagnetic Coupling of Fe Layers across Cr Interlayers. *Phys. Rev. Lett.*, 57:2442–2445, Nov 1986.
- [15] J.G. Bednorz and K.A. Müller. Possible high T_c superconductivity in the Ba-La-Cu-O system. *Zeitschrift für Physik B Condensed Matter*, 64(2):189–193, 1986.
- [16] P. A. Cox. *Transition Metal Oxides*. Clarendon Press, 1992.
- [17] D. Balz. über die Struktur des K_2NiF_4 . *Naturwissenschaften*, 40(8):241–241, 1953.
- [18] K. Miwa, I. Kagomiya, H. Ohsato, H. Sakai, and Y. Maeda. Electrical properties of the $\text{Sr}_2\text{Ru}_{1-x}\text{Ti}_x\text{O}_4$ solid solutions. *Journal of the European Ceramic Society*, 27(1315):4287 – 4290, 2007.
- [19] N. Suzuki, T. Noritake, and T. Hioki. Structure and properties of layered perovskite compounds $[\text{Sr}_2\text{VO}_{4-\delta}]$. *Materials Research Bulletin*, 27(10):1171 – 1184, 1992.
- [20] Tom Baikie, Zahara Ahmad, Madhavi Srinivasan, Antoine Maignan, Stevin S. Pramana, and T.J. White. The crystallographic and magnetic characteristics of Sr_2CrO_4 (K_2NiF_4 -type) and $\text{Sr}_{10}(\text{CrO}_4)_6\text{F}_2$ (apatite-type). *Journal of Solid State Chemistry*, 180(5):1538 – 1546, 2007.
- [21] Jean-Claude Bouloux, Jean-Louis Soubeyroux, Gilles Le Flem, and Paul Hagenguller. Bidimensional magnetic properties of $\beta\text{-Sr}_2\text{MnO}_4$. *Journal of Solid State Chemistry*, 38(1):34 – 39, 1981.
- [22] S.E. Dann, M.T. Weller, and D.B. Currie. The synthesis and structure of Sr_2FeO_4 . *Journal of Solid State Chemistry*, 92(1):237 – 240, 1991.
- [23] J. Matsuno, Y. Okimoto, Z. Fang, X.Z. Yu, Y. Matsui, N. Nagaosa, H. Kumigashira, M. Oshima, M. Kawasaki, and Y. Tokura. Novel metallic ferromagnet Sr_2CoO_4 . *Thin Solid Films*, 486(12):113 – 116, 2005.

- [24] R.C. Lobo, F.J. Berry, and C. Greaves. The synthesis and structural characterization of $\text{Sr}_2\text{CuO}_{4-x}$, $x \approx 0.1$. *Journal of Solid State Chemistry*, 88(2):513 – 519, 1990.
- [25] J.M. Longo and P.M. Raccach. The structure of La_2CuO_4 and LaSrVO_4 . *Journal of Solid State Chemistry*, 6(4):526 – 531, 1973.
- [26] A. Collomb, D. Samaras, and J. C. Joubert. Determination par diffraction neutronique des structures magnetiques des composés SrTCrO_4 ($T = \text{La}, \text{Nd}$). *physica status solidi (a)*, 50(2):635–642, 1978.
- [27] D. Senff, P. Reutler, M. Braden, O. Friedt, D. Bruns, A. Cousson, F. Bourée, M. Merz, B. Büchner, and A. Revcolevschi. Crystal and magnetic structure of $\text{La}_{1-x}\text{Sr}_{1+x}\text{MnO}_4$: Role of the orbital degree of freedom. *Phys. Rev. B*, 71:024425, Jan 2005.
- [28] J.L. Soubeyroux, P. Courbin, L. Fournes, D. Fruchart, and G. Le Flem. La phase SrLaFeO_4 : Structures cristalline et magnetique. *Journal of Solid State Chemistry*, 31(3):313 – 320, 1980.
- [29] Takashi Matsuura, Junji Tabuchi, Junichiro Mizusaki, Smgeru Yamauchi, and Kazuo Fueki. Electrical properties of $\text{La}_{2-x}\text{Sr}_x\text{CoO}_{4\delta}$: Structure, electrical conductivity, and Seebeck coefficient of single crystals $x = 0.0, 0.5, 1.0$ and 1.5). *Journal of Physics and Chemistry of Solids*, 49(12):1403 – 1408, 1988.
- [30] Grard Demazeau, Michel Pouchard, and Paul Hagenmuller. Sur quelques nouveaux composés oxygènes du nickel(III) de structure K_2NiF_4 . *Journal of Solid State Chemistry*, 18(2):159 – 162, 1976.
- [31] Mm.J.B. Goodenough, G. Demazeau, M. Pouchard, and P. Hagenmuller. Sur une Nouvelle Phase Oxygénée du Cuivre(III): SrLaCuO_4 . *Journal of Solid State Chemistry*, 8(4):325 – 330, 1973.
- [32] A. Rabenau and P. Eckerlin. Die K_2NiF_4 -Struktur beim La_2NiO_4 . *Acta Crystallographica*, 11(4):304–306, Apr 1958.
- [33] H.-H. Wu, M. Buchholz, C. Trabant, C.F. Chang, A.C. Komarek, F. Heigl, M.v. Zimmermann, M. Cwik, F. Nakamura, M. Braden, and C. Schüssler-Langeheine. Charge stripe order near the surface of 12-percent doped $\text{La}_{2-x}\text{Sr}_x\text{CuO}_4$. *Nat Commun*, 3, 2012.
- [34] D. Poilblanc and T. M. Rice. Charged solitons in the Hartree-Fock approximation to the large-U Hubbard model. *Phys. Rev. B*, 39:9749–9752, May 1989.

- [35] Jan Zaanen and Olle Gunnarsson. Charged magnetic domain lines and the magnetism of high- T_c oxides. *Phys. Rev. B*, 40:7391–7394, Oct 1989.
- [36] H. J. Schulz. Incommensurate antiferromagnetism in the two-dimensional Hubbard model. *Phys. Rev. Lett.*, 64:1445–1448, Mar 1990.
- [37] Kazushige Machida. Magnetism in La_2CuO_4 based compounds. *Physica C: Superconductivity*, 158(12):192 – 196, 1989.
- [38] J. M. Tranquada, B. J. Sternlieb, J. D. Axe, Y. Nakamura, and S. Uchida. Evidence for stripe correlations of spins and holes in copper oxide. *Nature*, 375:561–563, 1995.
- [39] M. Fujita, H. Goka, K. Yamada, J. M. Tranquada, and L. P. Regnault. Stripe order, depinning, and fluctuations in $\text{La}_{1.875}\text{Ba}_{0.125}\text{CuO}_4$ and $\text{La}_{1.875}\text{Ba}_{0.075}\text{Sr}_{0.050}\text{CuO}_4$. *Phys. Rev. B*, 70:104517, Sep 2004.
- [40] M. Hücker, M. v. Zimmermann, G. D. Gu, Z. J. Xu, J. S. Wen, Guangyong Xu, H. J. Kang, A. Zheludev, and J. M. Tranquada. Stripe order in superconducting $\text{La}_{2-x}\text{Ba}_x\text{CuO}_4$ ($0.095 \leq x \leq 0.155$). *Phys. Rev. B*, 83:104506, Mar 2011.
- [41] John M. Tranquada, Guangyong Xu, and Igor A. Zaliznyak. Superconductivity, antiferromagnetism, and neutron scattering. *Journal of Magnetism and Magnetic Materials*, 350(0):148 – 160, 2014.
- [42] D. J. Scalapino. A common thread: The pairing interaction for unconventional superconductors. *Rev. Mod. Phys.*, 84:1383–1417, Oct 2012.
- [43] Patrick A. Lee, Naoto Nagaosa, and Xiao-Gang Wen. Doping a Mott insulator: Physics of high-temperature superconductivity. *Rev. Mod. Phys.*, 78:17–85, Jan 2006.
- [44] Steven A. Kivelson and Eduardo Fradkin. How Optimal Inhomogeneity Produces High Temperature Superconductivity. In J. Robert Schrieffer and James S. Brooks, editors, *Handbook of High-Temperature Superconductivity*, pages 570–596. Springer New York, 2007.
- [45] R Szczesniak. Pairing mechanism for the high- T_c superconductivity: symmetries and thermodynamic properties. *PloS one*, 7(4), 2012.
- [46] M. L. Kulic. Importance of the Electron-Phonon Interaction with the Forward Scattering Peak for Superconducting Pairing in Cuprates. *eprint arXiv:cond-mat/0606063*, June 2006.
- [47] J. M. Tranquada, H. Woo, T. G. Perring, H. Goka, G. D. Gu, G. Xu, M. Fujita, and K. Yamada. Quantum magnetic excitations from stripes in copper oxide superconductors. *Nature*, 429:534–538, 2004.

- [48] B. Vignolle, S. M. Hayden, D. F. McMorrow, H. M. Ronnow, B. Lake, C. D. Frost, and T. G. Perring. Two energy scales in the spin excitations of the high-temperature superconductor $\text{La}_{2-x}\text{Sr}_x\text{CuO}_4$. *Nat Phys*, 3:163–167, 2007.
- [49] H. A. Hayden, S. M. and Mook, Pengcheng Dai, T. G. Perring, and F. Dogan. The structure of the high-energy spin excitations in a high-transition-temperature superconductor. *Nature*, 429:531–534, 2004.
- [50] C. Stock, W. J. L. Buyers, R. A. Cowley, P. S. Clegg, R. Coldea, C. D. Frost, R. Liang, D. Peets, D. Bonn, W. N. Hardy, and R. J. Birge-neau. From incommensurate to dispersive spin-fluctuations: The high-energy inelastic spectrum in superconducting $\text{YBa}_2\text{Cu}_3\text{O}_{6.5}$. *Phys. Rev. B*, 71:024522, Jan 2005.
- [51] C. Stock, R. A. Cowley, W. J. L. Buyers, C. D. Frost, J. W. Taylor, D. Peets, R. Liang, D. Bonn, and W. N. Hardy. Effect of the pseudogap on suppressing high energy inelastic neutron scattering in superconducting $\text{YBa}_2\text{Cu}_3\text{O}_{6.5}$. *Phys. Rev. B*, 82:174505, Nov 2010.
- [52] Guangyong Xu, G. D. Gu, M. Hucker, B. Fauque, T. G. Perring, L. P. Regnault, and J. M. Tranquada. Testing the itinerancy of spin dynamics in superconducting $\text{Bi}_2\text{Sr}_2\text{CaCu}_2\text{O}_{8+\delta}$. *Nat Phys*, 5:642–646, 2009.
- [53] S. Sugai, H. Suzuki, Y. Takayanagi, T. Hosokawa, and N. Hayamizu. Carrier-density-dependent momentum shift of the coherent peak and the LO phonon mode in p-type high- T_c superconductors. *Phys. Rev. B*, 68:184504, Nov 2003.
- [54] Masaki Fujita, Haruhiro Hiraka, Masaaki Matsuda, Masato Matsuura, John M. Tranquada, Shuichi Wakimoto, Guangyong Xu, and Kazuyoshi Yamada. Progress in Neutron Scattering Studies of Spin Excitations in High- T_c Cuprates. *Journal of the Physical Society of Japan*, 81(1):011007, 2012.
- [55] J.B. Goodenough and J. M. Longo. *Landolt-Börnstein Database, III/4a*. Springer-Verlag Berlin, 1970.
- [56] S. Nomura. *Landolt-Börnstein Database, III/12a*. Springer-Verlag Berlin, 1978.
- [57] V. M. Goldschmidt. Die Gesetze der Krystallochemie. *Naturwissenschaften*, 14:477–485, 1926.
- [58] R. D. Shannon and C. T. Prewitt. Effective ionic radii in oxides and fluorides. *Acta Crystallographica Section B*, 25(5):925–946, May 1969.

- [59] R. D. Shannon. Revised effective ionic radii and systematic studies of interatomic distances in halides and chalcogenides. *Acta Crystallographica Section A*, 32(5):751–767, Sep 1976.
- [60] S. N. Ruddlesden and P. Popper. New compounds of the K_2NiF_4 type. *Acta Crystallographica*, 10(8):538–539, Aug 1957.
- [61] K. S. Aleksandrov. 1. *Kristallografiya*, 32, 1987.
- [62] K. S. Aleksandrov, B. V. Beznosikov, and S. V. Misyul. Successive Phase Transitions in Crystals of K_2MgF_4 -Type Structure. *Phys. Status Solidi A*, 104, 1987.
- [63] D. M. Hatch and H. T. Stokes. Classification of Octahedral Tilting Phases in the Perovskitelike A_2BX_4 Structure. *Phys. Rev. B*, 35, 1987.
- [64] Dorian M. Hatch, Harold T. Stokes, K. S. Aleksandrov, and S. V. Misyul. Phase transitions in the perovskite-like structure. *Phys. Rev. B*, 39:9282–9288, May 1989.
- [65] H. Köppel, D. R. Yarkony, and H. Barentzen. *The Jahn-Teller Effect*. Springer-Verlag Berlin, 2009.
- [66] Susumu Yamamoto, Takeo Fujiwara, and Yasuhiro Hatsugai. Electronic structure of charge and spin stripe order in $La_{2-x}Sr_xNiO_4$ ($x=1/3, 1/2$). *Phys. Rev. B*, 76:165114, Oct 2007.
- [67] Holger Ulbrich and Markus Braden. Neutron scattering studies on stripe phases in non-cuprate materials. *Physica C: Superconductivity*, 481(0):31–45, 2012.
- [68] E Liarokapis, E Siranidi, D Lampakis, K Conder, and C Panagopoulos. Raman spectroscopic evidence of lattice effects across the phase diagram of $La_{2-x}Sr_xCuO_4$. *Journal of Physics: Conference Series*, 108(1):012023, 2008.
- [69] Maurizio Ferretti, Edoardo Magnone, and Myrta Napoletano. Structural Properties and Chemical Homogeneity of Underdoped $La_{2-x}M_xCuO_4$ Cuprates ($M = Sr, Ba$). *International Journal of Modern Physics B*, 13(09n10):979–984, 1999.
- [70] A. Manthiram and J.B. Goodenough. Thermal-expansion mismatch and intergrowth types in the system $La_{2-y}Nd_yCuO_4$. *Journal of Solid State Chemistry*, 92(1):231–236, 1991.

- [71] K. Yamada, M. Matsuda, Y. Endoh, B. Keimer, R. J. Birgeneau, S. Onodera, J. Mizusaki, T. Matsuura, and G. Shirane. Successive antiferromagnetic phase transitions in single-crystal La_2CoO_4 . *Phys. Rev. B*, 39:2336–2343, Feb 1989.
- [72] U. Lehmann and Hk. Müller-Buschbaum. Ein Beitrag zur Chemie der Oxocobaltate(II): La_2CoO_4 , Sm_2CoO_4 . *Zeitschrift für anorganische und allgemeine Chemie*, 470(1):59–63, 1980.
- [73] G. H. Lander, P. J. Brown, J. Spalek, and J. M. Honig. Structural and magnetization density studies of La_2NiO_4 . *Phys. Rev. B*, 40:4463–4471, Sep 1989.
- [74] J Rodriguez-Carvajal, M T Fernandez-Diaz, and J L Martinez. Neutron diffraction study on structural and magnetic properties of La_2NiO_4 . *Journal of Physics: Condensed Matter*, 3(19):3215, 1991.
- [75] W. Paulus, A. Cousson, G. Dhalenne, J. Berthon, A. Revcolevschi, S. Hosoya, W. Treutmann, G. Heger, and R. Le Toquin. Neutron diffraction studies of stoichiometric and oxygen intercalated La_2NiO_4 single crystals. *Solid State Sciences*, 4(5):565 – 573, 2002.
- [76] A. A. Colville and S. Geller. The crystal structure of brownmillerite, $\text{Ca}_2\text{FeAlO}_5$. *Acta Crystallographica Section B*, 27(12):2311–2315, Dec 1971.
- [77] A. Nemudry, M. Weiss, I. Gainutdinov, V. Boldyrev, and R. Schöllhorn. Room Temperature Electrochemical Redox Reactions of the Defect Perovskite $\text{SrFeO}_{2.5+x}$. *Chemistry of Materials*, 10(9):2403–2411, 1998.
- [78] J-C. Grenier, A. Wattiaux, J-P. Doumerc, P. Dordor, L. Fournes, J-P. Chaminade, and M. Pouchard. Electrochemical oxygen intercalation into oxide networks. *Journal of Solid State Chemistry*, 96(1):20 – 30, 1992.
- [79] M. Hücker, K. Chung, M. Chand, T. Vogt, J. M. Tranquada, and D. J. Buttrey. Oxygen and strontium codoping of La_2NiO_4 : Room-temperature phase diagrams. *Phys. Rev. B*, 70:064105, Aug 2004.
- [80] J.C. Grenier, A. Wattiaux, C. Monroux, M. Pouchard, and J.P. Locquet. Electrochemical oxygen insertion into La_2CuO_4 -related compounds. *Physica C: Superconductivity*, 235240, Part 1(0):79 – 82, 1994.
- [81] J.-C. Grenier, N. Lagueyte, A. Wattiaux, J-P. Doumerc, P. Dordor, J. Etourneau, M. Pouchard, J.B. Goodenough, and J.S. Zhou. Transport and magnetic properties of the superconducting $\text{La}_2\text{CuO}_{4+\delta}$ phases ($0 - \delta - 0.09$) prepared by electrochemical oxidation. *Physica C: Superconductivity*, 202(34):209 – 218, 1992.

- [82] M. Cyrot. On high T_c superconductivity in La_2CuO_4 type compounds. *Solid State Communications*, 62(12):821 – 823, 1987.
- [83] A. Demourgues, F. Weill, J.C. Grenier, A. Wattiaux, and M. Pouchard. Electron microscopy study of electrochemically prepared $\text{La}_2\text{NiO}_{4+\delta}$ ($0.17 \leq \delta \leq 0.26$). *Physica C: Superconductivity*, 192(34):425 – 434, 1992.
- [84] A. Demourgues, A. Wattiaux, J.C. Grenier, M. Pouchard, J.L. Soubeyrou, J.M. Dance, and P. Hagenmuller. Electrochemical Preparation and Structural Characterization of $\text{La}_2\text{NiO}_{4+\delta}$ Phases ($0 \leq \delta \leq 0.25$). *Journal of Solid State Chemistry*, 105(2):458 – 468, 1993.
- [85] C.N.R. Rao, P. Ganguly, K.K. Singh, and R.A.Mohan Ram. A comparative study of the magnetic and electrical properties of perovskite oxides and the corresponding two-dimensional oxides of K_2NiF_4 structure. *Journal of Solid State Chemistry*, 72(1):14 – 23, 1988.
- [86] J. D. Jorgensen, B. Dabrowski, Shiyu Pei, D. R. Richards, and D. G. Hinks. Structure of the interstitial oxygen defect in $\text{La}_2\text{NiO}_{4+\delta}$. *Phys. Rev. B*, 40:2187–2199, Aug 1989.
- [87] Loic Le Dreau. *Phase transitions and oxygen ordering in $\text{La}_2\text{CoO}_{4+\delta}$ and (T, T) - La_2CuO_4 : single crystal growth and structural studies using synchrotron and neutron diffraction methods*. PhD thesis, UMR CNRS 6226, Sciences Chimiques de Rennes, 2011.
- [88] J.E. Schirber, B. Morosin, R.M. Merrill, P.F. Hlava, E.L. Venturini, J.F. Kwak, P.J. Nigrey, R.J. Baughman, and D.S. Ginley. Stoichiometry of bulk superconducting $\text{La}_2\text{CuO}_{4+\delta}$: A superconducting superoxide? *Physica C: Superconductivity*, 152(1):121 – 123, 1988.
- [89] C. Chaillout, S.W. Cheong, Z. Fisk, M.S. Lehmann, M. Marezio, B. Morosin, and J.E. Schirber. The crystal structure of superconducting $\text{La}_2\text{CuO}_{4.032}$ by neutron diffraction. *Physica C: Superconductivity*, 158(12):183 – 191, 1989.
- [90] Myron Strongin, S. L. Qiu, Jie Chen, C. L. Lin, and E. M. McCarron. Question of superoxide in $\text{La}_2\text{CuO}_{4+\delta}$. *Phys. Rev. B*, 41:7238–7240, Apr 1990.
- [91] N. D. Shinn, J. W. Rogers, and J. E. Schirber. Reply to “Question of superoxide in $\text{La}_2\text{CuO}_{4+\delta}$. *Phys. Rev. B*, 41:7241–7242, Apr 1990.
- [92] J. W. Rogers, N. D. Shinn, J. E. Schirber, E. L. Venturini, D. S. Ginley, and B. Morosin. Reply to “Comment on ‘Identification of a superoxide in superconducting $\text{La}_2\text{CuO}_{4+\delta}$ by X-ray photoelectron spectroscopy’”. *Phys. Rev. B*, 39:12334–12335, Jun 1989.

- [93] Jianshi Zhou, Sanjai Sinha, and J. B. Goodenough. Comment on "Identification of a superoxide in superconducting $\text{La}_2\text{CuO}_{4+\delta}$ by X-ray photoelectron spectroscopy". *Phys. Rev. B*, 39:12331–12333, Jun 1989.
- [94] J. W. Rogers, N. D. Shinn, J. E. Schirber, E. L. Venturini, D. S. Ginley, and B. Morosin. Identification of a superoxide in superconducting $\text{La}_2\text{CuO}_{4+\delta}$ by X-ray photoelectron spectroscopy. *Phys. Rev. B*, 38:5021–5024, Sep 1988.
- [95] G. H. Lander, P. J. Brown, J. Spalek, and J. M. Honig. Structural and magnetization density studies of La_2NiO_4 . *Phys. Rev. B*, 40:4463–4471, Sep 1989.
- [96] M. Braden, P. Adelman, W. Paulus, P. Vigoureux, G. Andr, P. Schweiss, A. Cousson, A. Gukasov, S.N. Barilo, D.I. Zhigounov, and G. Heger. A study on the structural distortion of the T' phase. *Physica C: Superconductivity*, 235240, Part 2(0):793 – 794, 1994.
- [97] M. Medarde and J. Rodriguez-Carvajal. Oxygen vacancy ordering in $\text{La}_{2-x}\text{Sr}_x\text{NiO}_{4-\delta}$ ($x = 0 - 0.5$): the crystal structure and defects investigated by neutron diffraction. *Zeitschrift für Physik B Condensed Matter*, 102(3):307–315, 1997.
- [98] R. Le Toquin, W. Paulus, A. Cousson, G. Dhalenne, and A. Revcolevschi. Interstitial and apical oxygen orderdisorder in $\text{La}_2\text{CoO}_{4+\delta}$ observed by single-crystal neutron and X-ray diffraction. *Physica B: Condensed Matter*, 350(1-3):E269 – E272, 2004.
- [99] M. Crespin, J.M. Bassat, P. Odier, P. Mouron, and J. Choisnet. Synthesis and crystallographic characterization of the mixed-valence reduced nickelate $\text{La}_{1.6}\text{Sr}_{0.4}(\text{Ni(I),Ni(II)})\text{O}_{3.47}$. *Journal of Solid State Chemistry*, 84(1):165 – 170, 1990.
- [100] M. Crespin, C. Landron, P. Odier, J.M. Bassat, P. Mouron, and J. Choisnet. Evidence for nickel-(I)-rich mixed oxide with a defect K_2NiF_4 -type structure. *Journal of Solid State Chemistry*, 100(2):281 – 291, 1992.
- [101] A. Aguadero, J. A. Alonso, M. J. Martinez-Lope, M. T. Fernandez-Diaz, M. J. Escudero, and L. Daza. In situ high temperature neutron powder diffraction study of oxygen-rich $\text{La}_2\text{NiO}_{4+\delta}$ in air: correlation with the electrical behaviour. *J. Mater. Chem.*, 16:3402–3408, 2006.
- [102] Alexandr Nemudry, Peter Rudolf, and Robert Schöllhorn. Room temperature topotactic oxidation of lanthanum cobalt oxide $\text{La}_2\text{CoO}_{4.0}$. *Solid State Ionics*, 109(3-4):213 – 222, 1998.

- [103] A. Aguadero, L. Daza, and J.A. Alonso. Oxygen excess in $\text{La}_2\text{CoO}_{4+\delta}$: a neutron diffraction study. *Zeitschrift f. Naturforschung B: Chemical Sciences*, 63:615–622, 2008.
- [104] Elizabeth J. Opila, Harry L. Tuller, Bernhardt J. Wuensch, and Joachim Maier. Oxygen Tracer Diffusion in $\text{La}_{2-x}\text{Sr}_x\text{CuO}_{4-y}$ Single Crystals. *Journal of the American Ceramic Society*, 76(9):2363–2369, 1993.
- [105] Albert Tarancon, Monica Burriel, Jose Santiso, Stephen J. Skinner, and John A. Kilner. Advances in layered oxide cathodes for intermediate temperature solid oxide fuel cells. *J. Mater. Chem.*, 20:3799–3813, 2010.
- [106] Masatomo Yashima, Makiko Enoki, Takahiro Wakita, Roushown Ali, Yoshitaka Matsushita, Fujio Izumi, and Tatsumi Ishihara. Structural Disorder and Diffusional Pathway of Oxide Ions in a Doped Pr_2NiO_4 -Based Mixed Conductor. *Journal of the American Chemical Society*, 130(9):2762–2763, 2008.
- [107] Alexander Chroneos, David Parfitt, John A. Kilner, and Robin W. Grimes. Anisotropic oxygen diffusion in tetragonal $\text{La}_2\text{NiO}_{4+\delta}$: molecular dynamics calculations. *J. Mater. Chem.*, 20:266–270, 2010.
- [108] N F Mott. The Basis of the Electron Theory of Metals, with Special Reference to the Transition Metals. *Proceedings of the Physical Society. Section A*, 62(7):416, 1949.
- [109] J. Hubbard. Electron Correlations in Narrow Energy Bands. *Proceedings of the Royal Society of London. Series A. Mathematical and Physical Sciences*, 276(1365):238–257, 1963.
- [110] E. Pavarini, E. Koch, F. Anders, and Mark Jarrell. *Correlated electrons: from models to materials*. Forschungszentrum Julich GmbH Julich, 2012.
- [111] Neil W. Ashcroft and David N. Mermin. *Solid state physics*. Saunders College, 1976.
- [112] Masatoshi Imada, Atsushi Fujimori, and Yoshinori Tokura. Metal-insulator transitions. *Rev. Mod. Phys.*, 70:1039–1263, Oct 1998.
- [113] J. Zaanen, C. Westra, and G. A. Sawatzky. Determination of the electronic structure of transition-metal compounds: 2p x-ray photoemission spectroscopy of the nickel dihalides. *Phys. Rev. B*, 33:8060–8073, Jun 1986.
- [114] S. Hüfner. Analysis of the core level satellites in XPS spectra of Ni dihalides. *Solid State Communications*, 49(12):1177 – 1179, 1984.

- [115] Gerrit van der Laan. Electron correlation effects in the valence band photoemission spectra of copper dichloride. *Solid State Communications*, 42(3):165 – 168, 1982.
- [116] J. Zaanen, G. A. Sawatzky, and J. W. Allen. Band gaps and electronic structure of transition-metal compounds. *Phys. Rev. Lett.*, 55:418–421, Jul 1985.
- [117] Zhi-xun Shen, J. W. Allen, J. J. Yeh, J. S. Kang, W. Ellis, W. Spicer, I. Lindau, M. B. Maple, Y. D. Dalichaouch, M. S. Torikachvili, J. Z. Sun, and T. H. Geballe. Anderson Hamiltonian description of the experimental electronic structure and magnetic interactions of copper oxide superconductors. *Phys. Rev. B*, 36:8414–8428, Dec 1987.
- [118] Atsushi Fujimori and Fujio Minami. Valence-band photoemission and optical absorption in nickel compounds. *Phys. Rev. B*, 30:957–971, Jul 1984.
- [119] G. A. Sawatzky and J. W. Allen. Magnitude and Origin of the Band Gap in NiO. *Phys. Rev. Lett.*, 53:2339–2342, Dec 1984.
- [120] D. O. Smith. Magnetization of a Magnetite Single Crystal Near the Curie Point. *Phys. Rev.*, 102:959–963, May 1956.
- [121] Rudolf Peierls. *Surprises in Theoretical Physics*. Princeton Series in Physics, 1979.
- [122] Clarence Zener. Interaction between the *d*-Shells in the Transition Metals. II. Ferromagnetic Compounds of Manganese with Perovskite Structure. *Phys. Rev.*, 82:403–405, May 1951.
- [123] S. Jin, T. H. Tiefel, M. McCormack, R. A. Fastnacht, R. Ramesh, and L. H. Chen. Thousandfold Change in Resistivity in Magnetoresistive La-Ca-Mn-O Films. *Science*, 264(5157):413–415, 1994.
- [124] S. Jin, M. McCormack, T. H. Tiefel, and R. Ramesh. Colossal magnetoresistance in La-Ca-Mn-O ferromagnetic thin films (invited). *Journal of Applied Physics*, 76(10):6929–6933, 1994.
- [125] J. B. Goodenough. *Magnetism and the Chemical Bond*. Wiley, New York, 1963.
- [126] John B. Goodenough. Metallic oxides. *Progress in Solid State Chemistry*, 5(0):145 – 399, 1971.
- [127] P. W. Anderson. *Magnetism: A Treatise on Modern Theory and Materials*. New York: Academic Press, 1963.

- [128] Junjiro Kanamori. Superexchange interaction and symmetry properties of electron orbitals. *Journal of Physics and Chemistry of Solids*, 10(2-3):87 – 98, 1959.
- [129] S. Uchida, H. Eisaki, and S. Tajima. Electron correlation and optical conductivity in high-Tc copper oxides - origin of the mid-infrared absorption band. *Physica B: Condensed Matter*, 186188(0):975 – 980, 1993.
- [130] Patrick A. Lee, Naoto Nagaosa, and Xiao-Gang Wen. Doping a Mott insulator: Physics of high-temperature superconductivity. *Rev. Mod. Phys.*, 78:17–85, Jan 2006.
- [131] A.E. Bocquet, T. Saitoh, T. Mizokawa, and A. Fujimori. Systematics in the electronic structure of 3d transition-metal compounds. *Solid State Communications*, 83(1):11 – 15, 1992.
- [132] T. Ido, K. Magoshi, H. Eisaki, and S. Uchida. Optical study of the $\text{La}_{2-x}\text{Sr}_x\text{NiO}_4$ system: Effect of hole doping on the electronic structure of the NiO_2 plane. *Phys. Rev. B*, 44:12094–12097, Dec 1991.
- [133] S. Uchida, T. Ido, H. Takagi, T. Arima, Y. Tokura, and S. Tajima. Optical spectra of $\text{La}_{2-x}\text{Sr}_x\text{CuO}_4$: Effect of carrier doping on the electronic structure of the CuO_2 plane. *Phys. Rev. B*, 43:7942–7954, Apr 1991.
- [134] R. J. Cava, B. Batlogg, T. T. Palstra, J. J. Krajewski, W. F. Peck, A. P. Ramirez, and L. W. Rupp. Magnetic and electrical properties of $\text{La}_{2-x}\text{Sr}_x\text{NiO}_{4+\delta}$. *Phys. Rev. B*, 43:1229–1232, Jan 1991.
- [135] Y. Takeda, R. Kanno, M. Sakano, O. Yamamoto, M. Takano, Y. Bando, H. Akinaga, K. Takita, and J.B. Goodenough. Crystal chemistry and physical properties of $\text{La}_{2-x}\text{Sr}_x\text{NiO}_4$ ($0 \leq x \leq 1.6$) . *Materials Research Bulletin*, 25(3):293 – 306, 1990.
- [136] Xiang-Xin Bi and Peter C. Eklund. Polaron contribution to the infrared optical response of $\text{La}_{2-x}\text{Sr}_x\text{CuO}_{4+\delta}$ and $\text{La}_{2-x}\text{Sr}_x\text{NiO}_{4+\delta}$. *Phys. Rev. Lett.*, 70:2625–2628, Apr 1993.
- [137] A. P. Ramirez, P. L. Gammel, S-W. Cheong, D. J. Bishop, and P. Chandra. Charge Modulation in $\text{La}_{1.67}\text{Sr}_{0.33}\text{NiO}_4$: A Bulk Thermodynamic Study. *Phys. Rev. Lett.*, 76:447–450, Jan 1996.
- [138] Y. Moritomo, K. Higashi, K. Matsuda, and A. Nakamura. Spin-state transition in layered perovskite cobalt oxides: $\text{La}_{2-x}\text{Sr}_x\text{CoO}_4$ ($0.4 \leq x \leq 1.0$). *Phys. Rev. B*, 55:R14725–R14728, Jun 1997.

- [139] C. F. Chang, Z. Hu, Hua Wu, T. Burnus, N. Hollmann, M. Benomar, T. Lorenz, A. Tanaka, H.-J. Lin, H. H. Hsieh, C. T. Chen, and L. H. Tjeng. Spin Blockade, Orbital Occupation, and Charge Ordering in $\text{La}_{1.5}\text{Sr}_{0.5}\text{CoO}_4$. *Phys. Rev. Lett.*, 102:116401, Mar 2009.
- [140] M. Cwik. *The interplay of Lattice, Spin, and Charge Degrees of Freedom in Layered Cobaltates*. PhD thesis, Universität zu Kön, 2007.
- [141] D. Vaknin, S. K. Sinha, D. E. Moncton, D. C. Johnston, J. M. Newsam, C. R. Safinya, and H. E. King. Antiferromagnetism in La_2CuO_4 . *Phys. Rev. Lett.*, 58:2802–2805, Jun 1987.
- [142] G. Aeppli and D. J. Buttrey. Magnetic Correlations in $\text{La}_2\text{NiO}_{4+\delta}$. *Phys. Rev. Lett.*, 61:203–206, Jul 1988.
- [143] T. Thio, T.R. Thurston, N.W. Preyer, P.J. Picone, M.A. Kastner, H.P. Jenssen, D.R. Gabbe, C.Y. Chen, R.J. Birgeneau, and A. Aharony. Antisymmetric exchange and its influence on the magnetic structure and conductivity of La_2CuO_4 . *Physical Review B*, 38(1):905–908, 1988. cited By (since 1996)194.
- [144] M. Braden, G. Andr, S. Nakatsuji, and Y. Maeno. Crystal and magnetic structure of Ca_2RuO_4 : Magnetoelastic coupling and the metal-insulator transition. *Physical Review B - Condensed Matter and Materials Physics*, 58(2):847–861, 1998.
- [145] Nikolay Plakida. *High Temperature Cuprate Superconductors*. Springer, 2010.
- [146] Ch. Niedermayer, C. Bernhard, T. Blasius, A. Golnik, A. Moodenbaugh, and J. I. Budnick. Common Phase Diagram for Antiferromagnetism in $\text{La}_{2-x}\text{Sr}_x\text{CuO}_4$ and $\text{Y}_{1-x}\text{Ca}_x\text{Ba}_2\text{Cu}_3\text{O}_6$ as Seen by Muon Spin Rotation. *Phys. Rev. Lett.*, 80:3843–3846, Apr 1998.
- [147] J. M. Tranquada, J. D. Axe, N. Ichikawa, A. R. Moodenbaugh, Y. Nakamura, and S. Uchida. Coexistence of, and Competition between, Superconductivity and Charge-Stripe Order in $\text{La}_{1.6-x}\text{Nd}_{0.4}\text{Sr}_x\text{CuO}_4$. *Phys. Rev. Lett.*, 78:338–341, Jan 1997.
- [148] Hiroyuki Kimura, Kazuma Hirota, Hiroki Matsushita, Kazuyoshi Yamada, Yasuo Endoh, Seung-Hun Lee, Charles F. Majkrzak, Ross Erwin, Gen Shirane, Martin Greven, Young S. Lee, Marc A. Kastner, and Robert J. Birgeneau. Neutron-scattering study of static antiferromagnetic correlations in $\text{La}_{2-x}\text{Sr}_x\text{Cu}_{1-y}\text{Zn}_y\text{O}_4$. *Phys. Rev. B*, 59:6517–6523, Mar 1999.

- [149] S. Wakimoto, G. Shirane, Y. Endoh, K. Hirota, S. Ueki, K. Yamada, R. J. Birgeneau, M. A. Kastner, Y. S. Lee, P. M. Gehring, and S. H. Lee. Observation of incommensurate magnetic correlations at the lower critical concentration for superconductivity in $\text{La}_{2-x}\text{Sr}_x\text{CuO}_4$ ($x=0.05$). *Phys. Rev. B*, 60:R769–R772, Jul 1999.
- [150] John M. Tranquada. Neutron Scattering Studies of Antiferromagnetic Correlations in Cuprates. *arXiv:cond-mat/0512115v1*, 2005.
- [151] N. Bulut, D. Hone, D. J. Scalapino, and N. E. Bickers. Random-phase-approximation analysis of NMR and neutron-scattering experiments on layered cuprates. *Phys. Rev. Lett.*, 64:2723–2726, May 1990.
- [152] Qimiao Si, Yuyao Zha, K. Levin, and J. P. Lu. Comparison of spin dynamics in $\text{YBa}_2\text{Cu}_3\text{O}_{7-\delta}$ and $\text{La}_{2-x}\text{Sr}_x\text{CuO}_4$: Effects of Fermi-surface geometry. *Phys. Rev. B*, 47:9055–9076, Apr 1993.
- [153] N. Hasselmann, A. H. Castro Neto, and C. Morais Smith. Spin-glass phase of cuprates. *Phys. Rev. B*, 69:014424, Jan 2004.
- [154] Hiroyuki Kimura, Kazuma Hirota, Hiroki Matsushita, Kazuyoshi Yamada, Yasuo Endoh, Seung-Hun Lee, Charles F. Majkrzak, Ross Erwin, Gen Shirane, Martin Greven, Young S. Lee, Marc A. Kastner, and Robert J. Birgeneau. Neutron-scattering study of static antiferromagnetic correlations in $\text{La}_{2-x}\text{Sr}_x\text{Cu}_{1-y}\text{Zn}_y\text{O}_4$. *Phys. Rev. B*, 59:6517–6523, Mar 1999.
- [155] J.M Tranquada, N Ichikawa, K Kakurai, and S Uchida. Charge segregation and antiferromagnetism in high- T_c superconductors. *Journal of Physics and Chemistry of Solids*, 60(89):1019 – 1023, 1999.
- [156] H. Kimura, M. Kofu, Y. Matsumoto, and K. Hirota. Novel In-Gap Spin State in Zn-Doped $\text{La}_{1.85}\text{Sr}_{0.15}\text{CuO}_4$. *Phys. Rev. Lett.*, 91:067002, Aug 2003.
- [157] M. Kofu, H. Kimura, and K. Hirota. Zn and Ni doping effects on the low-energy spin excitations in $\text{La}_{1.85}\text{Sr}_{0.15}\text{CuO}_4$. *Phys. Rev. B*, 72:064502, Aug 2005.
- [158] Y. Sidis, P. Bourges, B. Hennion, L. P. Regnault, R. Villeneuve, G. Collin, and J. F. Marucco. Zinc-induced modification of the dynamical magnetic susceptibility in the superconducting state of $\text{YBa}_2\text{Cu}_3\text{O}_{6+x}$ as revealed by inelastic neutron scattering. *Phys. Rev. B*, 53:6811–6818, Mar 1996.
- [159] K. Kakurai, S. Shamoto, T. Kiyokura, M. Sato, J. M. Tranquada, and G. Shirane. Neutron-scattering study of magnetic fluctuations in Zn-substituted $\text{YBa}_2\text{Cu}_3\text{O}_{6.6}$. *Phys. Rev. B*, 48:3485–3490, Aug 1993.

- [160] J. M. Tranquada, D. J. Buttrey, V. Sachan, and J. E. Lorenzo. Simultaneous Ordering of Holes and Spins in $\text{La}_2\text{NiO}_{4.125}$. *Phys. Rev. Lett.*, 73:1003–1006, Aug 1994.
- [161] S. M. Hayden, G. H. Lander, J. Zarestky, P. J. Brown, C. Stassis, P. Metcalf, and J. M. Honig. Incommensurate magnetic correlations in $\text{La}_{1.8}\text{Sr}_{0.2}\text{NiO}_4$. *Phys. Rev. Lett.*, 68:1061–1064, Feb 1992.
- [162] C. H. Chen, S-W. Cheong, and A. S. Cooper. Charge modulations in $\text{La}_{2-x}\text{Sr}_x\text{NiO}_{4+y}$: Ordering of polarons. *Phys. Rev. Lett.*, 71:2461–2464, Oct 1993.
- [163] Kenji Nakajima, Yasuo Endoh, Syoichi Hosoya, Junichiro Wada, Detmar Welz, Hans-Michael Mayer, Hans-Anton Graf, and Michael Steiner. Neutron Scattering Study of Oxygen Ordering and Magnetic Correlations in $\text{La}_2\text{NiO}_{4.11}$ and $\text{La}_2\text{NiO}_{4.125}$. *Journal of the Physical Society of Japan*, 66(3):809–817, 1997.
- [164] J. M. Tranquada, J. E. Lorenzo, D. J. Buttrey, and V. Sachan. Cooperative ordering of holes and spins in $\text{La}_2\text{NiO}_{4.125}$. *Phys. Rev. B*, 52:3581–3595, Aug 1995.
- [165] J. M. Tranquada, P. Wochner, A. R. Moodenbaugh, and D. J. Buttrey. Field-induced staggered magnetic order in $\text{La}_2\text{NiO}_{4.133}$. *Phys. Rev. B*, 55:R6113–R6116, Mar 1997.
- [166] J. M. Tranquada, D. J. Buttrey, and V. Sachan. Incommensurate stripe order in $\text{La}_{2-x}\text{Sr}_x\text{NiO}_4$ with $x=0.225$. *Phys. Rev. B*, 54:12318–12323, Nov 1996.
- [167] J. M. Tranquada, P. Wochner, and D. J. Buttrey. Spin Dynamics in an Ordered Stripe Phase. *Phys. Rev. Lett.*, 79:2133–2136, Sep 1997.
- [168] H. Yoshizawa, T. Kakeshita, R. Kajimoto, T. Tanabe, T. Katsufuji, and Y. Tokura. Stripe order at low temperatures in $\text{La}_{2-x}\text{Sr}_x\text{NiO}_4$ with $0.289 \leq x \leq 0.5$. *Phys. Rev. B*, 61:R854–R857, Jan 2000.
- [169] P.D. Hatton, M.E. Ghazi, S.B. Wilkins, P.D. Spencer, D. Mannix, T. dAlmeida, P. Prabhakaran, A. Boothroyd, and S.-W. Cheong. X-ray scattering studies of charge stripes in $\text{La}_{2-x}\text{Sr}_x\text{NiO}_4$ ($x = 0.20 - 0.33$). *Physica B: Condensed Matter*, 318(4):289 – 294, 2002.
- [170] R. Kajimoto, K. Ishizaka, H. Yoshizawa, and Y. Tokura. Spontaneous rearrangement of the checkerboard charge order to stripe order in $\text{La}_{1.5}\text{Sr}_{0.5}\text{NiO}_4$. *Phys. Rev. B*, 67:014511, Jan 2003.
- [171] G. E. Bacon. Neutron diffraction. *Clarendon Press, Oxford*, 1975.

- [172] T. Kajitani, S. Hosoya, K. Hiraga, and T. Fukuda. Tetragonal Orthorhombic Phase Transition of $\text{La}_2\text{CoO}_{4+x}$. *J. Phys. Soc. Jpn.*, 59:562–570, 1989.
- [173] N. Sakiyama, I. A. Zaliznyak, S.-H. Lee, Y. Mitsui, and H. Yoshizawa. Doping-dependent charge and spin superstructures in layered cobalt perovskites. *Phys. Rev. B*, 78:180406, Nov 2008.
- [174] M. Cwik, M. Benomar, T. Finger, Y. Sidis, D. Senff, M. Reuther, T. Lorenz, and M. Braden. Magnetic Correlations in $\text{La}_{2-x}\text{Sr}_x\text{CoO}_4$ Studied by Neutron Scattering: Possible Evidence for Stripe Phases. *Phys. Rev. Lett.*, 102:057201, Feb 2009.
- [175] I. A. Zaliznyak, J. P. Hill, J. M. Tranquada, R. Erwin, and Y. Moritomo. Independent Freezing of Charge and Spin Dynamics in $\text{La}_{1.5}\text{Sr}_{0.5}\text{CoO}_4$. *Phys. Rev. Lett.*, 85:4353–4356, Nov 2000.
- [176] I. A. Zaliznyak, J. M. Tranquada, R. Erwin, and Y. Moritomo. Spin-entropy-driven melting of the charge order in $\text{La}_{1.5}\text{Sr}_{0.5}\text{CoO}_4$. *Phys. Rev. B*, 64:195117, Oct 2001.
- [177] Kenji Nakajima, Kazuyoshi Yamada, Syoichi Hosoya, Tomoya Omata, and Yasuo Endoh. Spin-Wave Excitations in Two Dimensional Antiferromagnet of Stoichiometric La_2NiO_4 . *Journal of the Physical Society of Japan*, 62(12):4438–4448, 1993.
- [178] A. T. Boothroyd, D. Prabhakaran, P. G. Freeman, S. J. S. Lister, M. Enderle, A. Hiess, and J. Kulda. Spin dynamics in stripe-ordered $\text{La}_{5/3}\text{Sr}_{1/3}\text{NiO}_4$. *Phys. Rev. B*, 67:100407, Mar 2003.
- [179] C. D. Batista, G. Ortiz, and A. V. Balatsky. Unified description of the resonance peak and incommensuration in high- T_c superconductors. *Phys. Rev. B*, 64:172508, Oct 2001.
- [180] Jan Zaanen. High-temperature superconductivity: The secret of the hourglass. *Nature*, 471, 2011.
- [181] A. T. Boothroyd, P. Babkevich, D. Prabhakaran, and P. G Freeman. An hour-glass magnetic spectrum in an insulating, hole-doped antiferromagnet. *Nature*, 471:341–344, 2011.
- [182] Thibault Broux, Carmelo Prestipino, Mona Bahout, Olivier Hernandez, Diptikanta Swain, Serge Paofai, Thomas C. Hansen, and Colin Greaves. Unprecedented High Solubility of Oxygen Interstitial Defects in $\text{La}_{1.2}\text{Sr}_{0.8}\text{MnO}_{4+\delta}$ up to $\delta \approx 0.42$ Revealed by In Situ High Temperature Neutron Powder Diffraction in Flowing O_2 . *Chemistry of Materials*, 25(20):4053–4063, 2013.

-
- [183] W.D. Kingery, H.K. Bowen, and D.R. Uhlmann. *Introduction to ceramics*. Wiley series on the science and technology of materials. Wiley, 1976.
- [184] C. Barry Carter and M. Grant Norton. *Ceramic Materials*. Springer New York, 2007.
- [185] W. Heywang. -. *Z. Naturforsch.*, 11a:238, 1956.
- [186] S.R. Coriell and M.R. Cordes. Theory of molten zone shape and stability. *Journal of Crystal Growth*, 42(0):466 – 472, 1977.
- [187] R.E. Green Jr. -. *J. Appl. Phys.*, 35:253, 1977.
- [188] C.W Lan. Three-dimensional simulation of floating-zone crystal growth of oxide crystals. *Journal of Crystal Growth*, 247(34):597 – 612, 2003.
- [189] R Hermann, J Priede, G Behr, G Gerbeth, and L Schultz. Influence of growth parameters and melt convection on the solidliquid interface during RF-floating zone crystal growth of intermetallic compounds. *Journal of Crystal Growth*, 223(4):577 – 587, 2001.
- [190] Tetsuo Munakata and Ichiro Tanasawa. Study on silicon melt convection during the RF-FZ crystal growth process: II. numerical investigation. *Journal of Crystal Growth*, 206(1-2):27 – 36, 1999.
- [191] Anita Fossdal, Mari-Ann Einarsrud, and Tor Grande. Phase equilibria in the pseudo-binary system SrOFe_2O_3 . *Journal of Solid State Chemistry*, 177(8):2933 – 2942, 2004.
- [192] V. L. MORUZZI and M. W. SHAFER. Phase Equilibria in the System La_2O_3 -Iron Oxide in Air. *Journal of the American Ceramic Society*, 43(7):367–372, 1960.
- [193] E.A. Tugova, V.F. Popova, I.A. Zvereva, and V.V. Gusarov. Phase diagram of the LaFeO_3 - LaSrFeO_4 system. *Glass Physics and Chemistry*, 32(6):674–676, 2006.
- [194] Official FullProf Suite website. <https://www.ill.eu/sites/fullprof/>. Accessed: 2014-05-19.
- [195] H. M. Rietveld. A profile refinement method for nuclear and magnetic structures. *Journal of Applied Crystallography*, 2(2):65–71, Jun 1969.
- [196] Juan Rodrguez-Carvajal. *An introduction to the program FullProf*. Laboratoire Lon Brillouin (CEA-CNRS), 2000.
- [197] J. Goldstein. *Scanning Electron Microscopy and X-ray Microanalysis: Third Edition*. Springer US, 2003.

- [198] L.H.J. Lajunen and Royal Society of Chemistry (Great Britain). *Spectrochemical Analysis by Atomic Absorption and Emission*. Royal Society of Chemistry, 1992.
- [199] J. Chadwick. Possible existence of a neutron. *Nature*, 129, 1932.
- [200] J. Chadwick. The Existence of a Neutron. *Proceedings of the Royal Society of London. Series A*, 136(830):692–708, 1932.
- [201] Official ILL IN22 website. <http://www.ill.eu/en/instruments-support/instruments-groups/instruments/in22/description/instrument-layout/>. Accessed: 2014-06-04.
- [202] Kimberly Chung. *Investigation of the structure and properties of LSNO*. PhD thesis, University of Delaware, 2008.
- [203] J.E. Millburn, M.A. Green, D.A. Neumann, and M.J. Rosseinsky. Evolution of the Structure of the K_2NiF_4 Phases $\text{La}_{2-x}\text{Sr}_x\text{NiO}_{4+\delta}$ with Oxidation State: Octahedral Distortion and Phase Separation ($0.2 \leq x \leq 1.0$). *Journal of Solid State Chemistry*, 145(2):401 – 420, 1999.
- [204] P. J. Heaney, A. Mehta, G. Sarosi, V. E. Lamberti, and A. Navrotsky. Structural effects of Sr substitution in $\text{La}_{2-x}\text{Sr}_x\text{NiO}_{4+\delta}$. *Phys. Rev. B*, 57:10370–10378, May 1998.
- [205] J. Gopalakrishnan, G. Colsmann, and B. Reuter. Studies on the $\text{La}_{2-x}\text{Sr}_x\text{NiO}_4$ ($0 \leq x \leq 1$) system. *Journal of Solid State Chemistry*, 22(2):145 – 149, 1977.
- [206] Donald F. Anthrop and Alan W. Searcy. Sublimation and Thermodynamic Properties of Zinc Oxide. *The Journal of Physical Chemistry*, 68(8):2335–2342, 1964.
- [207] N Hollmann, M W Haverkort, M Cwik, M Benomar, M Reuther, A Tanaka, and T Lorenz. Anisotropic susceptibility of $\text{La}_{2-x}\text{Sr}_x\text{CoO}_4$ related to the spin states of cobalt. *New Journal of Physics*, 10(2):023018, 2008.
- [208] N. Hollmann, M. W. Haverkort, M. Benomar, M. Cwik, M. Braden, and T. Lorenz. Evidence for a temperature-induced spin-state transition of Co^{3+} in $\text{La}_{2-x}\text{Sr}_x\text{CoO}_4$. *Phys. Rev. B*, 83:174435, May 2011.
- [209] Masashige Onoda, Shinichi Shamoto, Masatoshi Sato, and Syoichi Hosoya. Crystal Structures of $(\text{La}_{1-x}\text{M}_x)_2\text{CuO}_{4-\delta}$ ($\text{M}=\text{Sr}$ and Ba). *Japanese Journal of Applied Physics*, 26(4A):L363, 1987.

- [210] Zhiwei Hu. XAS ambient temperature measurements on highly doped cobaltates. private communication.
- [211] A. Komarek. Single Crystal X-Ray Diffraction Measurements. private communication.
- [212] Maurits W. Haverkort. Element Specific Monolayer Depth Profiling. private communication.
- [213] C. F. Chang, J. Schlappa, M. Buchholz, A. Tanaka, E. Schierle, D. Schmitz, H. Ott, R. Sutarto, T. Willers, P. Metcalf, L. H. Tjeng, and C. Schüsler-Langeheine. Intrinsic and extrinsic X-ray absorption effects in soft X-ray diffraction from the superstructure in magnetite. *Phys. Rev. B*, 83:073105, Feb 2011.
- [214] S. Subakti. Potentiometric titration results. private communication.
- [215] A. Sarapulova. Iodometric titration results. private communication.
- [216] W.M. Chen, C.C. Lam, J.F. Geng, L.Y. Li, K.C. Hung, and X. Jin. A new calculating formula of iodometric titration for high T_c superconductors. *Physica C: Superconductivity*, 270(12):155 – 158, 1996.
- [217] Zhiwei Hu. XAS measurement on ACK354. private communication.
- [218] Kazuyoshi Yamada, Tomoya Omata, Kenji Nakajima, Yasuo Endoh, and Syoichi Hosoya. Incommensurate magnetic correlations in $\text{La}_2\text{NiO}_{4.125}$: Magnetic phase diagram and two-dimensional hole-order. *Physica C: Superconductivity*, 221(34):355 – 362, 1994.
- [219] J. M. Tranquada, B. J Sternlieb, J. D Axe, Y Nakamura, and S Uchida. Evidence for stripe correlations of spins and holes in copper oxide. *Nature*, 375:561 – 563, 1995.
- [220] Official HRPD website. http://photon-science.desy.de/facilities/petra_iii/beamlines/p02_hard_x_ray_diffraction_beamline/hrpd/index_eng.html. Accessed: 2014-04-24.
- [221] P. Bourges, Y. Sidis, M. Braden, K. Nakajima, and J. M. Tranquada. High-Energy Spin Dynamics in $\text{La}_{1.69}\text{Sr}_{0.31}\text{NiO}_4$. *Phys. Rev. Lett.*, 90:147202, Apr 2003.
- [222] Hyungje Woo, A. T. Boothroyd, K. Nakajima, T. G. Perring, C. D. Frost, P. G. Freeman, D. Prabhakaran, K. Yamada, and J. M. Tranquada. Mapping spin-wave dispersions in stripe-ordered $\text{La}_{2-x}\text{Sr}_x\text{NiO}_4$ ($x=0.275, 0.333$). *Phys. Rev. B*, 72:064437, Aug 2005.

-
- [223] A. C. Komarek. *Complex ordering phenomena in transition metal oxides and oxyhalides*. PhD thesis, Universitaet zu Koeln, 2009.
- [224] A. Hammersley. Official Fit2D website. <http://www.esrf.eu/computing/scientific/FIT2D/>. Accessed: 2014-04-24.
- [225] V. Sachan, D. J. Buttrey, J. M. Tranquada, J. E. Lorenzo, and G. Shirane. Charge and spin ordering in $\text{La}_{2-x}\text{Sr}_x\text{NiO}_{4.00}$ with $x=0.135$ and 0.20 . *Phys. Rev. B*, 51:12742–12746, May 1995.
- [226] P. D. Spencer, M. E. Ghazi, S. B. Wilkins, P. D. Hatton, S. D. Brown, D. Prabhakaran, and A. T. Boothroyd. Charge stripe glasses in $\text{La}_{2-x}\text{Sr}_x\text{NiO}_4$ for $0.20 \leq x \leq 0.25$. *The European Physical Journal B - Condensed Matter and Complex Systems*, 46(1):27–32, 2005.
- [227] Pengcheng Dai, H. A. Mook, R. D. Hunt, and F. Dogan. Evolution of the resonance and incommensurate spin fluctuations in superconducting $\text{YBa}_2\text{Cu}_3\text{O}_{6+x}$. *Phys. Rev. B*, 63:054525, Jan 2001.
- [228] Official ill flatcone detector website. <http://www.ill.eu/en/html/instruments-support/instruments-groups/instruments/flatcone/characteristics/>. Accessed: 2014-06-12.
- [229] R. M. Moon, T. Riste, and W. C. Koehler. Polarization Analysis of Thermal-Neutron Scattering. *Phys. Rev.*, 181:920–931, May 1969.
- [230] Tapan Chatterji. *Neutron Scattering from Magnetic Materials*. Elsevier Amsterdam, 2006.
- [231] Frank Krüger and Stefan Scheidl. Spin dynamics of stripes. *Phys. Rev. B*, 67:134512, Apr 2003.
- [232] E. W. Carlson, D. X. Yao, and D. K. Campbell. Spin waves in striped phases. *Phys. Rev. B*, 70:064505, Aug 2004.
- [233] Kenji Nakajima, Kazuyoshi Yamada, Syoichi Hosoya, Tomoya Omata, and Yasuo Endoh. Spin-Wave Excitations in Two Dimensional Antiferromagnet of Stoichiometric La_2NiO_4 . *Journal of the Physical Society of Japan*, 62(12):4438–4448, 1993.
- [234] D. X. Yao, E. W. Carlson, and D. K. Campbell. Magnetic Excitations of Stripes near a Quantum Critical Point. *Phys. Rev. Lett.*, 97:017003, Jul 2006.
- [235] P. G. Freeman, M. Enderle, S. M. Hayden, C. D. Frost, D. X. Yao, E. W. Carlson, D. Prabhakaran, and A. T. Boothroyd. Inward dispersion of the spin excitation spectrum of stripe-ordered $\text{La}_2\text{NiO}_{4+\delta}$. *Phys. Rev. B*, 80:144523, Oct 2009.

- [236] M. Rotter and A. Komarek. Unpublished results. private communication.
- [237] M. Matsuda, M. Fujita, S. Wakimoto, J. A. Fernandez-Baca, J. M. Tranquada, and K. Yamada. Magnetic Dispersion of the Diagonal Incommensurate Phase in Lightly Doped $\text{La}_{2-x}\text{Sr}_x\text{CuO}_4$. *Phys. Rev. Lett.*, 101:197001, Nov 2008.
- [238] M. Arai, T. Nishijima, Y. Endoh, T. Egami, S. Tajima, K. Tomimoto, Y. Shiohara, M. Takahashi, A. Garrett, and S. M. Bennington. Incommensurate Spin Dynamics of Underdoped Superconductor $\text{YBa}_2\text{Cu}_3\text{O}_{6.7}$. *Phys. Rev. Lett.*, 83:608–611, Jul 1999.
- [239] P. Bourges, Y. Sidis, H. F. Fong, L. P. Regnault, J. Bossy, A. Ivanov, and B. Keimer. The Spin Excitation Spectrum in Superconducting $\text{YBa}_2\text{Cu}_3\text{O}_{6.85}$. *Science*, 288(5469):1234–1237, 2000.
- [240] N. B. Christensen, D. F. McMorrow, H. M. Rønnow, B. Lake, S. M. Hayden, G. Aeppli, T. G. Perring, M. Mangkorntong, M. Nohara, and H. Takagi. Dispersive Excitations in the High-Temperature Superconductor $\text{La}_{2-x}\text{Sr}_x\text{CuO}_4$. *Phys. Rev. Lett.*, 93:147002, Sep 2004.
- [241] O. J. Lipscombe, B. Vignolle, T. G. Perring, C. D. Frost, and S. M. Hayden. Emergence of Coherent Magnetic Excitations in the High Temperature Underdoped $\text{La}_{2-x}\text{Sr}_x\text{CuO}_4$ Superconductor at Low Temperatures. *Phys. Rev. Lett.*, 102:167002, Apr 2009.
- [242] V. Hinkov, P. Bourges, S. Pailhes, Y. Sidis, A. Ivanov, C. D. Frost, T. G. Perring, C. T. Lin, D. P. Chen, and B. Keimer. Testing the itinerancy of spin dynamics in superconducting $\text{Bi}_2\text{Sr}_2\text{CaCu}_2\text{O}_{8+\delta}$. *Nat Phys*, 3:780–785, 2007.
- [243] V. Hinkov, P. Bourges, S. Pailhes, Y. Sidis, A. Ivanov, C. D. Frost, T. G. Perring, C. T. Lin, D. P. Chen, and B. Keimer. Spin dynamics in the pseudogap state of a high-temperature superconductor. *Nat Phys*, 3, 2007.
- [244] Matthias Vojta, Thomas Vojta, and Ribhu K. Kaul. Spin Excitations in Fluctuating Stripe Phases of Doped Cuprate Superconductors. *Phys. Rev. Lett.*, 97:097001, Aug 2006.
- [245] G. Seibold and J. Lorenzana. Magnetic Fluctuations of Stripes in the High Temperature Cuprate Superconductors. *Phys. Rev. Lett.*, 94:107006, Mar 2005.
- [246] I. Eremin, D. K. Morr, A. V. Chubukov, K. H. Bennemann, and M. R. Norman. Novel neutron resonance mode in $d_{x^2-y^2}$ -wave superconductors. *Phys. Rev. Lett.*, 94:147001, Apr 2005.

- [247] Eric C. Andrade and Matthias Vojta. Disorder, Cluster Spin Glass, and Hourglass Spectra in Striped Magnetic Insulators. *Phys. Rev. Lett.*, 109:147201, Oct 2012.
- [248] Official ID22 homepage. <http://www.esrf.eu/UsersAndScience/Experiments/StructMaterials/ID22>. Accessed: 2014-04-24.
- [249] S.-H. Lee and S-W. Cheong. Melting of Quasi-Two-Dimensional Charge Stripes in $1/3$ LSNO. *Phys. Rev. Lett.*, 79:2514–2517, Sep 1997.
- [250] J. M. Tranquada, K. Nakajima, M. Braden, L. Pintschovius, and R. J. McQueeney. Bond-Stretching-Phonon Anomalies in Stripe-Ordered $\text{La}_{1.69}\text{Sr}_{0.31}\text{NiO}_4$. *Phys. Rev. Lett.*, 88:075505, Jan 2002.
- [251] D. Reznik, L. Pintschovius, M. Ito, M. Iikubo, S. and Sato, H. Goka, M. Fujita, K. Yamada, G. D. Gu, and J. M. Tranquada. Electron-phonon coupling reflecting dynamic charge inhomogeneity in copper oxide superconductors. *Nature*, 440, 2006.
- [252] M. Matsuda, G. E. Granroth, M. Fujita, K. Yamada, and J. M. Tranquada. Energy-dependent crossover from anisotropic to isotropic magnetic dispersion in lightly doped $\text{La}_{1.96}\text{Sr}_{0.04}\text{CuO}_4$. *Phys. Rev. B*, 87:054508, Feb 2013.
- [253] L. M. Helme, A. T. Boothroyd, R. Coldea, D. Prabhakaran, C. D. Frost, D. A. Keen, L. P. Regnault, P. G. Freeman, M. Enderle, and J. Kulda. Magnetic order and dynamics of the charge-ordered antiferromagnet $\text{La}_{1.5}\text{Sr}_{0.5}\text{CoO}_4$. *Phys. Rev. B*, 80:134414, Oct 2009.
- [254] P. Babkevich, D. Prabhakaran, C. D. Frost, and A. T. Boothroyd. Magnetic spectrum of the two-dimensional antiferromagnet La_2CoO_4 studied by inelastic neutron scattering. *Phys. Rev. B*, 82:184425, Nov 2010.
- [255] Oleg P. Sushkov and Valeri N. Kotov. Theory of Incommensurate Magnetic Correlations Across the Insulator-Superconductor Transition of Underdoped $\text{La}_{2-x}\text{Sr}_x\text{CuO}_4$. *Phys. Rev. Lett.*, 94:097005, Mar 2005.
- [256] Y. Drees, D. Lamago, A. Piovano, and A. C. Komarek. Hour-glass magnetic spectrum in a stripeless insulating transition metal oxide. *Nat Commun*, 4, Sep 2013.
- [257] Andreas Lüscher, Alexander I. Milstein, and Oleg P. Sushkov. Structure of the Spin-Glass State of $\text{La}_{2-x}\text{Sr}_x\text{CuO}_4$: The Spiral Theory. *Phys. Rev. Lett.*, 98:037001, Jan 2007.
- [258] N. Hasselmann, A. H. Castro Neto, and C. Morais Smith. Spin-glass phase of cuprates. *Phys. Rev. B*, 69:014424, Jan 2004.

-
- [259] John M. Tranquada. Cuprates Get Orders to Charge. *Science*, 337(6096):811–812, 2012.

List of Abbreviations

- **10Dq**: Crystal field splitting between e_g and t_{2g} orbitals
- **AF**: Antiferromagnet, antiferromagnetic
- **CSO**: Charge stripe order
- **CBCO**: Checkerboard charge order
- **CGHE**: Carrier gas hot extraction
- **CO**: Charge order
- **CT**: Charge transfer
- δ : Oxygen content off stoichiometry
- ϵ : The incommensurability is a component in the propagation vector of a superstructure which is incommensurate with the crystal lattice (with $\epsilon = \epsilon_{charge} = 2\epsilon_{magnetic}$).
- **EDX**: Energy dispersive spectroscopy
- **E_r** : Resonance energy - at T_c spectral weight is shifted to E_r in HTSC
- **FM**: Ferromagnet, ferromagnetic
- **HTSC**: High temperature superconductivity
- **ICP-OES**: Inductively coupled plasma atomic emission spectroscopy
- **INS**: Inelastic neutron scattering
- **LSCoO**: Lanthanum strontium cobalt oxide
- **LSCO**: Lanthanum strontium copper oxide
- **LSNO**: Lanthanum strontium nickel oxide

- **n_h** : Electron hole concentration
- **SC**: Superconductivity
- **SO**: Spin order
- **WDX**: Wavelength dispersive spectroscopy
- **T_c** : Critical temperature in HTSC
- **TG**: Thermogravimetry

Abstract

Single layered perovskites with the chemical formula $\text{La}_{2-x}\text{Sr}_x\text{TO}_4$ (T = transition metal) exhibit a variety of intriguing ordering phenomena. The most outstanding is the occurrence of high temperature superconductivity in $\text{La}_{2-x}\text{Sr}_x\text{CuO}_4$, which can be considered as the prototype system for the more complex cuprates. Some cuprates show incommensurate static charge order at low temperatures [38–40]. For others it is believed that charges are dynamically correlated [39, 147, 259]. Such effects are difficult to measure if the charges fluctuate.

In contrast to the cuprate $\text{La}_{2-x}\text{Sr}_x\text{CuO}_4$ the isostructural nickelates and cobaltates remain insulating over a wide doping range [112, 134, 135, 138]. While incommensurate charge stripe order is long known for the nickelates, recently also evidence for charge stripes in cobaltates has been published [174].

Single crystal rods, with ≈ 10 cm length and ≈ 0.8 cm diameter, have been grown by the traveling solvent floating zone technique using an optical four mirror furnace. We investigated strontium doped nickelates in the range $0.15 \leq x \leq 0.22$. In addition, also co-doped nickelates have been investigated. A large number of samples with different doping concentrations enabled us to systematically characterize the sample properties. Powder X-ray diffraction measurements were used to determine the lattice parameters. For the nickelates we could confirm the doping dependence of the lattice constants reported in literature [202].

The main interest for the cobaltate system was in the strontium doping range $1/3 \leq x \leq 1/2$. It was previously reported that the *ab*-lattice parameter exhibits an anomalous peak around a Sr doping $x \approx 1/3$ [140]. We could not confirm such an anomaly for our samples and, instead, we observe a strictly monotonic doping dependence of the lattice parameters which we attribute to the close to perfect stoichiometry of our samples.

Samples with the 214-layered perovskite structure can be synthesized over a wide range of oxygen off-stoichiometry. However, the oxygen content can have similarly strong influence on the sample properties as strontium doping. It is therefore essential for data interpretation to determine the oxygen off stoichiometry. EDX and WDX measurements were used to confirm the oxygen content

in our nickelates to be nearly stoichiometric. The oxygen content determination of the cobaltates is somewhat more difficult. Thermogravimetry measurements in a flow of Ar/H₂ confirmed a nearly stoichiometric oxygen content δ in La_{2-x}Sr_xCoO_{4+δ} for all samples.

We used neutron diffraction measurements to determine the magnetic order in our nickelate samples. In stripe ordered nickelates a small titanium co-doping of the order of 5 % is sufficient to suppress the incommensurate magnetism and restore antiferromagnetic order. Within the series of zinc co-doped nickelates three samples exhibit an incommensurability $\epsilon \approx 1/8$, indicating the stabilization of an intermediate stripe pattern with an eightfold unit cell. Compared to the $\epsilon \approx 1/3$ regime the correlation length is greatly reduced.

The magnon dispersion of two samples within the intermediate stripe phases with $\epsilon \approx 1/8$ and $\epsilon \approx 1/4$ has been measured with neutron spectroscopy. The observed dispersion neither resembles the one in the undoped nor the 1/3 strontium doped samples. Despite the amount of disorder in our co-doped nickelate materials there are no clear signs for the emergence of hourglass spectra which is most likely caused by a strong exchange interaction across the holes.

We investigated the charge and magnetic order in the incommensurate regime of La_{2-x}Sr_xCoO₄ with doping $0.33 \leq x \leq 0.5$ by elastic neutron scattering and hard X-ray synchrotron measurements. In contrast to the established opinion that this phase is characterized by charge stripe order we were able to show that no charge stripes are present. Instead we found that checkerboard charge order, which is most stable at $x = 1/2$, persists to a much lower doping than previously thought. The absence of charge stripes is also in agreement with the dispersion of the top most Co-O bond stretching phonon mode. Charge order can induce an anomaly in this branch according to the modulation vector \vec{q} . We observed a softening at $\vec{q} = (1/2 \ 1/2 \ 0)$, which is consistent with our expectations for a checkerboard charge ordered phase.

Inelastic neutron measurements revealed an additional high energy part of the hourglass dispersion which has not been reported so far. The entire low-energy spin excitations that belong to the classical hour-glass dispersion are mostly in-plane excitations, the newly discovered high-energy magnon mode arises from out-of-plane excitations. The resemblance between the low energy excitations below the neck of the hourglass with the excitations in La_{1.5}Sr_{0.5}CoO₄ and similarly between the high energy excitations with those observed in La₂CoO₄ suggests that the observed dispersion is not a single dispersion, but instead consists of two dispersions with distinct origin. In this model the low-energy dispersion arises mainly from magnetic excitations of hole doped regions and the high-energy part would be connected to magnetic excitations within the undoped islands.

The absence of charge stripe order in the insulating cobaltates in combination with an unmagnetic low spin state for Co⁺³ requires a different explanation

for the presence of incommensurate magnetic order. We propose a picture on the basis of the ideal checkerboard charge order of the half doped reference system. Decreasing the strontium concentration requires the replacement of Co^{+3} by Co^{+2} , effectively resulting in the competition between the antiferromagnetic order of the undoped and the antiferromagnetic order of the half doped compound. The induced frustration can be released by a twisting of magnetic moments away from their antiferromagnetic orientation, ultimately leading to the observed incommensurate magnetic order.

Acknowledgements

Now some words of thanks to all people whose advice, support and input made this thesis possible and even became part of it.

I would like to thank my supervisor Prof. L. H. Tjeng for the opportunity to write my thesis in the fascinating field of layered perovskites. His critical view concerning new results and hypotheses helped to refine the conclusions and to separate them from wishful thinking.

Thanks to Prof. Loewenhaupt for his willingness to act as second referee.

Many thanks to my supervisor A. C. Komarek with whom I could discuss everything extensively. He made most of the studied crystals, taught me the floating zone method and constantly guided me through the various projects that we pursued, always hunting for new and intriguing physics.

My thanks goes to all members of our institute for the good atmosphere and the willingness to always help each other physically and mentally: S. Agrestini, C. F. Chang, A. Efimenko, Zhiwei Hu, D. Kasinathan, K. T. Ko, C. Y. Kuo, Y. Lu, D. Mikhailova, A. Reisner, S. Rößler, Y. Utsumi, M. Valldor and S. Wirth. I appreciated the open door of M. Haverkort whose concern seemed to include every possible topic and who always gave constructive remarks. With his large experience P. Thalmeier helped refining the cobaltate results. Thanks to A. Sarapulova and S. Subakti for characterizing some samples by titration measurements. Special thanks to Z. Li with whom I had great times working closely together in the lab and on our numerous beamtimes. For the productive and relaxed climate in our office I would like to thank A. Karimzadehsharifabadi and A. Keil.

Thanks for sample characterization measurements and discussions to all members of the competence groups: G. Auffermann and her team for the chemical analysis, U. Burkhardt and his team for EDX/WDX measurements, M. Schmidt and his team for the oxygen content determination with TG and The XRD team H. Borrmann, Y. Prots and S. Hückmann for their numerous recorded X-ray patterns.

I thank the instrument responsables for their help and support during beam-times: D. Lamago and J. P. Castellan made the measurements at the instruments 1T1, 2T1, 3T1 and 4F2 possible. W. Schmidt ensured a smooth realization of the beamtimes at the instruments IN3, IN12 and IN22. The IN22 measurements also benefited from the aid of L. P. Regnault. A. Piovano and A. Ivanov taught me the features of the IN8 and how to control the instrument. H. P. Liermann provided a friendly user beamtime at his instrument P02. O. Gutowski and U. Rütt dedicated many efforts to a successful experiment at the beamline P07.

Finally, and most importantly, I would like to thank my wife S. Drees for her support, quiet patience, and keeping the family going during my absences and the challenging last few months.

List of Publications

- Z.W. Li, Y. Drees, H. Guo, C. Y. Kuo, D. Lamago, O. Sobolev, T. W. Pi, K. Mogare, Z. Hu, L. H. Tjeng, and A. C. Komarek
Incommensurate spin correlations in the highly hole-doped regime of $\text{La}_{2-x}\text{Sr}_x\text{CoO}_4$ ($1/2 < x < 1$)
submitted to Phys. Rev. Lett. (November 2014)
- Y. Drees, L. H. Tjeng, and A. C. Komarek
Single crystal growth of $\gamma\text{-CoV}_2\text{O}_6$ by the floating zone method
submitted to Journal of Crystal Growth (September 2014)
- Y. Drees, Z.W. Li, A. Ricci, M. Rotter, W. Schmidt, D. Lamago, O. Sobolev, U. Rtt, O. Gutowski, M. Sprung, A. Piovano, J. P. Castellan, & A. C. Komarek
Hour-glass magnetic excitations induced by nanoscopic phase separation in cobalt oxides
Nat Commun **5**, 6731 (2014)
- C.-Y. Kuo, Y. Drees, M. T. Fernández-Díaz, L. Zhao, L. Vasylechko, D. Sheptyakov, A. M. T. Bell, T. W. Pi, H.-J. Lin, M.-K. Wu, E. Pellegrin, S. M. Valvidares, Z. W. Li, P. Adler, A. Todorova, R. Kchler, A. Steppke, L. H. Tjeng, Z. Hu, and A. C. Komarek
 $k = 0$ magnetic structure and absence of ferroelectricity in SmFeO_3
Phys. Rev. Lett. **113**, 217203 (2014)
- Y. Drees, D. Lamago, A. Piovano & A.C. Komarek
Hour-glass magnetic spectrum in a stripeless insulating transition metal oxide
Nat Commun **4**, 3449 (2013)

Versicherung

Hiermit versichere ich, dass ich die vorliegende Arbeit ohne unzulässige Hilfe Dritter und ohne Benutzung anderer als der angegebenen Hilfsmittel angefertigt habe; die aus fremden Quellen direkt oder indirekt übernommenen Gedanken sind als solche kenntlich gemacht. Die Arbeit wurde bisher weder im Inland noch im Ausland in gleicher oder ähnlicher Form einer anderen Prüfungsbehörde vorgelegt.

Es haben keine früheren erfolglosen Promotionsverfahren stattgefunden.

Die Promotionsordnung vom 23.02.2011 wird anerkannt.

Datum, Unterschrift